Internally and externally driven flows of complex fluids: viscoelastic active matter, flows in porous media and contact line dynamics

HEMINGWAY, EWAN,JOHN

Internally and externally driven flows of complex fluids: viscoelastic active matter, flows in porous media and contact line dynamics

Ewan Hemingway

A Thesis presented for the degree of
Doctor of Philosophy

Supervised by Prof. Suzanne Fielding
Department of Physics
University of Durham
UK

July 2015

Abstract

We consider three varied soft matter topics from a continuum fluid mechanics perspective, namely: viscoelastic active matter, viscoelastic flows in porous media, and contact line dynamics.

Active matter. For the purposes of this thesis, the term active matter describes a collection of active particles which absorb energy from their local environment or from an internal fuel tank and dissipate it to the surrounding fluid. We explore the stability and dynamics of active matter in a biological context in the presence of a polymeric background fluid. Using a novel coarse-grained model, we generalise earlier linear stability analyses (without polymer) and demonstrate that the bulk orientationally ordered phase remains intrinsically unstable to spontaneous flow instabilities. This instability remains even as one takes an 'elastomeric limit' in which the polymer relaxation time $\tau_C \to \infty$. The 1D nonlinear dynamics in this limit are oscillatory on a timescale set by the rate of active forcing.

Then, by considering the rheological response of our model under shear, we explore the mechanism behind the above generic flow instability, which we show exists not only for orientationally ordered phases but also for disordered states deep in the isotropic phase. Our linear stability analysis in 1D for sheared suspensions predicts that initially homogeneous states represented by negatively sloping regions of the constitutive curve are unstable to shear-banding flow instabilities. In some cases, the shear-bands themselves are unstable which leads to a secondary instability that produces rheochaotic flow states.

Consistent with recent experiments on active cellular extracts (without applied shear) which show apparently chaotic flow states, we find that the dynamics of active matter are significantly more complex in 2D. Focusing on the turbulent phase that occurs when the activity ζ (or energy input) is large, we show that the characteristic lengthscale of structure in the fluid l^* scales as $l^* \propto 1/\sqrt{\zeta}$. While this lengthscale decreases with ζ, it also increases with the polymer relaxation time.

This can produce a novel 'drag reduction' effect in confined geometries where the system forms more coherent flow states, characterised by net material transport. In the elastomeric limit spontaneous flows may still occur, though these appear to be transient in nature. Examples of exotic states that arise when the polymer is strongly coupled to the active particles are also given.

Flows in porous media. The second topic treats viscoelastic flows in porous media, which we approximate numerically using geometries consisting of periodic arrays of cylinders. Experimentally, the normalised drag χ (i.e., the ratio of the pressure drop to the flow rate) is observed to undergo a large increase as the Weissenberg number We (which describes the ratio of the polymer relaxation time to the characteristic velocity-gradient timescale) is increased. An analysis of steady flow in the Newtonian limit identifies regions dominated by shear and extension; these are mapped to the rheological behaviour of several popular models for polymer viscoelasticity in simple viscometric protocols, allowing us to study and influence the upturn in the drag.

We also attempt to reproduce a recent study in the literature which reported fluctuations for cylinders confined to a channel at high We. At low numerical resolution, we observe fluctuations which increase in magnitude with the same scaling observed in that study. However, these disappear at very high resolutions, suggesting that numerical convergence was not properly obtained by the earlier authors.

Contact line dynamics. We finish by investigating the dynamics of the contact line, i.e., the point at which a fluid-fluid interface meets a solid surface, under an externally applied shear flow. The contact line moves relative to the wall, apparently contradicting the conventional no-slip boundary conditions employed in continuum fluid dynamics. A mechanism where material is transported within a 'slip region' via diffusive processes resolves this paradox, though the question of how the size of this region (i.e., slip length ξ) scales with fluid properties such as the viscosity η and the width of the interface between phases ℓ, remains disputed within the literature. We reconcile two apparently contradictory scalings, which are shown to describe different limits: (a) a diffuse interface limit where ξ/ℓ is small and (b) a

sharp interface limit for large ξ/ℓ. We demonstrate that the physics of the latter (which more closely resembles real fluids in macroscopic experimental geometries) can be captured using simulations in the former regime (which are numerically more accessible).

Declaration

The work in this thesis is based on research carried out under the supervision of Prof. Suzanne Fielding, in the Department of Physics, University of Durham, England. No part of this thesis has been submitted elsewhere for any other degree or qualification and it is all my own work unless referenced to the contrary in the text.

Publications

Hemingway, E. J., Maitra, A., Banerjee, S., Marchetti, M. C., Ramaswamy, S., Fielding, S. M., & Cates, M. E. (2015). "Active Viscoelastic Matter: From Bacterial Drag Reduction to Turbulent Solids". *Phys. Rev. Lett.*, **114**, 098302. *I performed the linear stability analysis and 2D nonlinear simulations, with supervision and feedback from S. M. Fielding. The model was derived by M. E. Cates, A. Maitra, S. Ramaswamy, S. Banerjee, and M. C. Marchetti. This work forms the basis of Chaps. 3 to 5.*

Manuscripts in preparation

Hemingway, E. J., Cates, M. E., & Fielding, S. M. "Viscoelastic active nematics: Linear instability and nonlinear dynamics". *In preparation. I performed the linear stability analysis and 1D/2D nonlinear simulations. M. E. Cates and S. M. Fielding provided supervision and feedback. This work forms the basis of Chaps. 3 to 5.*

Hemingway, E. J., Cates, M. E., & Fielding, S. M. "Spontaneous flow instabilities in isotropic active matter". *In preparation. I performed the linear stability analysis and 1D nonlinear simulations. M. E. Cates and S. M. Fielding provided supervision and feedback. This work forms part of Chap. 3 and Chap. 4.*

Mishra, P., Marchetti, M. C., **Hemingway, E. J.**, & Fielding, S. M, "Correlation lengths in active nematics". *In preparation. I contributed data using*

Model II. Prashant Mishra performed simulations with Model I and was the lead author. S. M. Fielding and M. C. Marchetti provided feedback and supervision. This work forms part of Sec. 5.2.

Kusumaatmaja, H., **Hemingway, E. J.** & Fielding, S. M. "Moving contact line dynamics: from diffuse to sharp interfaces". *Submitted to J. Fluid Mech. (see arXiv:1507.08945). I contributed numerical data using Method II, and additionally studied the effects of modifying the free energy and Poiseuille flows. This forms the basis of Chap. 7.*

Acknowledgements

Firstly, I am indebted to Suzanne Fielding for her continuous support, guidance and encouragement throughout my PhD. Her approach to research, which is incisive, careful and pragmatic, has influenced my own research methodology greatly. She has also provided me with invaluable career advice and opportunities, and I greatly look forward to continuing our strong working relationship in my postdoctoral position which starts later this year.

I would also like to extend thanks to those collaborators with whom I have had the great pleasure of working with throughout my PhD. Special thanks are owed to Mike Cates who has also supervised me throughout the extensive active matter project. His rigorous and concise approach to science has had a lasting impact on my research attitudes, and his patience in deciphering the key physics within my (rambling) progress reports is greatly appreciated. My time at the "Active Matter" programme at KITP in California was particularly illuminating, as were the resulting discussions with Christina Marchetti, Sriram Ramaswamy, Ananyo Maitra, and Prashant Mishra. Within Durham, I am thankful to Halim Kusumaatmaja for insightful discussions during our investigations into the dynamics of the contact line, and John Girkin for support as my second supervisor. I would also like to thank Dr Andrew Clarke at Schlumberger for support and discussions during the porous media study.

I have received much support from friends and colleagues during my time at Durham. Particular thanks are due to my office mates for stimulating discussions and advice (both academic and otherwise): Robyn Cooke, Ricard Matas-

Navaro, David Hoyle, Rangarajan Radhakrishnan, Katherine Carter, Lara Small, Rob Williams and Rahul Chacko. Thanks also go to my other friends within physics, Peter Byrne, Tom Frawley, Tom Hollins who have provided much entertainment with their perceived rivalry between the fields of soft and hard condensed matter (despite my protestations). I would also like to thank my former house mates from Ferens Park who have deepened my understanding of galaxy formation, whether I asked about it or not!

I would like to thank my close friends and family who, despite sounding suitably baffled whenever I talk about my research, have been continually supportive throughout my academic career. Finally, I would like to thank Kelly, who has been singularly supportive and loving throughout our time together, and whose delicious supply of tiffin has single-handedly fuelled my late night thesis writing.

Contents

List of Figures

List of Tables

1

Introduction

Natural flows of both great beauty and importance can be found across a vast span of lengthscales: from the organised subcellular transport of nutrients [1] ($10^{-7} \rightarrow 10^{-5}$ m), to rolling droplets on the hydrophobic surface of a butterfly's wing [2] ($10^{-2} \rightarrow 10^{-1}$ m), to the turbulent vortices surrounding the eye of Jupiter ($\sim 10^{4}$ m) [3]. Very broadly, in this thesis we categorise such flows by the nature of their forcing, which can be internal, external, or some combination of the two.

One example where internally driven flows have attracted particular interest is in the burgeoning field of biologically active soft matter. This concerns the dynamics of so-called 'active particles', where local flows are generated by, e.g., the rotating flagella of a bacterium or collections of molecular motors. While the microscopic flow field produced by these individual sub-units may be conceptually simple, the collective behaviour of many such particles is highly non-trivial. For example, spontaneous chaotic flows can form especially when the energy input (or activity) is large;

these are typically referred to as 'bacterial turbulence' [4, 5]. While this might appear qualitatively similar to inertial turbulence in an externally-driven passive fluid, the mechanism is reversed: energy is instead injected at the smallest scales which then 'cascades up' to form large scale vortex structures [5, 6]. Another important difference is that, for active systems, this effect generally occurs at vanishingly small Reynolds numbers.

Given the emergent complexity described above, it is unsurprising that many early works considered the stability and dynamics of active matter within a simple Newtonian background solvent. However, as the field develops, there is growing impetus to connect the insight gained for these idealised fluids with more biologically realistic environments [7, 8] as many examples of biological active matter are found to exist and interact within complex viscoelastic fluids, such as mucus [9]. Such environments can also be highly confined, e.g., as encountered by migrating cells within the extracellular matrix [10]. It has also been argued that confinement of subcellular active matter may be partly responsible for cytoplasmic streaming [1,11], an important biological process whereby coherent fluid flows provide circulation of nutrients and organelles within the cell [12].

As one might expect, the response of active matter to an externally applied flow is rich. Depending on the nature of their propulsion, active particles can increase [13] or reduce [14] the measured fluid viscosity relative to the passive equivalent (e.g., once the internal fuel source runs out); at high concentrations, the viscosity can practically vanish altogether producing superfluid states [15].

Ultimately, the study of active matter provides a fascinating insight into the physics of living systems [16]. For example, at the cellular level, it can further our understanding of cell motility [17], wound healing [18], and division [19, 20] processes. There is also great potential in active systems for developing of materials with tunable properties [21], and could be used in applications such as targeted drug delivery using artificial microswimmers [22].

The following chapters of this thesis consider topics that continue the theme of driven flow, though here the forcing is external, and not in a biological context. The first examines pressure driven flows of viscoelastic fluids in porous media. The

expansive/contractive nature of such geometries produces flow fields which provide a fascinating and non-trivial superposition of shear and extensional rheology. The effects of this are most noticeable for viscoelastic fluids, where experimental studies have repeatedly shown that at high flow rates relative to some intrinsic relaxation rate of the fluid (as characterised by the dimensionless Weissenberg number We), the pressure drop required to maintain a given flow rate increases dramatically [23]. Despite abundant experimental evidence of time-dependent states at high We, studies eager to capture a transition to viscoelastic turbulence in porous geometries have yet to reach a consensus as to whether this can be realised using 2D numerics [24, 25].

A final example of intriguing physics that arises under an externally driven flow concerns the contact line — the locus of points at which a fluid-fluid (or fluid-vapour) interface meets a solid surface — and the physics of the surrounding slip region. The equilibrium shape of a droplet under simple conditions can be calculated from free-energy considerations involving the surface tensions of the relevant interfaces [26]. The dynamics of the moving contact line, however, are intrinsically non-equilibrium and therefore require a more sophisticated approach, such as using diffuse interface models which prescribe a small interface of width ℓ between fluid phases. Importantly, the degree to which the size of the slip region depends on ℓ remains disputed, despite the ubiquity of such models in both analytical [27, 28] and numerical [29–31] treatments of multiphase flow.

Note that a more in depth introduction to each of the above topics may be found at the start of the corresponding chapter: we introduce viscoelastic active matter in Chaps. 3 to 5, flows in porous media in Chap. 6, and contact line dynamics in Chap. 7.

1.1 Layout of thesis

This thesis is organised as follows. In Chap. 2 we introduce the basic concepts common to all research presented in this thesis. This includes the two main approaches we use to solve Stokesian hydrodynamics (generalised to allow for vis-

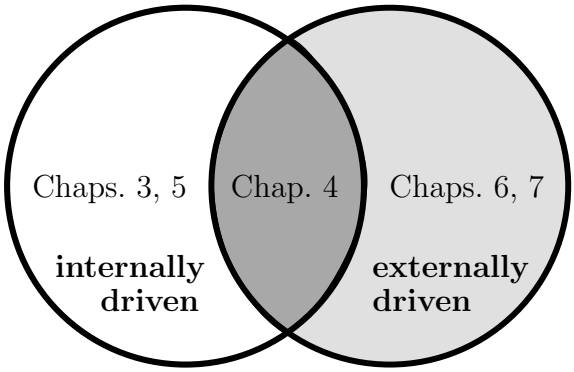

Figure 1.1: Overview of the chapters in this thesis according to the nature of the forcing, which may be internal (e.g., for biological active matter), external (e.g., pressure driven flow of multiphase fluids), or both (e.g., sheared active matter).

coelastic stresses), an introduction to shear and extensional rheology, and details of our numerical methods.

In Chaps. 3-5 we introduce and study our novel model for viscoelastic active matter. As is typical in hydrodynamical stability theory, we consider our model in a geometry of increasing dimensionality. We begin in Chap. 3 by describing our model which couples active liquid-crystal hydrodynamics with polymer viscoelasticity. Then, we consider the linear stability of a slab of active viscoelastic material confined between parallel plates in 0D/1D, with no externally applied shear. By separately treating the limits in which the liquid crystal forms isotropic and nematic phases, we derive critical activities for the onset of spontaneous flow, generalising earlier work without polymer, which we test with nonlinear simulations.

Then in Chap. 4 we map the shear rheology of our coupled model which, given the number of degrees of freedom, is rich and complex. Because of this, we first consider (a) polymer, (b) passive liquid-crystal, and (c) active matter rheology separately, allowing us to characterise and identify the variety of flow instabilities present. When these three contributions are combined, the resulting constitutive curves (which relate the theoretical shear stress at a given shear-rate) predict, e.g., multiple shear-banding instabilities, or spatio-temporal chaos. These predictions are confirmed by 1D nonlinear simulations.

Chap. 5 examines how the dynamical behaviour changes when we increase the dimensionality to include flow in 2D. We first report the results of a collaborative

study (without polymer) exploring precisely how liquid-crystal and velocity correlation lengths depend on the strength of the active stress [32]. Then by considering phase diagrams with and without polymer, we report an 'active drag reduction' effect whereby seemingly chaotic flows with no net material transport (without polymer) develop coherent flows as polymer is added. This, we argue, arises because the polymer acts to increase the correlation length of the fluid, suppressing small scale structure. We then treat materials where the polymer relaxation time becomes very long, where we find that activity-driven extensional flows can rapidly deform the polymer. This can drive oscillatory states which cycle between rapid extensional deformation and slow stress relaxation.

For the latter part of this thesis we leave the biological theme behind. In Chap. 6 we explore the flow of a viscoelastic fluid in a model porous medium which consists of periodic arrays of cylinders. Using an immersed boundary numerical method, we benchmark our code for Newtonian fluid, characterise the nature of the resulting flow field, and identify regions where shear or extension are expected to dominate. Then, using three popular models of polymer viscoelasticity, we map how the ratio of drag on the cylinder to throughput changes as the Weissenberg number (which characterises the ratio of flow and relaxation timescales) increases, and explore whether time-dependent states develop at high We.

Finally, in Chap. 7 we present simulation results for multiphase flows in planar Couette and Poiseuille flow protocols. We measure the slip length ξ and dynamic contact angle θ_d as a function of fluid properties such as the viscosity η or imposed flow rate V_0. Results are compared between independent numerical studies, demonstrating excellent agreement.

We conclude our findings and present ideas for future work in Chap. 8.

2

Theory & Methods

While the research presented in this thesis spans a diverse range of topics, these all contain a rheological theme, i.e., they all concern, in a general sense, the study of material deformation and flow. For the applications considered in this thesis, many of which are biological, these flows occur at scales where inertial effects can safely be ignored, allowing us to assume the zero Reynolds number ($\mathrm{Re} \to 0$) limit. There is, however, a high degree of viscoelasticity throughout our work which introduces nonlinearities into the equations of motion, rendering the resulting flow behaviour highly nontrivial.

In this chapter, we first introduce the generalised continuum equations for incompressible fluid flow, which include arbitrary stresses (e.g., describing polymer viscoelasticity) and forces (e.g., gravitational). Strategies for solving Stokesian (i.e., zero Re) hydrodynamics, generalised to include viscoelastic stresses, are also discussed. We then introduce basic concepts in shear and extensional rheology which

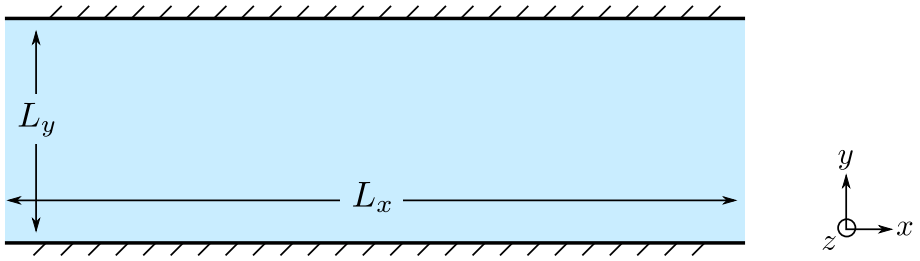

Figure 2.1: Schematic of the parallel plate geometry which we consider for the majority of this thesis. Flow is periodic in the x-direction, and bounded by solid walls in the y-direction. We assume invariance in the z-direction (into the page) throughout.

appear throughout this thesis, including popular constitutive models for polymer dynamics. Finally we describe the main numerical methods that we have implemented, specifically Fourier and finite difference schemes.

2.1 Hydrodynamics

We begin by writing the Navier-Stokes equations for incompressible flow, generalised to include contributions from an arbitrary additional stress $\boldsymbol{\sigma}$,

$$\rho\left(\partial_t + \mathbf{v}.\nabla\right)\mathbf{v} = \nabla.\left(2\eta\mathbf{D} - p\mathbf{I} + \boldsymbol{\sigma}\right) + \mathbf{f}, \tag{2.1a}$$

$$\nabla.\mathbf{v} = 0, \tag{2.1b}$$

where ρ and η respectively are the density and viscosity of the background Newtonian solvent. The velocity field is denoted $\mathbf{v}$ with the symmetrised velocity gradient tensor $\mathbf{D}$. The pressure, P, is determined by the incompressibility condition Eq. 2.1b. We also include an arbitrary stress $\boldsymbol{\sigma}$, which could in principle contain contributions from e.g., a polymeric fluid, or a liquid-crystal (see Sec. 2.2.3). Finally we include a body force term $\mathbf{f}$, which could be external (e.g., gravitational) or internal (e.g., immersed boundary forces, see Sec. 6.3.1) in nature. We adopt the quasi-2D channel geometry describe in Fig. 2.1 for the majority of this thesis, with no-slip and no-permeation boundary conditions (BCs) on the walls (each chapter also includes a detailed description of the geometry and BCs).

For all applications considered in this thesis the Reynolds number $\mathrm{Re} \ll 1$, so we can safely neglect the inertial terms on the LHS of Eq. 2.1a. We now illustrate how

one can conveniently describe hydrodynamics in this limit using the streamfunction formulation.

2.1.1 Streamfunction formulation

For simplicity, we can sum all additional stress and force contributions into a single term $\mathbf{s} = \mathbf{f} + \nabla.\boldsymbol{\sigma}$, so that Eq. 2.1a can be written (in the zero Re limit) as

$$\mathbf{0} = \eta\nabla^2\mathbf{v} - \nabla p + \mathbf{s}. \tag{2.2}$$

Then, for two-dimensional incompressible flows, one can define a streamfunction ψ where

$$\mathbf{v} = \nabla \times \boldsymbol{\psi}, \tag{2.3}$$

and where $\mathbf{v} = (v_x, v_y, 0)$, $\boldsymbol{\psi} = (0, 0, \psi)$. Note that ψ is only defined up to an arbitrary constant, i.e., taking $\psi \to \psi + A$ leaves Eq. 2.3 unchanged [33].

Substituting Eq. 2.3 into Eq. 2.2 and taking the curl, we eliminate the pressure term yielding

$$-\eta\nabla \times \left[\nabla^2 (\nabla \times \boldsymbol{\psi})\right] = \nabla \times \mathbf{s} \tag{2.4}$$

$$-\eta\nabla^2 \left[\nabla \times (\nabla \times \boldsymbol{\psi})\right] = \tag{2.5}$$

$$+\eta\nabla^4\psi = \partial_x s_y - \partial_y s_x. \tag{2.6}$$

Note that for the special case of 1D flow (where there is no variation in the x-direction), force balance reduces to a third order equation in ψ

$$0 = \partial_y \left(\eta\partial_y v_x\right) + s_x, \tag{2.7}$$

$$= \eta\partial_y^3\psi + s_x \tag{2.8}$$

The Fourier transformed equations are then

$$\eta\partial_y^3\psi = -s_x \qquad \text{for } k_x = 0, \tag{2.9}$$

$$+\eta\left[(ik_x)^4 + 2(ik_x)^2\partial_y^2 + \partial_y^4\right]\tilde{\psi} = ik_x s_y - \partial_y \tilde{s}_x \qquad \text{for } k_x \neq 0. \tag{2.10}$$

The third-order equation requires three boundary conditions at each wall. As ψ is only defined up to a constant we are free to impose $\psi|_{y=0} = 0$. Then using

$v_x = \partial_y \psi$, the second set of BCs result directly from the no-slip velocity BCs giving $\partial_y \psi|_{y=0,L_y} = v_x|_{y=0,L_y}$. For static walls these simply become $\partial_y \psi|_{y=0,L_y} = 0$. The additional boundary condition for the fourth-order equation (for $k_x \neq 0$) is then $\psi|_{y=L_y} = 0$ [34]. This is because $v_y|_{y=0,L_y} = -\partial_x \psi|_{y=0,L_y} = 0$, i.e., at the walls ψ cannot vary with x (and so the $k_x \neq 0$ modes must be zero).

While the streamfunction is convenient for describing two-dimensional flows, it does not generalise to 3D[1]. An alternative approach, which naturally generalises to 3D, is to follow the Oseen tensor formulation. We use this for the parts of this thesis that require biperiodic geometries, specifically the active defect study (Sec. 5.2) and the biperiodic array of cylinders in Chap. 6.

2.1.2 Oseen formulation

Taking the Fourier transform of Eq. 2.2 yields

$$\mathbf{0} = -\eta k^2 \tilde{\mathbf{v}}_k - i\mathbf{k}\tilde{p}_k + \tilde{\mathbf{s}}_k, \tag{2.11}$$

where $\mathbf{k}$ denotes the wavevector. Taking the divergence of Eq. 2.11, which in Fourier space corresponds to multiplication by $i\mathbf{k}$, and by using the incompressibility condition $\mathbf{0} = i\mathbf{k} \cdot \tilde{\mathbf{v}}_k$ (i.e., Eq. 2.1b in Fourier space), we find

$$\mathbf{0} = -k^2 \tilde{p}_k - i\mathbf{k} \cdot \tilde{\mathbf{s}}_k \quad \Rightarrow \quad \tilde{p}_k = -i\frac{\mathbf{k} \cdot \tilde{\mathbf{s}}_k}{k^2}. \tag{2.12}$$

Inserting Eq. 2.12 into Eq. 2.11 and rearranging yields

$$\tilde{\mathbf{v}}_k = \frac{1}{\eta k^2}\left(\boldsymbol{\delta} + \hat{\mathbf{k}}\hat{\mathbf{k}}\right) \cdot \tilde{\mathbf{s}}_k \tag{2.13}$$

This convenient form then allows one to easily calculate velocities for a given set of forces and stresses [35]. Eq. 2.13 is local in Fourier space, meaning the problem can be easily parallelised in a numerical implementation. Note that velocity gradients can also easily be calculated in Fourier space

$$i\mathbf{k}\tilde{\mathbf{v}} = \frac{i\mathbf{k}}{\eta k^2}\left(\boldsymbol{\delta} + \hat{\mathbf{k}}\hat{\mathbf{k}}\right) \cdot \tilde{\mathbf{s}}. \tag{2.14}$$

This Fourier representation naturally describes systems with periodic boundary conditions, and generalises to any number of dimensions.

[1] One exception is for 3D axisymmetric flow [33].

Implications. One important implication of Eq. 2.13 is that the $\mathbf{k} = \mathbf{0}$ mode of the velocity is undefined. An equivalent statement is that the velocity $\mathbf{v}$ in Eq. 2.2 is only defined up to an arbitrary constant.

We later model flow past a biperiodic array of cylinders (Chap. 6), where the solution must satisfy the usual no-slip boundary conditions on the cylinder surface. This constraint uniquely determines the solution of the zeroth mode [36]. However, e.g., when modelling active matter in a biperiodic geometry (Sec. 5.2), no such additional boundary condition exists. Thus it is impossible to determine the velocity uniquely. In that case, for simplicity, we choose this arbitrary constant $\mathbf{v}_0 = \mathbf{0}$ corresponding to no net displacement of the material.

Solid walls. However the inclusion of solid walls, e.g., with no-slip boundary conditions, is difficult. While in principle this can be achieved using additional image sources [37], the numerical implementation is very complex in practice.

An alternative approach could be to simulate solid walls using immersed boundaries (e.g., see Sec. 7.8). However this introduces additional numerical parameters to converge, which ideally we would like to avoid.

We have outlined the two formulations used to solve Stokesian hydrodynamics in this thesis: we use the streamfunction when solid walls are required, and the Oseen formulation when considering periodic systems. Details of the numerical solution of either formulation are given later in this chapter (see Sec. 2.3). We now consider flows of complex fluids and introduce basic concepts in shear and extensional rheology.

2.2 Rheology

The term rheology (from the Greek *rhéōs* meaning "flow") is the study of material response to flow deformation. In order to understand the properties of a material, and to examine the dynamics of internal microstructure, rheologists use a number of experimental techniques which often involve shearing a material between two plates. (See Fig. 2.2 for examples.)

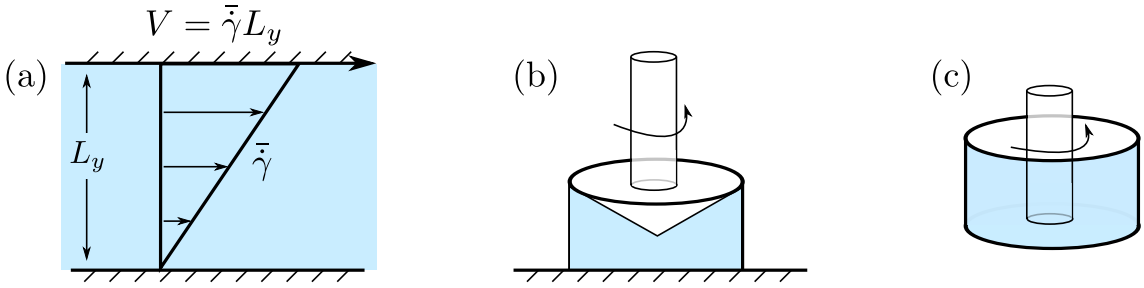

Figure 2.2: Illustration of some common experimental setups for producing shear flows. (a) Parallel plate (top plate moves with speed V relative to the bottom plate), (b) cone and plate, and (c) Taylor-Couette setups.

The simulations described in this thesis mainly focus on the parallel plate geometry for simplicity (Fig. 2.2a); in practice this is difficult to implement and experimentalists typically use either the cone and plate (Fig. 2.2b) or Taylor-Couette (Fig. 2.2c) setups [38]. Simulations in these curved geometries are certainly possible [39, 40]; one may also approximate them in parallel plate simulations by adding a biasing stress gradient [41]. However the parallel plate setup is normally sufficient as this can be seen as the limiting case in which the radii of the Taylor-Couette cylinders are taken to infinity (with fixed spacing).

The key pair of quantities to be controlled or measured in such shear-flow experiments are:

- the mean shear-rate, defined as $\bar{\dot{\gamma}} = V/L_y$,
- the total shear-stress, Σ_{xy},

where L_y is the separation of the plates, and V the velocity of the top plate. The protocol used to examine shear rheology in this thesis fixes an imposed shear rate and measures the stress response in time. Once the system reaches a steady state (i.e., the stress no longer varies in time), the measurement is made. In practice, either one of these quantities may be fixed to find the response of the other.

The experimentally measured relation between the total shear stress and strain rate is known as a *flow curve*. This is related to but distinct from the *constitutive curve* which tells us the predicted shear stress at an applied shear rate for a theoretical homogeneous system, i.e., where the shear-rate is constant across the cell. In many cases these curves coincide, but not in general, e.g., compare black solid

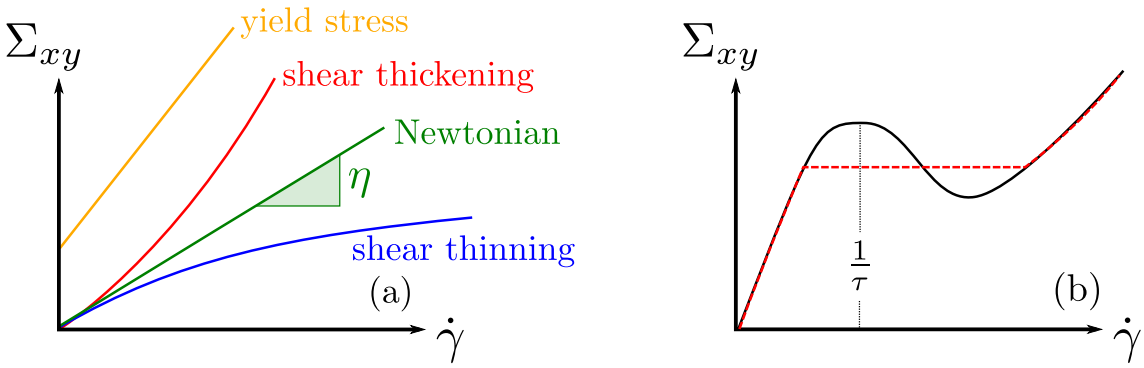

Figure 2.3: (a) Schematic flow curves for various classes of fluid in shear flow. (b) Illustration of the distinction between a theoretical constitutive curve (black solid line) and an experimentally measured flow curve (red dashed line).

line (constitutive curve) and red dotted line (flow curve) in Fig. 2.3b. For example, when shear-banding instabilities are observed, the measured stress would in general be different to that expected under the assumption of homogeneous flow (see Sec. 2.2.2 for more details). Such curves can be used to characterise a material into two main categories of complexity: Newtonian and non-Newtonian.

2.2.1 Newtonian and non-Newtonian fluids

The term *Newtonian fluid* is used to describe a simple material where shear-stress increases linearly with the shear-rate [38]. The resulting flow curve is simply a straight line through the origin, where the slope defines a constant viscosity, η (Fig. 2.3a, green curve).

While this picture is valid for simple fluids such as water, there exists a large class of *non-Newtonian fluids* which do not behave in this way, save perhaps at very low shear-rates. These materials are characterised by a non-linear flow curves, and are accompanied by a rich variety of phenomena. For example shear-thinning (thickening) materials become proportionally easier (harder) to produce a flow in as the stress increases, and yield stress fluids require a finite stress before they begin to flow [42] (Fig. 2.3). These properties are important industrially as many everyday materials (e.g., foods, cosmetics, paints, pastes) fall under these categories [43].

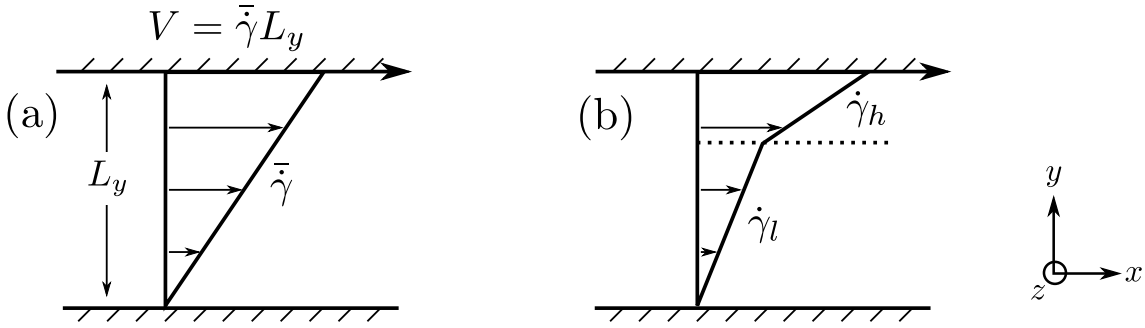

Figure 2.4: Illustrative velocity profiles for homogeneous / inhomogeneous shear flows, where the arrows denote fluid velocity. The x, y, and z directions are referred to as the flow, flow gradient, and vorticity directions respectively.

2.2.2 Shear-banding

Shear-banding is a particularly intriguing phenomenon that can be observed in non-Newtonian fluids, and is of both industrial and academic interest [44]. If we shear a simple Newtonian fluid with a constant applied shear-rate at negligible values of Re, we would expect (by solution of the Navier-Stokes equations or otherwise) that the resulting flow field is described by a homogeneous velocity gradient across the cell (Fig. 2.4a).

The term *complex fluids* generally refers to non-Newtonian materials with detailed mesostructure that relaxes on relatively long timescales. These materials can exhibit flow instabilities at large enough shear rates, that can manifest as macroscopic *shear-bands* of differing shear-rates and structure, where the more ordered state is generally found in the higher shear-band. (See Fig. 2.5 for examples.) While the mean shear-rate $\bar{\dot{\gamma}}$ across the channel is the same as it would be for a homogeneous flow profile, individual bands of different shear rates are observed to coexist (Fig. 2.4b).

Theoretically, shear-banding is predicted to occur at applied shear-rates where the underlying constitutive curve is non-monotonic, i.e., when $\frac{\partial \Sigma_{xy}}{\partial \bar{\dot{\gamma}}} < 0$ [44], though depending on previous deformation history, this phenomenon can also be observed in the surrounding metastable regions. The physical interpretation is that, if increasing the shear-rate lowers the total stress, then a homogeneous flow is mechanically unstable [40]. Systems with imposed shear-rates in this unstable region then recon-

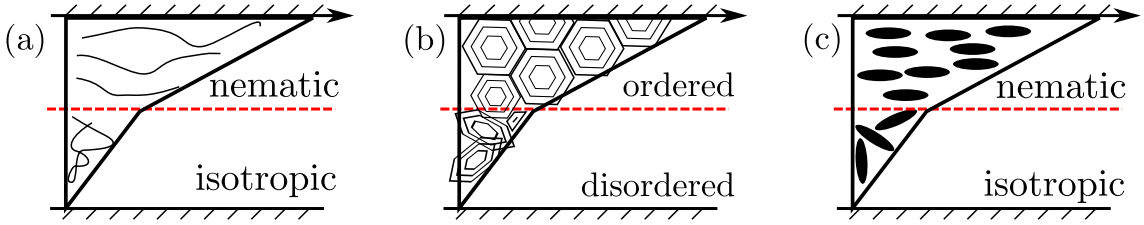

Figure 2.5: Examples of systems found to exhibit shear-banding instabilities. (a) Wormlike-surfactants (aggregates of amphiphilic molecules), (b) onion-surfactants, (b) liquid-crystals can exhibit both liquid and crystalline properties.

figure into low and high shear-bands. If one increases the imposed shear-rate then the proportion of the two bands will change according to a lever rule, but the stress remains constant.

This produces the stress plateau that is measured experimentally in flow curves (see e.g., Fig. 2.3b) for a wide range of materials including wormlike micelles [45], lyotropic lamellar[2] liquid-crystal (LC) phases [46], and entangled polymeric materials (e.g., polymer melts and solutions) [47]. Shear-banding has been directly observed for several of these materials (which we illustrate in Fig. 2.5), most notably in wormlike micelles using nuclear magnetic resonance (NMR) [48] and ultrasound techniques [49], but also for entangled polymers [50] and cellular proteins [51] using particle tracking velocimetry. As the form of mesoscopic structure generally has a strong flow dependence, bands with differing levels of ordering have also been observed using birefringence methods [52].

Such bands have been experimentally observed with layer normals either in the direction of the flow gradient (*gradient banding*) [53,54] or in the vorticity direction[3] (*vorticity banding*) [55,56]. In this thesis we focus on the more commonly observed gradient banding, restricting any numerical work to the flow-gradient only (1D) or flow/flow-gradient plane (2D).

[2]A structure consisting of bilayers of amphiphilic molecules.

[3]i.e. the z-direction in Fig. 2.4

2.2.3 Modelling complex fluids

Having introduced the key rheological quantities which can be probed in a typical shearing experiment, we now introduce some of the theoretical models one can use to describe complex fluids, with particular focus on shear-banding.

Complex fluids possess internal mesostructures, e.g., polymer chains or rod-like molecules, which contribute additional stress and strongly influence the rheological response of the fluid. To describe these effects, the stress that appears in the Navier-Stokes equation (Eq. 2.1a) can be augmented by an additional polymeric (or other mesoscopic) stress, $\boldsymbol{\sigma}$. Forms for this stress are typically derived in terms of the conformation or strain tensor, $\mathbf{C}$, a quantity that is motivated by treating polymer chains as pairs of beads connected by springs which form 'dumbbells' [38]. Here $\mathbf{C} \propto \langle \mathbf{rr} \rangle$, where $\mathbf{r}$ is the end-to-end vector of an entire polymer chain, or sub-chain, depending on the level of description required.

There are a wide range of models which describe the dynamics of $\mathbf{C}$ and therefore $\boldsymbol{\sigma} \propto \mathbf{C}$ [43] in response to a flow field $\mathbf{v}$. As a pedagogical example we will describe in brief the diffusive Johnson-Segalman model (dJS), before discussing improvements and generalisations.

2.2.3.1 Diffusive Johnson-Segalman (dJS) model

The model [40, 57] describes the dynamics of the polymeric stress

$$\boldsymbol{\sigma} = G\left(\mathbf{C} - \mathbf{I}\right), \tag{2.15}$$

which can be expressed in terms of the conformation tensor $\mathbf{C}$

$$\underbrace{\left(\partial_t + \mathbf{v}.\nabla\right)}_{\mathrm{A}}\mathbf{C} = \frac{-1}{\tau_C}\left(\mathbf{C} - \mathbf{I}\right) + \underbrace{\mathbf{C}\boldsymbol{\Omega} - \boldsymbol{\Omega}\mathbf{C}}_{\mathrm{B}} + 2a[\mathbf{CD}]^{\mathrm{S}} + \frac{\ell_C^2}{\tau_C}\nabla^2\mathbf{C}. \tag{2.16}$$

If there is no flow, Eq. 2.16 simply describes the relaxation of the polymeric stress towards the isotropic (undeformed) state $\mathbf{C} \to \mathbf{I}$; under an imposed flow the symmetric ($\mathbf{D}$) and antisymmetric ($\boldsymbol{\Omega}$) parts of the velocity gradient tensor $(\nabla\mathbf{v})_{ij} = \partial_i v_j$ will in general be non-zero and will load the polymer stress. Here a is a slip parameter that controls the ratio of deformation of the polymer with respect

to the fluid [57]. For $|a| < 1$, the polymer slips relative to the fluid and the constitutive curve is capable of non-monotonicity, one of the signatures of shear-banding. (See Sec. 4.3.1 for details.) The material derivative (term A) imposes translational (Galilean) invariance, and term B imposes rotational invariance. Parameters G (a plateau modulus relating to the elastic properties of the material), and τ (the relaxation time) can be measured experimentally using e.g., small amplitude oscillatory shear [58].

This formulation differs slightly from the original derivation of the Johnson-Segalman model [59] due to the inclusion of an additional diffusive term which prohibits structure forming at lengthscales smaller than the fluid microstructure ℓ. (We abbreviate non-diffusive [59] and diffusive [40] formulations of the model as JS and dJS respectively.) A consequence of this non-locality is that, if a homogeneous shear flow is unstable to the formation of shear-bands, the steady-state stress of the shear-banded state is uniquely selected [60], consistent with experimental results [61,62]. Without such a term, the selected stress can be history dependent [63], and the interface between bands can be infinitely sharp which is both unphysical and numerically problematic. Note that the dJS model reduces to the popular Oldroyd-B model (which we use extensively in Chap. 6) for $a = 1$, $\ell = 0$.

2.2.3.2 Finitely Extensible Nonlinear Elastic (FENE) models

While the JS model is unlikely to yield a microscopically faithful representation of any real fluid, it is capable of producing non-monotonic constitutive curves (for $\eta/G\tau < 1/8$) which are an essential feature in any study of shear-banding instabilities. However as is the case with its predecessor, the Oldroyd-B model, the behaviour of the JS model in strong extensional flows is unphysical [64]: polymer chains can become infinitely stretched in the vicinity of stagnation points where the extension rate is significant but the velocity field is zero. We first describe how this issue is addressed in microscopically motivated models, specifically the FENE-P and FENE-CR [65, 66] (finitely extensible nonlinear elastic) models, before illustrating the effect this has on the shear and extensional rheology.

The FENE models impose finite extensibility on the polymer chains using a

non-linear spring function of the form

$$k(\mathbf{C}) = \frac{1}{1 - \delta \mathrm{Tr}[\mathbf{C}]}, \tag{2.17}$$

where δ parametrises the degree of extensibility and where $\delta \to 0$ recovers the Oldroyd-B model. While the essential physics is the same, FENE-P and FENE-CR differ in how this term is incorporated into the constitutive equation and stress:

$$\partial_t \mathbf{C} = -\frac{1}{\tau}\left(k(\mathbf{C})\mathbf{C} - \mathbf{I}\right) + \cdots, \qquad \boldsymbol{\sigma} = G\left(k(\mathbf{C})\mathbf{C} - \mathbf{I}\right) \quad \text{FENE-P}, \tag{2.18a}$$

$$\partial_t \mathbf{C} = -\frac{1}{\tau}k(\mathbf{C})\left(\mathbf{C} - \mathbf{I}\right) + \cdots, \qquad \boldsymbol{\sigma} = Gk(\mathbf{C})\left(\mathbf{C} - \mathbf{I}\right) \quad \text{FENE-CR}. \tag{2.18b}$$

While the extensional rheology is unaffected by this distinction, the shear rheology differs between the two models, a fact which we later exploit in Chap. 6 in our study of viscoelastic flows in porous media.

We finish this section on constitutive modelling by presenting steady-state constitutive curves for the four models described above, both in simple shear and extension, and comment on their meaning.

2.2.4 Rheology of constitutive models

Under ideal viscometric conditions, the imposed velocity gradient tensor $\nabla \mathbf{v}|_{ij} = \partial_i v_j$, in simple shear and extension respectively, reads

$$\nabla \mathbf{v}|_{\text{shear}} = \dot{\gamma} \begin{pmatrix} 0 & 0 \\ 1 & 0 \end{pmatrix}, \quad \nabla \mathbf{v}|_{\text{ext}} = \frac{\dot{\varepsilon}}{2} \begin{pmatrix} 1 & 0 \\ 0 & -1 \end{pmatrix}, \tag{2.19}$$

where the incompressibility condition $\nabla.\mathbf{v} = 0$ is clearly satisfied in both cases. We determine the steady-state stress of a system subject to either flow, which can be found either by evolving 0D simulations to steady-state, or by analytically obtaining the steady-state solutions to the constitutive equation (i.e., by setting $\partial_t \mathbf{C} = 0$).

2.2.4.1 Shear flows

Fig. 2.6a shows constitutive curves for all models, in response to an applied flow of simple shear. Both Oldroyd B and FENE-CR possess a constant shear-viscosity (i.e., they do not shear thin). Given that their shear rheology is the same but their

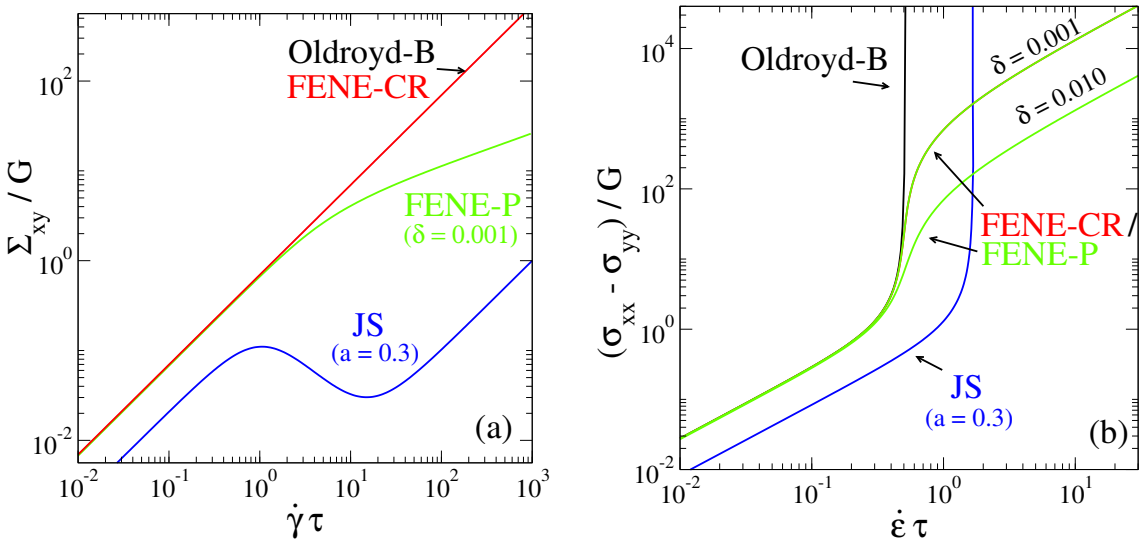

Figure 2.6: Constitutive curves for a range of models in (a) shear and (b) extension. For clarity we ignore the solvent stress $\boldsymbol{\Sigma}_{\text{sol}} = 2\eta\mathbf{D}$ in (b), as this simply adds a linear contribution. **Parameters:** FENE models $\delta = 0.001, 0.01$, JS model $a = 0.3$.

extensional rheology differs (see below), this can be exploited to isolate extensional-specific effects (see Sec. 6.5). The FENE-P model does shear thin however, though the effect is not as dramatic as in the JS model whose corresponding constitutive curve is non-monotonic. This implies that a homogeneous initial base state situated in the negatively sloping region is susceptible to shear-banding instabilities [67], as previously discussed in Sec. 2.2.2.

2.2.4.2 Extensional flows

The steady-state extensional constitutive curve is shown in Fig. 2.6b. First we notice that the extensional stress diverges at $\dot{\varepsilon}\tau = 1/2$ for the Oldroyd-B model. This is one of the simplest constitutive models, and describes polymer chains as beads with a Hookean (linear) restoring force. The observed divergence implies that a steady-state extensional stress cannot be obtained and that the dumbbells in the polymer model will become infinitely separated as $t \to \infty$ for dimensionless extension rates $\dot{\varepsilon}\tau > 1/2$. In the JS model this divergence still exists, although it is pushed out to larger extension rates $\dot{\varepsilon}\tau > {}^1/_{2a}$ [43].

The stress singularity can be mitigated by introducing a non-linear spring force (Eq. 2.17), which diverges as chain separation approaches the maximum set by

$\sqrt{1/\delta}$. Indeed this is the approach of the FENE-P and FENE-CR models, whose extensional stresses are indistinguishable in steady state.

2.2.4.3 Complex flows

We have introduced the rheological properties of a selection of constitutive equations that we will use throughout this thesis, both in simple shear and extension. While the response is clear in these idealised protocols, the behaviour in more complex geometries which contain some non-trivial combination the above flow types is less obvious (this is a major theme of Chap. 6).

At our disposal are combinations of models that are (a) identical in extension but differ in shear (FENE-P and FENE-CR), or (b) identical in shear and different in extension (Oldroyd-B and FENE-CR). This range of constitutive behaviour will allow us to determine which type of flow dominates in a given geometry, simply by noting the change in response between different constitutive equations.

2.3 Numerical Implementation

We finish this chapter by describing how the equations of motion are solved numerically. As a pedagogical example, we consider the Allen-Cahn reaction-diffusion equation [68, 69] in a channel between solid walls, where $\phi(\mathbf{r}, t)$ is a scalar order parameter which obeys

$$\partial_t \phi = -f'(\phi) + D\nabla^2 \phi, \tag{2.20}$$

$$f'(\phi) = \phi^3 - \phi, \tag{2.21}$$

with periodic boundary conditions in x and free boundary conditions at the walls, i.e.,

$$\phi|_{x=0} = \phi|_{x=L_x}, \quad \partial_y \phi|_{y=0,L_y} = 0. \tag{2.22}$$

(While we do not use the Allen-Cahn model in this thesis, it is structurally similar to the Cahn-Hilliard equation which forms a key part of the contact line study in Chap. 7.)

Numerically we represent ϕ on a discrete grid of points of spacing $\Delta x = L_x/N_x$ and $\Delta y = L_y/N_y$, and evolve the equation in time with timestep Δt. Note that generalisation of the methods described here to tensorial partial differential equations is trivial.

Solution of Eq. 2.20 may be split into two separate stages. First, we describe how the local term, $f'(\phi)$, is integrated in time, then separately consider the non-local diffusive term $\nabla^2\phi$.

2.3.1 Time-stepping scheme

Denoting the current timestep n, where $t = n\Delta t$, we can integrate Eq. 2.20 in time (at each grid point) using a generalised Euler time-stepping scheme

$$\frac{\phi^{n+1} - \phi^n}{\Delta t} = \theta f(\phi^{n+1}) + (1-\theta) f(\phi^n), \tag{2.23}$$

where $\theta \in [0, 1]$ is an parameter controlling the relative weight of explicit ($\theta = 0$) and implicit ($\theta = 1$) terms [70]. Unless specified otherwise, throughout this thesis we will use explicit Euler ($\theta = 0$) for solution of any local terms. However the notation of Eq. 2.23 will remain useful in describing the solution of non-local terms (e.g., see Sec. 7.3.1), which we now consider.

2.3.2 Fourier method

In the x-direction, the simulation box is taken to have length L_x with periodic boundary conditions. A convenient way to evaluate gradient terms in any constitutive equation is to decompose the relevant order parameter into a Fourier series

$$\phi(x,t) = \sum_k \tilde{\phi}_k(t) e^{ik_x x} \tag{2.24}$$

where $k_x = 2\pi k'_x/L_x$ is the wavevector [71]. Taking the Fourier transform of the non-local term, we obtain a set of uncoupled linear equations to be solved for each mode k

$$\partial_t \tilde{\phi}_k = (ik_x)^2 D \tilde{\phi}_k, \tag{2.25}$$

Using a semi-implicit time-stepping method (i.e., Eq. 2.23 with $\theta = 1/2$), this can be integrated in time,

$$\frac{\tilde{\phi}_k^{n+1} - \tilde{\phi}_k^n}{\Delta t} = -k^2 D \frac{\tilde{\phi}_k^{n+1} + \tilde{\phi}_k^n}{2}. \tag{2.26}$$

The benefits of the Fourier method become even clearer when considering higher order derivatives (for example 4th order derivatives are required for the streamfunction formulation described in Sec. 2.1.1) as

$$\partial_x^n \phi(x,t) \quad \rightarrow \quad \sum_k (ik_x)^n \hat{\phi}_k(t) e^{ik_x x}.$$

While finite-difference methods (described below) would require solution of an increasingly complex matrix problem (as more neighbouring grid points are involved), spectral methods implement higher order derivatives by simply multiplying increasing powers of (iq_k). The main numerical cost of the algorithm lies in taking Fourier Transforms, but efficient algorithms such as the FFT (Fast Fourier Transform [72]) render this manageable.

When the full nonlinear equation Eq. 2.20 is considered, the procedure for a given timestep is then:

1. time-step the local terms $f'(\phi)$ (Eq. 2.23)
2. take a forward Fourier transform
3. time-step the non-local terms $\nabla^2\phi$ in Fourier space (Eq. 2.26)
4. take a backward Fourier transform

The Fourier method outlined above naturally describes quantities in the periodic direction. However, depending on the boundary condition, it is not always possible to adopt this method in the y-direction (normal to the wall). For special cases one can use a subset of the Fourier basis, e.g., for the 'free BC' $\partial\phi|_{y=0,L_y} = 0$, a cosine basis may be used (e.g., see Sec. 7.3).

However, particularly for more complex boundary conditions (e.g., where BCs differ at each boundary), it is more convenient to use a finite difference discretisation in the y-direction.

2.3.3 Finite-difference method

The finite difference method discretises a continuous variable onto an evenly spaced grid of positions, where spatial derivatives can be approximated by a polynomial of values from nearby grid points. Coefficients for these polynomials can be derived using a Taylor expansion around neighbouring positions in space or time. For example, in Sec. 2.3.1 we approximated the first order time derivative of $\phi(y,t)$ as

$$\begin{aligned} \phi^{n+1} &= \phi^n + \Delta t \frac{\partial \phi}{\partial t}^n + \mathcal{O}(\Delta t^2) \\ \frac{\partial \phi}{\partial t} &= \frac{\phi^{n+1} - \phi^n}{\Delta t} + \mathcal{O}(\Delta t) \end{aligned} \tag{2.27}$$

where Δt is the time step (this is simply the explicit Euler scheme). In a similar fashion, a second order spatial derivative could be found by summing the following expansions

$$\begin{aligned} \phi_{j+1} &= \phi_j + \Delta y \phi'_j + \frac{\Delta y^2}{2!}\phi''_j + \frac{\Delta y^3}{3!}\phi'''_j + \mathcal{O}(\Delta y^4) \\ \phi_{j-1} &= \phi_j - \Delta y \phi'_j + \frac{\Delta y^2}{2!}\phi''_j - \frac{\Delta y^3}{3!}\phi'''_j + \mathcal{O}(\Delta y^4) \\ \phi''|_j &= \frac{\phi_{j+1} - 2\phi_j + \phi_{j-1}}{\Delta y^2} + \mathcal{O}(\Delta y^2) \end{aligned} \tag{2.28}$$

where Δy is the spacing between grid points and j is the index associated with the current grid point. Note that expressions for higher-order derivatives (e.g., the streamfunction formulation requires fourth-order derivatives) can be easily obtained by including higher order terms in the expansion.

At the walls, free boundary conditions (i.e., $\partial_y \phi|_{y=0,L_y} = 0$) can be implemented by the inclusion of 'phantom points'. If the spatial index j runs from 1 (at $y = 0$) to N_y (at $y = L_y$), then the phantom points at $j = 0, N_y + 1$ can be found using a finite difference approximation, e.g.,

$$\begin{aligned} \partial_y \phi_1 &\approx \frac{\phi_0 - \phi_2}{2\Delta y} = 0, \\ \phi_0 &= \phi_2, \end{aligned}$$

which then allows us to approximate $\partial_y^2 \phi$ at the wall

$$\partial_y^2 \phi_1 \approx \frac{\phi_0 - 2\phi_1 + \phi_2}{\Delta y^2} = \frac{2\phi_2 - 2\phi_1}{\Delta y^2}. \tag{2.29}$$

This can easily be extended to higher order methods by inclusion of additional phantom points ϕ_{-1}, ϕ_{-2} etc.

Using Eqs. 2.27/2.28, we can now solve the non-local terms of our model PDE using the following explicit scheme

$$\frac{\phi_j^{n+1} - \phi_j^n}{\Delta t} \approx D \frac{\phi_{j+1}^n - 2\phi_j^n + \phi_{j-1}^n}{\Delta y^2}. \tag{2.30}$$

Implicit schemes, where the RHS is evaluated at timestep t^{n+1}, instead require solution of a linear system of equations, typically by inverting a banded matrix. (Note that Eq. 2.29 allows us to incorporate the boundary conditions in this matrix form.) While this inversion can be numerically costly, the benefits include increased stability allowing for larger timesteps to be used at lower overall computational cost. Because of this, unless otherwise specified, any finite-difference simulations described in this report implement a semi-implicit Crank-Nicolson scheme (corresponding to $\theta = 1/2$ in Eq. 2.23). For brevity we have only introduced the basic ideas, for further details see e.g., Ref. [70].

2.3.4 Hybrid method

We have shown how one can solve our model PDE, using a Fourier method in the x-direction and finite-differencing in the y-direction. Full 2D solution then requires a hybrid method utilising both techniques. The result is a set of finite-difference equations which are solved for each k. The full Fourier-Crank-Nicolson scheme for the diffusion term then reads

$$\frac{\tilde{\phi}_{k,j}^{n+1} - \tilde{\phi}_{k,j}^n}{\Delta t} = -k^2 D \left[\frac{\left(\frac{\tilde{\phi}_{k,j+1}^{n+1} - 2\tilde{\phi}_{k,j}^{n+1} + \tilde{\phi}_{k,j-1}^{n+1}}{\Delta y^2} \right) + \left(\frac{\tilde{\phi}_{k,j+1}^{n} - 2\tilde{\phi}_{k,j}^{n} + \tilde{\phi}_{k,j-1}^{n}}{\Delta y^2} \right)}{2} \right]. \tag{2.31}$$

2.3.5 Convergence and validation

In any study, we check that our results are unchanged under a halving of (a) the spatial-step size $\Delta x = \Delta y$ and separately (b) the time-step Δt. While the detailed spatial structure and temporal trajectory of apparently chaotic states (see

e.g., Sec. 5.2) will differ during convergence tests, we have checked that key averaged quantities such as correlation lengths or mean velocities do indeed converge.

We strive to check our results for correctness against previous results (where possible). For example, we verify our model for flow in porous media against previous analytical expressions (Sec. 6.3.2). If such results are not available, we can also check that the growth rate of perturbations in any linear instability agrees with the analytical predictions of the linearised constitutive equation. (For a detailed example of this procedure see Sec. 4.2.)

2.4 Conclusions

In this chapter we have introduced the basic concepts in Stokesian hydrodynamics, which are applicable throughout this thesis. Depending on the geometry of interest, we showed that 2D incompressible flows can be conveniently expressed using either the Oseen or streamfunction formulations, where either method can include additional viscoelastic stresses with ease.

We then explained how experimentally measured flow curves can be used to categorise materials with non-Newtonian flow behaviour. The theoretical analogue (the constitutive curve), which considers the stress for an assumed homogeneous flow, is also explained with particular focus on the stability implications of non-monotonicity in shear flow. The details of the shear-banding flow instability (which will form a key part of our stability results in Chaps. 3, 4) were presented, with reference to the underlying constitutive curve. A selection of constitutive models were then introduced, and their rheological responses in simple shear and extensional were contrasted.

Finally we described how the above constitutive equations may be solved numerically, both in biperiodic and channel geometries. This included an explanation of how gradient terms are evaluated using a Fourier method in the periodic directions and a finite-difference method in the direction normal to the walls (if present). With the requisite background knowledge in place, we now present the first topic of study, which concerns the stability and dynamics of active viscoelastic matter.

3

Active viscoelastic matter:

0D and 1D (no applied shear)

3.1 Introduction

Active matter can be very generally defined as the class of materials whose constituents are capable of extracting energy from their environment in order to propel themselves or the surrounding fluid [16,73]. Examples of active matter can be found across a vast range of lengthscales, from shoals of fish (at the metre scale), to suspensions of swimming bacteria (micrometre scale), to cytoskeletal components within the cell (micro- to nanometre scale).

Such materials typically comprise elongated subunits, and can form ordered phases with broken symmetries reminiscent of those found in liquid-crystals (LCs). Accordingly, theoretical attempts to describe these systems using simple continuum models typically begin with the hydrodynamic equations for a fluid of rod-like ob-

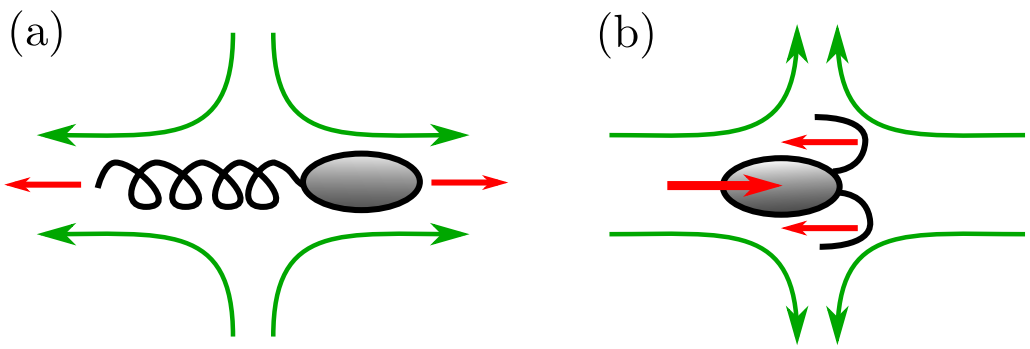

Figure 3.1: Schematic of the two types of force dipole possible, and a cartoon of two of the organisms known to produce them. Red lines indicate forces (which must sum to zero), and green lines are suggestive of the resulting velocity field. (a) An extensile bacterium, e.g., *B. subtilis*. (b) A contractile swimmer, e.g., *Chlamydomonas*.

jects which, depending on the nature of the symmetry, can be described by polar $\mathbf{p}$ or nematic $\mathbf{Q}$ order parameters [16]. Such equations describe a passive LC [74], where deviations from thermal equilibrium might result from a temperature quench or an external driving force such as shearing walls.

Active fluids form part of an exciting class of non-equilibrium systems which possess an additional *internal* forcing mechanism which originates at the microscopic level. In the absence of external forcing, an active particle must be force free. Therefore the simplest perturbation to the flow that can be constructed is a force dipole. Depending on the sign of the dipole, an active particle can be classed as extensile (where forces act from the centre of mass outwards towards the fluid) or contractile (forces act from fluid to centre of mass). The difference between these is most clearly illustrated for elongated particles (see Fig. 3.1 for a cartoon). However the distinction exists even for spherically symmetric particles because the orientation of the force dipole itself defines a director [75].

A second important distinction is the position of the force dipole centre relative to the centre of mass. Active particles for which these are not coincident are capable of net motion and are classed as 'movers' (i.e., polar), the converse being 'shakers' (i.e., apolar). In the following chapters we derive and study a model to describe the latter class, with focus on applications at the subcellular level.

Interestingly, the polarity (or lack thereof) of the individual active particles does not necessarily determine the symmetry of the macroscopic phases. For example

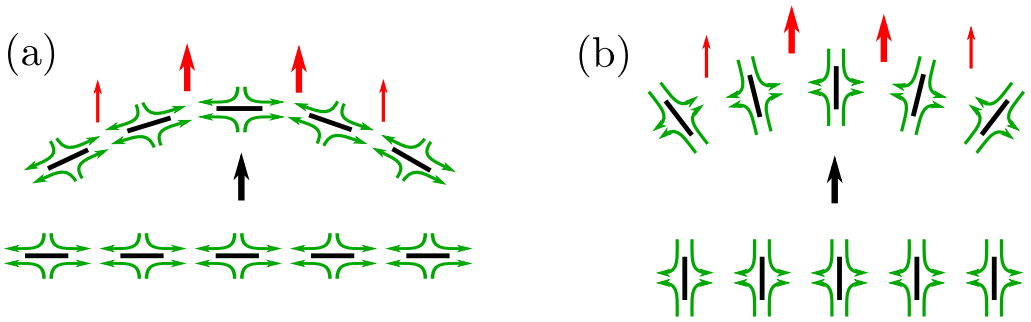

Figure 3.2: Schematic demonstrating generic spontaneous flow instabilities in a flow aligning nematic. (a) The bend mode in an extensile material. (b) The splay mode in a contractile material.

polar particles can form nematic phases (e.g., as might be seen when two sets of pedestrians pass in opposite directions at a zebra crossing). Indeed to lowest order, the active stresses in polar and apolar formulations are indistinguishable [73,76]. We will introduce the active stress in our model later in Eq. 3.26, where the magnitude is set by the activity parameter ζ for which positive (negative) values of ζ describe extensile (contractile) materials.

Flow instabilities. One of the most striking theoretical predictions concerning active matter is that a bulk homogeneous suspension of orientationally ordered particles is intrinsically unstable to heterogeneous perturbations [77, 78]. The origin of this instability can be understood by considering splay and bend distortions in LCs.

To illustrate this, consider an extensile material. Here fluid is drawn in from the particle sides and is ejected along the main axis. In a perfectly ordered material, these activity driven flows cancel and the material remains undeformed. However if an infinitesimal bend perturbation is introduced then these flows become unbalanced, producing net flow in the direction of the bend [79]. This positive feedback loop only halts once the competition between activity and distortion free energy balances. An analogous mechanism drives the splay instability. Pictorial demonstrations are given in Fig. 3.2. (An exhaustive exploration of these mechanisms for different activities and liquid-crystalline parameters is given in Ref. [80].) In essence, curvature in the apolar nematic director field produces a local polarity, which in turn generates local flow.

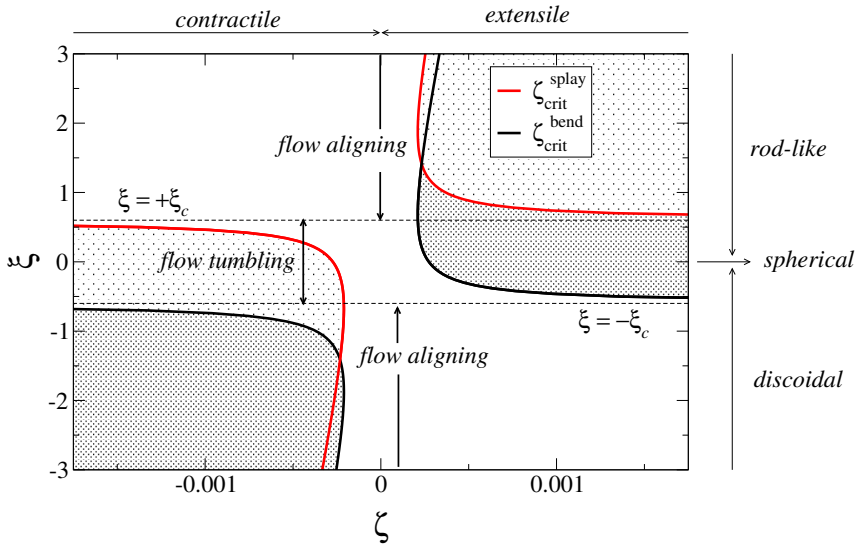

Figure 3.3: Phase diagram displaying regions where an active nematic is unstable to **splay** (red lines) and **bend** (black lines) instabilities in a finite system, as a function of activity ζ and the flow-alignment parameter ξ. Extensile (contractile) corresponds to ζ greater (less) than zero, and flow aligning (tumbling) corresponds to $|\xi|$ greater (less) than $|\xi_c|$.

However this flow instability can be suppressed in finite systems. Using a linear stability analysis, Voituriez *et al.* showed that no spontaneous flow occurs below a critical activity threshold $\zeta_c \propto G_Q \ell_Q^2 / L_y^2 \, (\eta/\gamma + \dots)$, where G_Q is the stress scale of the LC, ℓ_Q is a microscopic lengthscale[1], L_y is the system size and the bracketed term includes the ratio of solvent and LC viscosities [81]. The generic instability occurs for any value of the activity in bulk active nematics, because $\zeta_c \to 0$ in the infinite system size limit.

This critical activity also depends on the mode of instability. In a finite system, active nematics are unstable to bend and splay instabilities at distinct values of ζ_c [6]. The instability that first appears (as activity is increased) depends on the 'flow-alignment' properties of the LC, which we parametrise in our model using ξ. This parameter describes the relative influence of extensional and rotational flow contributions on the nematic director. For $|\xi| < |\xi_c|$, rotation dominates and the director continuously rotates in a tumbling motion. For $|\xi| > |\xi_c|$ extension and

[1]This is the lengthscale at which the free energy cost of elastic distortions (parametrised by Frank constant K) competes with the bulk free energy, and is defined as $\ell_Q = \sqrt{K/G_Q}$. See Sec. 3.2.1.1 for details.

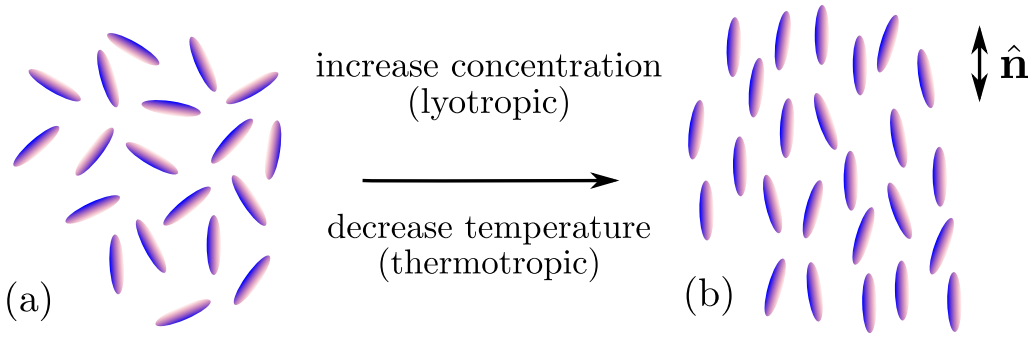

Figure 3.4: Schematic of (a) isotropic and (b) nematic phases of a LC. While neither state possesses translational ordering, the nematic exhibits orientational ordering.

rotation have equal effect and the director adopts a static orientation at an angle to the flow [80]. The sign of ξ characterises the shape of the particles where $\xi > 0$ describes rod-like, $\xi = 0$ spherical, and $\xi < 0$ discoidal active particles. A schematic stability diagram (generated using our linear stability analysis in Sec. 3.3) is given in Fig. 3.3, illustrating the importance of each parameter. In our study we exclusively focus on flow-aligning, rod-like particles, i.e., we choose $\xi > \xi_c > 0$.

In this chapter we focus exclusively on the flow instabilities that arise in systems where there is no externally applied shear. However in Chap. 4 we consider the shear rheology of our model.

Liquid crystals (LCs). As mentioned previously, theoretical descriptions of active matter frequently derive from simple continuum models for the hydrodynamics of a single-component fluid of rod-like objects which, depending on their symmetry, can be described by polar [81, 82] or nematic order parameters [16, 76, 77]. Such models were originally developed to describe passive LCs [74, 83], and because of this, the field of active matter naturally inherits key concepts and terminology from LC physics, which we now briefly introduce.

The term 'liquid-crystal' (LC) describes the fascinating phase of matter that lies partway between crystalline (solid) and isotropic (liquid) states [74]. Nematic LCs do not exhibit translational order, but do possess local orientational order which can be characterised by a nematic director $\hat{\mathbf{n}}$, which is symmetric under $\hat{\mathbf{n}} \to -\hat{\mathbf{n}}$ (see Fig. 3.4). More complex phases can also form, such as smectic LCs which form layers that can slide over each other. Experimentally, LCs undergo a phase transition from

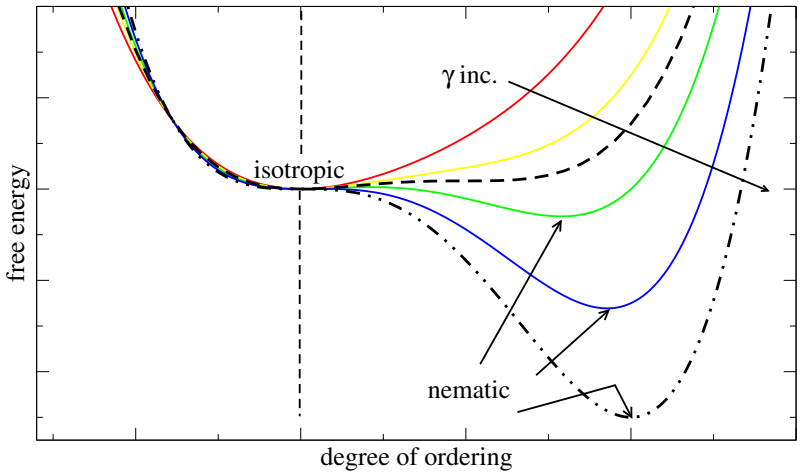

Figure 3.5: Schematic showing how the (zero-shear) free energy landscape changes as a function of IN-control parameter γ. For small values of γ there is only one minimum and therefore only one stable state, the isotropic state. At larger $\gamma = 2.7$ (black dashed curve) a second minimum (the nematic state) appears, though the non-zero energy barrier for the I $\rightarrow$ N transition means that the isotropic state remains metastable. Finally at $\gamma = 3$ (black dot-dashed line) this barrier disappears and only the nematic state remains stable. The stability of isotropic and nematic branches is also summarised in Fig. 3.6.

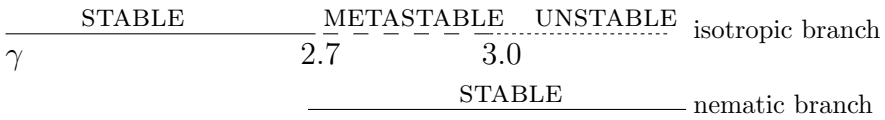

Figure 3.6: A summary of the stability of the two branches as a function of IN-control parameter γ (see also Fig. 3.5).

the disordered (isotropic) to the orientationally ordered (e.g., nematic) state as a control parameter, such as temperature or concentration, is varied.

In our model, without activity or shear, the isotropic-nematic (IN) transition is parametrised by γ, which controls the shape of the equilibrium free-energy landscape, see Fig. 3.5. For small $\gamma < 2.7$, the isotropic state $\mathbf{Q} = 0$ minimises the free energy. As γ is increased, a second minimum (the nematic state with $\mathbf{Q} \neq \mathbf{0}$) appears, though the non-zero energy barrier for the I $\rightarrow$ N transition means the isotropic state remains metastable. Finally at large $\gamma > 3$ this barrier disappears and only the nematic state remains stable. The stability of isotropic and nematic branches is summarised in Fig. 3.6.

Examples of active matter can be found in both isotropic and nematic phases, e.g., depending on concentration [84,85]. There has been much focus on the stability of orientationally ordered phases [77,81,86,87], or for phases close to the IN transition [15]. However we are not aware of any detailed study that explores the nature of the spontaneous flow instability as one transitions from a point deep in the isotropic phase ($\gamma < 2.7$) up to the nematic phase ($\gamma = 3$). In this chapter, we contrast the stability properties of both active-isotropic and active-nematic regimes. While these both exhibit the generic flow instability discussed above, we will show that the underlying mechanism is distinct.

Subcellular active matter. Fascinating examples of active matter can be found at the subcellular level. A paradigmatic example is actomyosin, a cytoskeletal structure in which clusters of myosin molecular motors generate contractile stresses between long actin filaments [88]. (See Fig. 3.7 for schematic.) In the cell cortex, actomyosin forms gel-like networks. In the presence of large crosslinking proteins such as *filamin*, myosin-driven activity has been observed to increase the elastic modulus by two orders of magnitude [89]. Numerical studies also suggest that crosslinked actin networks can exhibit LC elastomer behaviour, particularly when actin filaments are longer than the crosslinking proteins [90]. With crosslinking suppressed however, myosins can fluidise the actin network, significantly shortening the stress relaxation time [91]. Actin polymerisation plays a role in cell motility where it drives the protrusion of filopodia[2], allowing the cell to crawl. While polymerisation has previously been incorporated into cytoskeletal models [93], we do not include this effect in our study.

However cytoskeletal materials are not exclusively contractile in nature. Recent experiments [94, 95] explored the dynamics of clusters of kinesin molecular motors in a suspension of rigid microtubule filaments, finding the resulting dynamics to be extensile. Both kinesin and myosin (discussed above) molecular motors are powered by hydrolysis of adenosine triphosphate (ATP); the authors control the activity

[2]Filopodia are narrow protrusions that extend beyond the leading edge of the cell, and play a role in sensing and cell migration [92].

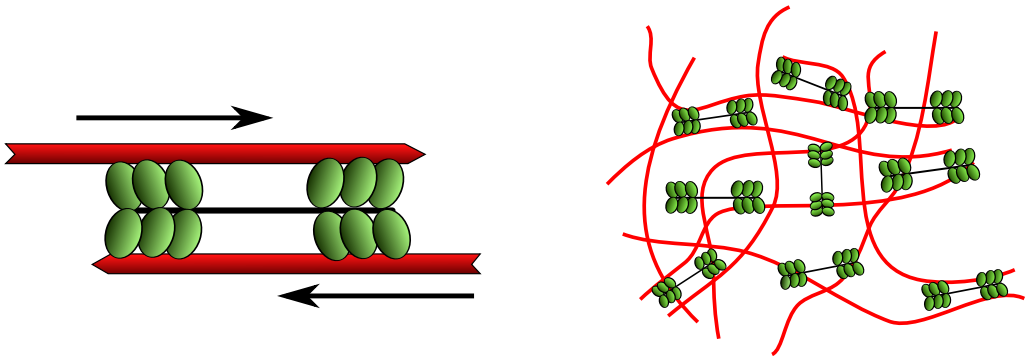

Figure 3.7: Left: Schematic illustrating how clusters of myosin molecular motors (green units) can generate forces between actin filaments (red lines). **Right:** Demonstration of how a gel-like network of such units can produce a distribution of active contractile stresses.

of the material by varying the concentration of ATP, reporting a transition from diffusive (at low activities) to ballistic (at high activities) dynamics. Both these examples motivate our study, which considers mainly extensile but also contractile dynamics within a subcellular context.

Viscoelasticity. While early studies mainly focused on the behaviour of these active materials in a Newtonian background solvent, there has been increasing interest in the dynamics of active matter in a complex, non-Newtonian environment. Swarms of motile bacteria reside in viscoelastic fluids such as mucus or saliva. Notably, many bacteria excrete their own polymers [96], suggesting an advantage in controlling the viscoelasticity of their surroundings. Subcellular active materials such as actomyosin interact with long-chain flexible polymers and other cytoplasmic components, with long (possibly divergent) relaxation times. Note that while LCs are somewhat viscoelastic (due to the slow motion of topological defects, see Sec. 5.1), within our model local relaxations of $\mathbf{Q}$ are fast relative to the cytoskeletal viscoelasticity we hope to address.

Theoretical and numerical attempts to model active matter in these environments focused first on the behaviour of individual swimmers. Single swimmers in a viscoelastic fluid have been modelled as infinite [7] and finite [97] oscillatory sheets, and as helices [98]. Depending on the size/frequency of oscillations, the geometry, and the properties of the fluid, swimming speed can be either enhanced or suppressed

relative to the Newtonian case. In Ref. [99], the authors examined the dynamics of several classes of swimmer (e.g., sliding spheres or squirmers) in shear-thinning fluids again finding that swimming speed is enhanced or hindered depending on model specifics.

However the collective dynamics of active fluids in a viscoelastic environment has received less attention. Bozorgi and Underhill model self-propelled polar entities using a Smoluchowski model, coupled through the velocity field to an Oldroyd-B fluid. In Ref. [100] the authors ignore diffusion and look at the stability of a homogeneous isotropic base state. In the infinite system size limit $k \to 0$, they find that the system is always unstable to heterogeneous perturbations, where the growth rate of the instability decreases as the polymer viscosity is increased. With diffusion included in the analysis [101], they find that a large (but finite) polymer viscosity can suppress the spontaneous flow instability in the infinite system size limit[3]. We will show in this chapter (see Sec. 3.3.3.4) that our results for an isotropic suspension generally agree with this study. We are unaware of any study on orientationally ordered phases in the presence of polymer viscoelasticity. Our results show that nematic phases remain intrinsically unstable (for any finite polymer elastic modulus G_C).

We introduce and derive a novel model exploring the competition between an active nematic LC in a viscoelastic background. In this chapter these sectors only influence each other indirectly via the velocity field, i.e., they are only coupled through the Navier-Stokes equation which contains stress contributions from both $\mathbf{Q}$ and $\mathbf{C}$. We define the geometry and boundary conditions of the problem, enumerate the key dimensionless groups and describe our numerical method.

Then by performing a linear stability analysis that includes the effect of the polymeric background, we generalise earlier results in the literature for the value of the critical activity for the onset of spontaneous flow. This criterion derives from two modes of instability: a viscous mode (at small polymer relaxation times) in which

[3]See the white region in Fig. 2a of Ref. [101]

the polymer acts purely as an additional source of viscosity, and an elastomeric mode (at large relaxation times), which surprisingly permits spontaneous flows at finite activity in what is effectively an elastic solid. Differences between bulk isotropic and nematic phases are also explored.

These results are then quantitatively verified using 1D non-linear simulations, revealing a variety of both static and oscillatory shear-banded states. The latter exhibit oscillations on a timescale set by the polymer relaxation time, confirming a direct role of the polymer (beyond simply providing an extra source of viscosity). This oscillatory spontaneous flow persists even for $\tau_C \to \infty$, consistent with our stability analysis, with the timescale of oscillation now set by the activity.

3.2 Description of model

We begin in this section by first describing our novel coarse-grained model for active viscoelastic matter, which marries the active LC hydrodynamics of orientable apolar particles [102] with polymer physics. The derivation of the model is explained from free energy and non-equilibrium statistical mechanical considerations. We then highlight the simplifications we make for the analytical and numerical studies in the following chapters, and specify the simulation geometry, boundary conditions, key dimensionless parameters and numerical details.

Credit for the derivation of the model is due to M. E. Cates, A. Maitra, S. Ramaswamy, S. Banerjee, and M. C. Marchetti. Additional discussion regarding of its construction can be found in the Supplementary Information of Ref. [103].

3.2.1 Full model

Nomenclature. For any second rank tensor $\mathbf{A}$, we define the symmetric, anti-symmetric and symmetric-traceless parts as

$$\mathbf{A}^S = {}^1\!/_2 \left(\mathbf{A} + \mathbf{A}^T\right), \tag{3.1}$$

$$\mathbf{A}^A = {}^1\!/_2 \left(\mathbf{A} - \mathbf{A}^T\right), \tag{3.2}$$

$$\mathbf{A}^{ST} = {}^1\!/_2 \left(\mathbf{A} + \mathbf{A}^T - {}^2\!/_3 \mathbf{I}\, \mathrm{Tr}[\mathbf{A}]\right). \tag{3.3}$$

We define the velocity gradient tensor $(\nabla \mathbf{v})_{ij} = \partial_i v_j$, and denote the symmetric and anti-symmetric forms as

$$\mathbf{D} = [\nabla \mathbf{v}]^{\mathrm{S}} = {}^1\!/_2 \left(\nabla \mathbf{v} + \nabla \mathbf{v}^T\right), \tag{3.4}$$

$$\mathbf{\Omega} = [\nabla \mathbf{v}]^{\mathrm{A}} = {}^1\!/_2 \left(\nabla \mathbf{v} - \nabla \mathbf{v}^T\right). \tag{3.5}$$

Order parameters. We describe the orientational order of the apolar liquid-crystalline active particles using a traceless, symmetric, second rank tensor $\mathbf{Q}$ which is constructed from the director $\hat{\mathbf{n}}$ as

$$Q_{\alpha\beta} = q\left(n_\alpha n_\beta - \delta_{\alpha\beta}/3\right). \tag{3.6}$$

The deformation of the polymer is modelled by a second rank conformation tensor $\mathbf{C}$ whose departure from isotropy measures local molecular strain. Depending on the level of description, $\mathbf{C}$ describes the dyadic product of the end to end vector $\mathbf{r}$ of either an entire polymer, or only a subsection of one.

While in principle one could additionally include variable concentration fields for either polymer or active particles (see e.g., Ref. [104]), we assume these to be uniform. This corresponds to the so-called large friction limit in which all components move with the same centre-of-mass velocity, $\mathbf{v}$.

We now describe the equations of motion that determine the dynamics of the three fields, $\mathbf{Q}$, $\mathbf{C}$ and $\mathbf{v}$. The present subsection may be skipped by the reader primarily interested in the results of our model; we also summarise the full equations of motion in Sec. 3.2.2.

3.2.1.1 Free energies

We begin by writing the total free energy functional for the system $F = \int f dV$, where $f = f_Q + f_C + f_{QC}$ contains respectively contributions from the nematic LC, polymer and a coupling between the two. For the liquid-crystalline free energy we use the standard form [83], which sums bulk and distortion contributions

$$f_Q = G_Q \left[\frac{\left(1 - \frac{\gamma}{3}\right)}{2}\mathrm{Tr}[\mathbf{Q}^2] - \frac{\gamma}{3}\mathrm{Tr}[\mathbf{Q}^3] + \frac{\gamma}{4}\left(\mathrm{Tr}[\mathbf{Q}^2]\right)^2\right] + \frac{K}{2}\left(\nabla_i Q_{jk}\right)^2, \tag{3.7}$$

where we have taken the standard one constant approximation for the non-local terms [74]. Here γ is the isotropic-nematic control parameter which sets the magnitude of order in a fully relaxed, passive system. Modulus G_Q and elastic constant K set the relative strengths of the bulk and distortion terms. The lengthscale at which these compete is given by the ratio $\ell_Q = \sqrt{K/G_Q}$.

For the polymer free energy, we follow Milner [105], setting

$$f_C = \frac{G_C}{2} \left(\mathrm{Tr}[\mathbf{C}] - \ln \det \mathbf{C} \right), \tag{3.8}$$

where G_C is the elastic modulus of the polymer. The first term describes the elastic potential energy of a deformation, while the second term accounts for the entropy associated with the sphericity of the molecular structure (which vanishes for isotropic $\mathbf{C} = \mathbf{I}$) [83]. While in principle one can include gradient terms in f_C analogous to the LC free energy, this would introduce diffusive terms to both the polymer constitutive equation and polymer stress [106]; for simplicity we follow Ref. [40] and only include a diffusive term of kinetic origin to the polymer constitutive equation (see below).

Finally, we prescribe the lowest order coupling between the $\mathbf{Q}$ and $\mathbf{C}$ sectors

$$f_{QC} = \kappa \mathrm{Tr}[\mathbf{Q}^2] \left(\mathrm{Tr}[\mathbf{C} - \mathbf{I}] \right) + 2\chi \mathrm{Tr}[\mathbf{CQ}]. \tag{3.9}$$

Here κ controls how the polymer pressure shifts the isotropic-nematic transition, and can be viewed as a rescaling of the first term in the bulk LC free-energy (Eq. 3.7). By construction, this term vanishes for a locally isotropic polymer network. The second term is dependent on the relative orientations of $\mathbf{Q}$ and $\mathbf{C}$, where it is preferential for $\mathbf{Q}$ and $\mathbf{C}$ to align for $\chi < 0$, and to be anti-parallel for $\chi > 0$.

3.2.1.2 Equations of motion

We now describe the equations of motion for the coupled fields $\mathbf{Q}$, $\mathbf{C}$ and $\mathbf{v}$. The couplings between these fall into three categories: *reversible* (no relaxation), *irreversible* (which in the absence of other couplings prescribes the relaxational dynamics of the order parameter towards the minimum free energy), and *active* (which break time-reversal symmetry).

Nematic. The dynamics of the nematic order parameter $\mathbf{Q}$ contain all three couplings,

$$\partial_t Q_{ij} = \underbrace{-v_k \partial_k Q_{ij} + \lambda^Q_{ijkl} \partial_l v_k}_{\text{reversible coupling}} + \underbrace{\Gamma^Q_{ijkl} H_{kl}}_{\text{irreversible coupling}} + \underbrace{\zeta_1 Q_{ij} + \zeta_2 [C_{ij}]^{\text{ST}}}_{\text{active coupling}}. \tag{3.10}$$

The first reversible coupling term simply describes advection by the flow; the second generalises this for rodlike molecules. To first order in $\mathbf{Q}$, the flow alignment tensor λ^Q_{ijkl} reads

$$\lambda^Q_{ijkl} = \frac{\lambda_0}{2}\left(\delta_{ik}\delta_{jl} + \delta_{jk}\delta_{il} - \frac{2}{3}\delta_{ij}\delta_{kl}\right) + \frac{1}{2}\left(\delta_{ik}Q_{jl} - \delta_{il}Q_{jk} + \delta_{jk}Q_{il} - \delta_{jl}Q_{ik}\right) + \frac{\lambda_1}{2}\left(\delta_{ik}Q_{jl} + \delta_{jk}Q_{il} + \delta_{jl}Q_{ik} + \delta_{il}Q_{jk} - \frac{4}{3}\delta_{ij}Q_{kl}\right). \tag{3.11}$$

From this point onwards, we restrict ourselves to the specific case of needle-like molecules and use the specific form of the flow-coupling coefficients, which can be derived from microscopic considerations [107], and set $\lambda_0 = 2\xi/3$ and $\lambda_1 = 2\xi$ where ξ is the flow alignment parameter. Particles are flow aligning if $|\xi| > 3q/(2+q)$ and flow-tumbling if not [108]. The sign of ξ determines shape, where $\xi > 0$ describes rod-like, $\xi = 0$ spherical, and $\xi < 0$ discoidal active particles (see also Fig. 3.3).

The third term on the RHS describes irreversible relaxation of $\mathbf{Q}$ towards the free energy minimum specified by the LC molecular field,

$$\mathbf{H} = -\frac{\delta F}{\delta \mathbf{Q}} + \frac{\mathbf{I}}{3}\text{Tr}[\frac{\delta F}{\delta \mathbf{Q}}] \tag{3.12}$$

$$= -G_Q\left[\left(1 - \frac{\gamma}{3}\right)\mathbf{Q} - \gamma\mathbf{Q}^2 + \gamma\mathbf{Q}^3\right] - G_Q\gamma\frac{\mathbf{I}}{3}\text{Tr}[\mathbf{Q}^2] + K\nabla^2\mathbf{Q} - 2\kappa\left(\text{Tr}[\mathbf{C}] - 3\right)\mathbf{Q} - 2\chi\left(\mathbf{C} - \frac{\mathbf{I}}{3}\text{Tr}[\mathbf{C}]\right). \tag{3.13}$$

We only expand the relaxation tensor Γ^Q_{ijkl} to zeroth order in fields and gradients, resulting in the scalar coefficient $\Gamma^Q_{ijkl} = (G_Q\tau_Q)^{-1}\delta_{ik}\delta_{jl}$. Here $G_Q\tau_Q$ gives the rotational viscosity of the LC, which we later refer to as η_Q.

The first active term in Eq. 3.10 can be absorbed into a redefinition of γ so we suppress it, setting $\zeta_1 = 0$. The second term describes polymers that are themselves active: in all that follows we consider the simpler case in which a passive polymer is driven by an active nematic, and also set $\zeta_2 = 0$.

Polymer. The constitutive equation for polymer conformation tensor $\mathbf{C}$ follows a similar form,

$$\partial_t C_{ij} = \underbrace{-v_k \partial_k C_{ij} + \lambda^C_{ijkl} \partial_l v_k}_{\text{reversible coupling}} + \underbrace{\Gamma^C_{ijkl} B_{kl} + \frac{\ell_C^2}{\tau_C} \nabla^2 C_{ij}}_{\text{irreversible coupling}}, \tag{3.14}$$

where here we have assumed, for simplicity, that the polymers are not themselves active and respond to nematic activity only through fluid advection. This captures the effect of adding polymer to (say) a cell extract; alternatively, this could describe the collective dynamics of bacterial suspensions in mucus. (In contrast, one could build a system of polymers directly from active elements [109].)

In order to connect with the widely used JS model (see Sec. 2.2.3.1), we expand the kinetic coupling tensor λ^C_{ijkl} to first order in $\mathbf{C}$,

$$\lambda^C_{ijkl} = \frac{a}{2}(\delta_{ik}C_{jl} + \delta_{jk}C_{il} + \delta_{jl}C_{ik} + \delta_{il}C_{jk}) + \frac{1}{2}(\delta_{ik}C_{jl} - \delta_{il}C_{jk} + \delta_{jk}C_{il} - \delta_{jl}C_{ik}), \tag{3.15}$$

where a is a slip parameter whose significance we discuss later (see Sec. 3.2.1.3).

The dissipative coupling through Γ^C_{ijkl} is more complicated: if, like in the LC equations, a constant isotropic kinetic coefficient is used, the resulting relaxational form is complicated and unphysical. We instead adopt the conformation-dependent relaxational kinetic coefficient used by Milner [105] to describe polymer gels,

$$\Gamma^C_{ijkl} = 2\tau_C^{-1} \left(\frac{\partial C_{ij}}{\partial \Sigma^{el}_{ml}} \right) C_{mk} \ , \tag{3.16}$$

where

$$\mathbf{\Sigma}^{el} = 2\mathbf{C} \cdot \delta F / \delta \mathbf{C} \ . \tag{3.17}$$

This reduces to a kinetic coefficient

$$\Gamma^C_{ijkl} = (G_C \tau_C)^{-1} (\delta_{ik}C_{jl} + \delta_{il}C_{jk} + \delta_{jl}C_{ik} + \delta_{jk}C_{il}) \ , \tag{3.18}$$

if one uses only the bare polymer free-energy, but is much more complicated if one retains couplings to the apolar order parameter, i.e., Eq. 3.9. Nevertheless, we will use this kinetic coefficient here to construct an active model that reduces to the JS model (as described in Sec. 2.2.3.1) in the absence of activity. Analogous with $\mathbf{H}$ in

the nematic sector, the polymer molecular field $\mathbf{B}$ is

$$\mathbf{B} = -\frac{\delta F}{\delta \mathbf{C}} \tag{3.19}$$

$$= -\frac{G_C}{2}\left(\mathbf{I} - \mathbf{C}^{-1}\right) - \kappa \mathbf{I}\mathrm{Tr}[\mathbf{Q}^2] - 2\chi\mathbf{Q}. \tag{3.20}$$

The final term in Eq. 3.14 allows for diffusion of the polymer order parameter, following earlier studies which generalise the JS model to include diffusive effects [40]. The shortest lengthscale at which structure may appear in $\mathbf{C}$ is set by ℓ_C and would, for example, describe the width of the interface between bands of differing shear-rate [41].

For polymer solutions, even without $\mathbf{Q}$, physically such a term might describe the microscopic Brownian motion of polymer molecules [110]. Within the cytoskeleton this could also represent diffusive transport of gel material. For a detailed evaluation of diffusion in the *nematic* order parameter field see, e.g., Ref. [111]. There are also practical numerical reasons to include a non-local term. While in theory $\mathbf{C}$ is coupled to $\mathbf{Q}$ which does contain gradient terms, in practice this coupling isn't strong enough and we find structure in $\mathbf{C}$ on the scale of the grid spacing Δx if the diffusive term is neglected.

Velocity. We work in the zero Reynolds number limit, in which the centre-of-mass velocity $\mathbf{v}$ is determined instantly by the dynamics of $\mathbf{Q}$ and $\mathbf{C}$. Stokes force balance then reads

$$\partial_\beta \Sigma_{\alpha\beta} = 0, \tag{3.21}$$

where $\Sigma_{\alpha\beta}$ is the total stress tensor. This sums contributions from an isotropic pressure P, reactive stresses in $\mathbf{Q}$ and $\mathbf{C}$, a dissipative Newtonian stress, and an active stress

$$\mathbf{\Sigma} = \underbrace{-P\mathbf{I} + \mathbf{\Sigma}^Q + \mathbf{\Sigma}^C}_{\text{reactive}} + \underbrace{\mathbf{\Sigma}^{diss}}_{\text{dissipative}} + \underbrace{\mathbf{\Sigma}^a}_{\text{active}}. \tag{3.22}$$

The reactive contributions are given by [83, 106, 112]

$$\Sigma^Q_{ij} = -(\partial_i Q_{kl})\frac{\delta F}{\delta\left(\partial_j Q_{kl}\right)} - \lambda^Q_{klij} H_{kl}\ , \tag{3.23}$$

$$\Sigma^C_{ij} = -(\partial_i C_{kl})\frac{\delta F}{\delta\left(\partial_j C_{kl}\right)} - \lambda^C_{klij} B_{kl}\ , \tag{3.24}$$

where the kinetic coefficients λ^Q_{ijkl}, λ^C_{ijkl} are defined as before. The dissipative stress is simply

$$\Sigma^{\text{diss}}_{ij} = 2\eta D_{ij} \ , \tag{3.25}$$

where η is the solvent viscosity, and $\mathbf{D} = {}^1\!/_2 \left(\nabla\mathbf{v} + \nabla\mathbf{v}^T\right)$ is the symmetrized velocity gradient tensor. Finally the active stress is

$$\Sigma^a_{ij} = -\zeta_3 C_{ij} - \zeta Q_{ij} \ , \tag{3.26}$$

where ζ_3, ζ are active parameters. We restrict ourselves to the simpler case of an active nematic in a passive polymer background and set $\zeta_3 = 0$. The only remaining activity parameter ζ forms a key parameter for our study of the model.

3.2.1.3 Significance of slip parameter

The slip parameter a describes the non-affine stretch of polymer dumbbells relative to the extension of the flow. For values of $|a| < 1$, the polymer slips, which can result in constitutive curves with non-monotonic behaviour, and for the JS model this occurs when viscosity ratio $\eta/G_C\tau_C < {}^1\!/_8$ [113].

For our model to remain thermodynamically admissible in the passive limit, particular care must be taken in the derivation of the polymeric stress, $\mathbf{\Sigma}^C$. Correct physical behaviour requires that slip parameter a appears in both the polymeric constitutive equation and stress (as both are derived from λ^C_{ijkl} which contains a). The previous derivations of the JS model (either with [40] or without diffusion [59]) set $\mathbf{\Sigma}^C = -2\mathbf{BC}$. This stress is only accidentally admissible through a renormalisation of G_C [106]. For the remainder of this thesis, we use this renormalised version of the model exclusively. In Sec. 4.3.1, we will explore the effect this revision has on the polymer shear rheology. In particular, we will show that constitutive curves are non-monotonic for $\eta/(a^2 G_C\tau_C) < {}^1\!/_8$ (see Sec. 4.3.1). Note that for $a = 1$, the polymeric sector reduces to the well studied Oldroyd-B model.

3.2.1.4 Asymmetry of the stress tensor

While the majority of the stress contributions are symmetric, $\mathbf{\Sigma}^Q$ contains an anti-symmetric piece. As such, care should be taken to preserve the correct order of

indices in Eq. 3.21. While in principle it is possible to work entirely with a symmetrised stress that produces the same velocity field $\mathbf{v}$ [114] (e.g., as in Ref. [115]), we retain the asymmetric version for simplicity.

3.2.2 Reduced model

We now briefly summarise the condensed equation set for the model after expanding out the kinetic and relaxational coefficients, and including our choice to set additional active and coupling parameters $\zeta_1 = \zeta_2 = \zeta_3 = \kappa = 0$.

Constitutive Equations

$$(\partial_t + \mathbf{v}.\nabla)\,\mathbf{Q} = \mathbf{Q\Omega} - \mathbf{\Omega Q} + 2\xi[\mathbf{QD}]^{\mathrm{ST}} + \frac{2\xi}{3}\mathbf{D} - 2\xi\mathbf{Q}\mathrm{Tr}[\mathbf{QD}] + \frac{1}{G_Q\tau_Q}\mathbf{H}$$

$$(\partial_t + \mathbf{v}.\nabla)\,\mathbf{C} = \mathbf{C\Omega} - \mathbf{\Omega C} + 2a[\mathbf{CD}]^{\mathrm{S}} + \frac{-1}{\tau_C}(\mathbf{C} - \mathbf{I}) + \frac{\ell_C^2}{\tau_C}\nabla^2\mathbf{C} + \frac{-4}{\tau_C G_C}\chi[\mathbf{QC}]^{\mathrm{S}}$$

Molecular Field

$$\mathbf{H} = -G_Q\left[\left(1 - \frac{\gamma}{3}\right)\mathbf{Q} - \gamma\mathbf{Q}^2 + \gamma\mathbf{Q}^3\right] - G_Q\gamma\frac{\mathbf{I}}{3}\mathrm{Tr}[\mathbf{Q}^2] + K\nabla^2\mathbf{Q} - 2\chi\left(\mathbf{C} - \frac{\mathbf{I}}{3}\mathrm{Tr}[\mathbf{C}]\right)$$

Force balance / Stresses

$$\begin{aligned}
\partial_\beta\Sigma_{\alpha\beta} &= 0 \\
\mathbf{\Sigma} &= -P_0\mathbf{I} + \mathbf{\Sigma}^Q + \mathbf{\Sigma}^C + \mathbf{\Sigma}^{diss} + \mathbf{\Sigma}^a \\
\mathbf{\Sigma}^Q &= -K\,(\nabla\mathbf{Q}) : (\nabla\mathbf{Q}) - \frac{2\xi}{3}\mathbf{H} - 2\xi[\mathbf{QH}]^{\mathrm{ST}} + 2[\mathbf{QH}]^{\mathrm{A}} + 2\xi\mathbf{Q}\mathrm{Tr}[\mathbf{QH}] \\
\mathbf{\Sigma}^C &= aG_C\,(\mathbf{C} - \mathbf{I}) + 4\chi\left(a[\mathbf{QC}]^{\mathrm{S}} + [\mathbf{QC}]^{\mathrm{A}}\right) \\
\mathbf{\Sigma}^{diss} &= 2\eta\mathbf{D} \\
\mathbf{\Sigma}^a &= -\zeta\mathbf{Q}
\end{aligned}$$

3.2.3 Geometry and boundary conditions

In the majority of our study we consider a slab of active material confined between parallel plates separated by L_y in the y-direction, as shown in Fig. 3.8. At the

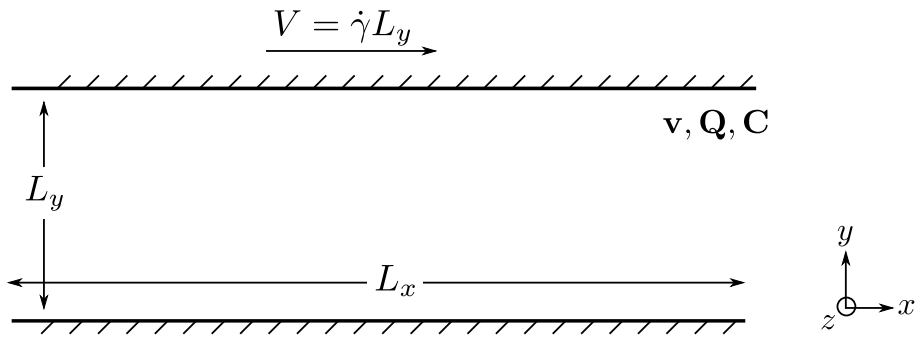

Figure 3.8: Schematic of the parallel plate geometry which we consider for the majority of the study. For the 1D study in Chaps. 3/4 we assume invariance in x and z directions, for later 2D studies (Chap. 5) we allow variation in x and y directions. We consider (i) static walls (Chaps. 3, 5) and (ii) sheared parallel plates (Chap. 4), where in the latter case the top plate moves with velocity $V = \bar{\dot{\gamma}} L_y$.

plates we choose no-slip and no-permeation boundary conditions (BCs) for $\mathbf{v}$ and zero-gradient BCs for $\mathbf{Q}$ and $\mathbf{C}$,

$$\begin{aligned} \partial_y Q_{\alpha\beta} = \partial_y C_{\alpha\beta} = 0 \quad \text{at} \quad y = \{0, L_y\} \quad \forall \alpha, \beta, \\ v_x = v_y = 0 \quad \text{at} \quad y = 0, \\ v_x = V \left(= \dot{\gamma} L_y\right), \; v_y = 0 \quad \text{at} \quad y = L_y, \end{aligned}$$

where $V = \dot{\gamma} L_y$ is the velocity of the top wall. The special case $\dot{\gamma} = 0$ gives the unsheared case studied in Chaps. 3, 5.

The above 'free boundary condition' employed for the nematic sector in the context of active materials has been considered previously [15, 80] whereas other studies have adopted anchoring BCs [116]. Different boundary conditions can result in quantitative differences (e.g., in the threshold activity for spontaneous flow), and care must been taken when comparing studies. However recent work in 2D employing both free and anchoring BCs has shown that the essential physics is qualitatively unchanged by this choice [87], particularly at larger activities where the state is independent of finite size effects.

Equivalent boundary conditions for $\mathbf{Q}$ and $\mathbf{C}$ at the boundaries also make the linear stability calculation analytically tractable (see Sec. 3.3). In our stability analysis, we will show that the initial condition can significantly impact the threshold for spontaneous flow, finding states where the director is initially aligned in the x- and y-

directions become separately unstable at activities an order of magnitude apart. We expect that a similar effect would be observed were we to instead choose boundary conditions that impose a director orientation at the wall, i.e., using strong anchoring conditions. Our results suggest that prescribing a director parallel (perpendicular) to the wall would result in a bias towards the formation of a splay (bend) shear-banded state. Recent experiments have demonstrated that living liquid-crystals, in which bacteria are embedded within a lyotropic LC, can be influenced by anchoring boundary conditions in a similar fashion [117].

This chapter focuses on the 1D dynamics where we assume all quantities are invariant in the x and z directions. We work with 3D tensors for both $\mathbf{Q}$ and $\mathbf{C}$ which, for example, allows $\hat{\mathbf{n}}$ to point out of plane. These are embedded in a space whose dimensionality is 0D, 1D (Chaps. 3, 4) and 2D (Chap. 5). In our simulations, only three independent entries of $\mathbf{Q}$ and $\mathbf{C}$ become non-zero in practice [118, 119], given that both order parameters are symmetric. In Sec. 5.2, we report the results of a collaborative project which studied how the correlation lengths in the turbulent active phase depend on activity. Our data (with 3D $\mathbf{Q}$) demonstrated excellent agreement with that from an independent numerical study (with 2D $\mathbf{Q}$), strongly suggesting that the key physics of such models is robust to the dimensionality of the order parameter. Velocities are purely in the $x-y$ plane, i.e., we impose $v_z = 0$.

3.2.4 Units and parameters

In all that follows we work in units of length $[L] = L_y = 1$, time $[T] = \tau_Q = 1$, and modulus $[G] = G_Q = 1$. All model parameters, including our choice of units are summarised in Table 3.1 for convenience.

As the cellular materials of interest are typically found at high concentrations, we mainly fix the IN-control parameter $\gamma = 3$ in our numerics, corresponding to the nematic phase in a passive LC. However we also consider the isotropic case where $\gamma < 2.7$ in our stability analysis. We work in the zero Reynolds number limit by setting $\rho \to 0$, and fix the solvent viscosity $\eta = 0.567$ to allow direct comparison with previous work [87]. We begin by setting the externally applied shear-rate $\dot{\gamma}$ to zero, but later explore the dynamics of a driven system where $\dot{\gamma} \neq 0$. In later 2D

studies the length in the flow (periodic) direction is fixed at $L_x = 4L_y$.

Unless otherwise stated, we fix $\xi = 0.7$ (flow-aligning) and slip parameter $a = 1$ (no-slip), to avoid introducing any additional tumbling or shear-banding instabilities associated with $\mathbf{Q}$ or $\mathbf{C}$ respectively. This allows us to focus on the role of activity in the spontaneous flow instability; we later explore the role of ξ and a on the shear rheology of our model in Chap. 4. The choice of $a = 1$ reduces the polymeric sector to an Oldroyd-B fluid, meaning only affine deformation is possible. Theoretical studies suggest this may be a reasonable assumption for dense cross-linked filaments [120, 121]. For most of our results we tune the polymer elastic modulus G_C to maintain constant polymer viscosity ($\eta_C \equiv \tau_C G_C = 1$), though this is briefly relaxed to explore states of infinite polymer viscosity (Sec. 3.4.2).

The microscopic lengthscale at which elastic distortions compete with the bulk free energies is $\ell_Q \equiv \sqrt{K/G_Q}$. Recasting the $\mathbf{Q}$ constitutive equation (Eq. 3.10) in this notation, the diffusive term (originating from the molecular field[4], see Eq. 3.13) then becomes $\frac{\ell_Q^2}{\tau_Q}\nabla^2\mathbf{Q}$. We include the analogous diffusive terms in the polymeric sector, where the interfacial lengthscale is set by ℓ_C. In the linear stability analysis we make no assumption about the relative strengths of these diffusive prefactors. However unless stated otherwise, in our numerical results we constrain

$$\frac{\ell_Q^2}{\tau_Q}\left(\equiv \frac{K}{\eta_Q}\right) = \frac{\ell_C^2}{\tau_C} = \Delta. \tag{3.27}$$

Our choice to equate diffusivities allows us to take an elastomeric limit $\tau_C \to \infty$ whilst retaining spatial gradients in $\mathbf{C}$.

For the majority of our study, coupling between the $\mathbf{Q}$ and $\mathbf{C}$ sectors is mediated via the fluid velocity $\mathbf{v}$, i.e., polymer and nematic are only coupled in the sense that they both contribute stresses to the Navier-Stokes equation. Recall that these sectors can additionally be coupled thermodynamically at the free energy level for $\chi \neq 0$ (Eq. 3.9). We briefly explore the effect of this explicit coupling in Sec. 5.6 by setting $0 < \chi < \min(G_Q, G_C)$, where the effects on the dynamical behaviour are dramatic.

Having fixed the majority of model parameters to appropriate values (see Table 3.1 for a full list), three parameters remain to be varied: activity (ζ), diffusivity

[4]Note that ℓ_Q also appears in the stress which contains gradients in $\mathbf{Q}$.

parameter	dimensions	value	description
system (or shared) parameters			
η	$[ML^{-1}T^{-1}] = [GT]$	0.567 (fixed)	solvent viscosity
L_x	$[L]$	4 (fixed)	length in periodic direction
L_y	$[L]$	1 (fixed)	distance between walls
nematic liquid-crystal parameters (Q)			
G_Q	[G]	1 (fixed)	**Q** modulus (appears in bulk free energy density)
τ_Q	[T]	1 (fixed)	**Q** relaxation time
γ	[1]	3 (fixed)	IN control parameter, deep in nematic phase
ξ	[1]	0.7 (fixed)	flow aligning ($\xi > 3/5$)
$\ell_Q = \sqrt{\frac{K}{G_Q}}$	$[L]$	$0.002 \to 0.025$ (vary $\Delta = \frac{\ell_Q^2}{\tau_Q}$)	Frank length
polymer parameters (C)			
G_C	[G]	chosen to fix $\eta_C = 1$ (vary)	**C** elastic modulus
τ_C	[T]	$10^{-2} \to 10^6 \to \infty$ (vary)	**C** relaxation time
ℓ_C	[L]	$\frac{\ell_Q^2}{\tau_Q} = \frac{\ell_C^2}{\tau_C} = \Delta$ (slaved to ℓ_Q)	diffusive lengthscale
a	[1]	1 (fixed)	slip parameter (where $a = 1$ is Oldroyd-B)
activity parameters (Q)			
ζ	$[ML^{-1}T^{-2}] = [G]$	0.001$\to$ 10 (vary)	extensile activities ($\zeta > 0$)
explicit coupling parameters (Q + C)			
χ	$[G]$	$\chi \ll G_Q, G_C$ (vary) or 0 (fixed)	free energy coupling parameter

Table 3.1: Full list of model parameters, **grey** rows show our choice for units of length $[L]$, modulus $[G]$, and time $[T]$ respectively. Values for parameters that are fixed (unless stated otherwise) are given.

(Δ), and polymer relaxation time (τ_C). These are made dimensionless as

$$\tilde{\zeta} = \frac{\zeta}{G_Q},$$
$$\tilde{\Delta} = \frac{\Delta \tau_Q}{L_y^2} \left(= \frac{K}{G_Q L_y^2} = \frac{\ell_Q^2}{L_y^2} \right),$$
$$\tilde{\tau}_C = \frac{\tau_C}{\tau_Q},$$

but by construction, in our units the tildes are redundant and we now drop them.

parameter	value	description
$\tilde{\zeta} = \zeta/G_Q$	$0.001 \rightarrow 10$	activity ($\zeta > 0$)
$\tilde{\Delta} \equiv \frac{K}{G_Q L_y^2}$	$10^{-5} \rightarrow 6.4 \times 10^{-4}$	diffusive constant
$\tilde{\tau}_C \equiv \tau_C/\tau_Q$	$10^{-2} \rightarrow 10^6 \rightarrow \infty$	ratio of relaxation times
$\tilde{\chi} \equiv \chi/G_Q$	$\chi \ll G_Q, G_C$ or 0	explicit coupling strength

Table 3.2: List of key dimensionless parameters which we vary, from this point onwards we drop tildes for clarity. (Note that we also use the symbol χ in a separate context in Chap. 6 to denote the normalised drag.)

Note that in principle there is a 4th dimensionless parameter $\tilde{\eta} = \eta/(\tau_Q G_Q)$, but we fix this $\tilde{\eta} = 0.567$ to remove this arguably less interesting dimension of parameter space (the specific value is inherited from an earlier numerical study [87]). These key dimensionless groups are summarised in Table 3.2.

3.2.4.1 Experimental parameter estimates

While it is very difficult to provide a direct mapping of our model parameters to experimentally measurable quantities, we can at least provide sensible order-of-magnitude estimates to guide our numerical study.

Our choice of dimensionless control parameters in Table 3.2 might describe a cytoskeletal gel similar to the recent experiments of Sanchez *et al.* [94], which captured the extensile ($\zeta > 0$) dynamics of a kinesin-microtubule mixture. The strength of the activity was tuned experimentally using the concentration of ATP [94]. The modulus of a contractile actin gel increases by a factor of 10 in the presence of myosin motor activity [89] suggesting an upper bound of $\zeta/G_Q \approx 10$. Values for Δ are selected so that $\Delta x < \ell_Q \ll L_y$ (where Δx is the numerical grid size). The velocity correlation length for kinesin microtubule mixtures has been estimated at $l_v \approx 100\mu m$ [94], and if we assume ℓ_Q is an order of magnitude smaller (see results in Sec. 5.2), our simulations then imply a channel width in the range $400\mu m \rightarrow 3mm$ as would be found in a typical microfluidic setup.

While the rheological properties of the cytoskeleton are highly complex and de-

pendent on the cell type [122], representative values for a crosslinked actin gel might be $\tau_Q \sim 5s, G_Q \sim 1\text{Pa}$ [89]. A logical extension to previous studies (without polymer) then sets comparable LC, polymer and solvent viscosities $G_Q\tau_Q = G_C\tau_C \sim \eta$. In our model, the polymer could in principle describe a range of viscoelastic behaviours within the cell, including e.g., the cytosol, which comprises of entangled protein filaments and organelles [123]. To encompass this diversity, we vary the polymer relaxation time over several decades from $\tau_C = 10^{-2}$ (for which the polymeric dynamics is rapid and only contribute extra viscosity) to $\tau_C \to \infty$ (where the polymer effectively acts as an elastic solid). The latter limit in our model describes an nematic elastomer, i.e., a cross-linked polymer network with liquid-crystalline orientational order [124, 125]. We will refer to this limit in our results as the elastomeric limit.

3.3 Linear stability analysis

We have introduced our model for active viscoelastic matter, indicating the simplifications made for our analytical and numerical work. We also have defined the key dimensionless parameters and geometry of the problem. It is unclear *a priori* which regions of our parameter space, which is of large dimensionality, contain the most interesting dynamical behaviour, especially as experimental suggestions for the model parameters only yield order-of-magnitude estimates.

Therefore we proceed by first analytically considering the linearised version of our model. This allows us to rapidly locate the key stability features such as the thresholds for spontaneous flow, or regions where oscillatory behaviour is to be expected. This then informs parameter selection for our non-linear numerical studies which require significantly longer runtimes.

In this chapter we perform a stability analysis on an initially non-flowing active viscoelastic material confined between parallel plates L_y apart. We generalise previous results to obtain an analytical critical activity for the onset of the spontaneous flow instability in the presence of a polymeric background. In finite systems, if the polymer viscosity is increased at fixed τ_C by increasing G_C, we find that this

critical activity is increased. Taking the infinite viscosity limit in this fashion then completely suppresses the instability (for any finite activity). However, if instead we fix polymer modulus G_C and increase τ_C, the critical activity tends to a finite constant, even in the limit $\tau_C \to \infty$. This surprising result implies that the activity driven spontaneous flow instability is possible in what is effectively an elastic solid, a result that we later confirm numerically.

While these results are common to both isotropic and nematic materials, their behaviour in the infinite system size limit differs. We show that the critical activity vanishes as $L_y \to \infty$ for nematic materials (recovering earlier works without polymer), but remains finite for isotropic materials consistent with Ref. [101]. We rationalise this difference using a rheological argument. We finish by commenting on the generality of our results, which are robust to the inclusion of polymer diffusion. Differences that might arise under different boundary conditions are also discussed.

3.3.1 General procedure

We begin by outlining the general procedure for the linear stability analysis, then separately apply it to nematic then isotropic suspensions. We examine the linear stability of an initially non-flowing, homogeneous base state to 1D perturbations in the flow gradient direction, y. (In Chap. 4 we generalise these results to include sheared suspensions, though the lack of an analytical base state for $\dot{\gamma} \neq 0$ means the eigenvalue problem must then be evaluated numerically.) Consider first the homogeneous base state

$$\overline{Q}_{\alpha\beta} = q\left(n_\alpha n_\beta - \delta_{\alpha\beta}\right), \tag{3.28a}$$

$$\overline{C}_{\alpha\beta} = \delta_{\alpha\beta}, \tag{3.28b}$$

$$\overline{\dot{\gamma}} \equiv \overline{\partial_y v_x} = 0, \tag{3.28c}$$

where q is the magnitude of the order parameter. For isotropic materials $q = 0$, whereas for nematics we choose coordinates such that $\hat{\mathbf{n}} = (1, 0, 0)$ or $(0, 1, 0)$, corresponding to a director oriented parallel and perpendicular to the walls respectively. While perturbations can grow in $\bar{\dot{\gamma}}$, the other elements of the velocity gradient tensor remain zero (as $v_y = v_z = 0$, and because we assume invariance in the x/z direc-

tions). To simplify the notation, we introduce a vector $\boldsymbol{\phi} = (\mathbf{Q}, \mathbf{C}, \dot{\gamma})$ and perturb the base state by writing

$$\boldsymbol{\phi} = \overline{\boldsymbol{\phi}} + \delta\boldsymbol{\phi} \tag{3.29}$$

where $\overline{\boldsymbol{\phi}} = \left(\overline{\mathbf{Q}}, \overline{\mathbf{C}}, \overline{\dot{\gamma}}\right)$. We write the perturbations as the sum of Fourier modes

$$\delta\boldsymbol{\phi} = \sum_k \boldsymbol{\phi}^k(t)\cos(ky) \ , \tag{3.30}$$

with Fourier amplitudes $\boldsymbol{\phi}^k = \left(\mathbf{Q}^k, \mathbf{C}^k, \dot{\gamma}^k\right)$, and where the wavevector k may only take discrete values: $k = \pi\tilde{k}/L_y$ where $\tilde{k}$ is an integer. We linearise our full set of hydrodynamic equations about the base state to obtain coupled linear algebraic equations for the Fourier amplitudes. Using the Stokes equation, $\nabla \cdot \boldsymbol{\Sigma} = 0$, with $\boldsymbol{\Sigma}$ the total stress tensor given in Eq. 3.22, we can express $\dot{\gamma}^k$ in terms of $\mathbf{Q}^k$ and $\mathbf{C}^k$ as

$$\dot{\gamma}^k = \frac{-1}{\eta}\left(\delta\boldsymbol{\Sigma}_A^k + \delta\boldsymbol{\Sigma}_Q^k + \delta\boldsymbol{\Sigma}_C^k\right)_{xy},$$

where $\delta\boldsymbol{\Sigma}^k$ denotes the k-th Fourier amplitude of the linearised part of the corresponding contribution to the stress tensor. Eliminating $\dot{\gamma}^k$ we finally obtain a linearised set of algebraic equations for the six Fourier amplitudes $\mathbf{p}^k = \big(Q_{xx}^k, Q_{xy}^k, Q_{yy}^k, C_{xx}^k, C_{xy}^k, C_{yy}^k\big)^T$ of the form

$$\partial_t \mathbf{p}^k = \mathbf{M}^k \cdot \mathbf{p}^k \ . \tag{3.31}$$

The eigenvalues of the matrix $\mathbf{M}^k$ yield the dispersion relations ω_k of the linear modes of the system as functions of wavevector k. The real part of such eigenvalues is the growth rate of the Fourier amplitudes of the perturbations in the hydrodynamic fields. The two non-trivial eigenvalues are of quadratic form $\omega^{\pm} = -B \pm \sqrt{B^2 - 4AC}/2A$, where all quantities are functions of wavevector (details are given in Apx. 3.6, including full expressions for A, B, and C). We then ask at what value of the activity does the linear instability first appear, i.e., we find the critical activity ζ_c such that

$$Re(\omega^+) = 0, \tag{3.32}$$

where ω^+ is the eigenvalue of $\mathbf{M}^k$ with the largest real part.

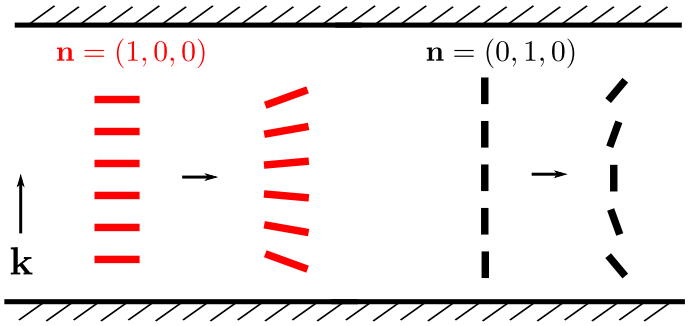

Figure 3.9: Schematic demonstrating two director configurations considered in our stability analysis. We probe the linear stability of these uniformly ordered states to splay (left) and bend (right) instabilities respectively. The wavevector **k** is oriented perpendicular to the walls.

There exist two solutions to Eq. 3.32, where the critical activity with the smaller magnitude determines the threshold of instability. The crossover between these criteria depends on the separation of relaxation times in the problem. When the ratio τ_C/τ_Q is small (we later quantify this), the polymer acts purely as an additional source of viscosity, resulting in a *viscous criterion*. However when the ratio is very large, a new mode of instability dominates resulting in a *elastomeric criterion* independent of τ_C.

The active LC under consideration can initially be in an isotropic or a nematic state. While the above criteria remain qualitatively similar for both in many respects, differing behaviour is observed in the infinite system size limit. The critical activity remains non-zero for isotropic suspensions, while for nematic suspensions it vanishes. We later rationalise this result by considering the shear rheology in the limit of $\dot{\gamma} \to 0$ (see Sec. 4.3.3).

3.3.2 Nematic case

Numerous examples of active biological matter can be found at high concentrations, displaying nematic or polar order [94, 126]. Many analytical studies focus on the stability and dynamics of such orientationally ordered phases [77, 78, 81, 87], and in order to connect with these studies and others, we begin our study in this regime. We later generalise our results to include isotropic base states.

The stability calculation for a nematic base state is more involved than for

isotropic materials as the tensor $\mathbf{Q}$ in the base state is non-zero. In order to simplify the algebra, we fix the IN control parameter $\gamma = 3$ corresponding to the end of isotropic metastability (recall Fig. 3.6), though we have explicitly checked using Mathematica [127] that our results for nematics are qualitatively unchanged to this choice.

We explore two director configurations $\hat{\mathbf{n}} = (1, 0, 0)$, $\hat{\mathbf{n}} = (0, 1, 0)$ which respectively probe splay and bend instabilities (see Fig. 3.9). Note that the wavevector $\mathbf{k}$ is perpendicular to the former and parallel with the latter configuration. Experimentally, a particular orientation could be selected by choice of boundary condition [117].

The non-trivial eigenvalues of the stability problem can be written in the quadratic form

$$\omega^{\pm} = \frac{-B \pm \sqrt{B^2 - 4AC}}{2A}, \tag{3.33}$$

where full expressions for A, B, and C are given in Apx. 3.6.1.2. We proceed by considering separately the cases when the discriminant $D = B^2 - 4AC$ is positive and negative. The former case, which occurs for small τ_C, results in purely real eigenvalues and our critical activity, which requires solution of $Re(\omega^+) = 0$, can simply be found by solving $AC = 0$. The latter case (for large τ_C) results in a pair of complex conjugate eigenvalues, the real part of which changes sign when $B = 0$.

One can show (see Apx. 3.6.1) that the point of crossover between these criteria (i.e., $AC = B = 0$, and therefore $D = 0$) occurs at

$$\tau_C^* \approx \frac{1 + \ell_C^2 k^2}{\ell_Q^2 k^2} \tau_Q. \tag{3.34}$$

The full analytical form of τ_C^* is too unwieldy to reproduce here so we use an approximation that in practice results in a marginally smaller value of τ_C^*. (See Apx. 3.6.1 for details of the approximation.)

Interestingly, τ_C^* diverges in the infinite system size limit $k \to 0$ implying that only the viscous criterion ζ_c^{visc} applies to bulk systems. This is visualised in Fig. 3.10 (left) where the crossover point between criteria (blue circles) is pushed out towards $\tau_C \to \infty$ as we increase the system size. We will show that ζ_c^{visc} is the only relevant criterion in this infinite system size limit as it tends to zero (black curves in Fig. 3.10), 'trumping' the (non-zero) elastomeric criterion.

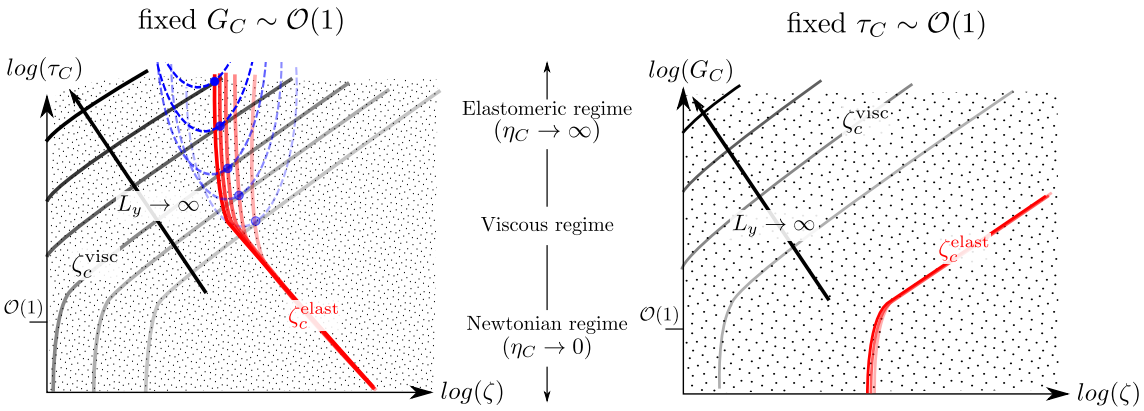

Figure 3.10: Schematic phase diagram demonstrating how viscous and elastomeric criteria (black/red lines) behave as we approach the infinite system size limit for a nematic. Curves of decreasing transparency are for increasing L_y, blue dashed line bounds the oscillatory region. Every point on the phase diagram is unstable (dotted area) for $L_y \to \infty$. **Left:** At fixed $G_C \sim \mathcal{O}(1)$, the crossover between criteria (τ_C^*, blue circles) is pushed to increasingly larger τ_C as we increase the system size. The viscous criteria tends to zero as $L_y \to \infty$, whereas the elastomeric criterion converges to a constant value. **Right:** At fixed $\tau_C \sim \mathcal{O}(1)$ the same limiting behaviour is observed (though there is no crossover).

However all our numerical results assume a finite system size, justifying exploration of both viscous and elastomeric criteria. For our choice to fix $\ell_Q/L_y \sim \mathcal{O}(10^{-2})$, the crossover typically occurs at $\tau_C^* \sim \mathcal{O}(10^3)$. The physical significance of τ_C^* can best be seen by taking the small k limit directly in Eq. 3.34 in which one recovers $\tau_C^* \approx \eta_Q/(Kk^2)$. This is the orientational relaxation time for long-wavelength distortions in the nematic phase. If the polymer relaxation time is longer than this, then the polymer will appear as an elastic solid from the perspective of the active nematic (this is the elastomeric limit). Conversely if the polymer stress can relax faster than τ_C^*, then the polymer plays the role of a viscous fluid. The appearance of oscillatory behaviour in the elastomeric limit is consistent with the recent work of Bozorgi and Underhill [101] which we later discuss in Sec. 3.3.3.4.

3.3.2.1 Viscous criterion: nematic

When $\tau_C < \tau_C^*$, the discriminant ($D = B^2 - 4AC$) remains positive and the eigenvalue problem simplifies to $AC = 0$. Solving for ζ yields the critical activity,

$$\zeta_c^{\text{visc}} = \frac{k^2 \ell_Q^2}{\Lambda \tau_Q} \left(\eta + 2\Lambda^2 \eta_Q + \frac{a^2}{1 + k^2 \ell_C^2} \eta_C \right), \tag{3.35}$$

where

$$\Lambda = \begin{cases} (5\xi - 3)/12 & \text{for } \hat{\mathbf{n}} = (1, 0, 0)\,, \\ (5\xi + 3)/12 & \text{for } \hat{\mathbf{n}} = (0, 1, 0)\,. \end{cases} \tag{3.36}$$

Note that the orientation of the director in the base state plays an important role. In our simulations we typically fix $\xi = 0.7$ meaning that Λ, and therefore ζ_c, changes by an order of magnitude depending on the director orientation in the initial base state.

The lowest possible mode ($\tilde{k} = 1 \Rightarrow k = \pi/L_y$) is the first to become unstable. Substituting this into Eq. 3.35 and using $K \equiv \ell_Q^2 G_Q$ recovers a form consistent with earlier studies of orientationally ordered active matter (without polymer) [80, 81],

$$\zeta_c^{\text{visc}} \propto \frac{K}{L_y^2} \left[1 + A\frac{\eta}{\eta_Q} + B(\ell_C/L_y)\frac{\eta_C}{\eta_Q} \right]. \tag{3.37}$$

In essence, the critical activity describes the active stress required to overcome the energetic cost of distorting the director field (parametrised by the Frank constant K) within a confined space of size L_y. Gradients in the director field are an essential ingredient of the generic flow instability, recall Fig. 3.2. The effort required to create the distorted state also increases with solvent or polymer viscosity, as by definition a more viscous fluid requires a larger stress to maintain a given shear-rate. Note that if we were to adopt antagonistic anchoring boundary conditions where the director is prescribed a different orientation at each wall, then even the passive LC state would be distorted: in this case the critical activity vanishes and spontaneous flow will occur for any activity [108].

We briefly validate the above criterion in the **Q**-only limit (i.e., $\eta_C \to 0$) by comparison with Ref. [87], which measured the threshold for the splay instability in an extensile material, with parameters $\eta = 0.567, \xi = 0.7, \tau_Q = G_Q = L_y = 1$. Inserting the lowest possible mode $k(\tilde{k} = 1) = \pi/L_y$ exactly recovers their result $\ell_Q = 0.086\zeta_c^{1/2}$.

Importantly, Eq. 3.37 also reveals that in the infinite system size limit, $L_y \to \infty$, the critical activity $\zeta_c^{\text{visc}} \to 0$ (see black curves in Fig. 3.10). This means that even with polymer present, a bulk homogeneous nematic base state is intrinsically unstable at any level of activity, however small. This feature is unique to the orientationally ordered phase; we will later show that while the spontaneous flow instability still exists for isotropic phases, it requires finite active stress to set in.

Note that for this viscous criterion, the polymer effectively renormalises the solvent viscosity η, i.e., $\eta \to \eta + a^2\eta_C/(1 + k^2\ell_C^2)$. At the threshold of instability, $\omega = 0$ and the associated timescale $\tau_\omega \propto 1/\omega$ is effectively infinite. Therefore τ_C is instantaneous in comparison and therefore does not appear directly in Eq. 3.35, appearing only indirectly in the viscosity $\eta_C = G_C\tau_C$. The onset of the spontaneous flow instability in finite systems can be delayed by increasing polymer viscosity η_C. The large polymer viscosity limits (a) $\tau_C \to \infty$ at fixed G_C and (b) $G_C \to \infty$ at fixed τ_C are indistinguishable from the perspective of the viscous criterion Eq. 3.35 (equivalently one cannot distinguish black curves in Fig. 3.10 left from right).

However we will now show that this is not the case in the elastomeric regime where $\tau_C > \tau_C^*$. In this limit, the resulting elastomeric criterion remains finite even for $\tau_C \to \infty$.

3.3.2.2 Elastomeric criterion: nematic

The above solution assumed that the discriminant D in the eigenvalue problem was always positive. However for $\tau_C > \tau_C^*$, the discriminant changes sign and the $\sqrt{D}$ term in ω^+ then contributes an imaginary part to the eigenvalue, indicative of oscillatory behaviour [128]. The elastomeric stability criterion is then obtained by solution of $B = 0$, yielding

$$\zeta_c^{\text{elast}} = \frac{\eta\left(1 + \ell_C^2k^2 + \ell_Q^2k^2\frac{\tau_C}{\tau_Q}\right) + 2\ell_Q^2k^2\tau_C\Lambda^2G_Q + a^2G_C\tau_C}{\Lambda\tau_C}. \tag{3.38}$$

Crucially, in contrast to the viscous criterion (Eq. 3.35), this threshold remains finite in the elastomeric limit $\tau_C \to \infty$ at fixed G_C,

$$\lim_{\substack{\tau_C\to\infty,\\ k\to 0}} \zeta_c^{\text{elast}} = \frac{a^2G_C}{\Lambda}, \tag{3.39}$$

where we have also temporarily taken the infinite system size limit for clarity of expression (see red curves in Fig. 3.10). Fascinatingly this result suggests that the classical nematic spontaneous flow instability can still occur in what is effectively an elastic solid, at finite activity. We later quantitatively confirm this with numerical simulations in both 1D (Sec. 3.4.2) and 2D (Sec. 5.5.3).

Therefore, contrary to the viscous criterion, the large polymer viscosity limits (a) $\tau_C \to \infty$ at fixed G_C and (b) $G_C \to \infty$ at fixed τ_C are **not** equivalent: the critical activity remains finite in the former limit whereas it diverges for the latter. This provides strong evidence that polymer viscoelasticity plays a direct role in the instability, as τ_C and G_C enter the above criterion independently, not just as a viscosity renormalisation. This occurs because above τ_C^* at the threshold of instability ($Re(\omega_\pm) = 0$) there is a timescale associated with the imaginary component $\tau_{osc} = 2\pi/Im(\omega_\pm)$ which is non-zero. This timescale can be explicitly seen in our simulation results (for a later example see Fig. 3.13 right).

3.3.2.3 Summary: nematic

In summary, we have applied our linear stability analysis to an nematic active LC, coupled through the flow to a polymeric background. A full analytical treatment of the eigenvalue problem required that we consider the regimes of small and large τ_C/τ_Q separately, resulting in the derivation of viscous and elastomeric critical activities respectively.

In the viscous criterion the polymer simply contributes additional viscosity, renormalising the solvent viscosity. At the onset of instability, the timescale associated with the instability is infinite; as τ_C is instantaneous in comparison, it may only appear indirectly as part of the polymer viscosity. Were $\bar{\zeta}_c^{\text{visc}}$ the only criterion, one could always suppress spontaneous flow by increasing η_C (at fixed τ_C or G_C).

However for large τ_C, we discovered a new mode of instability. Unlike the viscous criterion, this remains finite as $\tau_C \to \infty$ (at fixed τ_C) permitting spontaneous flow in what is effectively a solid of infinite viscosity. As the eigenvalue associated with this elastomeric mode has a non-zero imaginary part at the onset of instability, τ_C and G_C can appear independently in the criterion $\bar{\zeta}_c^{\text{elast}}$. Note that this novel effect

requires the inclusion of polymer.

3.3.3 Isotropic case

Having considered the stability of the nematic phase, we now generalise our results to include the disordered or isotropic phase, for which there is no net orientation at any given point in the fluid. Experimentally this could describe, for example, dilute bacterial suspensions [117, 126].

In our model, without activity or shear, the isotropic state is thermodynamically stable when the IN-control parameter $\gamma < 2.7$, metastable for $2.7 < \gamma \leq 3$, and unstable for $\gamma > 3$ [15]. We later explore the impact of this parameter on the rheology of active materials in Sec. 4.3.3. For an isotropic state at rest, $\mathbf{Q} = \mathbf{0}$ which significantly simplifies the base state

$$\overline{Q}_{\alpha\beta} = 0, \tag{3.40a}$$

$$\overline{C}_{\alpha\beta} = \delta_{\alpha\beta}, \tag{3.40b}$$

$$\overline{\dot{\gamma}} = 0. \tag{3.40c}$$

As for our nematic calculation, the non-trivial eigenvalues of the stability problem can be written in the quadratic form

$$\omega^{\pm} = \frac{-B \pm \sqrt{B^2 - 4AC}}{2A}, \tag{3.41}$$

where full expressions for A, B, and C are given in Apx. 3.6.1.1. As before, we consider separately the two regimes when the discriminant $D = B^2 - 4AC$ is positive and negative. The former, which occurs for small τ_C, results in purely real eigenvalues and our critical activity, which requires solution of $Re(\omega^+) = 0$, can simply be found by solving $AC = 0$. The latter case (for large τ_C) results in a pair of complex conjugate eigenvalues, the real part of which changes sign when $B = 0$. These criteria then determine the minimum active stress required for a homogeneous and isotropic base state to spontaneously flow.

One can show (see Apx. 3.6.1) that the point of crossover between these criteria (i.e., $AC = B = 0$, and therefore $D = 0$) now occurs at

$$\tau_C^* \approx \frac{1 + \ell_C^2 k^2}{\bar{\Gamma} + \ell_Q^2 k^2} \tau_Q. \tag{3.42}$$

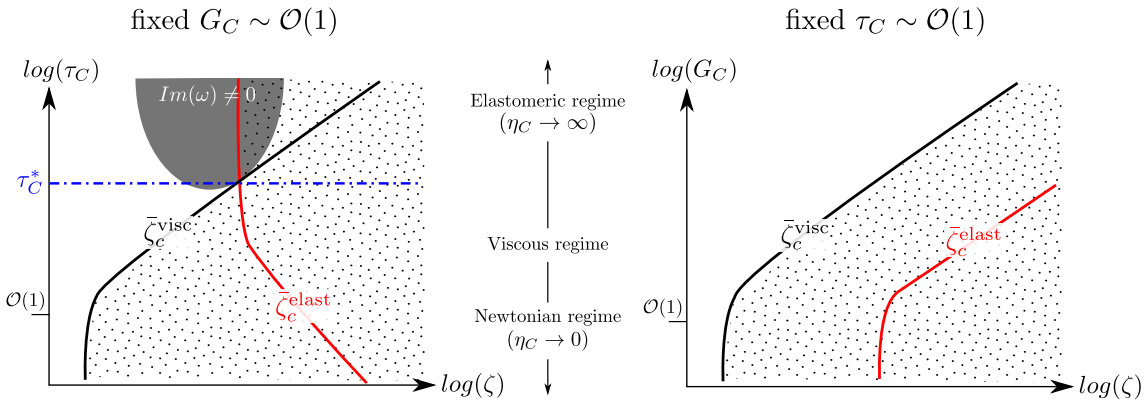

Figure 3.11: Schematic stability diagrams showing both isotropic criteria in the infinite system size limit (solid red/black lines), the lower of which bounds the region of instability (black dotted region). **Left:** (ζ, τ_C) phase diagram at fixed G_C, showing that at the point of intersection, the most unstable mode develops an oscillatory part, i.e., $Im(\omega) \neq 0$ (grey filled region). **Right:** (ζ, G_C) phase diagram at fixed $\tau_C \sim \mathcal{O}(1)$, showing that the criteria don't intersect. Here, an instability at fixed activity can always be suppressed at large enough G_C.

where $\bar{\Gamma} = 1 - \gamma/3$. For typical parameter values, τ_C^*/τ_Q ranges from $\mathcal{O}(10^1)$ when deep in isotropic phase to $\mathcal{O}(10^3)$ as γ approaches the end of metastability. We retain the terminology of the nematic calculation and refer to the regimes where τ_C is less or greater than τ_C^* as *viscous* and *elastomeric* respectively. Schematic stability diagrams are given in Fig. 3.11 which mark both criteria and the crossover point τ_C^*.

3.3.3.1 Viscous criterion: isotropic

Beginning in the limit of small $\tau_C < \tau_C^*$ where the discriminant D is positive, one can show (see Apx. 3.6.1.1) that $Re(\omega^+) = 0$ when

$$\zeta = \bar{\zeta}_c^{visc} = \frac{\bar{\Gamma} + k^2\ell_Q^2}{\bar{\Lambda}\tau_Q}\left(\eta + 2\bar{\Lambda}^2\eta_Q + \frac{a^2\eta_C}{1 + k^2\ell_C^2}\right), \tag{3.43}$$

where $\bar{\Lambda} = \xi/3$, $\bar{\Gamma} = 1 - \gamma/3$. (We use bars to denote quantities specific to the isotropic regime.) This criterion is marked with solid black lines in Fig. 3.12 for the limit $L_y \to \infty$. Note that as before, the lowest possible mode ($\tilde{k} = 1 \Rightarrow k = \pi/L_y$) is the first to become unstable.

The most striking change when compared to the equivalent nematic result (Eq. 3.35) is that in the infinite system size limit $k \to 0$, the criterion $\bar{\zeta}_c^{visc}$ remains non-zero. This means that while the generic instability does occur in bulk isotropic suspen-

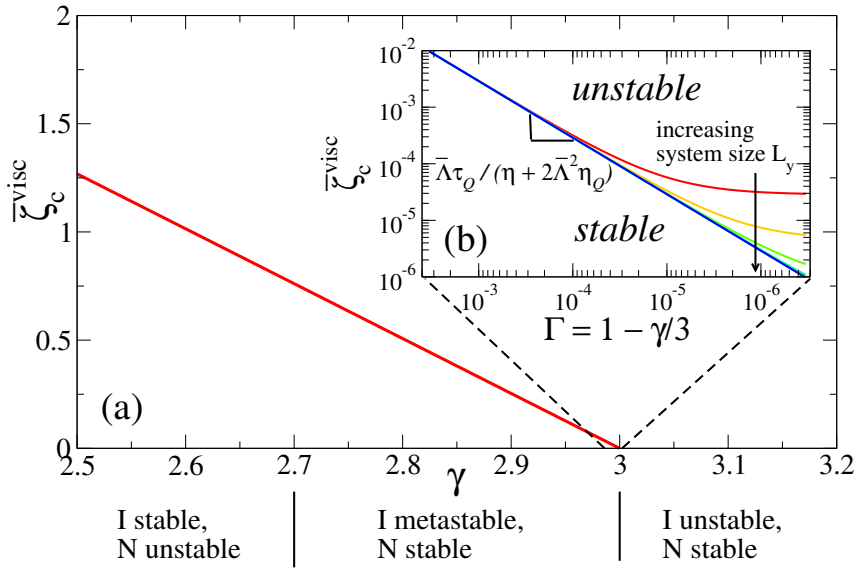

Figure 3.12: (a) Critical activity $\bar{\zeta}_c^{\text{visc}}$ (Eq. 3.43) against γ in the limit $L_y \to \infty$. (b) Inset shows behaviour for finite systems in the vicinity of $\gamma = 3$, with multiple curves for $\ell_Q/L_y = 10^{-2}$ (red) $\to 10^{-5}$ (blue). For clarity, we assume $\eta_C = 0$ (no polymer), as the only contribution is to renormalise the solvent viscosity, see Eq. 3.43.

sions [101], it only appears above a threshold active stress.

Note that this general result can be specialised to the case of no polymer by taking $\eta_C \to 0$. In this limit, the existence of a spontaneous flow instability has been previously reported in analytical studies of isotropic phases [78,129,130]. Direct comparison is not possible however, as both models employed in these studies include a variable concentration field (in our model the concentration is held fixed), and Ref. [78] also only includes an active stress in the Stokes force balance equation (our study additionally includes liquid-crystalline stresses).

The effect of the IN-control parameter is shown in Fig. 3.12. While the critical activity is appreciable at values of γ deep in the isotropic phase, it remains finite and the spontaneous flow instability is predicted for large enough activities. As expected from the form of Eq. 3.43, this threshold decreases linearly as we approach the end of isotropic (meta)stability $\gamma \to 3^-$ where it vanishes. This limit is consistent with our stability results for bulk nematics in the previous section (Sec. 3.3.2), and earlier studies [77, 78, 81], all of which predict that critical activities should vanish for bulk orientationally ordered suspensions.

Note that as for the nematic case, the polymer effectively renormalises the solvent

viscosity, i.e., $\eta \to \eta + a^2\eta_C/(1+k^2\ell_C^2)$. The timescale of the instability $\tau_\omega \propto 1/\omega$ is infinite at the threshold $\omega = 0$; τ_C is instantaneous in comparison and therefore does not appear directly in Eq. 3.43. Taken by itself, Eq. 3.43 implies that one can always suppress the spontaneous flow instability by increasing η_C (see black line in Fig. 3.11). However we will now show that the elastomeric criterion (relevant for $\tau_C > \tau_C^*$) remains finite even for $\eta_C \to \infty$, and the spontaneous flow instability can be accommodated, consistent with our nematic results.

3.3.3.2 Elastomeric criterion: isotropic

For polymer relaxation times in the elastomeric regime ($\tau_C > \tau_C^*$), the discriminant in Eq. 3.41 becomes negative and $\omega^\pm$ becomes a complex conjugate pair. The critical activity for which $Re(\omega^+) = 0$ can then be found by solution of $B = 0$, yielding

$$\bar{\zeta}_c^{\text{elast}} = \frac{\eta\left[\left(\bar{\Gamma}+\ell_Q^2k^2\right)\frac{\tau_C}{\tau_Q}+(1+\ell_C^2k^2)\right]+2\left(\bar{\Gamma}+\ell_Q^2k^2\right)\Lambda^2G_Q\tau_C+a^2G_C\tau_C}{\Lambda\tau_C}. \quad (3.44)$$

As with the viscous isotropic criterion, this also clearly remains non-zero in the infinite system size limit $k \to 0$. Our intriguing results in the nematic elastomer limit $\tau_C \to \infty$ remain for isotropic base states

$$\lim_{\tau_C\to\infty}\lim_{k\to 0}\bar{\zeta}_c^{\text{elast}} = \frac{\bar{\Gamma}\left(\frac{\eta}{\tau_Q}+2\Lambda^2G_Q\right)+a^2G_C}{\Lambda}, \quad (3.45)$$

where we have taken the infinite system size limit for clarity of expression. This implies that the spontaneous flow instability persists in materials that are effectively solid at sufficient activities, for both isotropic and nematic phases.

Note that this analysis only informs us about the linear behaviour. Once the magnitude of perturbations become sufficiently large, non-linear terms in the constitutive equations become relevant and we can no longer make quantitative predictions about the long term behaviour. However we find that our linear results can qualitatively describe the nonlinear behaviour, e.g., simulation runs with parameters for which unstable oscillatory growth is predicted ($Im(\omega_\pm) \neq 0$), generally develop into nonlinear oscillatory states. For example, our simulations in Sec. 3.4.1 reveal shear-banded flowing states where the interface position oscillates back and forth on a timescale set by τ_C.

3.3.3.3 Summary: isotropic

In summary, we have extended our linear stability analysis to describe an isotropic active LC, coupled through the flow to a polymeric background. As for nematic phases, solution of the eigenvalue problem required that we consider viscous and elastomeric limits separately. Our analytics showed that, perhaps surprisingly, isotropic suspensions are also capable of spontaneous flow instabilities at finite active stress. Previous studies have shown that this can occur for $\gamma < 3$ in the vicinity of the IN transition [15], but it was previously unclear to what extent this instability remained as one descended deeper into the isotropic phase (by lowering γ further). One might imagine that close to the IN transition, the flow instability simply arises because activity induces a transition from the (thermodynamically) metastable isotropic state to the stable nematic. However our results demonstrate that spontaneous flow can occur even if the nematic state is unstable, i.e., we are deep in the isotropic phase with $\gamma < 2.7$.

Related with this is the significant difference between the isotropic and nematic criteria in the infinite system size limit $L_y \to \infty$. The isotropic criterion $\bar{\zeta}_c$ remains non-zero, as the active stress must both (a) generate enough shear to induce orientational order and simultaneously (b) distort this to produce a spontaneously flowing state. In contrast, the nematic criterion ζ_c vanishes as $L_y \to \infty$, as the active stress required to deform a state that already possesses nematic order vanishes (this instability mechanism, for orientationally ordered phases, is well understood).

It is also instructive to contextualise our results in a (ζ, τ_C) phase diagram, which we do in Fig. 3.13 for an infinite system size at fixed G_C. For small τ_C, the viscous criterion $\bar{\zeta}_c^{\text{visc}}$ is the first encountered as activity is increased. This is simply a constant in the Newtonian limit $\tau_C \to 0$. Then as τ_C increases, so does the polymer viscosity $\eta_C = G_C\tau_C$ and therefore $\bar{\zeta}_c^{\text{visc}}$ increases. Then at τ_C^*, the elastomeric criterion $\bar{\zeta}_c^{\text{elast}}$ crosses $\bar{\zeta}_c^{\text{visc}}$ and becomes the relevant criterion. At the point of intersection, the eigenvalue splits into a complex conjugate pair signifying that the instability is oscillatory in nature. This transition is characteristic of a Hopf bifurcation.

We confirm these results numerically in Fig. 3.13b for each key region of the

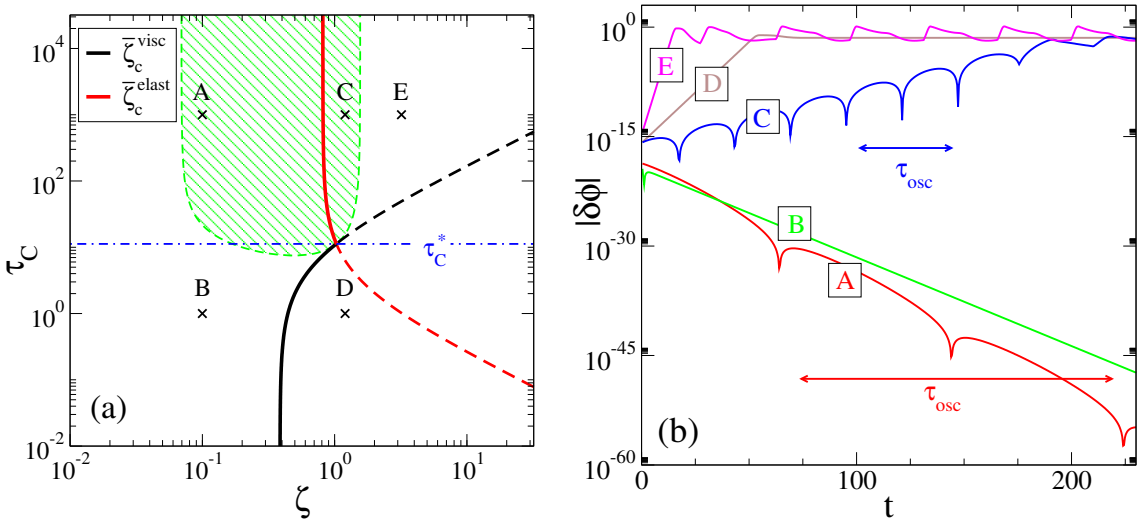

Figure 3.13: (a) Phase diagram for an isotropic suspension, where phase boundaries are constructed from the two critical activities in the infinite system size limit (though boundaries for a finite system would be practically indistinguishable). The region to the right of the solid lines is unstable, and the green shaded area marks where the dominant eigenvalue has an imaginary part. The crossover from viscous to elastomeric behaviour is marked by the blue dashed line. (b) For the points marked on the left phase diagram, we plot the growth of perturbations in simulations (with $\tilde{k} = 1, L_y = 1$). Consistent with our analytics, perturbations at A, B decay and those at C, D and E grow. Points inside the green shaded region (A, C) also exhibit oscillatory behaviour during the linear instability on a timescale $\tau_{osc} = 2\pi/Im(\omega_{\pm})$. **Parameters:** $\gamma = 2.6$, $G_C = 0.1$, $\ell_Q = \ell_C = 0.01$.

phase diagram. Consistent with our analytics, we find that perturbations decay when ζ is below the critical activity (points A, B) and grow when above it (points C, D, and E). Additionally points inside the region where $Im(\omega^{\pm}) \neq 0$ (A, C) show oscillatory behaviour, as evidenced by the fluctuations in the magnitude of perturbations.

3.3.3.4 Connection to recent work

Recently, a paper appeared addressing similar topics from a somewhat different perspective [101]. The authors analytically studied the spontaneous flow instability of an active suspension embedded in a viscoelastic fluid in 2D, also by linearising about an isotropic base state. The model used there is distinct from our **Q** and **C** formulation. For example liquid-crystalline stresses are not included, the active

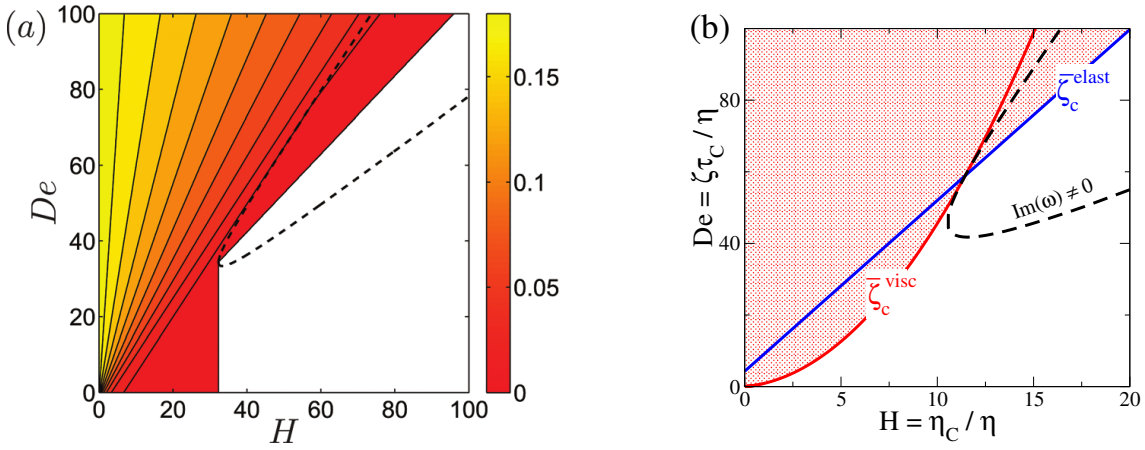

Figure 3.14: Stability diagrams in the limit $k \to 0$ for the dimensionless quantities $\mathrm{De} = \tau_C \zeta / \eta$ and $H = \eta_C / \eta$. **Left:** Data from Ref. [101], where colourscale marks growth-rate ω (white regions are stable with $\omega < 0$) and dashed black line bounds the oscillatory region. **Right:** Our results cast in the same dimensionless groups, showing $\bar{\zeta}_c^{\mathrm{visc}}$ (Eq. 3.43) and $\bar{\zeta}_c^{\mathrm{elast}}$ (Eq. 3.44). **Parameters:** $\gamma = 2.5$, $G_C = 1$.

particles are self-propelled (i.e., movers rather than shakers), and the concentration field can vary in space (we assume a homogeneous concentration). Despite these differences, we find striking similarities with our isotropic results. These can readily by visualised if we adopt the analogous dimensionless groups used in their study, namely $\mathrm{De} = \tau_C \zeta / \eta$ and $H = \eta_C / \eta$. (Note that this definition of De is distinct from the Deborah number later defined in our 2D study in Chap. 5.) We plot data from both studies in Fig. 3.14.

Firstly, both works predict that increasing H at fixed De can eventually suppress the spontaneous flow instability, even in the infinite system size limit. Above a certain value of De, both studies also find a region where $Im(\omega^{\pm}) \neq 0$ predicting oscillatory behaviour, the upper part of which is predicted to be unstable. The authors also remark on the same viscosity renormalisation that we observe in the viscous regime.

The results differ slightly when both De and H are small. We find that a critical De must be exceeded for spontaneous flow, whereas their study appears to report instability as $\mathrm{De} \to 0$. This may in part be due to their definition of De which conflates two limiting cases: the active polymer-free limit ($\tau_C \to 0$) and the passive polymer limit ($\zeta \to 0$) limit which are both represented by $\mathrm{De} \to 0$.

criterion	$L_y \to \infty$	$G_C \to \infty$ (fixed τ_C)	$\tau_C \to \infty$ (fixed G_C)
isotropic			
$\bar{\zeta}_c^{\text{visc}}$	$\neq 0$, finite	∞	∞
$\bar{\zeta}_c^{\text{elast}}$	$\neq 0$, finite	∞	finite
nematic			
ζ_c^{visc}	$\to 0$	∞	∞
ζ_c^{elast}	$\neq 0$, finite	∞	finite

Table 3.3: Summary of critical activities for isotropic and nematic suspensions, and their values for several limiting cases. Limits where a criterion is not relevant, i.e., where the other criterion in the viscous/elastomeric pair is smaller, are shaded grey.

3.3.4 Comparison of isotropic and nematic cases

Having explored the linear stability of both isotropic and nematic limits in detail, we now briefly review our results in a wider context. We summarise the key limiting cases in Table 3.3.

In finite systems, we found that both isotropic and nematic materials exhibit similar characteristics. For small τ_C, both are susceptible to spontaneous flow instabilities above a viscous critical activity ζ_c^{visc}, proportional to the sum of viscosities. For large τ_C, an elastomeric criterion ζ_c^{elast} dominates instead. The limiting behaviour as $\eta_C \to \infty$ then depends on what quantities are held fixed. Critical activities remain finite as $\tau_C \to \infty$ at fixed G_C, but diverge for $G_C \to \infty$ at fixed τ_C.

Where isotropic and nematic materials differ is in the infinite system size limit. We find that nematic materials remain unstable for vanishingly small activities, consistent with earlier work [77]. In the isotropic limit however, the stability threshold remains non-zero, implying that a bulk (homogeneous) isotropic state will only produce spontaneous flow above a threshold active stress. This fundamental difference between isotropic and nematic states can be cleanly rationalised from a rheological perspective. We later explore this in detail in Sec. 4.3.3, where a non-zero externally

applied shear is included in the problem. Essentially materials which possess a negative zero-shear viscosity are mechanically unstable at rest, i.e., conditions for which $\eta^0 < 0$ then determine the onset of flow instabilities. To summarise our argument, we will demonstrate that as one increases the activity from zero, the zero-shear viscosity in 0D[5]:

- decreases slowly for an **isotropic** material until it becomes negative at a non-zero threshold ζ_c (i.e., at the point where the negative active stress exceeds the positive solvent and LC stresses).
- becomes instantly negative for any positive activity in a **nematic**.

3.3.5 Summary: linear stability analysis

In this section, we have considered the 1D linear stability of a homogeneous slab of active viscoelastic material initially at rest. This generalises earlier works to include the effects of coupling to a polymeric background; it also extends previous work on nematic phases to include isotropic (or disordered) phases.

Our results revealed two modes of instability. For short polymer relaxation times the polymer acts as an additional source of viscosity ($\eta \to \eta + \eta_C$). Thus in a finite system, the spontaneous flow instability at a given activity can be suppressed by large enough viscosity η_C. However for large τ_C, a new elastomeric mode of instability appears, independent from the polymer viscosity. This predicts a finite critical activity even in materials with $\tau_C \to \infty$, i.e., in elastic solids. These results are general to both isotropic and nematic materials.

However, in the infinite system size limit differences appear. The critical activity vanishes for nematic materials, and the spontaneous flow instability occurs for any non-zero activity. Conversely isotropic materials remain stable below a threshold $\bar{\zeta}_c$. Experimentally one could test this in a suspension of microtubules and kinesin molecular motors [94], where the IN control parameter γ could be controlled by varying the concentration and activity could be controlled by varying the concentration of ATP.

[5]Here 0D is equivalent to the infinite system size limit as there is no meaningful lengthscale.

While our results were obtained using the linearised set of equations, we expect them to be instructive even in the non-linear regime. With parameter choices informed by our findings, we now explore the full nonlinear dynamics using 1D simulations, quantitatively verifying the existence of both modes of instability.

3.4 Spontaneous flow instabilities

In the previous section, we generalised the results of earlier analytical studies by deriving the critical activity for a linear instability to the onset of spontaneous flow when polymer is added to an active material. In particular, we have shown that this critical activity remains finite even for divergent polymer relaxation times. We now numerically explore the 1D non-linear dynamics of our model in the context of these linear stability results, and focus in particular on the nematic regime (with $\gamma = 3$).

Our aims in this section are twofold: (a) to quantitatively verify our analytical stability threshold using non-linear simulations, and (b) to study and characterise the dynamics once above this threshold.

There are three competing timescales in our model: the LC relaxation time τ_Q, the polymer relaxation time τ_C, and the active forcing timescale $\tau_a = \eta/\zeta$ as identified in Ref. [131]. The first of these defines our unit of time; the second and third will then form the axes of our phase diagram. Related to τ_a is the rescaled active timescale $\bar{\tau}_a = \eta/(\zeta - \zeta_c)$ that accounts for the non-zero critical activity that arises in finite systems (note that for nematic phases, $\bar{\tau}_a \to \tau_a$ as $L_y \to \infty$ or $\zeta \to \infty$).

If the active timescale is faster than the other relaxational timescales, then we might expect oscillatory dynamics [131]. We will show that this is indeed the case, first for a material of fixed polymer viscosity $\eta_C = 1$ (where the dominant period of oscillation τ_{osc} is set by τ_C) then for an elastomeric material (where $\tau_{osc} \propto \bar{\tau}_a$). Such oscillatory states are of particular biological interest. For example, shape oscillations have been observed in fibroblast cells, with the period of oscillation proportional to the myosin motor activity [132]. Schaller *et al.* also observed travelling density bands in cytoskeletal extracts [133].

We begin by exploring the competition between $\bar{\tau}_a$ and τ_C at fixed polymer viscosity, where we verify our analytical results for the onset of the spontaneous flow instability, and map the phase diagram finding a range of static and oscillatory shear-banded states. We then take the limit $\tau_C \to \infty$. Consistent with our analytics, spontaneous flows occur above the predicted threshold ζ_c. The resulting non-linear states are oscillatory with the dominant period of oscillation set by $\bar{\tau}_a$.

3.4.1 Phase diagram: fixed total viscosity

We begin by considering a fluid with fixed total viscosity (and fixed polymeric viscosity), but with variable polymer relaxation time. While this is arguably an artificial construction, it allows us to check that the relevant phase boundaries aren't dependent purely on the viscous polymer contribution, allowing us to confirm the direct role of the polymer relaxation time τ_C in the dynamics. We now explore the competition between active stresses and polymer relaxation processes using full nonlinear 1D simulations. Note that in this section we consider the special case where polymer diffusion is not included, though we will later comment on the effects of its inclusion.

In Fig. 3.15a we plot the (ζ, τ_C) phase diagram, noting that our constraint of $\eta_C = 1$ means that G_C decreases linearly as τ_C increases. First we demonstrate that our critical activity accurately predicts the onset of spontaneous flowing states: we find quiescent states (marked by crosses) below $\zeta_c = min(\zeta_c^{\text{visc}}, \zeta_c^{\text{elast}})$ and flowing states above (marked by circles). Once this threshold is exceeded, but for ζ or τ_C small, the flow field simply forms static shear-bands as is the case without polymer [87]. However for τ_C or ζ large enough, we find novel oscillatory states which we will describe in detail below.

In order to understand the mechanism behind these oscillatory states, it is instructive to recast our data in terms of the active timescale $\bar{\tau}_a = \eta/(\zeta - \zeta_c)$ (Fig. 3.15b). The $(\bar{\tau}_a, \tau_C)$ phase diagram clearly shows that oscillatory states occur when $\tau_c > 200\bar{\tau}_a$ (blue line). This quite general result apparently holds across several decades of data. The large separation of timescales required here to see oscillations is reminiscent of earlier work which employed a coupled toy model in the context of shear-driven rheochaos [134].

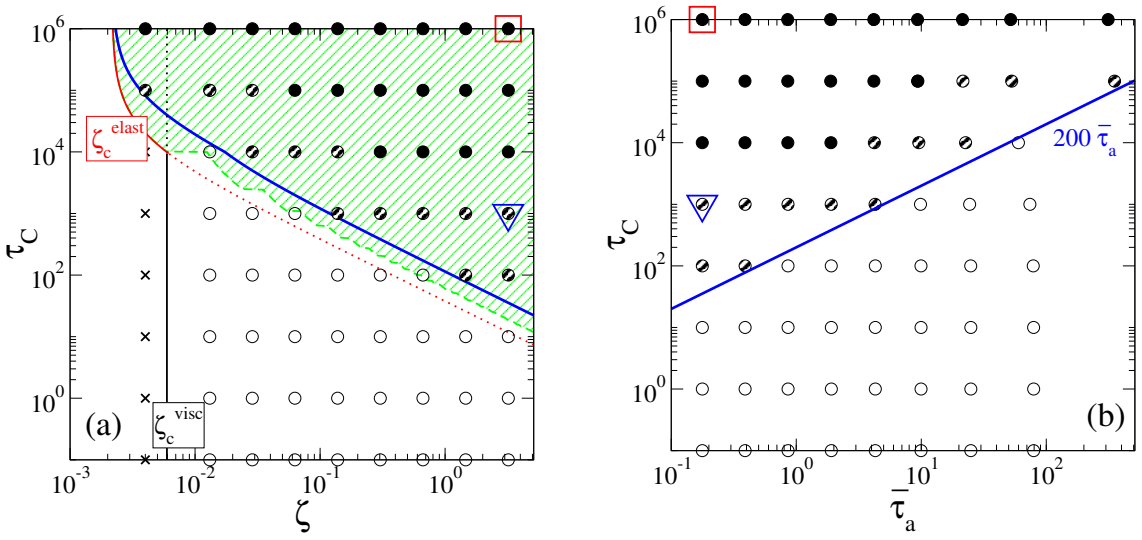

Figure 3.15: Phase diagrams (for the same data) for 1D runs with fixed $\eta_C = 1$ (e.g., large τ_C is matched by small G_C). Marked are the critical activities ζ_c^{visc} (Eq. 3.35, black line) and ζ_c^{elast} (Eq. 3.38, red line). States are denoted by symbols: quiescent (crosses), static bands (empty circles), oscillating bands (striped circles) or oscillating and flipping bands (filled circles) where the flow switches direction. Examples of the states highlighted with the triangle and square are given in Fig. 3.16 (left and right respectively). (a) Phase diagram for (ζ, τ_C). Green region denotes parameters where unstable oscillatory growth is expected (from linear stability analysis). (b) Phase diagram for (τ_a, τ_C), where oscillations are observed for $\tau_C/\bar{\tau}_a > 200$. **Parameters:** $\eta_C = 1$, $\ell_Q = 0.004$, $\ell_C = 0$, $\gamma = 3$.

If the active timescale is sufficiently long, then both the polymer and the LC can relax any activity-driven deformation, and the resulting shear-banded steady-state is time-independent. However if the polymer cannot relax the activity induced stress fast enough, the polymer dynamics lag behind producing oscillatory dynamics. This is analogous to the mechanism described in Ref. [131], where the coupling was to the concentration field (rather than a polymer as considered here).

These nonlinear results are also consistent with our linear stability analysis. We can ask for what parameters does $Re(\omega_k) > 0$ and $Im(\omega_k) \neq 0$ at any k, i.e., when do we see unstable oscillatory growth at any wavevector (see green shaded region in Fig. 3.15a). This accurately describes the region where oscillatory states are observed. To gain a clearer insight into these oscillatory states, we now focus on two examples from the phase diagram in Fig. 3.15.

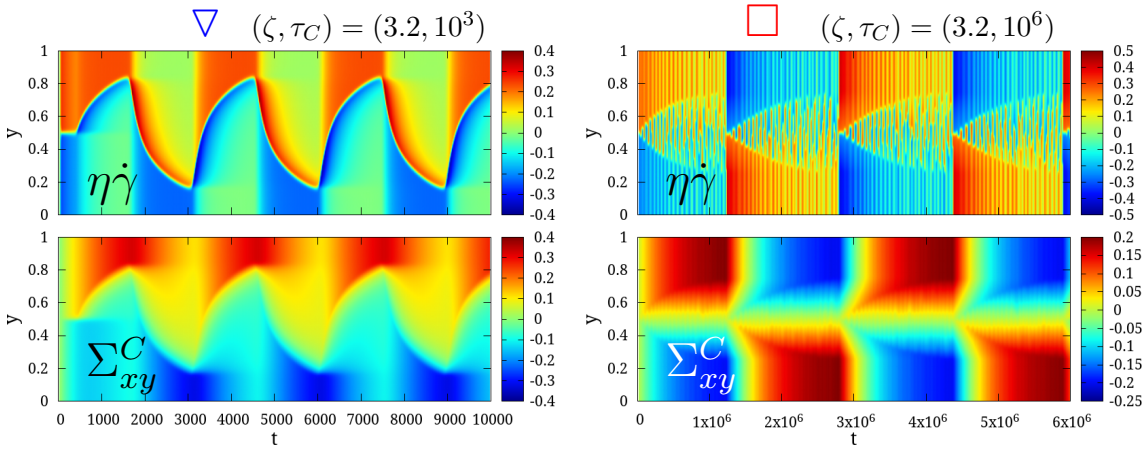

Figure 3.16: Space time plots for the marked coordinates in the phase diagram in Fig. 3.15. The x-axis time is t, y-axis position y, and colourscale: $\eta\dot{\gamma}$ (top row), Σ^C_{xy} (bottom row). **Left col:** State with oscillating interface ($\zeta = 3.2$, $\tau_C = 10^3$), **Right col:** State with oscillating interface, flow direction also switches ($\zeta = 3.2$, $\tau_C = 10^6$).

Oscillatory interface. In the first example (Fig. 3.16 left column), we observe that the position of the interface between the shear-bands begins to oscillate, with the period of oscillation set roughly by τ_C. Similarly, both the total shear stress and throughput (defined as $\Psi = \int_0^{L_y} v_x dy$) develop time-dependent signals (not shown). The flow direction however remains the same (i.e., the sign of the throughput remains constant). A space-time plot of $\dot{\gamma}$ is shown (Fig. 3.16 left top panel).

To probe the origin of these interfacial oscillations, it is instructive to also examine the polymeric contribution to the stress, $\mathbf{\Sigma}^C$. Plotting the shear component Σ^C_{xy} (Fig. 3.16, bottom left) reveals that as the interface position deviates from the centre, large polymeric stresses develop in the band occupying the smaller fraction of the channel. Once Σ^C_{xy} reaches some large threshold, the interface is forced to return in the opposite direction. As the period of this oscillation is roughly τ_C, it is clear that oscillations are mediated by the polymeric sector. Our results are also reminiscent of the propagating stress waves observed during tissue growth [135,136] which are thought to play a role in wound healing [137].

Oscillatory interface (flow direction switches). For larger τ_C/τ_a still, a second oscillatory state develops where the interface oscillates as before on some fast timescale, but now the flow also reverses direction on a timescale set by $\bar{\tau}_C$. The

corresponding space-time plots of $\dot{\gamma}$ and Σ^C_{xy} are shown in Fig. 3.16 (right column).

By a similar mechanism to the above, the interface position during the fast oscillations deviates increasingly from the centre. The polymer shear stress builds during this process and, once large enough to be comparable with other stresses, forces the flow direction to switch.

Polymer diffusion. The above results were presented for the simple case where no polymer diffusion is included (i.e., $\ell_C = 0$). However if we include such a term, with $\Delta = \ell_Q^2/\tau_Q = \ell_C^2/\tau_C$, we find the initial linear stability is not oscillatory, consistent with our linear stability results (see Apx. 3.6.2). Transient oscillations may appear at early times in the nonlinear dynamics, but these eventually become damped and a static shear-banded state is restored.

Having confirmed our prediction of oscillatory behaviour for large $\tau_C/\bar{\tau}_a$, we now turn to the elastomeric limit of $\tau_C \to \infty$.

3.4.2 Spontaneous flow in a solid

Consider a fluid in which the polymer relaxation time is infinite. Numerically we achieve this by completely disabling the relaxation term $\frac{1}{\tau_C}(\mathbf{C}-\mathbf{I})$. Recall that in this limit the critical activity becomes (see Eq. 3.56),

$$\zeta_c \approx a^2 G_C/\Lambda. \tag{3.46}$$

We now fix $\Delta = \ell_Q^2/\tau_Q = \ell_C^2/\tau_C$, $G_C = 0.1$, and use the default values of $a = 1$, $\xi = 0.7$ to numerically examine the full non-linear dynamics for activities on either side of[6] $\zeta_c \approx 2.4$. We do so by considering a homogeneous initial condition in which the director is orientated in the x-direction (Fig. 3.9), which we seed with a perturbation of the form $\delta\dot{\gamma} = \delta \sum_{\tilde{k}} \cos(\pi \tilde{k} y/L_y)$, where $\delta \sim \mathcal{O}(10^{-10})$ and where $\tilde{k} = 1 \to 16$.

Fig. 3.17a plots the time evolution of the largest shear rate perturbation, as the activity is varied from $\zeta = 2 \to 3.2$ (crossing the critical activity). Below ζ_c, the

[6]The actual value of ζ_c is very slightly larger as the form given in Eq. 3.46 assumes the infinite system size limit.

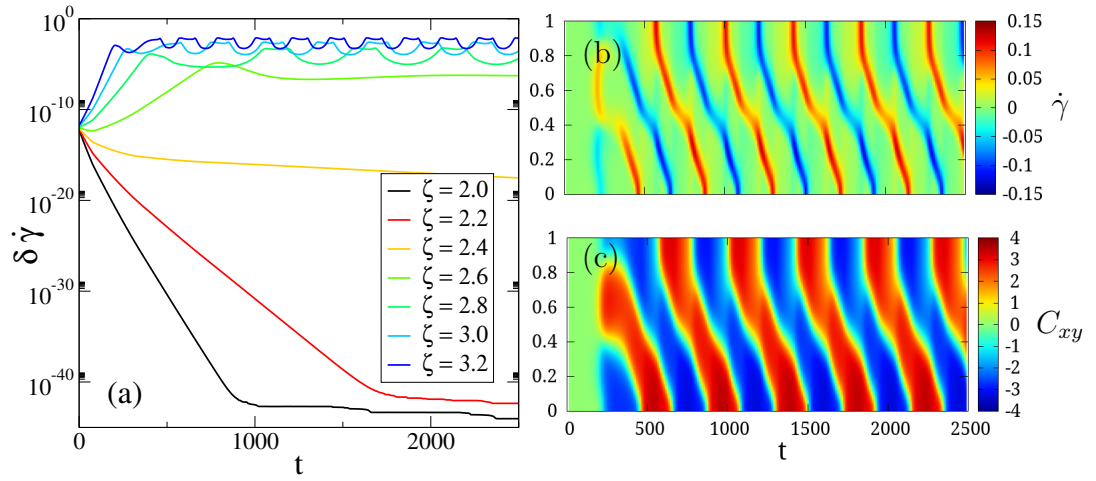

Figure 3.17: 1D simulations with infinite polymer relaxation time, for a range of activities ζ. (a) Evolution of shear-rate perturbations, showing growth for $\zeta > \zeta_c$. Panels on right show space-time plots for $\zeta = 3.2 > \zeta_c$, where the x-axis is time t, the y-axis is position y, and the colourscale shows (b) shear-rate $\dot{\gamma}$, (c) C_{xy}. **Parameters:** $a = 1$, $\xi = 0.7$, $\tau_C \to \infty$, $G_C = 0.1$, $\Delta = 10^{-4}$.

magnitude of each perturbation decays until it reaches the level of machine precision. However for $\zeta > \zeta_c$, the perturbations grow until a non-linear state is reached. As expected, the growth rate also increases with ζ.

Focusing on the run with large $\zeta = 3.2$, we examine the resulting dynamics once the perturbation becomes large enough for non-linearities to become relevant. Without any polymer stress relaxation, a fixed shear-rate profile would result in the polymer undergoing continuous loading and the strain would eventually diverge.

By plotting the shear-rate profile $\dot{\gamma}(y)$ as a function of time (Fig. 3.17b), we show that such a static shear-profile doesn't persist. Instead, travelling bands of local shear-rate $\dot{\gamma} = \pm 0.15$ develop where the flow direction continuously switches, effectively loading and unloading the polymer (as seen in the previous section). This can clearly be seen in the C_{xy} component (Fig. 3.17b), which changes sign in phase with the flow direction. These results are reminiscent of travelling density bands seen experimentally in cytoskeletal extracts [133]. Interestingly, as τ_C is infinite, the period of oscillation must be set by a separate timescale.

To explore the origin of this timescale, we perform simulations for a range of ζ, for 3 values of η. By taking the Fourier transform of the throughput-time signal $\Psi(t) = \langle v_x(t) \rangle_y$, we can identify the dominant period of oscillation τ_{osc} (see Figs. 3.18a,b).

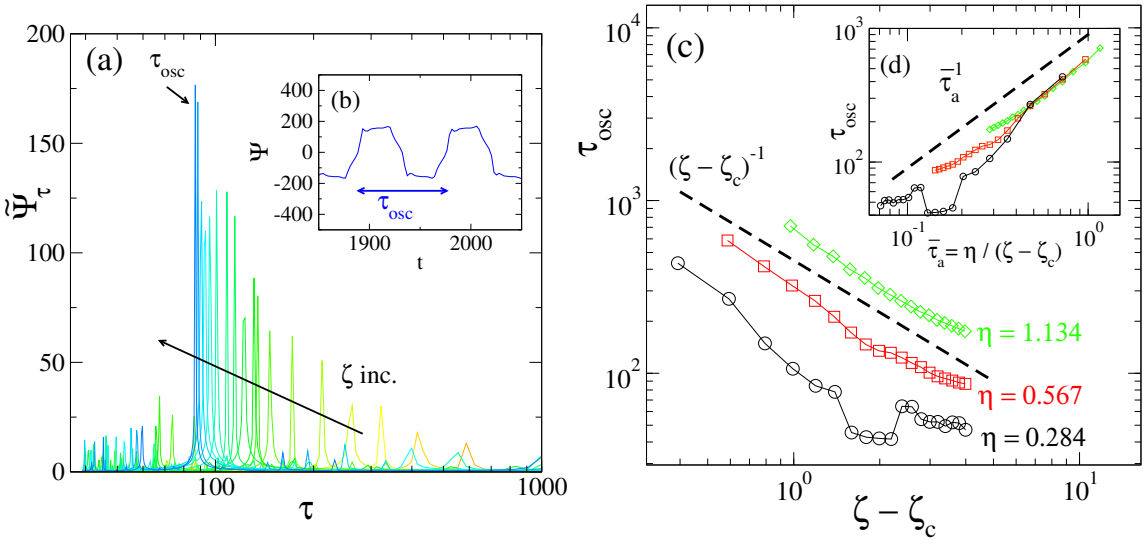

Figure 3.18: Exploration of how the dominant period of oscillation depends on activity and solvent viscosity η. (a) Fourier amplitudes $\tilde{\Psi}_\tau$ obtained from the throughput time series for $\eta = 0.567$ which allow us to identify the dominant period, τ_{osc}. (b) Inset showing τ_{osc} for an example time-series. (c) Plot of τ_{osc} against the activity-above-threshold demonstrating an inverse proportionality. (d) When recast in terms of $\bar{\tau}_a$, the data in (c) roughly collapses onto a single linear curve. **Parameters:** $a = 1$, $\xi = 0.7$, $\tau_C \to \infty$, $G_C = 0.1$, $\Delta = 10^{-4}$.

Plotting this against $\zeta - \zeta_c$ for a range of activities (Fig. 3.18c), we find that this period of oscillation is inversely proportional to $\zeta - \zeta_c$. With τ_C infinite, the only remaining timescale that can be constructed is then

$$\bar{\tau}_a = \eta/(\zeta - \zeta_c), \tag{3.47}$$

and indeed, rescaling our results in terms of $\bar{\tau}_a$ results in a reasonable curve collapse with τ_{osc} linearly proportional to $\bar{\tau}_a$ (see Fig. 3.18d). For particularly large values of the activity the flow becomes increasingly aperiodic and τ_{osc} becomes less clearly defined resulting in minor deviations from the power law.

Physically $\bar{\tau}_a$ represents the timescale of active forcing, as identified in Ref. [131]. As discussed in that study, as the active forcing is faster than the relaxation timescales (i.e., $\tau_a < \tau_Q \ll \tau_C$), both the LC and the polymeric dynamics lag behind, resulting in oscillatory behaviour.

3.4.3 Summary: spontaneous flow instabilities

We have numerically verified our analytical linear stability predictions for the onset of spontaneous flow, both at finite τ_C (at fixed η_C) and in the elastomeric limit $\tau_C \to \infty$.

In the former case, without polymer diffusion, oscillations of period τ_C were observed once the polymer relaxation time exceeded the timescale of active forcing $\bar{\tau}_a$ by a factor of ~ 200. The onset of these oscillatory states is consistent with our earlier linear stability analysis. Inclusion of polymer diffusion suppresses the oscillations, at least for the parameters explored. Oscillations were also observed in the elastomeric limit. However as the polymeric timescale is infinite in this limit, the timescale of oscillation is instead proportional to the only remaining timescale, $\bar{\tau}_a$.

3.5 Conclusions

We have introduced a novel model for the study of viscoelastic active matter which couples the dynamics of a nematic LC to a polymeric background. Constitutive equations and stresses for the respective order parameters ($\mathbf{Q}$ and $\mathbf{C}$) were derived from free energy considerations. These are then supplemented by an additional active stress of the form $\mathbf{\Sigma}^A = -\zeta\mathbf{Q}$. The two sectors are then coupled via the centre of mass velocity field $\mathbf{v}$ which obeys Stokesian hydrodynamics.

By focusing on the parallel plate geometry, we explored the competition between active stresses and the distortion free energy to understand the spontaneous flow instability in finite systems. Specifically, we generalised previous 1D linear stability analyses to include the effects of polymer, allowing us to derive a critical activity for the spontaneous flow instability expressed in terms of system size (L_y), viscosities (η, η_Q, η_C), coherence lengths (ℓ_Q, ℓ_C), and polymer relaxation time (τ_C).

For small to medium values of τ_C, we found that the polymer simply renormalises the solvent viscosity, reproducing the form of earlier criteria, e.g., as in Ref. [81]. This would seem to imply that one can always suppress the spontaneous flow instability with large enough polymer viscosity.

However for very large τ_C (at fixed G_C), we discovered a new 'elastomeric' mode of instability which predicts a distinct critical activity. Fascinatingly, this remains finite in the limit $\tau_C \to \infty$, suggesting that materials that are effectively solid are at least transiently unstable to spontaneous flow instabilities.

While these criteria were derived in a channel geometry of finite width L_y, they also provide insight into bulk behaviour in the limit $L_y \to \infty$. For nematics we found that the critical activity vanishes, as in previous work (without polymer). In contrast, isotropic materials remain stable below a non-zero critical activity. This difference can be understood by considering the zero-shear viscosity, and forms part of our rheological study in the following chapter.

Finally we verified that our analytical results quantitatively agree[7] with our 1D simulations, even for $\tau_C \to \infty$. The nonlinear dynamical behaviour of the resulting 1D states depends on the ratio of polymeric and active forcing timescales (τ_C and $\bar{\tau}_a$ respectively). For small $\tau_C/\bar{\tau}_a$, the polymer can relax any activity-driven deformation and a static shear-banded state forms. However for $\tau_C/\bar{\tau}_a > 200$, the relaxational dynamics lag behind, resulting in oscillatory states that fluctuate on a timescale $\sim \tau_C$.

As experiments on model active systems become increasingly sophisticated, it is natural to ask how one might test our predictions. The recent work of Sanchez *et al.* [94] on kinesin-microtubule mixtures allows one to make a tentative mapping between activity and ATP concentration, which in principle could allow one to extract the active forcing timescale (τ_a) discussed above. Polymer viscoelasticity could be effected by the inclusion of wormlike micelles with characteristic relaxation rate τ_C [138]; our results suggest that oscillatory states may form for $\tau_C \gg \tau_a$.

In this chapter we have assumed that our active material was initially at rest. In this case the linear stability of our model was analytically tractable. We now turn our attention to the more general case where an external shear is applied, and map the shear rheology. However the additional complexity of the stability problem under applied shear means numerical solution is now essential, except in the limit of small shear-rates. The coupled dynamics of the model, which possesses

[7]For a detailed description of this verification process for the general case of $\bar{\dot{\gamma}} \neq 0$, see Sec. 4.2.

multiple relaxation times, provide a rich spectrum of rheological features which we now explore.

3.6 Appendix I

This appendix provides additional details of the linear stability calculation, and includes comments on the generality of our results.

3.6.1 Eigenvalues

Recall that the linearised set of equations for a given wavevector k can be expressed in the matrix form

$$\partial_t \mathbf{p}^k = \mathbf{M}^k \cdot \mathbf{p}^k,$$

where $\mathbf{p}$ is a vector of Fourier amplitudes $\mathbf{p}^k = \left(Q^k_{xx}, Q^k_{xy}, Q^k_{yy}, C^k_{xx}, C^k_{xy}, C^k_{yy}\right)^T$. If the eigenvalue with the largest real part is positive for a given wavevector k, perturbations of wavelength π/k will grow and the system is unstable. Of the six eigenvalues of $\mathbf{M}$, four are trivially negative describing only relaxational and diffusive modes, e.g., $-1/\tau_C - k^2\ell_C^2/\tau_C$. The two remaining modes can be expressed in the quadratic form

$$\omega^{\pm} = \frac{-B \pm \sqrt{B^2 - 4AC}}{2A}. \tag{3.48}$$

The exact expressions for A, B, and C are dependent on whether we are considering a suspension that is isotropic or nematic in the passive unsheared limit. We begin in the isotropic limit (stable for $\gamma < 2.7$, metastable for $\gamma \leq 3$), then repeat the analysis for the nematic case where we fix the IN control parameter $\gamma = 3$.

3.6.1.1 Isotropic phase

For $\gamma < 2.7$ the isotropic state is stable (and is metastable for $\gamma < 3$). The corresponding $\mathbf{Q}$ base state is simply $\bar{\mathbf{Q}} = 0$. Coefficients A, B, and $\mathbf{C}$ are then

$$A = \eta\tau_C\tau_Q,$$
$$B = \tau_C\tau_Q\left[a^2G_C + 2G_Q\bar{\Lambda}^2\left(\bar{\Gamma} + \ell_Q^2k^2\right) - \zeta\bar{\Lambda}\right] + \eta\left[\tau_Q\left(\ell_C^2k^2 + 1\right) + \tau_C\left(\bar{\Gamma} + \ell_Q^2k^2\right)\right],$$
$$C = \left(\bar{\Gamma} + \ell_Q^2q^2\right)\left[a^2G_C\tau_C + \eta\left(1 + \ell_C^2q^2\right)\right] + \tau_Q\left(\ell_C^2q^2 + 1\right)\left[2G_Q\bar{\Lambda}^2\left(\bar{\Gamma} + \ell_Q^2q^2\right) - \zeta\bar{\Lambda}\right],$$

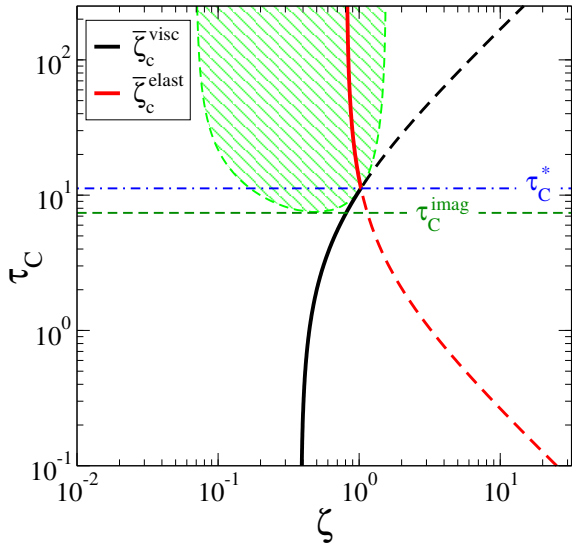

Figure 3.19: Illustration of how we approximate the crossover between ζ_c^{visc} and ζ_c^{elast} (at $\tau_C = \tau_C^*$) by the onset of the imaginary region (at $\tau_C = \tau_C^{imag}$).

where $\bar{\Lambda} = \xi/3$ and $\bar{\Gamma} = 1 - \gamma/3$.

At small τ_C/τ_Q, the discriminant $D = B^2 - 4AC$ is positive and we can simply obtain the viscous critical activity from $Re(\omega^+) = 0$ by solving $C = 0$ for ζ. For large τ_C/τ_Q, the discriminant is negative and the square-root only contributes an imaginary part. The elastomeric criteria is then obtained by solving $B = 0$ for ζ.

The crossover between viscous and elastomeric criteria occurs at τ_C^*, which can be found by equating ζ_c^{visc} and ζ_c^{elast}. However the resulting expression is too complex to be of practical use. Fortunately, τ_C^* approximately coincides with the first appearance of the imaginary region at τ_C^{imag}, which has a much simpler form.

To find τ_C^{imag}, we first find the activities at the upper and lower bounds of the imaginary region, $\zeta_\pm^{imag}$, by solving $D = 0$ for ζ. The imaginary region then begins when $\zeta_-^{imag} = \zeta_+^{imag}$, which after rearranging for τ_C, yields

$$\tau_C^{imag} \equiv \frac{1 + \ell_C^2 k^2}{1 + \ell_Q^2 k^2 - \frac{\gamma}{3}} \tau_Q \approx \tau_C^*. \tag{3.49}$$

The slight difference between τ_C^* and τ_C^{imag} is illustrated in Fig. 3.19.

3.6.1.2 Nematic phase ($\gamma = 3$)

For $\gamma = 3$, the coefficients in the quadratic (Eq. 3.48) are

$$A = \eta\tau_C\tau_Q, \tag{3.50}$$

$$B = \tau_Q\left[\left(1+\ell_C^2k^2\right)\eta + \tau_C\left(a^2G_C - \zeta\Lambda\right)\right] + \ell_Q^2k^2\tau_C\left[\eta + 2G_Q\Lambda^2\tau_Q\right], \tag{3.51}$$

$$C = \ell_Q^2k^2\left[\left(1+\ell_C^2k^2\right)\eta + a^2\eta_C\right] - \left(1+\ell_C^2k^2\right)\left(\zeta - 2G_Q\ell_Q^2k^2\Lambda\right)\Lambda\tau_Q, \tag{3.52}$$

where

$$\Lambda = \begin{cases} (5\xi-3)/12 & \text{for } \hat{\mathbf{n}} = (1,0,0)\,, \\ (5\xi+3)/12 & \text{for } \hat{\mathbf{n}} = (0,1,0)\,. \end{cases} \tag{3.53}$$

The procedure for viscous and elastomeric criteria is exactly as above, where the crossover now occurs at

$$\tau_C^* \approx \tau_C^{\text{imag}} \equiv \frac{1+\ell_C^2k^2}{\ell_Q^2k^2}\tau_Q. \tag{3.54}$$

We finish this appendix by making some comments about the generality of our results with regard to diffusion in the polymeric sector and boundary conditions.

3.6.2 Generality of results

3.6.2.1 Polymer diffusivity

In our analytical results so far, we have made no assumptions about the form of the diffusive terms, $\frac{\ell_Q^2}{\tau_Q}\nabla^2\mathbf{Q}$, $\frac{\ell_C^2}{\tau_C}\nabla^2\mathbf{C}$. For reasons of numerical stability, in any simulation results we fix diffusivities $\Delta = \ell_Q^2/\tau_Q = \ell_C^2/\tau_C$ unless specified otherwise. If we had instead set $\ell_Q = \ell_C$ for example, the limit $\tau_C \to \infty$ implies a vanishingly small polymer diffusion lengthscale, permitting infinitely sharp gradients in $\mathbf{C}$. We now explore the implications of this choice, finding that our key linear stability results are qualitatively unchanged. Focusing on the nematic case, we plot in Fig. 3.20 both stability criteria for three cases:

1. no polymer diffusion $\ell_C \to 0$,
2. polymer diffusion with $\ell_C = \ell_Q$,
3. polymer diffusion with $\Delta = \ell_Q^2/\tau_Q = \ell_C^2/\tau_C$.

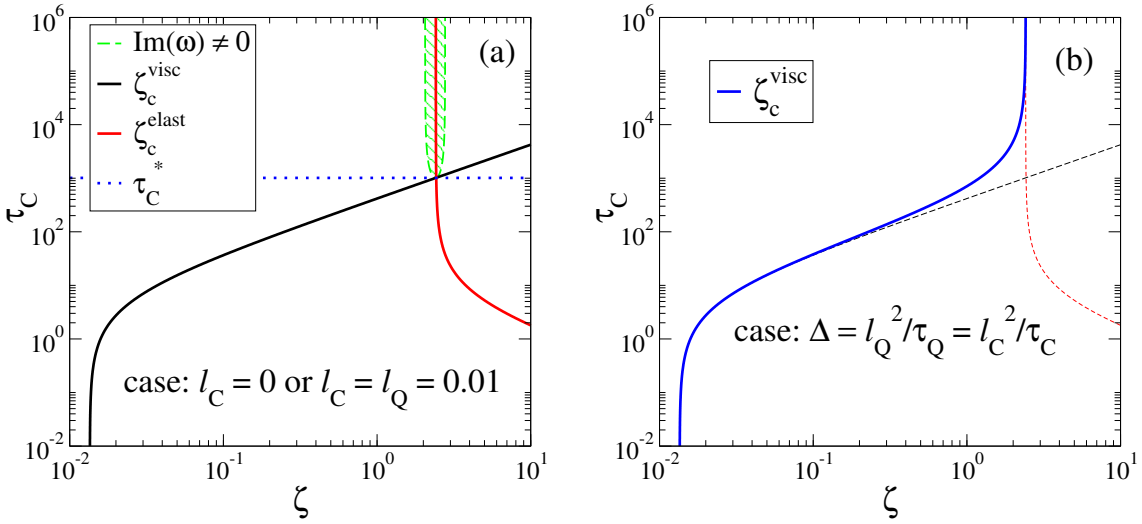

Figure 3.20: Phase diagram which demonstrates how critical activities are affected by the inclusion of polymer diffusion. (a) Curves for $\ell_C = 0$ or $\ell_C = \ell_Q$ are indistinguishable. (b) When diffusivities $\Delta = \ell_Q^2/\tau_Q = \ell_C^2/\tau_C$ are equated, a smoothing between the criteria with ℓ_C fixed or zero (dashed lines). The region where ω has an imaginary component disappears. **Parameters:** $G_C = 0.1$.

The first and second cases are indistinguishable within the resolution of the graph. Both also exhibit the oscillatory region where $Im(\omega^{\pm}) \neq 0$. However in the third case when the ratios are equated, we find a smooth transition between viscous (at low τ_C) and elastomeric (at high τ_C) criteria. The origin of this effect can be seen by substituting Δ into the viscous criterion Eq. 3.35,

$$\zeta_c^{\text{visc}} = \frac{k^2 \Delta \tau_Q}{\Lambda \tau_Q} \left(\eta + 2\Lambda^2 \eta_Q + \frac{a^2}{1 + k^2 \Delta \tau_C} G_C \tau_C \right), \tag{3.55}$$

which in the limit $\tau_C \to \infty$ becomes

$$\lim_{\tau_C \to \infty} \zeta_c^{\text{visc}} = \frac{a^2 G_C k^2 \Delta}{\Lambda k^2 \Delta} = \frac{a^2 G_C}{\Lambda} = \zeta_c^{\text{elast}}, \tag{3.56}$$

i.e., the same as the elastomeric criterion Eq. 3.39.

The other notable change when we fix diffusivities is the disappearance of the oscillatory region. To understand why, we rearrange our crossover criterion $\tau_C \gtrsim \tau_C^*$ (Eq. 3.34). This shows that the oscillatory region occurs when

$$\tau_C \gtrsim \frac{1}{\frac{k^2 \ell_Q^2}{\tau_Q} - \frac{k^2 \ell_C^2}{\tau_C}}, \tag{3.57}$$

which diverges if we fix $\ell_Q^2/\tau_Q = \ell_C^2/\tau_C$.

3.6.2.2 Importance of boundary condition

Throughout our linear stability analysis we have employed free boundary conditions (BCs), i.e., $\partial_y Q_{\alpha\beta}|_{y=0,L_y} = \partial_y C_{\alpha\beta}|_{y=0,L_y} = 0$. This choice considerably simplifies the analytics as it permits a spatially homogeneous base state. Because of this, spatial variations can easily be expressed in a cosine basis (see Eq. 3.30). More antagonistic anchoring BCs can lead to inhomogeneous base states, complicating the analysis.

We can also speculate on the stability with homogeneous anchoring BCs. We have shown that splay and bend become separately unstable at critical activities an order of magnitude apart. One might then imagine that the effect of anchoring conditions parallel (perpendicular) to the plate produces similar results to the splay (bend) states probed in Eq. 3.35.

4

Active viscoelastic matter:

0D and 1D (externally applied shear)

4.1 Introduction

In the previous chapter we introduced our novel model of viscoelastic matter, coupling active nematic matter to a viscoelastic polymer background. By linearising around an initially non-flowing base state, we were able to analytically determine the stability properties of an initially homogeneous state for both isotropic and nematic suspensions.

In this chapter we generalise these results to describe systems under the influence of an externally applied shear flow. We begin by reviewing previous work before introducing the techniques and concepts used to explore the shear rheology of our model.

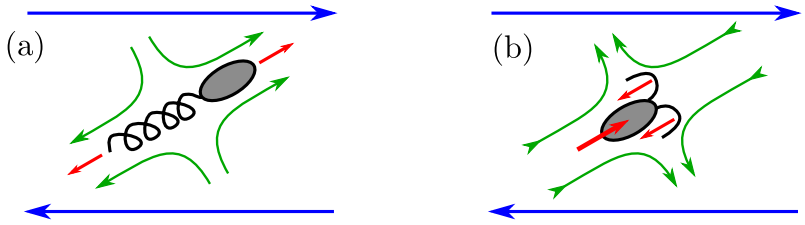

Figure 4.1: Demonstration of how a sheared active swimmer modifies the shear viscosity (for the example organisms given in Fig. 3.1). Under an applied shear, the long axis of an elongated swimmer will tend to align with the flow. This alignment effect (a) is enhanced for an extensile swimmer reducing the viscosity and (b) is resisted for a contractile swimmer leading to an increase in viscosity.

Literature review. Early theoretical studies made striking and general predictions about the viscosity of a suspension of active particles under shear. Working with an active stress proportional to the nematic order parameter $\mathbf{Q}$, Hatwalne *et al.* theorised that the shear viscosity should decrease (increase) for extensile (contractile) swimmers relative to the passive case [73]. Under an imposed shear flow, elongated active particles will tend to orient with the flow direction. A contractile force dipole will then pull fluid back in along its long axis against the underlying flow, whereas the opposite effect occurs for an extensile dipole (see Fig. 4.1). Evidence for this result was later seen experimentally: the viscosity was indeed observed to decrease in suspensions of extensile *B. subtilis* bacteria [14], and increase in suspensions of contractile *Chlamydomonas* algae [13].

These results can be used to gain insight into the mechanism behind the spontaneous flow instability as explored in detail in the previous chapter. Cates *et al.* showed that the constitutive curve for an extensile nematic exhibits a negative yield stress, implying a region of negative viscosity at small shear-rates [15]. When the constitutive equations are integrated numerically (in 1D) for an *extensile* active nematic initially at rest, Cates *et al.* observed a shear-banding instability and the negative viscosity region was replaced by a 'superfluid' flowing state of zero shear-stress. This is analogous to earlier studies of complex (but passive) fluids where non-monotonic constitutive curves where shown to be indicative of shear-banding instabilities, see e.g., Ref. [40]. An important difference, however, is that the stress plateau is at zero stress.

Interestingly, shear-banding instabilities were recently observed in a solution of *passive* actin filaments, which are a key component of the cell cytoskeleton [51]. The authors speculated that the observed flow inhomogeneities may help explain the formation of local cell protrusions called pseudopodia which play a role in cell locomotion. (For an exploration of related banding instabilities in the polymeric sector of our model see Sec. 4.3.1.)

Microrheological techniques (where the rheological response is obtained using local probes such as optical beads [139]) have also been successfully employed in the context of active matter. For example, the effect of myosin molecular motors on the mechanical properties of crosslinked cytoskeletal networks was studied using optical traps revealing marked violations of the fluctuation dissipation theorem and an increase in the stiffness of the network in the presence of ATP (myosin fuel source, analogous to $\zeta \neq 0$ in our model) [140]. Connecting with such experimental studies, Foffano *et al.* numerically modelled the microrheology of an active nematic suspension by dragging a spherical probe through the fluid. The authors found that the effective viscosity (which can be obtained from the drag on the probe) can vary for a given active fluid, depending on how it is measured and the probe size [141,142]. This illustrates the care that must be taken when measuring the properties of intrinsically non-equilibrium materials. While microrheological techniques can allow one to obtain shear rheological properties (such as the shear viscosity), they are generally not suitable for studying dynamic phenomena such as shear-banding [139] which can be more cleanly observed in microfluidic setups [143].

The complexity of the biological systems of interest to our study, combined with the large uncertainties in typical values for the various model parameters, currently makes it difficult to compare our simulations directly with experiment. However by characterising the general rheological features of our model in terms of the key dimensionless parameters (see Sec. 3.2.4), we map out a phase diagram and invite comparison with future experimental studies. We now briefly introduce the analytical and numerical methods used to explore the shear rheology of our model.

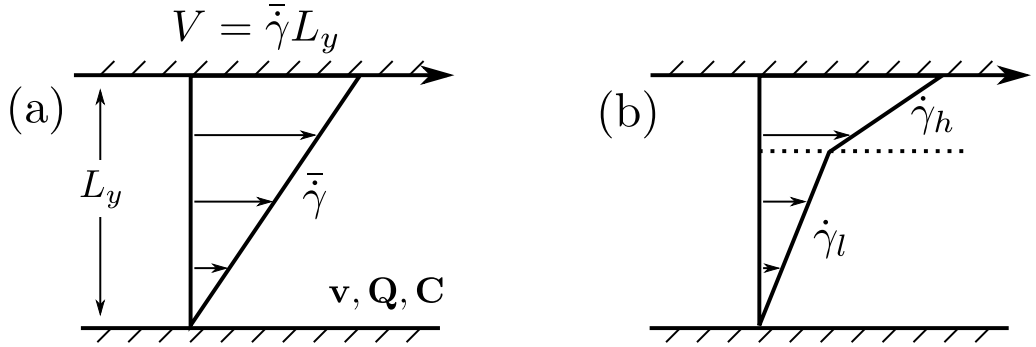

Figure 4.2: Schematic illustrating the difference between (a) homogeneous and (b) heterogeneous shear flows, where the length of the arrow indicates fluid velocity. The *constitutive curves* presented in this chapter are produced under the assumption of a constant velocity gradient $\dot{\gamma}(y) \equiv \partial_y v_x(y) = \bar{\dot{\gamma}}$. Our linear stability analysis examines the stability of these homogeneous states to heterogeneous perturbations, which if determined as unstable can result in the formation of macroscopic bands of differing shear-rate (where $\int_0^{L_y} \dot{\gamma}(y) dy = \bar{\dot{\gamma}} L_y$) as shown in (b). Plotting stress against shear-rate, allowing for such heterogeneities, produces a *flow curve*.

Methodology. The simplest approach one can take to understand the rheology of a given constitutive model is to assume that the velocity gradient tensor and order parameters are homogeneous in all dimensions, as in Fig. 4.2a. Recall that under the assumption of a homogeneous flow gradient $\bar{\dot{\gamma}}$, one may produce theoretical *constitutive curves* which plot the shear-stress (Σ_{xy}) against shear-rate ($\bar{\dot{\gamma}}$). Note that in our case, the stress in the liquid-crystal sector must be calculated numerically due to strong non-linearities in the constitutive equation (in contrast to the polymer stress which has an analytical solution).

The homogeneous state $\bar{\phi} = \left(\bar{\mathbf{Q}}, \bar{\mathbf{C}}, \bar{\dot{\gamma}}\right)$ which determines the total shear stress Σ_{xy} at a given $\bar{\dot{\gamma}}$ then forms the base state which we linearise about. This allows us to examine the stability of the base state to heterogeneous perturbations in the y-direction, which can ultimately lead to, for example, shear banding flow instabilities. This process must also be evaluated numerically (see Sec. 4.2 for details).

We then verify our linear stability results using 1D non-linear simulations that allow heterogeneities to develop (see Fig. 4.2b). By recording the shear-stress at a given $\bar{\dot{\gamma}}$, we can produce flow curves which can, but do not in general, coincide with the 0D constitutive curves. Particularly for the coupled, highly nonlinear model considered here for active matter, the dynamical behaviour revealed by simulations

can be time-dependent and possibly chaotic. Examples of such simulations are given in Sec. 4.4.

In this chapter we apply these three modelling tools (0D constitutive curves, 1D stability analyses, and 1D nonlinear simulations) to enumerate and comprehensively explore the several types of flow instability that can arise from either $\mathbf{Q}$ and $\mathbf{C}$ sectors. We then use this knowledge to influence the relative contributions of each instability using experimentally realisable control parameters such as the polymer relaxation time τ_C. This can result in exotic flow curves with multiple stress plateaus and strong hysteretic effects, or 'rheochaotic' systems that display spatio-temporal chaos.

4.2 Numerical solution of linear stability analysis

In generalising the stability analysis in Sec. 3.3 to describe materials driven by external shear, i.e., $\bar{\dot{\gamma}} \neq 0$, the problem becomes analytically intractable for two reasons. Firstly, while the polymeric base state $\bar{\mathbf{C}}$ can be obtained analytically for arbitrary $\dot{\gamma}$, non-linearities in the liquid-crystal constitutive equation mean that the liquid-crystalline base state $\bar{\mathbf{Q}}$ must be obtained numerically, either by time-stepping or by setting $\partial_t \mathbf{Q} = 0$ and using a non-linear root finder. We take the latter approach, using the SciPy `fsolve` library routine [144].

Secondly the stability matrix $\mathbf{M}^k$ becomes considerably more dense due to the additional shear loading terms. To handle the additional complexity, we numerically calculate the eigenvalues of $\mathbf{M}^k$ using the NumPy numerical computing library [145]. So while we can still solve the stability problem, in practice both the base state $\bar{\phi}$ (Eq. 3.29) and the eigenvalues of the stability matrix $\mathbf{M}^k$ (Eq. 3.31) must be calculated numerically.

We now briefly validate this procedure by comparing our (numerically evaluated) stability analysis with our full non-linear code (in the linear regime). First we impose that both order parameters and $\dot{\gamma}$ are homogeneous, and evolve the system

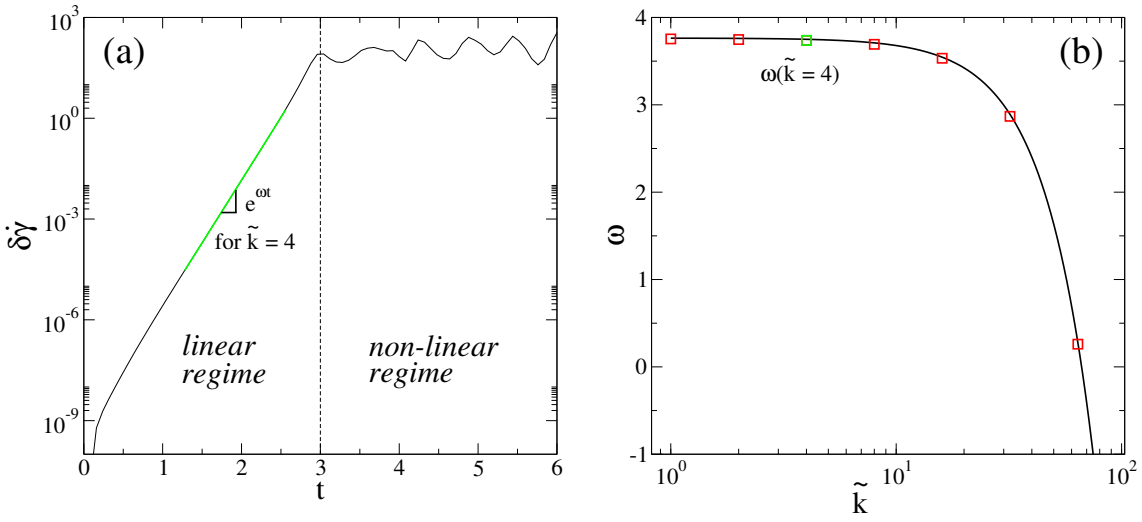

Figure 4.3: Verification of our (numerically solved) linear stability analysis. (a) Illustration of how ω is extracted from nonlinear simulations by measuring the growth of perturbations in the linear regime, where we have seeded the system with a perturbation $\delta\dot{\gamma} = \varepsilon\cos(\pi\tilde{k}y/L_y)$ with $\tilde{k} = 4, \varepsilon = 10^{-8}$. (b) Dispersion relation which shows the growth rate ω at mode number $\tilde{k}$, as calculated by a (numerically evaluated) linear stability analysis (solid black line) and as measured from non-linear 1D simulations (squares), demonstrating excellent agreement. **Parameters:** $\zeta = 0.5$, $a = 0.3$, $\tau_C = G_C = 1$, $\Delta = 8 \times 10^{-5}$, $\dot{\gamma} = 4$.

of equations to steady-state (this steady-state is the same as the base state in our linear stability analysis). We then allow heterogeneity in the y-direction, and seed our simulations with a perturbation $\delta\dot{\gamma} = \varepsilon\cos(\pi\tilde{k}y/L_y)$ where $\varepsilon = 10^{-8}$. For a given mode number $\tilde{k}$, we extract the growth rate of the perturbation ω from the slope of a log-linear plot in the linear regime (i.e., while perturbations are small enough, see Fig. 4.3a).

In Fig. 4.3b we plot the extracted growth rate of perturbations (square symbols) for a range of $\tilde{k}$ to produce a dispersion relation. On the same plot we mark the growth rate as calculated by our (numerically evaluated) linear stability analysis[1]. This demonstrates excellent agreement between our non-linear code and our stability analysis across the full range of wavevectors tested. We now apply this technique separately to the liquid-crystal and polymer sectors before considering the rheology of the composite model, which couples both **Q** and **C** sectors kinematically, i.e., via

[1]This is continuous as we can evaluate the eigenvalue problem at any $\tilde{k}$, not just integer values. Our numerics, however, are restricted to quantised perturbations.

instability	parameter range	shear-rate	description	example
C shear-banding	$\lvert a\rvert < 1$, $\eta/\eta_C a^2 < \frac{1}{8}$	$\dot{\gamma}\tau_C \approx 1/\sqrt{1-a^2}$	JS banding instability	Fig. 4.4a
Q shear-banding	$\xi > \xi^*(\gamma)$	$\dot{\gamma}\tau_Q \approx 1$	arises from loading terms in **Q** analogous to JS	Fig. 4.4b
Q free energy	$\gamma < 2.7$	$\dot{\gamma}\tau_Q \approx 0.02$	shear-induced IN transition, constit. curve can be multi-valued in Σ_{xy}, or Σ_{xy} and $\dot{\gamma}$, depending on γ	Fig. 4.5
Q free energy + activity	$\gamma < 2.7$, $\zeta > \zeta^*$	$\dot{\gamma} = 0$	large enough activity results in $\partial\Sigma_{xy}/\delta\dot{\gamma} < 0$ at the origin	Fig. 4.9
Q free energy + activity	$\gamma \geq 2.7$, $\zeta > 0$	$\dot{\gamma} = 0$	discontinuity at origin gives negative yield stress (due to nematic branch)	Fig. 4.10
Q + **C** (new)	$\zeta \neq 0$	*various*	resulting from coupling of **Q** and **C**	Fig. 4.15

Table 4.1: List of possible flow instabilities in the separate **Q** and **C** sectors and the typical parameter values required to observe them. We also later show that the combination of **Q** and **C** can result in new instabilities.

the fluid.

4.3 Exploration of flow instabilities

Even individually, both the liquid-crystal and polymeric sectors display rich and exotic rheological responses. For example passive liquid-crystals exhibit a shear-induced isotropic-nematic transition [146], extensile active nematics display an unusual negative yield stress [15], and the JS model is capable of shear-banding instabilities [41]. We begin by describing the individual flow instabilities in both **Q** and **C** sectors using the generalised linear stability analysis described in the previous section. We also summarise these instabilities in Table 4.1.

Detailed knowledge of these instabilities and the parameter ranges in which they appear will then allow us to construct exotic and novel constitutive curves which combine two (or more) of these instabilities in the same system and so allow us to

predict e.g., rheochaotic behaviour or multiple stress plateaus (see Sec. 4.4).

4.3.1 C-only instability

While the model used to describe the polymeric sector derives from the JS model, the stress, when derived in a thermodynamically rigorous way (see Sec. 3.2.1.3), gains an additional prefactor of a (the slip parameter) relative to the definition that has typically been used in the existing literature (e.g., as in Ref. [110]). This affects the stability properties under shear, albeit in a minor way.

In the original formulation of the JS model [59] the constitutive curve is multivalued, and therefore capable of describing shear-banding instabilities, if $|a| < 1$ and $\eta/G_C\tau_C < 1/8$ [113, 147]. In other words, as long as there exists some slip (i.e., $|a| < 1$), it is solely the viscosity ratio that determines the monotonicity. One can show that the instability first appears at shear-rates $\bar{\dot{\gamma}}\tau_C \approx 1/\sqrt{1-a^2}$ [57]. Therefore the limit $a \to 1$ can be seen as the limit in which the non-monotonic region is pushed out towards $\dot{\gamma} \to \infty$. We now generalise these results to account for the thermodynamically correct polymer stress, showing that slip parameter a plays a more direct role.

By setting $\partial_t \mathbf{C} = 0$, and assuming homogeneity in all dimensions, we can obtain the steady state stress analytically

$$\Sigma^C_{xy} = \frac{G_C\tau_C\dot{\gamma}a^2}{1+(1-a^2)\left(\dot{\gamma}\tau_C\right)^2}, \tag{4.1}$$

where $\dot{\gamma}$ is the applied shear-rate. Force balance dictates that that the total stress Σ^T_{xy} obeys $\Sigma^C_{xy} + \eta\dot{\gamma} - \Sigma^T_{xy} = 0$. Substituting Eq. 4.1 into this expression then produces a cubic in $\dot{\gamma}$

$$\eta\tau_C^2(1-a^2)\dot{\gamma}^3 - \Sigma^T_{xy}\tau_C^2(1-a^2)\dot{\gamma}^2 + (\eta + a^2G_C\tau_C)\dot{\gamma} - \Sigma^T_{xy} = 0. \tag{4.2}$$

The discriminant,

$$\Delta^{\dot{\gamma}} = \alpha_4(\Sigma^T_{xy})^4 + \alpha_2(\Sigma^T_{xy})^2 + \alpha_0, \tag{4.3}$$

tells us that three solutions exist for the cubic in Eq. 4.2 if $\Delta^{\dot{\gamma}} > 0$, i.e., assuming homogeneous flow, there exists 3 shear rates $\dot{\gamma}_L, \dot{\gamma}_M, \dot{\gamma}_H$ of common stress Σ^T_{xy}. (The middle shear-rate solution would be unstable were we to relax our assumption of

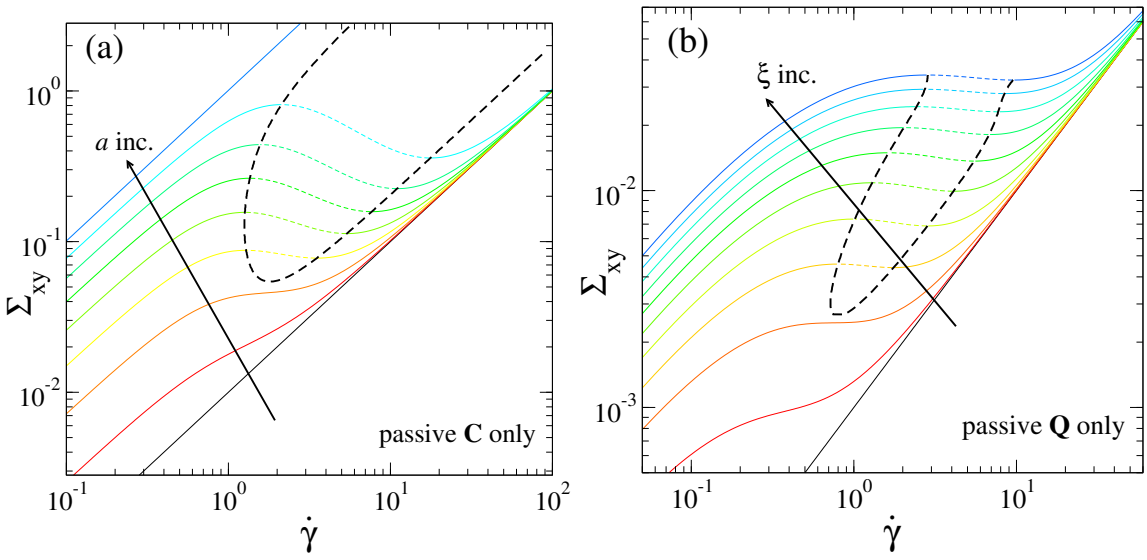

Figure 4.4: Constitutive curves in the passive limit with regions determined to be unstable by the stability analysis in Sec. 3.3 marked by dashed lines. This coincides exactly with regions where $\frac{\partial \Sigma_{xy}}{\partial \dot{\gamma}} < 0$. The thick black dashed lines mark the predicted spinodal limit of stability of homogeneous states. (a) Constitutive curves for polymer only, with $a = 0$ (black) $\rightarrow 1.0$ (blue, Oldroyd-B). The plot shows that instabilities occur above the critical a^* predicted in Eq. 4.4, i.e., for $1 > a > a^* = \sqrt{8\eta/\eta_C} \approx 0.28$. **Parameters:** $G_Q = \tau_Q = 0$, $\tau_C = G_C = 1$, $\eta = 0.01$. (b) Constitutive curves for a passive, flow-aligning liquid-crystal, for $\xi = 0.6$ (black) $\rightarrow 1.0$ (blue). The plot shows that instabilities (analogous to those seen with polymer) occur above a critical $\xi^* \approx 0.68$. **Parameters:** $\gamma = 3$, $G_Q = \tau_Q = 1$, $\tau_C = G_C = 0$, $\eta = 0.01$.

homogeneity.) The discriminant $\Delta^{\dot{\gamma}}$ is a quadratic in $(\Sigma^S_{xy})^2$, and is always positive if

$$\frac{\eta}{a^2 \eta_C} < 1/8, \qquad |a| < 1. \tag{4.4}$$

We confirm this result by plotting in Fig. 4.4a constitutive curves as a function of slip parameter a, marking regions determined as unstable by our linear stability analysis with dashed lines. This confirms that susceptibility to banding occurs for slip parameters $a^* < a < 1$ where the critical slip $a^* \equiv \sqrt{8\eta/\eta_C}$. Interestingly this result contrasts with the original JS model (i.e., without the renormalised stress), as it implies that a^2 can always be made small enough to restore monotonicity at a given viscosity ratio, and therefore stability of the homogeneous flow state. As the polymer stress is directly proportional to a, vanishingly small a means the total stress is dominated by the Newtonian solvent, which is linear in the applied shear

rate (i.e., monotonically increasing). The limit $a \to 0$ corresponds to total slip in which the polymer can only be oriented and not stretched by the flow [57]. As with the original JS model, we observe that the shear-rate at which non-monotonicity first appears is pushed out towards $\dot{\gamma} \to \infty$ as $a \to 1$. We now consider the analogous flow instability in a passive liquid-crystal, then examine the instabilities resulting from the shear-induced isotropic-nematic transition.

4.3.2 Passive Q instabilities

Even for passive liquid-crystals, we can identify two classes of shear-driven instabilities. The first is analogous to the above JS banding instability, where now the flow-alignment parameter ξ is the corresponding slip parameter. As with the polymer, this instability originates from terms in the $\mathbf{Q}$ constitutive equation that couple the velocity field to the liquid-crystal (notice the similarities between the reversible coupling terms in Eqs. 3.10, 3.14). Recall that passive particles will tend to align with the flow for $|\xi| > \xi_c$ (as we fix $\gamma = 3$, here $\xi_c = 3/5$ [108]). We restrict ourselves to this flow-aligning regime; the flow-tumbling case ($|\xi| < \xi_c$) has been considered elsewhere [80, 102]. We plot in Fig. 4.4b several constitutive curves as a function of ξ, which reveal that non-monotonic regions appear for $\xi > \xi^* > \xi_c$.

The nature of the second instability is dependent on the value of the IN control parameter, and can be viewed from both free energy (for $\bar{\dot{\gamma}} = 0$) and shear rheology ($\dot{\gamma} \neq 0$) perspectives.

Case $\bar{\dot{\gamma}} = 0$: Recall that for an unsheared liquid-crystal, varying an experimental control parameter such as temperature or concentration (in thermotropic or lyotropic LCs respectively) can drive a transition from the isotropic state (where there is no net orientation at any given point) to the nematic state (where local orientation can be described by an apolar director $\hat{\mathbf{n}}$). In the dynamical equation for $\mathbf{Q}$, the IN-control parameter γ determines the shape of the free-energy landscape and therefore, in the unsheared passive limit, determines which state will form. The stability properties of the isotropic and nematic branches are illustrated in Fig. 3.6.

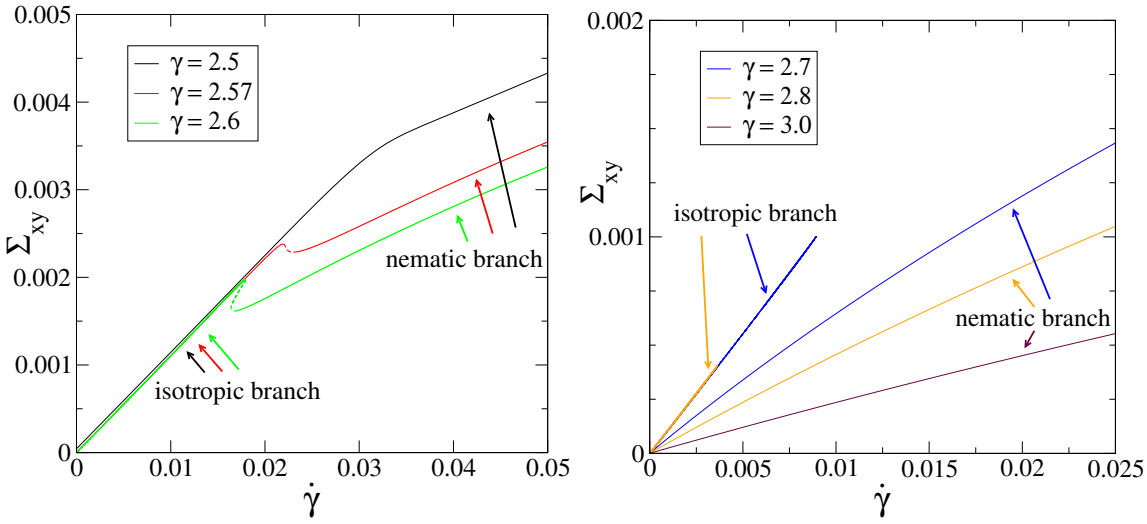

Figure 4.5: Constitutive curves illustrating the shear driven isotropic-nematic transition. The nematic branch is 'pulled in' towards the origin as γ is increased. At larger γ still, the isotropic branch retracts in towards the origin before disappearing altogether for $\gamma > 3$. **Parameters:** $\xi = 0.7$, $\eta = 0.001$, $\tau_C = G_C = \zeta = 0$.

Case $\bar{\dot{\gamma}} \neq 0$: This transition, just described for $\bar{\dot{\gamma}} = 0$, can also be visualised by examining constitutive curves in the limit $\bar{\dot{\gamma}} \to 0$, as γ is increased (see Fig. 4.5), following [146]. For small $\gamma < 2.7$, at $\dot{\gamma} = 0$ only the isotropic[2] branch is present. As $\gamma \to 2.7$, the nematic branch (at $\dot{\gamma} \neq 0$) is 'pulled in' towards the origin. Then as $\gamma \to 3$, the isotropic branch retracts towards the origin until it disappears altogether at $\gamma = 3$ (cf. Fig. 3.6 for $\bar{\dot{\gamma}} = 0$).

More generally (for non-zero $\bar{\dot{\gamma}}$) the constitutive curves in Fig. 4.5 describe how a liquid crystal in the isotropic phase ($\gamma < 2.7$) undergoes a shear-driven transition to the nematic phase at large enough $\bar{\dot{\gamma}}$. Depending on the value of γ, the constitutive curves can be either multivalued in $\dot{\gamma}$ or both $\dot{\gamma}$ and Σ_{xy} indicative of either shear or vorticity banding [44].

4.3.3 Active Q instabilities

The instabilities considered in this chapter so far pertain to purely passive systems. We now ask how the rheological response is affected when the liquid crystal becomes internally driven, i.e., when the active stress $\boldsymbol{\Sigma}^a$ becomes non-zero. As detailed in

[2]The low-shear isotropic branch is also often referred to as the paranematic branch [146].

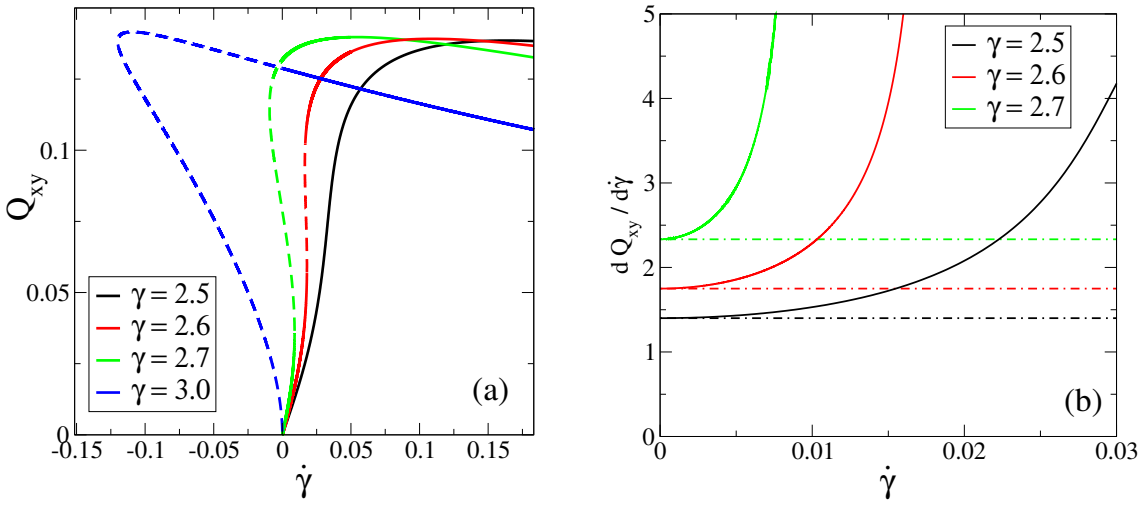

Figure 4.6: (a) Plot of Q_{xy} (which sets the active shear stress $\Sigma^A_{xy} = -\zeta Q_{xy}$) against shear-rate for several values of the IN control parameter γ. Dashed lines mark solutions where the corresponding constitutive curve is unstable. (b) Plot of $\partial Q_{xy}/\partial\dot{\gamma}$, which tends to $\frac{\bar{\Lambda}\tau_Q}{\bar{\Gamma}}$ in the limit $\dot{\gamma} \to 0$ (dash-dotted lines).

Sec. 3.2.1, the only change we need make to the liquid-crystal equations to describe the active systems of interest is the inclusion of an active stress $\boldsymbol{\Sigma}^a = -\zeta\mathbf{Q}$. As we will show in what follows, the rheological consequences of this seemingly minor addition are far-reaching.

We begin by exploring the origin of the spontaneous flow instability from a rheological perspective, treating the isotropic and nematic limits separately. As the nematic spontaneous flow instability has already attracted significant attention [15, 87, 148], we focus mainly on the isotropic regime. Ref. [149] studied the rheology of contractile isotropic solutions using a microscopic model of sliding filaments. However we are unaware of any detailed study of the *extensile* rheology in this regime, nor that which explores the spontaneous flow instability from shear rheology considerations (as we do here).

4.3.3.1 Isotropic spontaneous flow instability.

As we showed in the passive limit, for $\gamma < 2.7$ only one solution exists at $\bar{\dot{\gamma}} = 0$: the isotropic state. This state has $Q_{xy} = 0$ at $\bar{\dot{\gamma}} = 0$ and so contributes no active shear stress $\Sigma^A_{xy} = -\zeta Q_{xy}$ (see Fig. 4.6a). The total stress is then single-valued and continuous at $\bar{\dot{\gamma}} = 0$ (see Fig. 4.9). Recall that our linear stability analysis in

Sec. 3.3.3 predicted that an isotropic base state is susceptible to the spontaneous flow instability above a critical activity, which remains non-zero even in the limit $L_y \to \infty$.

In order to gain a physical understanding of this instability in the language of constitutive curves, we now consider the total shear stress Σ_{xy} in the limit of small shear-rate, where only terms linear in $\mathbf{Q}$ and $\dot{\gamma}$ remain. We are left with contributions from the solvent, (passive) liquid-crystal, and active stress

$$\begin{aligned}\Sigma_{xy} &= \eta\dot{\gamma} + \frac{2}{3}\xi H_{xy} + \Sigma^A_{xy}, \\ &= \eta\dot{\gamma} + 2\bar{\Lambda}\bar{\Gamma}G_Q Q_{xy} - \zeta Q_{xy}. \end{aligned} \tag{4.5}$$

Using the linearised constitutive equation for $\mathbf{Q}$, one can show that (see also Fig. 4.6b)

$$\frac{\partial Q_{xy}}{\partial\dot{\gamma}}|_{\dot{\gamma}\to 0} = \frac{\bar{\Lambda}\tau_Q}{\bar{\Gamma}}, \tag{4.6}$$

which diverges as $\gamma \to 3^-$ [15]. The zero shear viscosity then reads

$$\eta^0 \equiv \frac{\partial\Sigma_{xy}}{\partial\dot{\gamma}}|_{\dot{\gamma}\to 0} = \eta + 2\bar{\Lambda}^2\eta_Q - \zeta\frac{\bar{\Lambda}\tau_Q}{\bar{\Gamma}}, \tag{4.7}$$

where the 1st term is the passive (positive) Newtonian viscosity, the 2nd term is the passive (positive) liquid-crystal viscosity, and the 3rd term is the 'active viscosity' (negative for $\zeta > 0$). Intuition from shear-banding studies tells us that negatively sloping regions of the constitutive curve are indicative of flow instabilities. Therefore the threshold at which η^0 changes sign can be used to derive a critical activity for the spontaneous flow instability

$$\bar{\zeta_c} = \frac{\bar{\Gamma}}{\bar{\Lambda}\tau_Q}\left(\eta + 2\eta\bar{\Lambda}^2\right). \tag{4.8}$$

This is simply our isotropic stability result (see Eq. 3.43 in the limit $k \to 0$).

In order to relate this isotropic flow instability to the classical shear-banding instability, consider the schematic in Fig. 4.7. First recall that if one subjects a passive material to an applied shear-rate within the unstable region of the corresponding constitutive curve (dashed line in Fig. 4.7a), an initially homogeneous shear-flow state will be unstable and perturbations in the shear-rate will grow until they form stable shear-bands at some $\dot{\gamma}_l$, $\dot{\gamma}_h$ (see inset). The constitutive curve for a homogeneous, isotropic material is negatively sloping at the origin for $\zeta > \zeta_c$, as shown

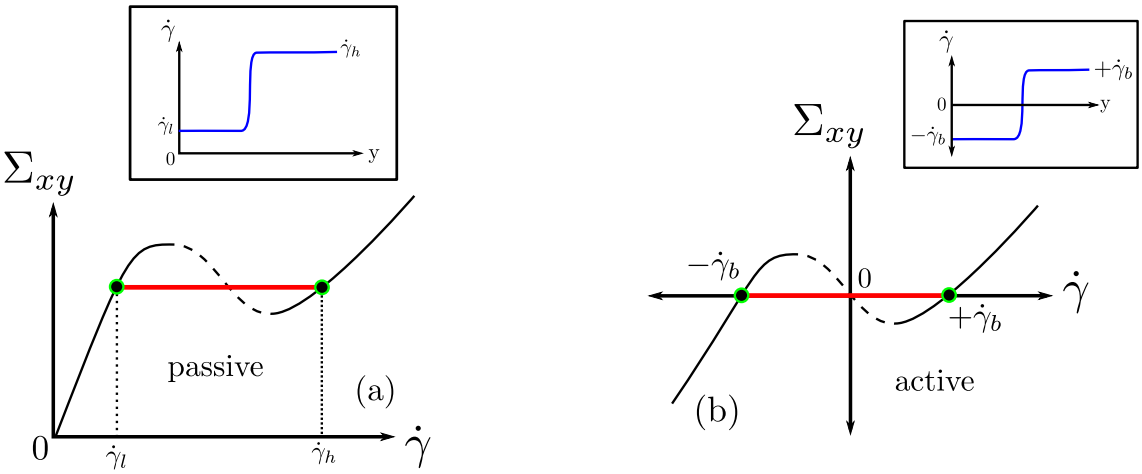

Figure 4.7: Schematic showing similarities and differences between passive and active banding shear banding instabilities. Red lines mark the selected stress, and green circles denote the shear-rates that form the two shear-bands. Insets mark possible profiles of $\dot{\gamma}$ across the channel. (a) Constitutive for a passive material, which would be expected to exhibit shear-banding instabilities for applied shear-rates in the unstable (dashed) region. (b) Constitutive curve for an active isotropic material with $\zeta > \zeta_c$. The curve is downward sloping at the origin, and the system is unstable to forming shear-bands at $\pm\dot{\gamma}_b$ (see also inset).

in Fig. 4.7b. Analogously, for this system perturbations in the shear-rate will grow eventually forming steady shear-bands at $\pm\dot{\gamma}_b$ (see also inset). While passive and active instabilities are similar in the above respects, an important difference is that the stress plateau is at zero stress in the active case.

We now demonstrate that our results are also consistent with earlier numerical studies. Cates *et al.* [15] measured the zero-shear viscosity in the vicinity of the IN transition using 1D finite-difference simulations with free boundary conditions (as in our study) finding that as one approaches the IN transition point in an isotropic material, η^0 vanishes for extensile materials (see Fig. 4.8b red circles). The authors speculated that the region of superfluidity occurs in extensile materials close to the IN transition for $\gamma_c(\zeta, L_y) < \gamma < 3$, though the functional form for $\gamma_c(\zeta, L_y)$ was not given.

Our stability analysis results now allow us to determine $\gamma_c(\zeta, L_y)$. Rearranging Eq. 3.41 (in the limit of no polymer, i.e., $\eta_C \to 0$) produces

$$\gamma_c(\zeta, L_y) = 3\left[1 - \frac{\pi^2 \ell_Q^2}{L_y^2} - \frac{\zeta \bar{\Lambda} \tau_Q}{\eta + 2\bar{\Lambda}^2 \eta_Q}\right]. \tag{4.9}$$

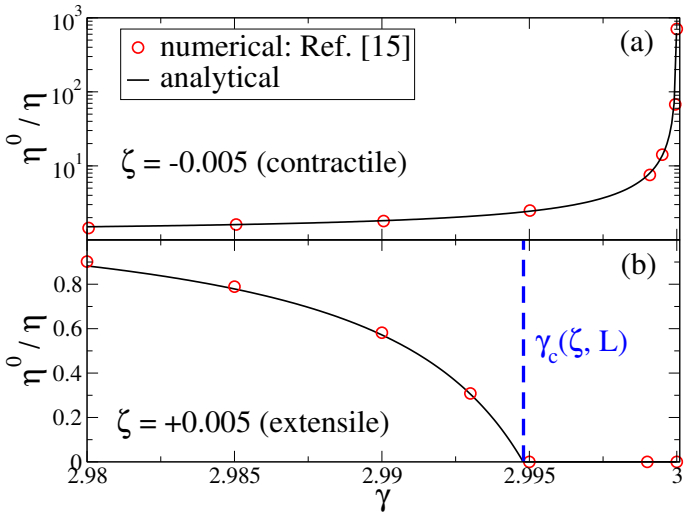

Figure 4.8: We plot the numerical data obtained with free BCs in Ref. [15] (red circles) and our analytics (black line, Eq. 4.7), for (a) $\zeta = -0.005$ and (b) $\zeta = +0.005$ (extensile). Blue dashed line marks the start of the superfluid window $\gamma_c(\zeta, L)$ for an extensile material (Eq. 4.9). **Parameters:** $\eta = 5/3$, $\ell_Q/L = 5 \times 10^{-4}$, $\tau_Q = \eta_Q = 2.9607$.

Note that in the bulk ($L_y \to \infty$) limit for vanishingly small activities ($\zeta \to 0$), $\gamma_c \to 3$, i.e., the value at which isotropic metastability ends in a passive LC. In Fig. 4.8 we show that both the zero-shear viscosity (η^0, Eq. 4.7) and the start of the window of superfluidity for extensile materials ($\gamma_c(\zeta, L_y)$, Eq. 4.9) are in excellent agreement with Ref. [15]. In experimental active systems, γ would typically parametrise the concentration of rod-like active particles. Eq. 4.9 then implies that the critical concentration, above which superfluid states of negative viscosity first appear, can be made arbitrarily small by increasing the activity. Our results therefore show that states deep in the isotropic phase, e.g., that might describe a dilute bacterial suspension, can always form spontaneous flows if endowed with a large enough active stress.

While we have mainly focused on the rheology of extensile materials so far (for which $\zeta > 0$), the results for contractile systems (for which $\zeta < 0$) are also interesting. As we approach the isotropic-nematic transition, $\bar{\Gamma} \to 0$ and the zero-shear viscosity $\eta^0 \propto -\zeta/\bar{\Gamma}$ diverges towards positive infinity. Experiments on contractile algae suspensions have shown [13] a sharp increase in the viscosity as the concentration is increased. Our results are also consistent with earlier analytical [149] and numerical [15] studies of contractile active matter. We can compare directly with

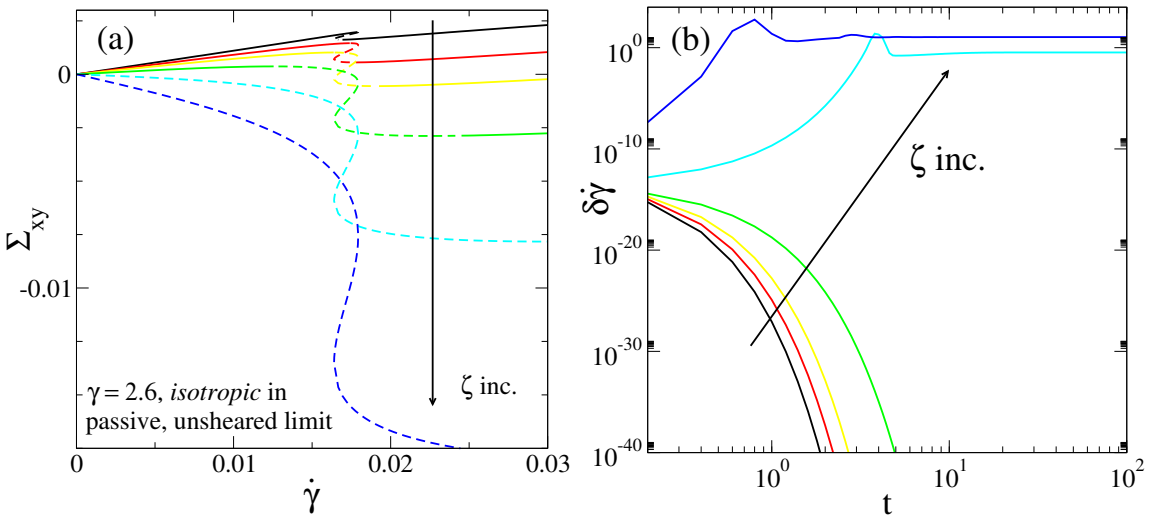

Figure 4.9: (a) Constitutive curves for increasing activities ($\zeta = 0, 0.01, 0.02, 0.04, 0.08, 0.16$) with $\gamma = 2.6$ (corresponding to the isotropic state in an unsheared passive system). For activities above our analytically determined threshold ($\zeta > \bar{\zeta}_c$, see Eq. 3.43), active stresses dominate the Newtonian stress ($\eta\dot{\gamma}$) resulting in a negatively sloping region at the origin. This instability is also captured by our (numerically solved) linear stability analysis (where dashed line indicates instability). (b) For each activity in the left panel, we record the evolution of perturbations in the 1D non-linear code at $\bar{\dot{\gamma}} = 0$. Perturbations grow when $\zeta > \bar{\zeta}_c$, i.e., when the corresponding constitutive curve is negatively sloping at the origin. **Parameters:** $\tau_C = G_C = 0$, $\gamma = 2.6$, $\xi = 0.7$, $\eta = 0.001$, $\bar{\dot{\gamma}} = 0$.

the latter numerical study, where our analytical expression demonstrates excellent quantitative agreement (compare red circles and black lines in Fig. 4.8a).

Finally, to further verify our results, we perform 1D nonlinear simulations. We plot the growth of perturbations about an isotropic base state in Fig. 4.9b. This shows that perturbations grow and develop into a non-linear flowing state when the corresponding constitutive curve has a negative slope at $\bar{\dot{\gamma}} = 0$. The point at which the slope becomes negative (Eq. 4.8) evaluates to $\bar{\zeta}_c \approx 0.063$ for the parameters in Fig. 4.9. We find that perturbations for systems with $\zeta < \bar{\zeta}_c$ decay and those with $\zeta > \bar{\zeta}_c$ grow, consistent with our analytics.

4.3.3.2 Nematic spontaneous flow instability.

In the passive limit, for $2.7 < \gamma < 3.0$ we find the coexistence of both isotropic and nematic branches at $\bar{\dot{\gamma}} = 0$. Without activity, these both have zero shear stress at

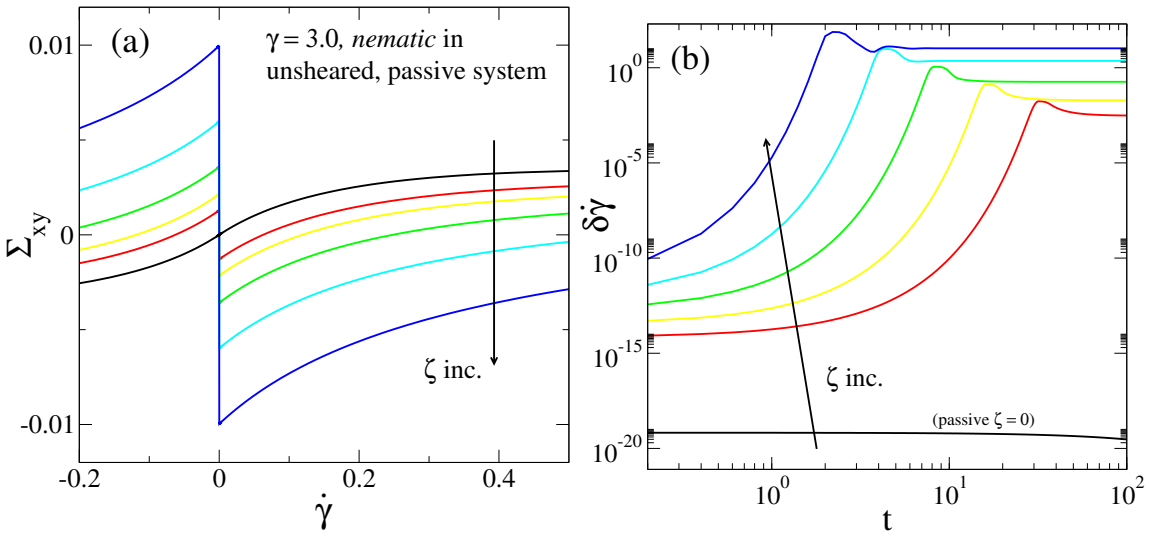

Figure 4.10: (a) Constitutive curves for increasing activity ($\zeta = 0, 0.01, 0.02, 0.04, 0.08, 0.16$) with $\gamma = 3.0$ (corresponding to a nematic in the unsheared passive limit). As the nematic state has $Q_{xy}|_{\bar{\dot{\gamma}}=0} \neq 0$, there is a non-zero active stress at the origin. For extensile systems ($\zeta > 0$), this discontinuity implies a spontaneous flow instability. (b) For each activity in the left panel, we record the evolution of perturbations in the 1D non-linear code at $\bar{\dot{\gamma}} = 0$. Perturbations grow for all $\zeta > 0$ as the corresponding constitutive curves all have a negative zero-shear viscosity. **Parameters:** $\tau_C = G_C = 0$, $\gamma = 3.0$, $\xi = 0.7$, $\eta = 0.001$, $\bar{\dot{\gamma}} = 0$.

$\bar{\dot{\gamma}} = 0$. However the latter branch has $Q_{xy} \neq 0$ as $\bar{\dot{\gamma}} \to 0$, and thus contributes a non-zero active stress $\Sigma^a_{xy} = -\zeta Q_{xy}$ [15]. For extensile systems ($\zeta > 0$) this results in a 'negative yield stress' where that the shear-stress is discontinuous at the origin, and the zero-shear viscosity $\eta^0 < 0$, see Fig. 4.10a. By a similar argument as for the isotropic case, an ordered nematic state (represented by a point at the origin) is unstable to spontaneous flow instabilities and will form shear-bands at $\pm\dot{\gamma}_b$ (similar to Fig. 4.7b). However in contrast to the isotropic case, η^0 is negative *for any* $\zeta > 0$. This rheological interpretation was first reported by Cates *et al.* [15].

Repeating the procedure used above for isotropic materials, we again test our predictions with 1D simulations. (See Fig. 4.10b.) This shows that (excluding the passive case $\zeta = 0$) perturbations grow for all activities shown, however small, lending weight to our argument that the threshold[3] $\zeta_c \approx 0$.

[3]Note that our simulations are intrinsically finite-size, and therefore at small enough activities perturbations will be suppressed. For the parameters in Fig. 4.10, $\zeta_c = 8.5 \times 10^{-5}$ (see Eq. 3.35).

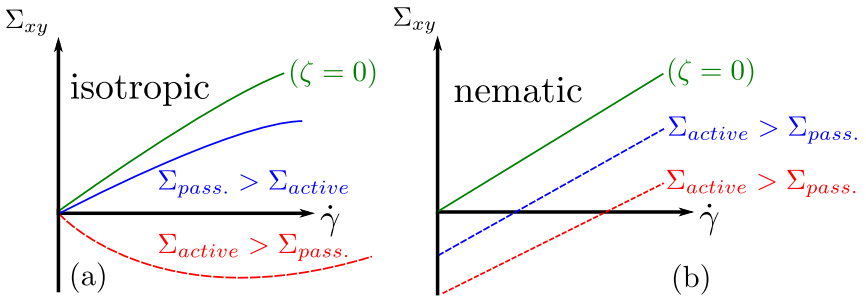

Figure 4.11: Selection of fundamental differences in the constitutive curves for active isotropic and active nematic materials as one approaches $\dot{\gamma} \to 0$. (a) For isotropic materials, the active stress must exceed a non-zero passive stress before the zero-shear viscosity η^0 becomes negative. (b) For a nematic, any active stress will create a discontinuity at the origin (with η^0 negative for extensile). This is because $\mathbf{Q} \neq 0$ even at the origin, which the active stress 'activates' for $\zeta \neq 0$.

4.3.3.3 Consistency with linear stability analysis.

In this section we have presented a rheological argument for the activity-driven spontaneous flow instability purely by examination of 0D constitutive curves. To summarise: for an isotropic material, there is a positive passive stress (which sums viscous and liquid crystal contributions) that the negative active stress must overcome before the spontaneous flow instability can occur (see Fig. 4.11a and recall Fig. 4.9). Equivalently, large enough ζ is required to make η^0 (Eq. 4.7) negative. For nematics, η^0 is negative for *any* positive activity (see Fig. 4.11b). This arises because Q_{xy} is non-zero as $\dot{\gamma} \to 0$, which generates a non-zero active stress $\Sigma^a_{xy} = -\zeta Q_{xy}$.

In this section we have demonstrated excellent quantitative agreement for the thresholds of both isotropic and nematic active flow instabilities between:

1. a 0D analytical rheological argument (by examining stress contributions to the zero-shear viscosity)

2. a 1D analytical stability analysis (by calculating ζ_c)

3. 1D simulation results (by measuring the growth rate of perturbations at early times in our full nonlinear code, starting from a homogeneous base state)

4.3.4 Summary of flow instabilities

We now briefly recap the flow instabilities which we have studied using our (numerically evaluated) stability analysis. These are also collated at the start of this section in Table 4.1. In our model, the polymeric sector is described by a constitutive equation identical to the JS model, apart from a renormalisation of the stress $\mathbf{\Sigma}^C = aG_C(\mathbf{C} - \mathbf{I})$. We presented new results for this renormalised stress which predict shear-banding instabilities for slip parameters in the range $8\eta/\eta_C < a^2 < 1$, generalising earlier work. (See Fig. 4.4a for constitutive curves.)

The analogous instability in passive liquid-crystals (resulting from similar terms which couple $\mathbf{Q}$ to the flow) was also explored, and shear-banding was predicted for $\xi > \xi^*$. (No analytical form is given for ξ^*.) We also reproduced earlier work [146] to describe the shear-induced IN transition, where the isotropic and nematic branches of the constitutive curve are connected by unstable regions. (See Fig. 4.4b / Fig. 4.5 for constitutive curves.)

For active liquid-crystals, we characterised the spontaneous flow instability at $\dot{\gamma} = 0$. The nature of this instability is dependent on the IN control parameter γ. At small $\gamma < 2.7$, a passive equilibrium LC will form an isotropic phase with $\mathbf{Q} = 0$. This can also be seen by examining the constitutive curve for a passive LC, where only the isotropic branch of the solution remains in the limit $\bar{\dot{\gamma}} \to 0$. This isotropic state contributes no active stress at $\bar{\dot{\gamma}} = 0$ (as $\mathbf{Q} = \mathbf{0}$). For large enough activities, the (negative) active stress overcomes the (positive) passive LC and solvent stresses and the zero-shear viscosity becomes negative, implying that the initially homogeneous, isotropic base state becomes unstable. Indeed the threshold at which η^0 changes sign recovers our linear stability results, as is confirmed by our numerics. While previous work has demonstrated that spontaneous flow can occur close to the IN transition point [15], our results show that this instability can occur arbitrarily deep into the isotropic phase.

Above $\gamma = 2.7$, there exists a nematic branch at $\bar{\dot{\gamma}} = 0$, with non-zero Q_{xy}. This contributes an active shear stress which, for extensile systems, is negative. This results in a negative yield stress, and therefore a negative zero-shear viscosity: the

state is then mechanically unstable and results in spontaneous flow. In contrast to the isotropic case, this mechanism exists for any $\zeta > 0$. Our results reproduce and complement the work of Cates *et al.* [15].

We now exploit our detailed knowledge of flow instabilities in both $\mathbf{Q}$ and $\mathbf{C}$ sectors, in both the passive and active regimes, to construct novel constitutive curves that incorporate competing liquid-crystal, polymer, active and viscous stresses and exhibit various exotic combinations of the above instabilities in the same system. These combinations of instabilities are, to our knowledge, novel to our model.

4.4 Composite constitutive curves

Having elucidated the individual sources of instabilities, we now consider the effect when liquid crystal and polymeric sectors are coupled kinematically via the fluid velocity field, i.e., coupling between $\mathbf{Q}$ and $\mathbf{C}$ occurs because both contribute stresses to the Navier-Stokes equation and both react to the resulting velocity field $\mathbf{v}$. We present a selection of examples which showcase the diversity of active shear rheology.

4.4.1 Multiple shear instabilities

Recall that inclusion of non-local terms in the polymeric constitutive equation leads to a uniquely selected plateau stress in shear-banding problems [60, 110] (see Sec. 2.2.3.1 for details). We revisit this effect where now the total stress includes contributions from both $\mathbf{Q}$ and $\mathbf{C}$ sectors, which *both* contain gradient terms in their respective constitutive equations. The mechanism for stress selection when multiple gradient terms are included is unclear *a priori*.

In the following example we combine the active $\mathbf{Q}$ instability (in the vanishing $\dot{\gamma}$ limit) with the polymeric shear banding instability (at $\dot{\gamma}\tau_C \approx 1$). This produces a constitutive curve with multiple unstable regions (as determined either by a linear stability analysis or by inspection for regions where $\partial_{\dot{\gamma}}\Sigma_{xy} < 0$). See Fig. 4.12a/b (black line). It is unclear *a priori* whether a single stress is selected for both unstable regions or if multiple stress plateaus will result instead. We will now demonstrate using non-linear 1D simulations that the latter mechanism is observed, and that the

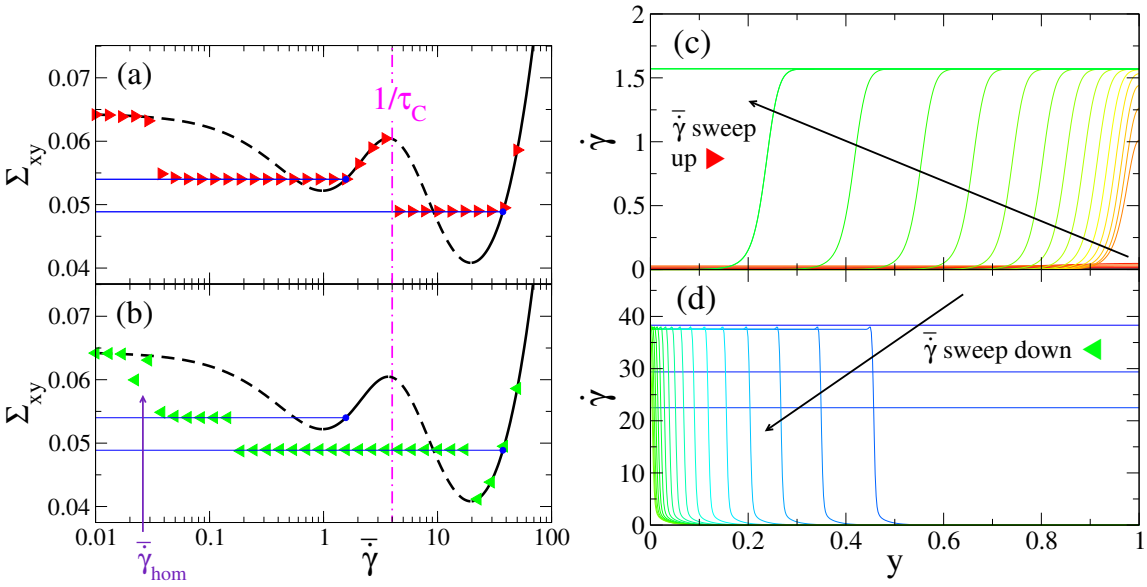

Figure 4.12: Left column: Black lines show the constitutive curves for a homogeneous system exhibiting multiple instabilities (regions marked with dashed lines). Overlaid are flow curves measured from 1D simulations which allow heterogeneity, sweeping $\bar{\dot{\gamma}}$ up (red triangles, top left) and down (green triangles, bottom left). Two distinct selected stresses are found (marked by solid blue horizontal lines), where the selected state is dependent on previous deformation history. At very small applied shear-rates $\bar{\dot{\gamma}} < \bar{\dot{\gamma}}_{hom}$ the flow becomes homogeneous again, because the high shear-band becomes narrower than the lengthscale set by diffusive terms and the interface becomes absorbed into the wall (we expect $\bar{\dot{\gamma}}_{hom}$ will be smaller for smaller ℓ_Q). **Right column:** Slices of $\dot{\gamma}$ across the channel for small $\bar{\dot{\gamma}} < 1.6$ sweeping up (top right) and large $\bar{\dot{\gamma}} > 3.5$ sweeping down (bottom right). The stress from each slice is marked by triangles in the corresponding left column. **Parameters:** $\eta = 0.001$, $\zeta = -0.5$, $a = 0.3$, $\tau_C = 0.25$, $G_C = 1$, $\Delta = 10^{-4}$.

chosen plateau is dependent on previous deformation history.

We adopt a protocol where we increment the applied shear-rate $\bar{\dot{\gamma}}$, wait for the system to reach a steady-state, record the shear stress, then repeat; this is typical in shear experiments [49, 56]. We also repeat the protocol but instead sweep $\dot{\gamma}$ from high to low shear-rates, which should reveal any hysteretic effects.

In Figs. 4.12a/b we overlay numerical data from two sweeps of the applied shear-rate $\bar{\dot{\gamma}}$, spanning nearly four decades. Firstly sweeping from low to high (Fig. 4.12a, red triangles) reveals that for small shear-rates, the system is unstable forming two shear-bands of shear-rate $\dot{\gamma}_{\text{low}} = 0$, $\dot{\gamma}_{\text{high-1}} \approx 1.6$, plotted in detail in Fig. 4.12c. Interestingly this results in a zero-shear band at the lower wall, which in this example

produces a zero-velocity band[4]. At intermediate shear-rates the constitutive curve becomes metastable again and homogeneous flow is restored. At higher shear-rates still ($\dot{\gamma}\tau_C \approx 1$), the polymeric instability then appears, forming two shear-bands of $\dot{\gamma}_{\text{low}} = 0$, $\dot{\gamma}_{\text{high 2}} \approx 38$, this time with a lower selected stress. Finally at very high shear-rates, stability and therefore homogeneous flow are restored.

The reverse protocol instead sweeps $\bar{\dot{\gamma}}$ from high to low (Fig. 4.12b, green triangles). We find that once the unstable region is reached at $\bar{\dot{\gamma}} \approx 20$, the system becomes shear-banded at the lower selected stress. This banded state persists as we decrease $\bar{\dot{\gamma}}$, including shear-rates in the metastable region where $\partial\Sigma_{xy}/\partial\bar{\dot{\gamma}} > 0$. At $\bar{\dot{\gamma}} \approx 0.2$ the system switches to the second banded state, at a higher selected shear-stress.

This ambiguity over state selection suggests that the shear-banded states at low shear-rates are bistable, though whether this degeneracy would survive if our simulations included noise at every timestep is unclear. If measured experimentally, we might expect previous deformation history to noticeably affect the rheological response [56]. Multiple stress plateaus have been observed in other contexts. For example a study of copolymer spherical micelle solutions found three states of increasing degree of ordering as the shear-rate was increased. The transitions between these states were marked by two stress plateaus, where multiple states were observed to coexist [150].

While multiple instabilities were present in this example, a time-independent steady state was always reached. We now explore some contrasting examples where time-dependent, rheochaotic states develop. Initially, to introduce the theory behind such flow states, we consider the case without externally applied shear before going on to apply the understanding gained to the sheared case.

4.4.2 Rheochaos: zero applied shear

We plot in Fig. 4.13a constitutive curves for two activities. At the lower activity (black curve), we expect an unsheared sample ($\bar{\dot{\gamma}} = 0$) to be unstable to the spon-

[4]If the order of the shear-bands was reversed then both bands would have $v_x \neq 0$

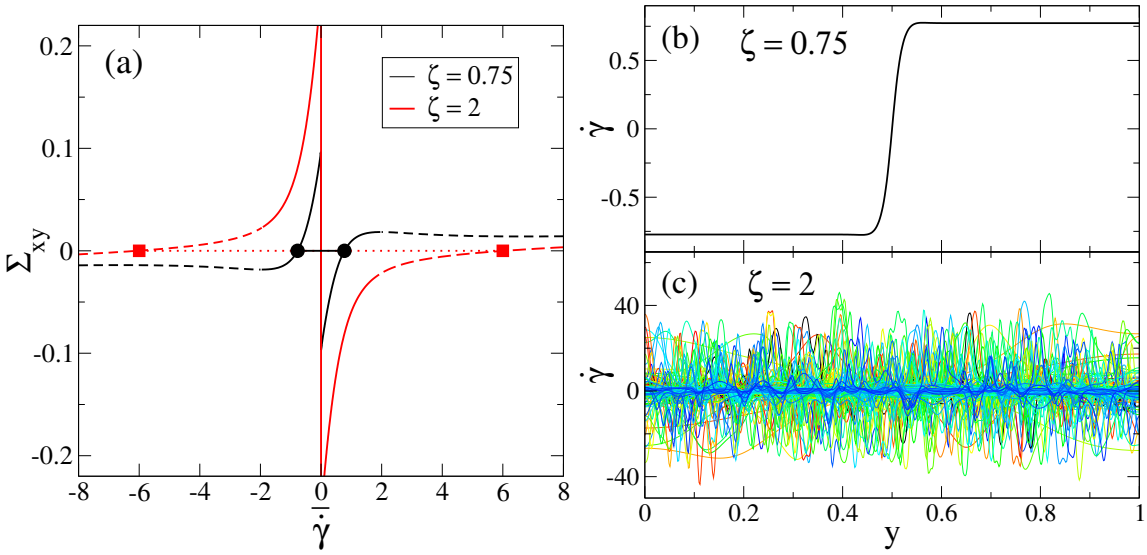

Figure 4.13: Left: Constitutive curves for two activities $\zeta = 0.75$ (black) $\zeta = 2$ (red), where unstable regions are marked by dashed lines. The spontaneous flow instability (resulting from the negative yield stress) predicts that shear-bands should form at the shear-rates given by solid symbols. Our stability analysis predicts stable bands for $\zeta = 0.75$, but unstable bands for $\zeta = 2$. **Right:** Slices of $\dot{\gamma}$ across the cell for both activities. The time-dependent flow state for $\zeta = 2$ can be visualised more clearly in the space-time plot in Fig. 4.14. **Parameters:** $\eta = 0.001$, $\zeta = 0.5$, $a = 0.3$, $\tau_C = G_C = 1$, $\Delta = 8 \times 10^{-5}$.

taneous flow instability due to the negative yield stress argument described earlier (see Sec. 4.3.3). We then might expect the resulting state to consist of equal and opposite static shear-bands at zero stress (black circles), which according to our stability analysis are stable (i.e., line is solid). Indeed, we find that our 1D numerics are consistent with this picture, and a stable banded state forms with shear-bands at $\dot{\gamma}_b \approx \pm 0.77$, see Fig. 4.13b.

However for larger activity (red curve), the region where the constitutive curve passes through $\Sigma_{xy} = 0$ is predicted to be unstable by a linear stability analysis (line is dashed). Therefore the bands that would form at $\dot{\gamma}_b \approx \pm 6.0$ are themselves unstable and could form further sub-bands that may not be able to settle to steady-state.

Performing 1D numerics for this larger activity reveals that a time-dependent state indeed develops with constantly shifting shear-bands, which we plot in Fig. 4.13c. However the complex spatial structure makes it difficult to fully appreciate the dy-

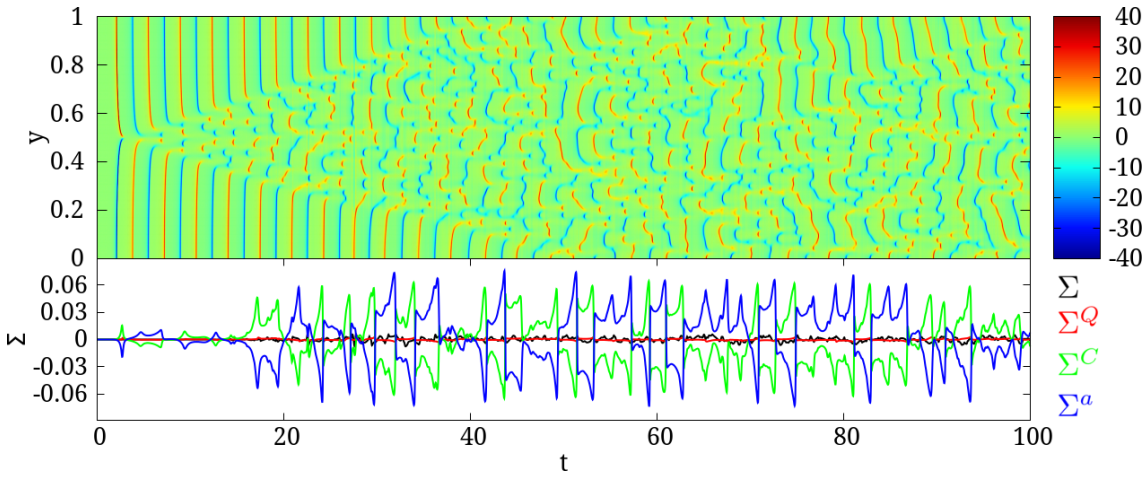

Figure 4.14: A simulation demonstrating a rheochaotic state, with zero applied shear. **Top:** Space-time plot where the x-axis is time, the y-axis position y and the colourscale denotes shear-rate $\dot{\gamma}$. **Bottom:** Components of the shear stress (black total stress Σ_{xy}, red liquid-crystal stress Σ^Q_{xy}, green polymer stress Σ^C_{xy} and blue active stress Σ^a_{xy}). **Parameters:** $\bar{\dot{\gamma}} = 0$, $\eta = 0.001$, $\zeta = 2$, $a = 0.3$, $\tau_C = G_C = 1$, $\Delta = 8 \times 10^{-5}$.

namics. Visualising the same data using a space-time plot provides a clearer way to see the state, see Fig. 4.14 (top). This reveals that initially a pair of shear-bands form (as seen for smaller activity) which then destabilise into further 'sub-bands' until the whole channel consists of bands continuously forming and disappearing.

Examining the stress-time signal (Fig. 4.14 bottom) we find correspondingly aperiodic behaviour. While the time average of each stress component is zero, we find the dynamics to be driven by significant fluctuations of individual stress components about this mean. This is particularly dramatic for the active and polymer stresses (blue and green time series respectively) which appear out of phase with each other, and which (nearly) cancel to produce a total stress close to zero. This competition is reminiscent of our elastomeric results in which activity-driven flows would load the polymer until some threshold polymer stress was reached, at which point the flow direction would switch (see Sec. 3.4.1).

The state we observe is aperiodic, and possibly chaotic. However as we do not measure Lyaponov exponents, we are unable to distinguish truly chaotic states from e.g., quasi-periodic states [151]. (In all that follows we neglect the distinction and use the terms interchangeably.) This phenomenon can be labelled as *rheochaos*, which refers to flow driven chaotic behaviour which is viscoelastic rather than inertial in

nature [152–154]. However in previous studies, the forcing arises from external shear rather than internal active stresses. Our results are reminiscent of those obtained using a (passive) toy model of wormlike micelles subject to an applied shear, where the micellar stress is coupled to microstructure (specifically the micellar length) [153]. The authors found that when coupling was included, the high shear-rate branch developed regions where the underlying base state was predicted to be unstable to perturbations in the flow field. As in our study, nonlinear simulation of this toy model revealed rheochaotic behaviour in the shear-banding regime. The authors determined that rheochaotic behaviour is dependent on some degree of coupling between the relevant order parameters. Our model, which couples **Q** and **C** sectors via the velocity field, clearly satisfies this requirement.

4.4.3 Rheochaos: applied shear

As mentioned above, it is not only at zero applied shear that this phenomenon can be observed. Replotting the above constitutive curves for $\zeta = 0.75$ to include high-shear regions (Fig. 4.15), we find another example where one might expect rheochaotic behaviour. This time the flow instability originates in the polymeric sector and the unstable region starts at $\dot{\gamma}\tau_C \approx 1$.

If we apply a shear-rate in the negatively sloping unstable region $\bar{\dot{\gamma}} = \dot{\gamma}_m$, we might expect the equivalent passive system to form static shear-bands at some $\dot{\gamma}_l$ and $\dot{\gamma}_h$. The linear stability analysis reveals that while the low-shear branch resides in a stable region, the high shear region in which $\dot{\gamma}_h$ is likely to fall is predicted to be unstable and oscillatory, i.e., $Re(\omega) > 0$, $Im(\omega) \neq 0$ where ω is the most unstable eigenvalue (see Fig. 4.15, left).

Numerical solution for an applied shear-rate in this region of negatively sloping stress produces a state with coexistence between a spatially homogeneous shear-band and a rheochaotic region. This can be clearly visualised using the space-time plot in Fig. 4.15 (right). By averaging in time, we estimate the mean and standard-deviation of the shear-rate in either region, and repeat this for the total shear-stress. Overlaying these on the constitutive curve in Fig. 4.15 (left, blue error bars), we find the non-linear simulation results are consistent with our explanation. Our

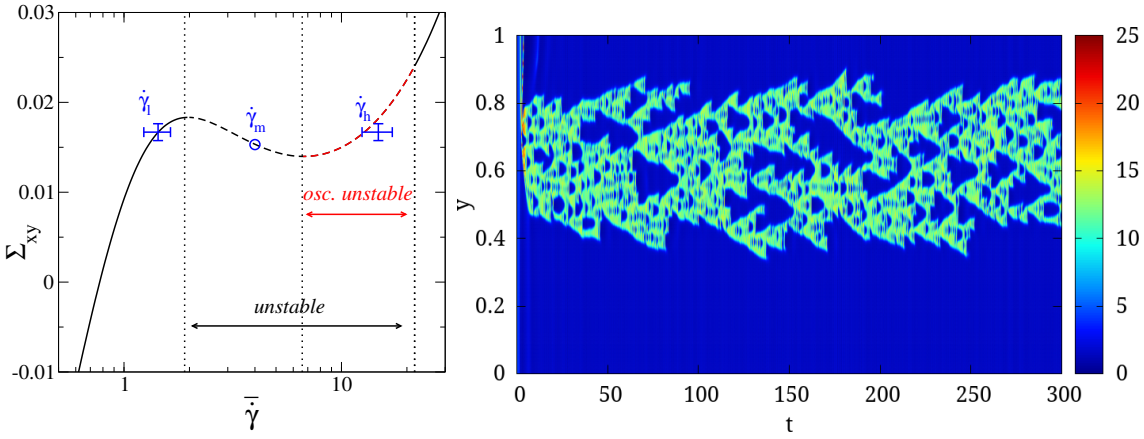

Figure 4.15: Example of rheochaotic behaviour under applied shear $\bar{\dot{\gamma}} = 4$. **Left:** Constitutive curve where both the negatively sloping and high shear-rate regions are unstable. As the system is unstable for our applied shear-rate $\bar{\dot{\gamma}} = 4$, shear-bands form at $\dot{\gamma}_l, \dot{\gamma}_h$. Our linear stability analysis predicts oscillatory growth of perturbations in the higher band, which results in chaotic fluctuations. Variations in shear-rate and shear-stress are marked by blue error bars. **Right:** Space-time plot showing coexistence of chaotic (high $\dot{\gamma}$, lighter colours) and homogeneous (low $\dot{\gamma}$, dark blue) regions. **Parameters:** $\bar{\dot{\gamma}} = 4$, $\eta = 0.001$, $\zeta = 0.75$, $a = 0.3$, $\tau_C = G_C = 1$, $\Delta = 8\times10^{-5}$.

results are also consistent with those obtained using a model for wormlike micelles in Ref. [155] where the authors reported linear instabilities in the high shear branch of the constitutive curve when coupling was turned on. Chakrabarti *et al.* reported rheochaotic behaviour in sheared, passive nematics (although without hydrodynamic coupling to the fluid velocity). They found that strong non-linearities in the liquid crystal equations (when driven by an imposed homogeneous shear flow) can also result in spatiotemporal chaos [154].

4.5 Conclusions

In this chapter we have studied the shear rheology of our novel model for active viscoelastic matter, using three related techniques. Firstly we produce 0D constitutive curves under the assumption of homogeneous flow. While this is analytically possible for the polymeric sector, the liquid-crystal model requires numerical solution. We then use this solution as a base state in our linear stability analysis, which we have generalised from the analytics of Chap. 3 (which set $\bar{\dot{\gamma}} = 0$) to include sheared materials (for which $\bar{\dot{\gamma}} \neq 0$). Finally we solve the nonlinear constitutive equations

in 1D, i.e., allowing heterogeneities in the y-direction.

We first applied these methods numerically to enumerate the possible flow instabilities in **Q** and **C** sectors separately. We validated our methods by reproducing earlier results including the shear-induced isotropic-nematic (IN) transition in passive nematics [146], and the LC shear-banding instability. We also presented new results in which we derived the spinodal limit of stability in the **C**-only model, generalising earlier work to include the effect of the renormalised polymer stress. In principle, these results could allow one to map our model to the recent experiments of Kunita *et al.* [51] which demonstrated shear-banding in solutions of actin filaments as might be found in the cell cytoskeleton.

Interestingly, the nature of the active spontaneous flow instability depends on whether the equivalent unsheared passive system forms an isotropic or nematic phase. In the former case, we described a mechanism in which a sufficiently large active stress is required to produce a negative zero-shear viscosity by considering contributions to the total shear stress in the limit $\dot{\gamma} \to 0$ (base states with negative viscosities are mechanically unstable and are indicative of flow instabilities). Our results show that spontaneous flows can occur even deep into the isotropic phase, given sufficiently large extensile activity. In the latter (nematic) case, we reproduced the results of earlier work that showed that any extensile activity results in a negative yield stress and therefore a negative zero-shear viscosity [15]. We also demonstrated that our rheological arguments are entirely consistent with both our linear stability analysis (Sec. 3.3) and our 1D nonlinear numerics.

Then by exploiting these results, we generated constitutive curves with exotic rheological features. For example, we showed how the combination of **Q** and **C** stresses can produce constitutive curves with multiple stress plateaus. We simulated two protocols where we sweep the applied shear-rate up or down. These produced flow curves which were not coincident in general, demonstrating that hysteretic effects are present. Particularly at low shear-rates, we observe banded plug flows where the lower shear-band is characterised by zero shear-rate. This is reminiscent of inhomogeneous streaming flows that play a role in slime mould locomotion [156] where it is thought that cellular protrusions could be driven by such flow instabilities

[51].

Finally we explored the dynamics of a system characterised by an intriguing constitutive curve where one or more of the shear bands (that would form according to the classical shear-banding mechanism) are themselves predicted to be unstable. Simulations revealed the non-linear dynamics to be be aperiodic and possibly chaotic, producing highly time dependent states where shear bands continuously form and disappear. This is consistent with earlier studies that used models with some degree of coupling between order parameters. Our results suggest that if one subjects a solution of active particles embedded in a viscoelastic medium to an applied shear $\dot{\gamma}\tau_C \approx 1$, the resulting behaviour can be chaotic if energy input (i.e., activity) is large enough. This could be realised, for example, with microfluidic experiments on living liquid-crystals [117] in a dilute polymer solution.

In the preceding chapters, we have considered the stability and dynamics of active matter in 1D, both with and without externally applied shear and using a range of both analytical and numerical techniques. We now investigate the differences that arise when we allow spatial variations in two dimensions. We will show that while the analytical critical activities derived in this chapter remain applicable, the resulting dynamical behaviour when these thresholds are exceeded is, in general, strongly 2D in nature.

5

Active viscoelastic matter:

2D (no applied shear)

5.1 Introduction

In the previous chapter, assuming invariance of all hydrodynamic fields in all dimensions (0D) allowed us to map the rheology of active viscoelastic matter by producing constitutive curves under the assumption of homogeneous flow. Even in this reduced dimensionality, we were able to make striking predictions about the nature of the spontaneous flow instability (in the infinite system size limit) based solely on rheological arguments. Specifically we identified fundamental differences between isotropic and nematic suspensions as we approach the infinite system size limit: the critical activity vanishes for nematic states but remains finite for isotropic states.

By relaxing this assumption of homogeneity in the y-direction (normal to the walls), we studied the growth of spatial perturbations in the order parameter fields.

Retaining invariance in the x-direction however kept the governing equations analytically tractable. This allowed us to develop analytical insight into the spontaneous flow instability in confined viscoelastic active matter, where the free energy cost of distortions (required for the flowing state) competes against the active stress. We predicted a novel mode of instability that occurs when polymer of long relaxation times is added.

As is typical in hydrodynamic stability theory [157], we have studied our model in a space of increasing dimension (0D, 1D, and in this chapter, 2D). Each successive dimension informs the next, and in this chapter we will demonstrate that our lower dimensional results remain highly relevant for our two dimensional study, accurately predicting the onset of the spontaneous flow instability in 2D.

Due to the additional computational cost involved, we do not consider the dynamics of active viscoelastic matter in 3D in this thesis. However as many experimental studies involve quasi-2D geometries such as thin films [158], confined chambers [117], or droplet surfaces [94, 159], we expect our 2D results to be relevant experimentally. We now review the existing literature, particularly that which focuses on the 2D confined geometries considered in this chapter.

Confinement. Active materials, particularly when confined in bounded geometries, present a fascinating competition between active stresses and elastic distortions. In Chap. 3, we generalised earlier work to include the effect of adding polymer, deriving the critical activity that must be exceeded before the active stress can overcome the energetic cost required to produce a distorted director field. We showed that, in the nematic phase, this critical activity is inversely proportional to the smallest lengthscale of confinement L_y (see Eq. 3.37). In this chapter we continue to explore this theme of confinement in 2D showing that, particularly when polymer is added, confined active matter breaks a macroscopic symmetry by developing net flows within the channel. From here onwards we focus on the nematic phase observed in many biological examples of active matter, particularly for cytoskeletal materials such as the kinesin-microtubule mixtures studied in Ref. [94]. (By focusing on the nematic phase, for which $\gamma = 3$, we also keep the parameter space manageable.)

Recent experimental studies in confined geometries motivate our study. By studying suspensions of *B. subtilis*, Wioland *et al.* observed the formation of stable macroscopic spiral vortex structures when the bacteria were confined to an appropriately sized droplet [160]. It has been argued that such confinement of *subcellular* active matter may be in part responsible for cytoplasmic streaming [1, 11], an important biological process where directed, coherent fluid flows provide circulation of nutrients and organelles within the cell [12].

Keber *et al.* confined a kinesin-microtubule mixture to the surface of a small spherical droplet, where geometric constraints fix the number of topological defects (see below for an introduction to defects in active matter). This produced a range of novel oscillatory states and dynamical changes in shape driven by protrusions reminiscent of those seen in crawling cells [159]. In a related study, larger droplets were squeezed between two parallel plates forming a quasi-2D material. These droplets were observed to develop spontaneous motility, tracing out periodic patterns in the fluid [94]. Such experiments have provided inspiration for several numerical and theoretical studies of 'active droplets' as a minimal model of cell motility. These typically adopt a phase field (similar to that used in Chap. 7) to describe the shape of a deformable droplet [20, 161–163].

At the cellular scale, the motility of crawling leukocytes in confined 3D environments was studied both *in-vivo* and *in-vitro* where it was found that contractile stresses, driven by the actomyosin complex, are responsible for propelling the nucleus through narrow gaps [164]. Vedula *et al.* studied the migration of cells in an artificial channel geometry, where they observed that the mean cell velocity increased as the channel was narrowed [165]. The flow in wide channels was characterised by vortex-like structures whereas the flow was more directed and coherent in narrower channels ('coherence' was quantified using an orientational order parameter). In Sec. 5.4.2 we explore an effect where the correlation length of an active LC is increased as polymer is added, resulting in more coherent flows and thus net material motion.

Solid walls can have important hydrodynamic effects. Hernandez-Ortiz *et al.* showed that even for dilute, independent swimmers with no collective behaviour,

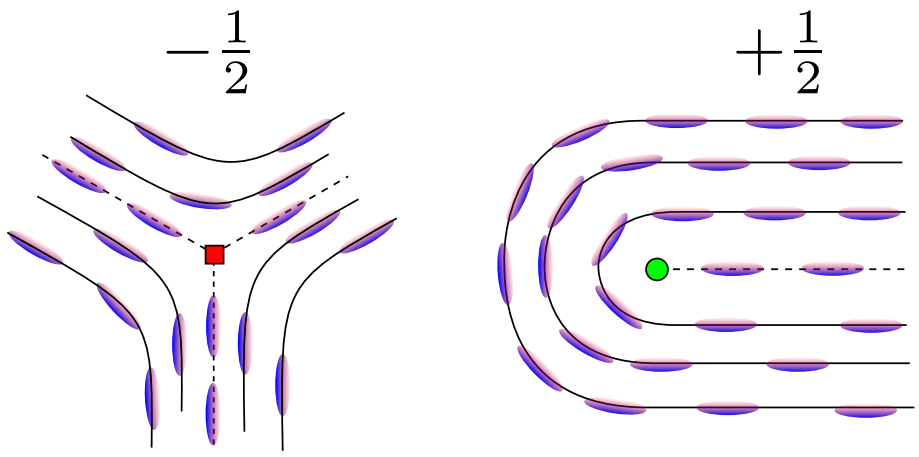

Figure 5.1: Schematic illustrating some of the topological defects found in nematic liquid crystal phases, here for elongated apolar molecules. The red square and green circle mark the singularities at the defect cores; we adopt this notation to label defects in any further 2D plots. **Left:** $-\frac{1}{2}$ defect, note the threefold rotational symmetry. **Right:** $+\frac{1}{2}$ defect, note the lack of rotational symmetry defines a defect orientation with the defect 'head' to the left and 'tail' to the right.

walls can produce spatial fluid correlations in a confined domain that do not appear in unbounded flows [166]. The above studies motivate us to further explore the walled geometry which we previously considered for 1D systems in Chaps. 3, 4.

Defects. With the increase in dimensionality comes a corresponding increase in topological complexity. Of significant importance to active matter systems is the role of topological defects. Given a general order parameter, which may vary in space, a topological defect can be defined as the point, line or surface where the order parameter is discontinuous [167, 168]. In our 2D study, it is point defects of the nematic order parameter $\mathbf{Q}$ that are specifically relevant.

Such defects can be characterised by the winding number, defined as the line integral of the director angle around the core [74]. Due to the head-tail symmetry of the nematic director, this net rotation can only take values

$$\Delta\theta = 2\pi m \tag{5.1}$$

where m is an integer or half-integer. In Fig. 5.1 we illustrate the two half-integer defects commonly found in nematic liquid crystals. Note that the dimensionality of both the order parameter and the space in which it exists are important. In our

study we employ a 3D $\mathbf{Q}$ tensor in 2D space for which $\pm\frac{1}{2}$ defects are topologically equivalent[1].

These defects can be generated in a passive nematic by, for example, a rapid quench from the disordered to the ordered state, or by an externally applied field. Allowing the system to equilibrate, the defect texture coarsens as oppositely charged defects annihilate until a homogeneous state is reached, minimizing the free energy. The defect density n, defined as the total number of defects per unit area, typically decays as a power law in time $n \sim t^{-1}$ [169].

It is not only the relaxational dynamics that drive this coarsening process. The hydrodynamical coupling of the director field to the velocity results in a backflow which can accelerate $+1/2$ defects and slow $-1/2$ defects [170]. For sufficiently large activity, an analogous 'active backflow' effect can dominate, dependent on the symmetry of the defect [171]. The threefold rotational symmetry of the $-1/2$ defect means that active stresses do not contribute to the net defect motion. In contrast the $+1/2$ defect has a defined polarity, and moves in the direction of the head (tail) for extensile (contractile) systems (as defined in Fig. 5.1).

The dynamics of defect-driven active matter have been studied experimentally with remarkable clarity in quasi-2D confined geometries [94, 159]. For sufficiently large concentrations of ATP (parametrised by activity ζ in our simulations), concentrated suspensions consisting of microtubule filament bundles and clusters of kinesin molecular motors were observed to form spontaneously flowing chaotic states consisting of many $\pm 1/2$ defects [94]. In contrast to actomyosin, which is contractile [172], the resulting dynamics is extensile with the motion of $+1/2$ defects consistent with the 'active backflow' mechanism in Ref. [171].

Particularly in the chaotic regime that we explore later, the dynamics is driven by continual, activity-driven creation and annihilation of defects. The total topological charge is exactly conserved for the biperiodic case, i.e., at any point in time there are equal numbers of $+1/2$ defects and $-1/2$ defects. However when solid walls are included, defects can additionally form and annihilate at the boundaries which, in general, can lead to a net topological charge.

[1]Note that $\pm\frac{1}{2}$ defects are distinct only if both space and order parameter are strictly 2D [168].

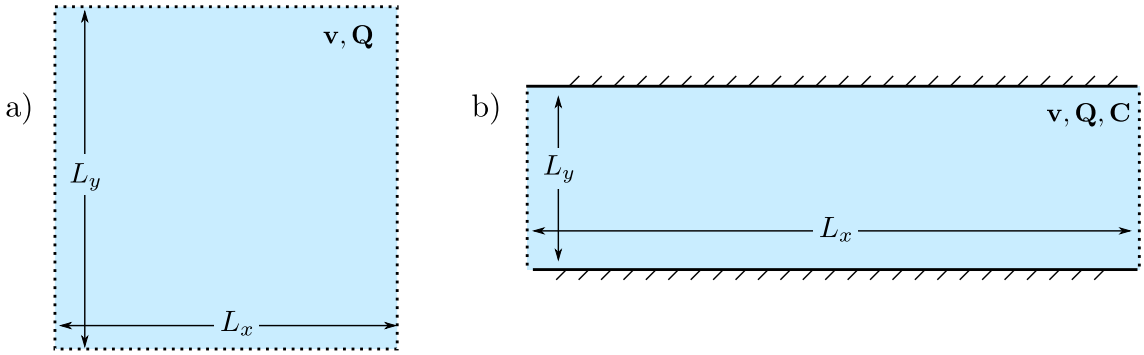

Figure 5.2: Schematic of the two geometries considered in this chapter, where dotted lines indicate periodic boundaries. a) Biperiodic geometry used to study defect dynamics (without polymer), with sides of length $L_x = L_y = 1$ (see Sec. 5.2). b) Channel geometry used for the studying confinement effects, periodic only in the x-direction (see Secs. 5.3 to 5.6). We fix $L_x = 4L_y$.

The first section of this chapter focuses on the steady state dynamics of defects in the chaotic phase, relating correlation lengths to the activity. The most natural geometry in which this can be studied is the biperiodic system (i.e., without walls) shown in Fig. 5.2a. However for the latter sections of this chapter where we study the effects of polymer on confined active flows, we include solid walls as in Chaps. 3, 4 (see Fig. 5.2b).

Drag reduction. Beyond a critical Reynolds number, pressure-driven pipe flow of a passive, Newtonian fluid develops turbulent, time-dependent structure. Recent theoretical, numerical and experimental studies of active matter (without polymer) have noted similarities between this inertial turbulence and so called 'active turbulence' (which occurs even for $\mathrm{Re} \to 0$), for example demonstrating that the latter possesses the multiscale structure and energy spectra characteristic of the former [173, 174].

When this pipe flow is in the turbulent regime, a marked increase in throughput is observed experimentally when high molecular weight polymer is added, resulting in a drag reduction effect [175]. In this chapter we explore the analogous effect in active systems: by adding polymer to (say) a fluid showing bacterial turbulence, we will argue that one could effectively 'reduce drag' by enhancing throughput at fixed active stress (see Sec. 5.4). Such an effect may be relevant to the cytoplasmic streaming processes discussed above, which require coherent flows to transport nutrients within

the cell.

In this chapter we take a numerical approach and study the 2D dynamics of our coupled model for active viscoelastic matter. We begin in the simplest limit where the polymer relaxation is so rapid that it does not contribute to the dynamics. In the biperiodic geometry we examine the relation between activity and the underlying lengthscale of the 'active turbulent' state l^*, as determined by multiple correlation lengths. Using careful numerics we unambiguously obtain the scaling $l^* \sim \ell_Q \sqrt{G_Q/\zeta}$, in agreement with an independent numerical study performed by our collaborators.

Then remaining briefly in the limit of no polymer, we return to the parallel plate geometry considered previously in 1D and verify our 2D code by reproducing earlier work [87]. This is then generalised to account for multiple initial conditions, revealing that the onset of spontaneous flow can occur at activities an order of magnitude smaller for bend instabilities than for splay. The phase diagram, particularly in the chaotic region, is characterised by states with no net flow in any particular direction.

However when polymer is added we demonstrate that this macroscopic symmetry can be broken and flows with net throughput can develop. This, we argue, results from an 'active drag reduction' effect whereby polymer calms small scale structure resulting in more coherent flow states. We quantitatively confirm this by studying the dependence of the defect density with polymer relaxation time, τ_C.

We then explore the limit of diverging polymer relaxation time τ_C, first at fixed polymer viscosity (i.e., we take $\tau_C \to \infty$, $G_C \to 0$ so that $\eta_C = G_C \tau_C$ is constant), then with fixed modulus G_C (so that $\eta_C \to \infty$). Perhaps surprisingly, both limits reveal that transient spontaneous flows are possible in a material that is effectively a solid, a result quantitatively consistent with our 1D analytics in Sec. 3.3 above.

Finally we provide a selection of novel examples when the active nematic is thermodynamically coupled to the polymer, i.e., at the level of the free energy ($\chi \neq 0$ in Eq. 3.9). These include: an example where an initially chaotic state is driven into an ordered, shear banded flow (which can be seen as an extreme example of drag reduction), and shuffling, oscillatory states.

5.2 Defect dynamics ($\eta_C \to 0$)

We begin in the limit where the polymer relaxational dynamics is so fast that the polymeric stress is negligible[2]. This limit provides a simple starting point for studying the dynamics of active matter in 2D. To avoid sampling complications introduced by solid walls, we adopt the biperiodic geometry in this section (Fig. 5.2a), allowing us to obtain clear statistics for the correlation lengths with ease. We solve the equations of motion described in Sec. 3.2 numerically (without polymer, i.e., $\eta_C \to 0$) using the Fourier method described in Sec. 2.3.2.

As discussed previously, depending on the strength of the activity, active matter can form different phases in which the nature of collective motion ranges from laminar (at low activities) to turbulent (at high activities). For example, recent experiments on kinesin-microtubule mixtures have revealed turbulent states which appear to be driven by the continual creation and annihilation of defects [94, 95]; at larger scales, dense bacterial suspensions are observed to form similar phases [126]. In order to connect minimal theoretical models with such experiments, it is important to identify the underlying lengthscales of the system and how they relate to key dimensionless parameters. While there have been several recent attempts to ascertain the relation between activity and the lengthscale of nematic structure [6, 173, 176, 177], a consensus has yet to be reached.

Scaling arguments. Previous simulation studies of active nematics [87, 108] (and our own results, see Sec. 5.4) have shown that at low activities, the director field forms structures which span the system size L, whereas larger activities generate states that are both spatially and temporally aperiodic and whose structure is independent of the system size. However, while it is clear that the correlation length of the nematic director decreases with activity in the way just described, the precise nature of the scaling is unclear.

Once free of the system size $L\,(= L_x = L_y)$, dimensional analysis tells us that

[2] In practice, we simply omit the $\mathbf{C}$ dynamics and stress from our simulations altogether, so that $\eta_C \to 0$.

the characteristic lengthscale l^* of structure in the fluid should scale with the only remaining length $\ell_Q \equiv \sqrt{K/G_Q}$ and with the following dimensionless groups

$$l^* = \ell_Q \; f\left(\frac{G_Q}{\zeta}, \frac{\eta}{\eta_Q}\right). \tag{5.2}$$

By considering the lengthscale at which active and passive stresses balance [173], we might further expect that

$$l^* \propto l_a \equiv \ell_Q \sqrt{\frac{G_Q \eta}{\zeta \eta_Q}} \left(= \sqrt{\frac{K\eta}{\zeta \eta_Q}} \right). \tag{5.3}$$

(This is also consistent with our linear stability analysis results, in which $\sqrt{\zeta_c} \propto \ell_Q$, where ζ_c is the threshold for spontaneous flow.) Note that at large enough activities l^* will reach the microscopic lengthscale ℓ_Q at which it will presumably saturate. The activities explored in our simulations are not large enough to produce this effect however.

Giomi [173] obtained the scaling $l^* \propto \zeta^{-1/2}$ numerically, consistent with the above form. In contrast, recent simulations by Thampi *et al.* [177] suggest that $l^* \propto \zeta^{-1/4}\ell_Q$. A possible source for this inconsistency in scaling exponents could be due to differences in the $\mathbf{Q}$ tensor formalism: the former study uses a 2D order parameter in 2D space, whereas the latter adopts a 3D order parameter in 2D space (as we have done throughout this thesis).

The main aim of this section is then to resolve this discrepancy and verify the functional form proposed in Eq. 5.3. We achieve this by performing careful numerics in which we vary the activity over several decades. We have also engaged in a collaborative project with Christina Marchetti and Prashant Mishra at Syracuse University, in which two common variants of the $\mathbf{Q}$ tensor formalism are compared, using independently developed numerical codes [32]. Excellent agreement was obtained between both studies, demonstrating that our results are robust to both the dimensionality of the order parameter and the specific details of the model.

Full details of the collaborative project can be found in Ref. [32], which additionally includes (a) an investigation of how correlation lengths in the velocity field scale with activity, and (b) results demonstrating that the same scaling laws are obtained for contractile active matter.

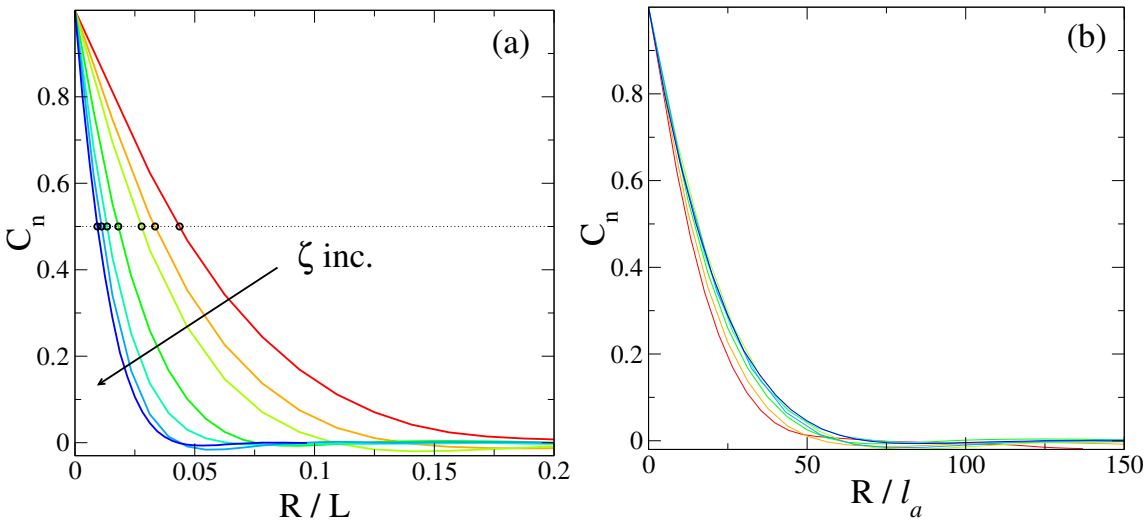

Figure 5.3: Example showing the decrease of director correlation length as activity is increased, once in the defect dominated chaotic regime. (a) Director correlation C_n as a function of R/L (see Eq. 5.4). Correlation lengths (defined as R^* for which $C_n(R^*) = 1/2$) are marked with black circles, and correspond to green crosses in Fig. 5.4. (b) Director correlation C_n, where R has been scaled by l_a (Eq. 5.3). This shows a reasonable curve collapse for all activities shown, strongly suggesting that the correct scaling behaviour has been obtained. **Parameters:** $\Delta = 5 \times 10^{-6}$

5.2.1 Correlation lengths

There are multiple correlation lengths that one can define to describe the spatial structure of an active nematic. We adopt two methods for obtaining the nematic correlation length; in principle one can also examine analogous correlations in the velocity field [32, 177].

5.2.1.1 Director correlation length

We define the director correlation function

$$C_n(R) = \frac{2\langle \hat{\mathbf{n}}(R).\hat{\mathbf{n}}(0)\rangle - 1}{2\langle \hat{\mathbf{n}}(0).\hat{\mathbf{n}}(0)\rangle - 1}, \tag{5.4}$$

which yields the correlation in the nematic director $\hat{\mathbf{n}}$ between two points R apart. Angular brackets $\langle\cdot\rangle$ in the above equations indicate an average over space and time. We then define the nematic correlation length l_n such that $C_n(l_n) \equiv 1/2$. An example of this procedure is given in Fig. 5.3a.

5.2.1.2 Defect density length

We define the areal defect density n as the total number of defects divided by the simulation area $L_x L_y$. The method for numerically counting defects is described in detail in Apx. 5.8, following Ref. [178]. By assuming a homogeneous distribution of defects, as is reasonable in the regime of active turbulence, we then define the defect separation length as

$$l_d \equiv \frac{1}{\sqrt{n}}. \tag{5.5}$$

5.2.2 Results

We now present the results of 2D simulations for a range of activities in the regime of fully developed turbulence, i.e., small enough to avoid saturation at the microscopic length, but large enough to avoid finite system-size effects [173]. We also repeat these simulations for several values of ℓ_Q/L in order to confirm the functional form of Eq. 5.2. While the focus here is on extensile materials ($\zeta > 0$), we find that our results are generic and also hold for the contractile activities [32] (data not shown).

We begin in Fig. 5.4a by plotting the scaling of nematic and defect spacing correlation lengths (l_n, l_d respectively) against ζ/G_Q. At small activities we observe saturation in the correlation lengths due to finite-size effects (see shoulder in top left of the plot). However as the activity is increased, any dependence on the system size is lost. Once sufficiently deep into the turbulent phase, both correlation lengths clearly appear to scale as $(\zeta/G_Q)^{-1/2}$ (black dashed line). Eventually we might expect both correlation lengths to saturate as $l_n, l_d \sim \ell_Q$, though the activities in our simulations are not large enough to observe this effect.

Note that the defect spacing correlation length is consistently larger than l_n by a factor ~ 3. This is to be expected: as l_n effectively measures the radius of a vortex structure around a defect, the spacing between a pair of vortex centres will be at least twice this.

If we now rescale both correlation lengths by ℓ_Q, each set of data collapses onto a single curve (see Fig. 5.4b). This, combined with the excellent agreement with the

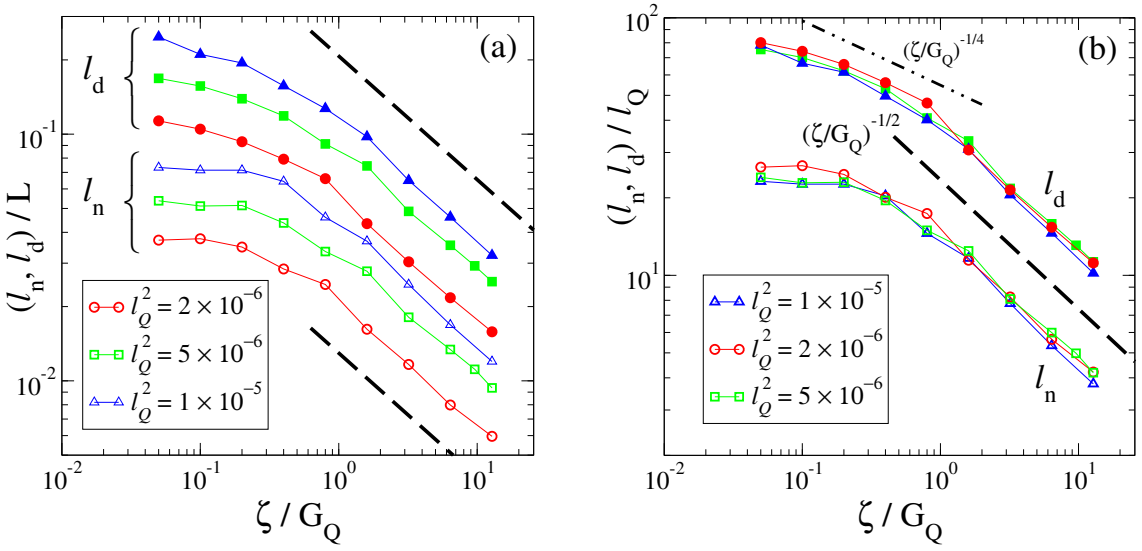

Figure 5.4: Nematic (l_n, empty symbols) and defect (l_d, filled symbols) correlation lengths against dimensionless activity ζ/G_Q for an extensile nematic ($\zeta > 0$). Data shown for $\ell_Q^2 = 2 \times 10^{-6}$ (red circles), 5×10^{-6} (green squares), and 1×10^{-5} (blue triangles). (a) Both lengthscales scale as $\sim (\zeta/G_Q)^{-1/2}$ (dashed black line). (b) The data in (a) collapses onto a single curve when (l_n, l_d) are rescaled by ℓ_Q. **Note:** For reference, the dash-dotted line shows the scaling $(\zeta/G_Q)^{-1/4}$ obtained in Ref. [177].

plotted power law (black dashed line), strongly suggests the scalings

$$l_d, l_n \propto \ell_Q \sqrt{G_Q/\zeta}, \tag{5.6}$$

consistent with the functional form proposed in Eq. 5.2. To demonstrate this further, we plot in Fig. 5.3b the nematic correlation function $C_n(R)$, where R is rescaled by $l_a = \ell_Q \sqrt{G_Q \eta/\zeta\gamma}$. As expected, this shows a reasonable curve collapse for activities in the regime of fully developed turbulence.

Our results also reveal a possible reason for the discrepancy with Thampi *et al.* [177]: if one is not sufficiently deep into the regime of active turbulence, then a fit will only capture the 'shoulder' of the data, and therefore a power law with an exponent greater than $-1/2$. To illustrate this, we also display the $\zeta^{-1/4}$ scaling obtained in Ref. [177] in Fig. 5.4b (dash-dotted line).

5.2.3 Summary: defect dynamics

In summary, we have shown that once in the regime of fully developed active turbulence, the lengthscale of structure in the director field (as determined by two distinct

correlation lengths) unambiguously scales as

$$l^* \propto \ell_Q \sqrt{G_Q/\zeta}. \tag{5.7}$$

Results from a collaborative study [32] confirmed the above scaling, and generalised these findings to examine the functional dependence on η_Q, finding that

$$l^* \propto \ell_Q \sqrt{G_Q \eta/\zeta \eta_Q}, \tag{5.8}$$

as originally theorised (Eq. 5.3). We speculate that discrepancies in the literature over the scaling exponents may be due to finite-size effects, whereby correlation lengths saturate at the system size L at low activities.

5.3 Phase diagrams ($\eta_C \to 0$)

By considering the 2D dynamics of our model in the limit of no polymer (i.e., $\eta_C \to 0$), we have shown that the biperiodic geometry is ideal for the study of defect dynamics, particularly in the regime of fully developed turbulence. This allowed us to unambiguously obtain the scaling law that relates the nematic correlation length to activity in the 'active turbulent' state, in agreement with an independent numerical study [32].

Remaining briefly in this limit, we now return to the walled geometry studied previously in 1D (Chaps. 3, 4) to introduce the phenomenology of confined active matter in 2D. Within this geometry we will first explore, without polymer present, the competition between activity and the distortion free energy in the channel geometry. We previously explored this competition for a 1D system using analytical linear stability calculations (Sec. 3.3), which predicted a non-zero critical activity for finite channel width L_y. In this section we demonstrate that these results still inform the behaviour of 2D systems, and further perform full 2D simulations for the nonlinear dynamics.

Geometry and boundary conditions For the remainder of this chapter we model flows in a channel periodic in the x-direction with length $L_x = 4L_y$, with

solid walls L_y apart (see Fig. 5.2b), and spatially invariant in the z-direction. The boundary conditions at the walls are as specified in the previous two chapters, i.e.,

$$\partial_y Q_{\alpha\beta}(x, y = 0, L_y) = \partial_y C_{\alpha\beta}(x, y = 0, Ly) = v_\alpha(x, y = 0, L_y) = 0,$$

with periodic boundary conditions in the x-direction.

5.3.1 Throughput criterion

At time t, the throughput of the system is defined as

$$\Psi(t) = \frac{1}{L_y} \int_0^{L_y} v_x(t) dy = \langle v_x(t) \rangle_y \ , \tag{5.9}$$

where $\Psi(t)$ is independent of x because of fluid incompressibility. As this quantity generally exhibits significant fluctuations in time, particularly in the chaotic regime, we define our criterion for significant or 'net' throughput as being when the mean of the throughput time-series μ_Ψ exceeds the standard deviation σ_Ψ, i.e.,

$$\frac{\mu_\Psi}{\sigma_\Psi} > 1, \tag{5.10}$$

where

$$\mu_\Psi = \frac{1}{t} \int_0^t \Psi(t') dt', \tag{5.11a}$$

$$\sigma_\Psi = \sqrt{\frac{1}{t} \int_0^t \left(\Psi(t') - \mu_\Psi\right)^2 dt'} \tag{5.11b}$$

converge to constant values, which are in general non-zero, as $t \to \infty$. Note that under this definition, even states that technically do have non-zero mean throughput will fail the criterion if this mean is less than the standard deviation of the time-series.

In practice, we find that the flow direction can periodically switch (e.g., as shown in Fig. 5.5a) which, if naively averaged, would produce zero mean throughput, at least as $t \to \infty$. Therefore instead of using Eq. 5.11 directly, we perform a least-squares fit, fitting the throughput histogram with two Gaussians of width σ_Ψ, centred at $\pm\mu_\Psi$. We have explicitly checked that our results are robust to the number of histogram bins used. Examples of both throughput and non-throughput states are

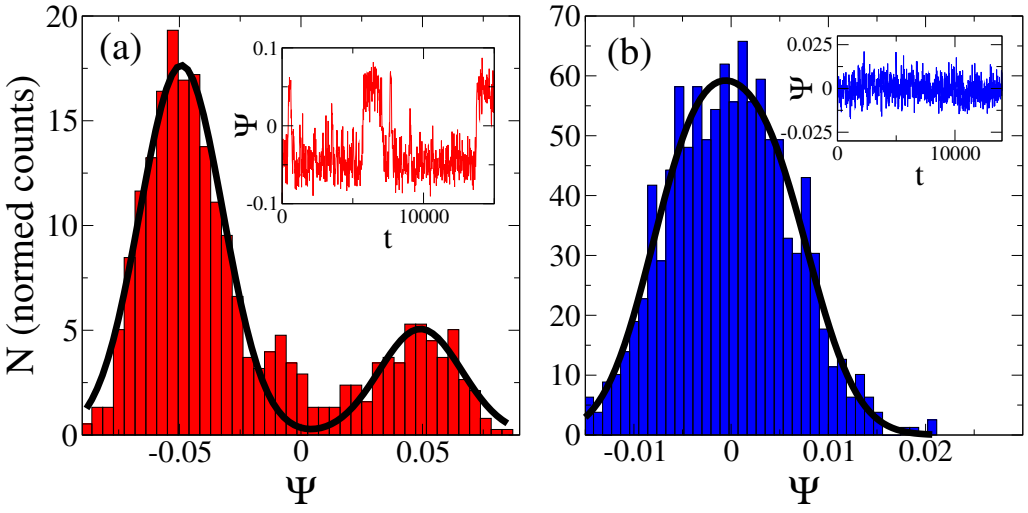

Figure 5.5: Method for determining throughput, Ψ. (a) A state with net throughput, in which the throughput direction switches. The red bins show the normalized histogram of $\Psi(t)$, the solid black line is a fit using two Gaussians at $\pm\mu_\Psi$. In this example, the positive throughput state lasted for shorter simulation time, hence the difference in heights (means and standard deviations are the same). Both peaks will tend to the same height in the limit $t \to \infty$. Here $\zeta = 5$, $\Delta = 3.2 \times 10^{-4}$, $\tau_C = 1$. (b) A state with no net throughput for comparison, with $\zeta = 5$, $\Delta = 10^{-5}$, $\tau_C = 1$. **Insets:** Examples of throughput-time series for each run.

given in Fig. 5.5. We mark states satisfying this criterion in the following phase diagrams with solid symbols, and those failing it with empty symbols. In the next section, Sec. 5.4, we will explore the relationship between the polymer relaxation time and throughput, where we will find that net throughput states become increasingly prevalent as we increase τ_C.

5.3.2 Phase diagram

We begin by reviewing the results of Ref. [87] which, in the limit $\eta_C \to 0$, mapped the phase diagram exploring the competition between activity ζ and the Frank coherence length $\ell_Q = \sqrt{K/G_Q}$. The authors observed that in 1D above a critical activity ζ_c (extracted by examination of 1D flow profiles for decreasing ℓ_Q), the system undergoes a spontaneous flow instability forming shear-banded states. Repeating the phase diagram in 2D, these 1D shear-banded states were always observed to destabilise forming steady (i.e., time-independent), oscillatory, or aperiodic 2D flowing states. Their results were obtained using simulations with an initial condi-

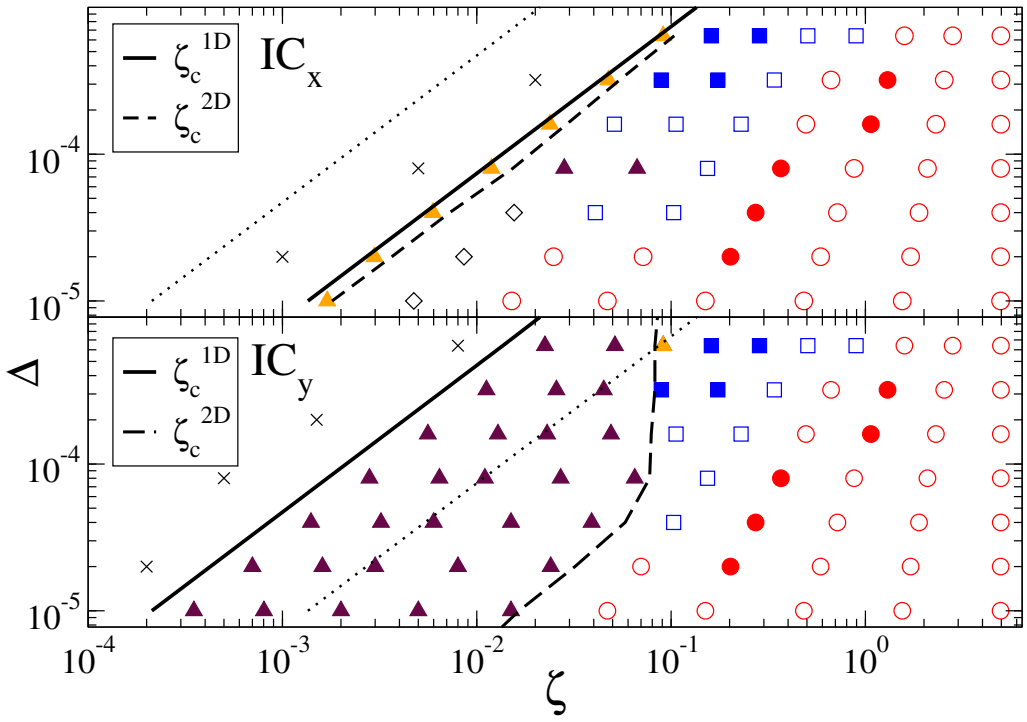

Figure 5.6: Phase diagrams for 2D runs in the no-polymer limit $\eta_C \to 0$. States are: quiescent (black crosses ×), banded (triangles, orange splay ▲ / purple bend ▲), rolls (black diamonds ◇), oscillatory (blue squares □), aperiodic (red circles ◯). Filled symbols denote a net throughput according to Sec. 5.3.1. All states are detailed in Table 5.1. Analytical stability thresholds for the onset on spontaneous flow (ζ_c^{1D}) are plotted using Eq. 3.35, where dotted lines mark ζ_c^{1D} for the other initial condition. The thresholds above which the 1D state is unstable to 2D perturbations (ζ_c^{2D}) are also plotted (these are determined numerically). **Top:** 2D runs with IC$_x$ (as in Ref. [87]). **Bottom:** 2D runs with IC$_y$, demonstrating that the bend flow instability appears at significantly smaller activities than for splay. Note the large region of steady 1D banded states at small activities. **Parameters:** $\xi = 0.7$, $\eta = 0.567$

tion (IC) designed to invoke the bend instability where the director is orientated in the x-direction, i.e., $\hat{\mathbf{n}} = (1, 0, 0)$. We will refer to this as IC$_x$.

First we verify our 2D code by reproducing these results with IC$_x$, then report new results exploring the onset of the splay instability using a second IC where the director is aligned in the y-direction, $\hat{\mathbf{n}} = (0, 1, 0)$, which we label IC$_y$. As one might expect from our linear stability analysis (Sec. 3.3.3.1), we find that the phase diagram is dependent on initial condition at small activities.

5.3.2.1 Initial condition: $\hat{\mathbf{n}} = (1, 0, 0)$

In Fig. 5.6a we plot the phase diagram for the same parameters as in Ref. [87], but for a larger range of ζ and $\Delta = \ell_Q^2/\tau_Q$. As in that study, for small Δ and ζ, we observe steady roll states with system-size dependent structure (Table 5.1C). At intermediate values of ζ, these rolls destabilise to form streaky, defect-driven states with aperiodic and possibly chaotic[3] dynamics. However, remnants of the system size still remain with transient structures appearing on a lengthscale $\mathcal{O}(L_y)$. Finally for very large activities, the resulting aperiodic state is defect-rich and contains no obvious influence of the system size (Table 5.1G). This is the same regime of fully developed 'active turbulence' required for our study of correlation lengths in the previous section. These states, particularly in the chaotic regime, typically do not posses a net throughput.

For larger values of Δ, we observe a range of oscillatory states at intermediate activities, again consistent with Ref. [87]. These include a limit-cycle like state that switches between banded and roll states (Table 5.1D), and a state in which defect pairs travel along the channel in a sinusoidal fashion (Table 5.1E). As the activity is increased, these oscillatory states gain additional frequency components when plotting a given scalar observable (e.g., throughput) against time. When there is no longer any discernible periodicity, we term the state aperiodic.

We also observe a narrow region where steady 1D banded states remain stable in 2D (Table 5.1B). We label the upper bound of this region, which must be found numerically[4], as ζ_c^{2D}. These states, which were not seen in Ref. [87], were presumably only captured in our study due to the higher resolution of sampling in the phase diagram. A comprehensive list of all the states observed is given in Table 5.1, which qualitatively describes each state and provides example snapshots of the director field.

[3]As previously discussed in Sec. 4.4.3, we (and the authors of Ref. [87]) do not make the distinction between truly chaotic and e.g., quasiperiodic states. We use the terms aperiodic and chaotic interchangeably for the remainder of this chapter.

[4]We find the exact position of the boundary using a bisection method, where we start with points either side of the boundary and iterate, testing whether 2D perturbations grow or decay.

Also plotted on our phase diagram in Fig. 5.6 is our analytical 1D critical activity ζ_c^{1D} (which is initial condition dependent) as derived in Sec. 3.3.2. This shows quantitative agreement with the regions of the phase diagram exhibiting spontaneous flowing states (i.e., any state that isn't quiescent). This also quantitatively agrees with the phase boundary plotted in Ref. [87].

5.3.2.2 Initial condition: $\mathbf{n} = (0, 1, 0)$

We now repeat the phase diagram, this time with the director initially orientated in the y-direction. Our 1D linear stability analysis predicted that the bend instability (arising from IC_y) should first appear at smaller ζ than the splay (arising from IC_x), see Eq. 3.36. Fig. 5.6b confirms this numerically, revealing that the shear-banded state (purple triangles) first appears at activities an order of magnitude smaller than for splay.

Interestingly, these 1D states remain stable in 2D for a much larger region of the phase space, up to the (numerically measured) critical activity ζ_c^{2D}. Therefore at small activities, depending on the initial condition, significantly different states can develop, e.g., rolls for IC_x or shear-banded states for IC_y. Then, for activities above ζ_c^{2D}, the phase diagram is indistinguishable from that resulting from IC_x.

5.3.2.3 Alternative boundary conditions

Both our analytical and numerical results reveal the importance of initial condition on the resulting phase diagram. However initial conditions are difficult to control experimentally, particularly in the biological systems of interest here. Experimentally, it may be more feasible to impose a fixed director configuration at the walls (e.g., as in Ref. [117]), where $\hat{\mathbf{n}}$ is set perpendicular (parallel) to the walls to provoke initial conditions that predispose the system to the bend (splay) instability.

5.3.3 Summary: phase diagrams

In this section, we have introduced the phenomenology of active matter in the limit of no polymer ($\eta_C \to 0$), comprehensively classifying states in the (ζ, Δ) phase space according to their temporal and spatial periodicities, reproducing earlier work [87].

ID	symbol	net Ψ	description	snapshot of $(n_x n_y)^2$
A	×	no	quiescent state (i.e., no flow), occurs if below critical activity	
B	▲ / ▲	yes	the 1D splay / bend banded states can persist in 2D	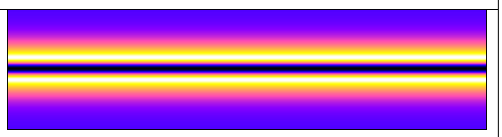
C	◇	no	stationary rolls	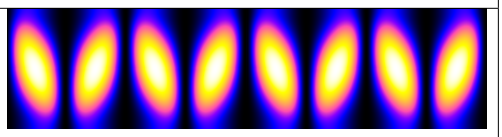
D	■	yes	oscillates between **B** (banded) and **C** (rolls)	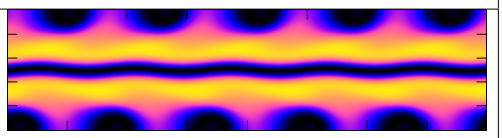
E	□	no	oscillatory states where throughput is precisely zero	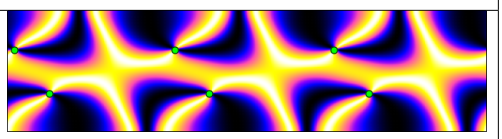
F	■	yes	some oscillatory states can also result in net throughput	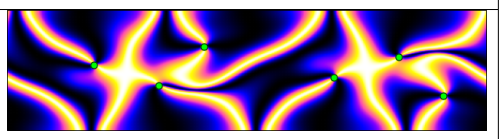
G	○	no	chaotic states with too much energy ($\zeta \to \infty$) appear to disrupt any directed motion	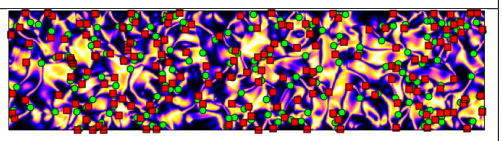
H	●	yes	chaotic states with intermediate ζ can sustain net throughput indefinitely (rare without polymer)	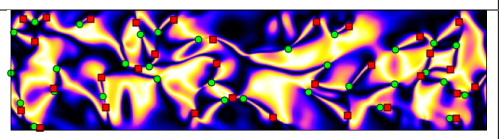

Table 5.1: Description of the rich array of 2D states found in the channel geometry, all of which can be found with or without polymer. Tabulated are: (a) symbols used in phase diagrams, (b) whether the state has a net throughput Ψ (as defined in Sec. 5.3.1), (c) a qualitative description of the state, (d) a snapshot of $(n_x, n_y)^2$ where $\hat{\mathbf{n}}$ is the nematic director (colour scale is 0 (black) to 0.25 (white)). States are roughly ordered by increasing activity, see Fig. 5.6 for their positions in the phase diagram.

At large activities, only a small number of the resulting chaotic states develop a net flow of material along the channel, with the direction spontaneously chosen. We have defined a criterion based on the mean and standard deviation of the throughput to categorise such states.

We then provided new results for a second initial condition where the nematic director is aligned in the y-direction, generalising the study in Ref. [87]. Our 1D analytics predicted this configuration to be susceptible to bend instabilities at significantly smaller activities then when the director is orientated in the x-direction. This prediction is quantitatively confirmed using 2D numerics, highlighting the importance of initial condition. Experimentally, we expect that surface treatment could be used to influence the initial condition (via the boundary conditions). We now study how the (ζ, Δ) phase diagram described above changes as polymer with increasingly long relaxation times is added, finding that the number of states with net throughput dramatically increases.

5.4 Viscoelastic active matter

As discussed in the previous section, even without polymer we find a wide array of states in the channel geometry which, depending on the strength of the activity ζ and the diffusivity Δ, demonstrate either system-size dependent structures with rolls (reminiscent of Taylor vortices) or defect-heavy system-size independent chaotic states.

In this section we study the effect of adding polymer, which is dramatic. Particularly in the chaotic regime at large activities we show that, as polymer relaxation time τ_C is increased, the parameter range where states are found with a macroscopic broken symmetry (specifically the net throughput in the periodic direction) is greatly extended. This result may have particular biological significance in the context of cytoplasmic streaming, where it is theorised that cytoskeletal materials such as actomyosin play a role in generating coherent flows for the transport of nutrients and organelles [1, 11].

We consider the case where the polymer relaxation time τ_C is at most two orders

of magnitude larger than the nematic relaxation time τ_Q. This means it remains feasible to resolve steady state dynamics on polymeric timescales in our numerics. We later consider the elastomeric limit $\tau_C \to \infty$, for which it is very difficult to obtain true steady-states numerically; there we focus on the transient behaviour instead. For the remainder of this chapter we set slip parameter $a = 1$, for which the polymeric sector becomes equivalent to an Oldroyd-B fluid. This choice means only affine deformation is possible, which some theoretical studies suggest may be a reasonable assumption for the dense cross-linked filaments found in the cytoskeleton [120, 121]. In the following sections we also assume that any coupling between LC and polymer order parameters is indirect, i.e., mediated via the fluid velocity field. However in the final section of this chapter we briefly examine a more direct coupling at the level of the free energy.

5.4.1 Phase diagram

In the previous section we showed that of the 2D flow states observed, only a small fraction of these produce a net throughput when in the defect-heavy chaotic regime typically observed experimentally. We now examine how this changes when polymer is added with a relaxation time comparable to or greater than that of the LC.

In Fig. 5.7 we display phase diagrams without and with polymer side-by-side, where $\eta_C = 0$ and $\eta_C = 1$ respectively. We find that our general picture of the (ζ, Δ) phase diagram obtained in the limit $\eta_C \to 0$ still holds. Ordered states with structure spanning the system size appear at low activity (e.g., banded or oscillatory states), whereas disordered aperiodic states independent of the system size appear at higher activities. Phase boundaries are also qualitatively similar in both cases. However, particularly in the aperiodic regime seen at large ζ, we see the dramatic effect of polymer: the majority of states now exhibit a net throughput (i.e., the phase diagram predominantly consists of filled symbols).

Having demonstrated that even polymer of modest relaxation time results in a significant qualitative change to the phase diagram, we now provide an argument for this phenomenon by drawing an analogy with drag reduction in the context of inertial turbulence, and study this effect quantitatively.

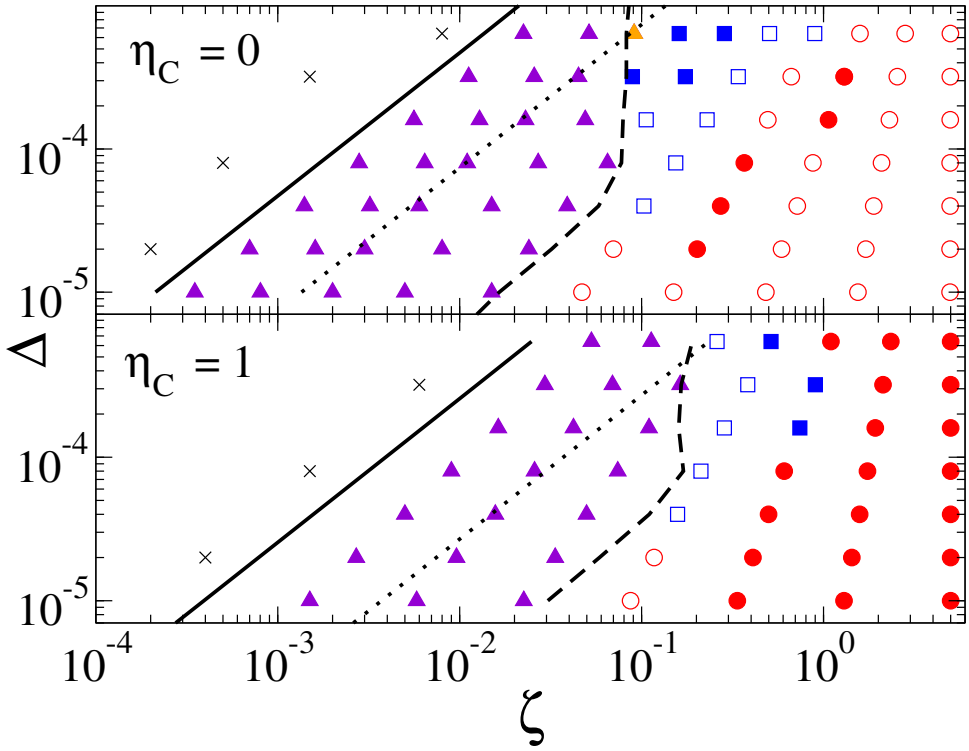

Figure 5.7: Phase diagrams for 2D runs with IC_y, both with and without polymer. These demonstrate the significant increase in the number of states with net throughput in the presence of polymer (filled symbols). Lines show (solid) the 1D instability (bending mode) of the specified initial condition; (dotted) that of the splay mode for IC_x, and (dashed) the observed crossover line ζ_c^{2D} beyond which 1D states always destabilise. **Top:** Data reproduced from Fig. 5.6 for IC_y where $\eta_C = 0$. **Bottom:** Simulations with polymer of relaxation time $\tau_C = 4\tau_Q$. Notice that the majority of chaotic states now have a net throughput. **Parameters:** $\eta_C = 1$, $a = 1$.

5.4.2 Drag reduction

Recall that, for large Reynolds numbers, the flow field of a passive Newtonian fluid in a pressure-driven pipe flow becomes turbulent, leading to noticeably reduced throughputs [179] for a given pressure drop. When a high molecular weight polymer is added, a marked increase in throughput is observed experimentally, resulting in a 'drag reduction' effect [175].

While in our model (which assumes $\mathrm{Re} = 0$) the turbulence is 'active' rather than 'inertial' in nature, we observe an analogous effect. By adding polymer to a fluid showing activity-driven turbulence, we argue that one could effectively 'reduce drag' by enhancing throughput at fixed active stress. We observe that the polymer

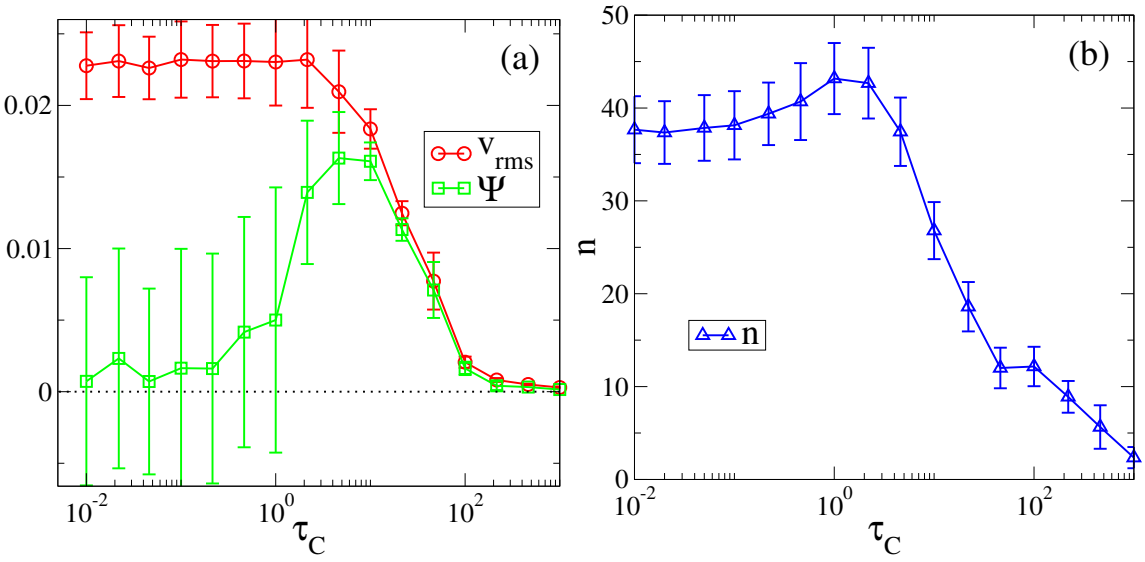

Figure 5.8: Demonstration of increased throughput at intermediate τ_C. We pick a point deep in the chaotic region of the phase diagram Fig. 5.7 (top) and perform 2D runs for a number of τ_C. We plot the time-averaged value of each quantity in steady-state, where vertical bars denote the standard deviation. **Left:** The steady state rms velocity, $v_{\rm rms} = \sqrt{\langle |\mathbf{v}|^2 \rangle_{\mathbf{x}}}$ (red line), is a monotonically decreasing function of τ_C, but the throughput Ψ (green line) has a maximum at intermediate τ_C. States where green error bars pass through zero (dotted line) fail our net throughput criterion (see Apx. 5.3.1). **Right:** The time averaged defect density n is large when the polymer relaxation is rapid but decreases as τ_C is increased. **Parameters:** $\zeta = 3.2$, $\Delta = 2 \times 10^{-5}$, $\eta_C = 1$.

calms the short scale structure of the active flow, decreasing the nematic defect density and increasing the flow correlation length towards the system size, thereby favouring restoration of a more organized flow state.

We now explore this idea quantitatively by examining this relationship between throughput and defect density. We do so by selecting parameters representative of fully developed active turbulence, and sweep τ_C at fixed $\eta_C = 1$. In Fig. 5.8a, we first notice that the root mean square velocity, defined as $v_{\rm rms} = \sqrt{\langle |\mathbf{v}|^2 \rangle_{\mathbf{x}}}$, decreases monotonically as we increase the polymer relaxation time. For small τ_C the polymer simply contributes an additional solvent viscosity and the rms velocity remains constant. However as $\tau_C > \tau_Q$, the (fixed) active stress has to work against an increasingly elastic fluid as the large polymeric stresses cannot relax fast enough. As τ_C becomes very large the polymer effectively arrests the flow (at least in steady state, see Sec. 5.5.3 for examples of transient flow) and $v_{\rm rms}$ drops off towards zero.

The dependence of throughput Ψ on τ_C is not monotonic however. At small τ_C, as was shown in the previous section without polymer, the chaotic state generally has no net throughput. Our throughput criterion (that the bimodally fitted mean of Ψ is larger than the standard deviation) is satisfied when error bars in Fig. 5.8 do not pass through zero. As τ_C increases, not only does the mean throughput increase but fluctuations about it decrease suggesting a more coherent flow state. Finally as τ_C becomes very large the flow is arrested and the magnitude of the throughput decreases (as discussed above).

To quantitatively demonstrate the greater coherence of states once polymer dynamics become relevant, we also examine the defect density n shown in Fig. 5.8b. (Alternatively we could measure correlation lengths as in Sec. 5.2, though in practice we find that the influence of walls makes it difficult to obtain reliable statistics). This demonstrates that v_{rms} is reasonably correlated with the defect density, consistent with our findings without polymer (Sec. 5.2). Noticeably, the peak throughput coincides with the point at which the defect density starts to decay.

5.4.2.1 Summary: Viscoelastic active matter

By considering the 2D dynamics of active viscoelastic matter when the polymer and nematic relaxation times differ by at most 2 orders of magnitude, we can obtain reliable steady state statistics. (This becomes numerically unfeasible for much larger τ_C.) We compared phase diagrams in the (ζ, Δ) plane with and without polymer of relaxation time $\tau_C = 4\tau_Q$. This demonstrated that while the phase boundaries separating static, oscillatory, and aperiodic states remain largely the same, when polymer is added the majority of these states now break a macroscopic symmetry and develop net flow in the $\pm x$ direction.

This change is most dramatic in the region of the phase diagram that is chaotic (without polymer) where we have shown that adding polymer of increasingly large relaxation time leads to a calming drag reduction effect where the defect density n is reduced, favouring a more coherent flowing state with net throughput. Once τ_C becomes large, however, flows become increasingly arrested by polymeric stresses and the typical velocity scale of these coherent states reduces. Competition be-

tween these mechanisms leads to a peak throughput when τ_C is roughly an order of magnitude greater than τ_Q.

By restricting ourselves to comparably short polymer relaxation times, we were able to reliably resolve steady state polymeric dynamics using our numerics. We now consider the elastomeric limit where $\tau_C \gg \tau_Q$, for which this becomes increasingly difficult. However we will show that even the transient dynamics can be very rich, illuminating the origin of an instability where the polymer undergoes rapid growth. The long time behaviour in this limit can also be speculated on by examining the resulting power law behaviour.

5.5 Elastomeric active matter

As just discussed, even polymer of modest relaxation time has a significant effect on the phase space of confined active nematics. We have studied in detail the dramatic drag reduction effect that promotes throughput in chaotic active states. However new and unexpected physics can also arise when this polymeric time scale becomes effectively infinite. In the passive limit, our model could describe e.g., a nematic elastomer [124]. Here we consider the active counterpart as could be found in an active nematic (such as an actomyosin cell extract) within a background of lightly cross-linked elastomer. We now address this limit in two ways: first by increasing τ_C (holding $\eta_C = 1$), then with τ_C infinite at small finite G_C (giving infinite η_C).

A priori, one might expect the flow instabilities reported in the previous section for modest relaxation times to be completely absent in what is, after all, a solid material. However our 1D stability analysis in Sec. 3.3 predicts that such materials are at least transiently unstable. In this section we demonstrate using 2D numerics that this result is generic: at large but finite activity, complex LC textures can result from this instability which then slowly coarsen as a power law in time.

We first investigate in detail the transient dynamics of this instability, demonstrating that the rapid extensional deformation observed in the polymer for large relaxation times can be understood by analogy with extensional instabilities in the passive limit. This analysis is then applied to help explain a novel oscillatory state

at large but finite τ_C. Biologically, shape oscillations in developing cells are believed to be driven by actomyosin networks [180], which have been described theoretically using an elastic model [181].

5.5.1 Startup kinetics

In 1D, we showed both analytically and numerically that above the critical activity ζ_c, perturbations in $\mathbf{Q}$ and $\mathbf{C}$ about the homogeneous state undergo exponential growth in time until saturating (once the dynamics become non-linear). In 2D we will show that when polymer relaxation is rapid, this activity driven spontaneous flow instability is mostly unaffected and after the initial exponential growth of the linear instability, a flowing steady state is quickly reached. However for polymer relaxation times comparable or larger than the LC timescale τ_Q, we observe further rapid, nonlinear extensional growth. As this effect also occurs at short times, we can study the transient dynamics for particularly large values of τ_C, for which steady-state simulations (which resolve the dynamics on a timescale τ_C) are unfeasible.

We begin by imposing the constraint $\eta_C = 1$ to ensure our results aren't affected by viscosity changes. This means the elastic modulus G_C is small for large τ_C; a polymer stress of $\mathcal{O}(G_Q \equiv 1)$ when τ_C is large then implies large strains. With initial condition $\mathbf{C} = \mathbf{I}$, the polymer stress $\mathbf{\Pi}_\mathbf{C} = G_C(\mathbf{C} - \mathbf{I})$ is initially negligible and the system is effectively dominated by the active nematic dynamics. For large activities, a turbulent flow state is quickly generated including regions with significant extension rates. As the polymer has no mechanism by which to relax its stress, this results in considerable deformation, and particularly for $\tau_C \gtrsim 2$ we find that very large polymer strains accumulate in a short time.

For our choice of $a = 1$, deformation is purely affine and the polymeric model reduces to Oldroyd-B. Recall that for this model, the polymer will undergo exponential extensional growth while the extension rate (made dimensionless by τ_C) exceeds $1/2$, and will never reach a steady-state (see Sec. 2.2.3.2). As the flow fields generated by the active nematic in 2D are considerably more complex than pure extension, it is instructive to consider a spatially averaged measure of extensional flow rates. We define an extensional Deborah number De as the product of the frame invariant

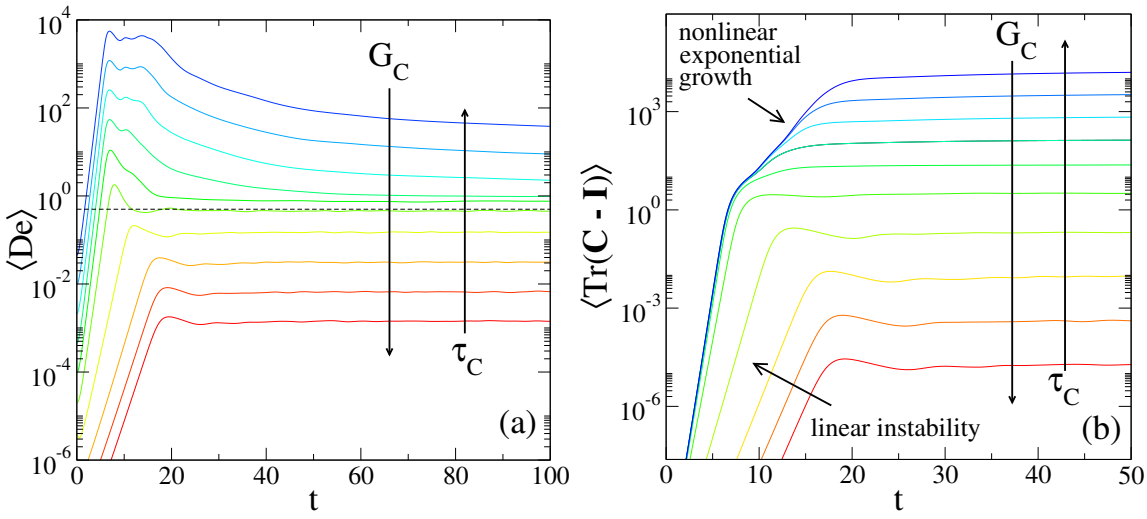

Figure 5.9: Results from 2D runs examining the short time dynamics of a point in the chaotic region of the phase diagram. We vary τ_C from 10^{-2} (red) $\rightarrow$ 10^{4} (blue) with logarithmic spacing, keeping η_C constant by decreasing G_C. (a) Time series of the mean Deborah number $\mathrm{De} = \tau_C \sqrt{1/2\,(\mathbf{D} : \mathbf{D})}$ for increasing τ_C. Also marked is the threshold $\mathrm{De}_{\mathrm{crit}} = 1/2$ above which we might expect non-linear exponential growth (dashed line). (b) Spatial average of $\mathrm{Tr}[\mathbf{C} - \mathbf{I}]$ quantifying the mean polymer deformation. When $\langle \mathrm{De} \rangle > \mathrm{De}_c$ (see left), we observe non-linear, exponential loading of the polymer in very short times. **Parameters:** $\zeta = 2.2$, $\Delta = 4 \times 10^{-5}$, $\eta_C = 1$.

extension rate and the polymer relaxation time τ_C

$$\mathrm{De} = \tau_C \sqrt{1/2\,(\mathbf{D} : \mathbf{D})}, \tag{5.12}$$

where $\mathbf{D} = 1/2\left(\nabla \mathbf{v} + \nabla \mathbf{v}^T\right)$. By analogy with the pure extensional case, we might then expect strains to grow exponentially when $\mathrm{De} > \mathrm{De}_c \approx 1/2$. Note that the activity driven flow field is considerably more complex than for pure extensional flow and the comparison is only approximate.

In Fig. 5.9a we plot the spatial average of the Deborah number, $\langle \mathrm{De} \rangle$, against time for a range of τ_C. For small τ_C (warm colours), while $\langle \mathrm{De} \rangle$ initially grows with the linear instability, it remains much smaller than De_c. As such the corresponding spatial average of the polymer deformation $\langle \mathrm{Tr}[\mathbf{C} - \mathbf{I}] \rangle$, Fig. 5.9b, exhibits only the initial linear instability at small τ_C.

However for large enough τ_C (cold colours), we find De exceeds $\mathrm{De}_{\mathrm{crit}} \approx 1/2$. The effect on the polymer is dramatic: following the initial growth of the linear instability, we observe a second period of exponential extensional growth which generates huge strains in very short times, see Fig. 5.9b. This process is only halted once the

polymer stress becomes comparable with the LC, active, and solvent stresses. Note that physically this growth would ultimately be cut off by finite extensibility or chain rupture, neither of which are in the polymer model considered here. However we expect the general features of this mechanism, whereby activity-driven extensional flows subject the polymer to extensional deformation, to hold regardless of model specifics.

We have shown here that the onset of non-linear exponential growth in the polymer observed for large τ_C correlates strongly with when the average Deborah number exceeds $\mathrm{De}_c \approx 1/2$. This is consistent with polymer-only studies in pure extensional flows [64], and indeed our own studies in porous media (see Chap. 6). We now apply this insight to explain the mechanism behind a novel state observed only with polymer, where a limit cycle transitioning between banded and oscillatory states develops.

5.5.2 Limit cycle

So far we have explored a large volume of parameter space, with the activity ζ, diffusivity Δ and polymer relaxation time τ_C all spanning several decades. This broad overview has, for example, provided insight into the role of polymer in promoting net throughput states. However, we have not yet reported in detail the dynamics of any specific states within the phase diagram. Therefore we now provide an example of a novel state which explicitly demonstrates the direct role of polymer viscoelasticity in the dynamics of our coupled model.

By choosing a large polymer relaxation time $\tau_C = 1000$, we can clearly separate polymeric and active timescales, allowing us to identify their respective roles in the dynamics. We observe that at moderate activities, independent of initial condition (IC_x or IC_y), for the parameters chosen the system generally settles on a limit cycle transitioning between quasi-1D splay and bend banded states via an intermediary 2D state.

This cycle can be clearly visualised by examining the power spectrum $P(k_x, t)$. For a given wavevector k_x, this integrates the k_x^{th} Fourier component of both dimensionless order parameters over y. (For a full definition see Apx. 5.9.) A purely 1D

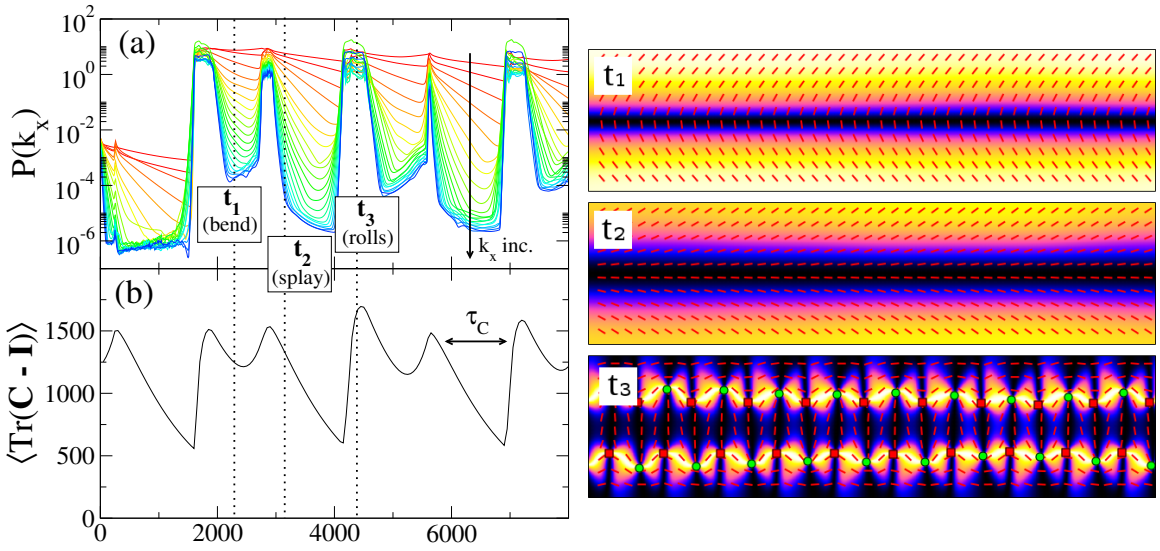

Figure 5.10: Example of a limit-cycle state where the system continuously oscillates between bend and splay shear-banded states via an intermediate roll state. (a) Plotted is the power spectrum $P(k_x)$ (as defined in Apx. 5.9) for the first 20 Fourier modes k_x ($k_x = 1$ (red) $\rightarrow$ $k_x = 20$ (blue)). The transitions between states are 2D in nature, as shown by the periodic spikes in $P(k_x)$. (b) Plot of mean polymer deformation as measured by $\langle \mathrm{Tr}[\mathbf{C}-\mathbf{I}] \rangle$. **Right:** Snapshots for the times marked in (a)/(b) of $(n_x n_y)^2$ (colourmap), director $\hat{\mathbf{n}}$ (red lines), and defects (symbols). **Parameters:** $\zeta = 1.24$, $\Delta = 1.6 \times 10^{-4}$, $\tau_c = 1000$, $\eta_C = 1$.

state would therefore measure $P(k_x, t) = 0$ for $k_x > 0$. This allows us to quantitatively describe the degree of inhomogeneity in the x direction, which we plot in Fig. 5.10a.

Allowing time first for the system to reach a steady-state (i.e., $t < 2000$), the initial state that forms (see $t_1 = 2300$) is a quasi-1D shear-banded state, with flow resulting from the bend deformation. As $P(k_x, t)$ is non-zero, the state is not truly 1D. However variations of the order parameters in x are negligible and cannot easily be discerned by eye.

At large activities in 1D the bend state destabilises to form the splay banded state [182]. A similar mechanism also occurs here in 2D, where the director in the central region rotates by $\pi/2$ to form a splay banded state (see $t_2 = 3620$). This process initially happens at a single x position, then the instability propagates along the interface until the whole system is splayed. This symmetry breaking results in a brief spike in $P(k_x, t)$ (e.g., at $t = 2800$).

This splay state then apparently remains stable for a time $\sim \tau_C$, before devel-

oping a roll-like instability (see $t_3 = 4400$) characterised by alternative pairs of $\pm 1/2$ defects. This is captured by the rapid growth in $P(k_x, t)$ which displays significant weight at non-zero wavevectors, even for large k_x, indicating short scale structure. This structure then relaxes, with the highest modes relaxing quickest, and the system returns to the initial bend state where the cycle repeats.

The effective dimensionality of the state directly impacts the polymeric dynamics, which we characterise using $\langle \mathrm{Tr}[\mathbf{C} - \mathbf{I}] \rangle$ as before (Fig. 5.10b). Due to incompressibility, extensional flows can only exist in two or more dimensions, and therefore are not observed in the quasi-1D shear-banded states. As such the polymer trace in these states simply relaxes on a timescale τ_C. However the 2D roll state permits, and indeed contains, regions of extensional flow. Consistent with the mechanism described in the previous section, τ_C can exceed the timescale of these flows resulting in the same non-linear exponential growth of $\mathbf{C}$, resetting the cycle.

We have analysed, in detail, a state with visible influence from polymeric coupling. Reminiscent of the 1D instability of the bend state at high activity [182], we observe a quasi-1D bend $\rightarrow$ splay transition. Contrary to the 1D case however, this splay state is then itself unstable to 2D perturbations forming a transient roll-like state. This produces extensional flows which, consistent with our earlier results, rapidly generates significant polymeric deformation. Finally the 2D structure relaxes and the cycle repeats.

So far we have approached the elastomeric limit at fixed polymer viscosity (with finite τ_C). In the final part of this section, we demonstrate the generality of our results by setting $\tau_C \rightarrow \infty$ at fixed elastic modulus G_C.

5.5.3 Spontaneous flow in a solid

Earlier work [80,81,108] and our own linear stability results in the polymer-free limit (Sec. 3.3) showed that the active spontaneous flow instability in a finite system can always be suppressed by a large enough viscosity. By approaching the elastomeric limit $\tau_C \rightarrow \infty$ at fixed $\eta_C = 1$ in the preceding sections, we have avoided the implications of such an effect. However, the vanishingly small elastic modulus required to maintain this constraint may be unphysical.

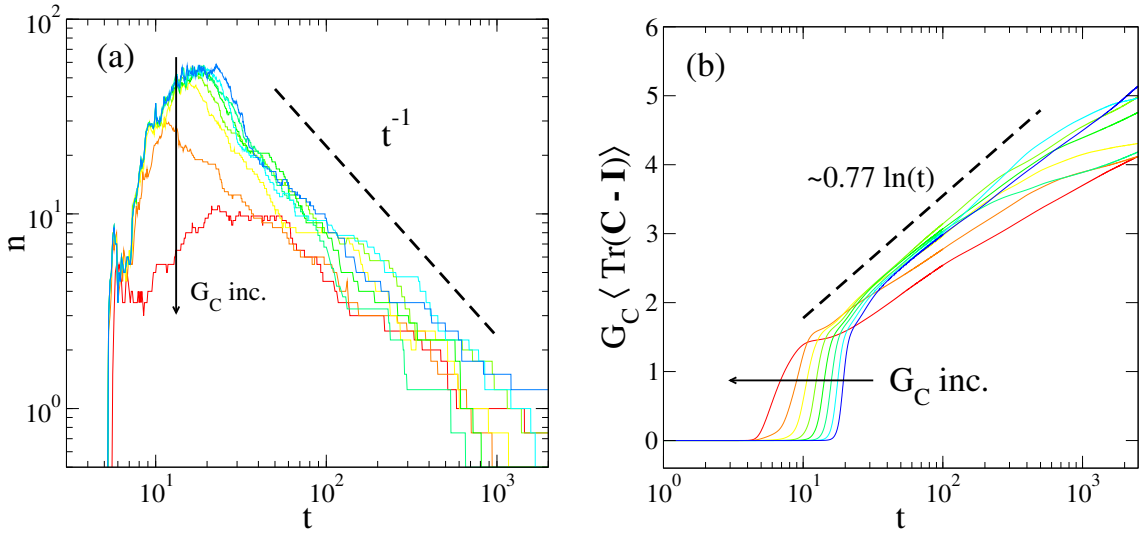

Figure 5.11: Results from 2D runs with $\tau_C \to \infty$. We vary G_C from 10^{-8} (blue) $\to 10^{-1}$ (red) with logarithmic spacing. (a) Areal defect density n against time. Steps arise because n is discrete. (b) Scalar measure of polymer stress $G_C\langle \mathrm{Tr}[\mathbf{C}-\mathbf{I}]\rangle$. **Parameters:** $\zeta = 3.2$, $\Delta = 8\times10^{-5}$, $\tau_C \to \infty$.

Therefore we now demonstrate the generality of our spontaneous flow results by additionally considering the limit $\tau_C \to \infty$ at fixed G_C. Without polymer, an infinite viscosity might imply that spontaneous flow is always suppressed. However our 1D results with polymer showed both analytically and numerically that such an instability is possible due to the existence of an elastomeric instability mode that implies that ζ_c remains finite as $\tau_C \to \infty$: we now show that this result also holds in 2D. Numerically we implement this limit simply by disabling the polymer relaxation term in Sec. 3.2.2 altogether, i.e., $\frac{-1}{\tau_C}(\mathbf{C}-\mathbf{I}) \to 0$.

In Fig. 5.11 we plot the defect density of the LC and the mean extensional stress of the polymer against time, for a range of polymer elastic moduli $G_C = 10^{-8} \to 10^{-1}$. As $G_C \ll G_Q$, the sample can strongly deform before its small elastic modulus has appreciable influence[5]. This effect can be seen in the rapid growth of the defect density n at early times, Fig. 5.11a, indicating the formation of complex LC textures. As we showed previously in Sec. 5.5.1, regions of extensional flow rapidly stretch the polymer resulting in exponential growth at early times. (See Fig. 5.9b.)

However once the polymer stress $\sim \mathcal{O}(G_Q)$, the turbulent state arrests into a complex but almost frozen defect pattern. Thereafter the defect density decays

[5]A similar phenomenon is observed in the context of polymeric glasses [183].

slowly, roughly as t^{-1}, which is the classical result for passive nematic coarsening [169]. This process is slow enough that the strain pattern created by the arrested active turbulence might easily be mistaken for a final steady state. Particularly as no polymer relaxation can occur, the polymer trace continues to grow at long times. However the process is slow, occurring only logarithmically in time. Our arrest mechanism, where strong polymer stretching in extensional flow regions creates strong stresses in opposition, may relate closely to the drag reduction effects reported earlier.

5.5.3.1 Summary: elastomeric active matter

In this section we examined the limit in which the polymeric relaxation time τ_C is effectively infinite, corresponding to an active nematic elastomer. This might describe, for example, crosslinked actin networks found in the cytoskeleton [90].

We first approached this limit by holding viscosity η_C fixed. By studying the startup behaviour, we observed that at early times the polymer stress is negligible and the dynamics is mainly prescribed by the active nematic. The extensional flows generated by the resulting turbulent state can induce large polymeric strains which grow exponentially in time. Drawing analogy with the known extensional catastrophe in the Oldroyd-B model, we produced a criterion for the appearance of this rapid polymer growth based on a Deborah number describing the ratio of extensional and relaxational timescales.

Insight into this extensionally driven polymer deformation then helped explain a novel state that cycles between bend (quasi-1D) $\rightarrow$ splay (quasi-1D) $\rightarrow$ roll-like (2D) states, on a timescale set by τ_C ($\gg \tau_Q$). The 2D state generates extensional flows that rapidly deform the polymer, resetting the cycle. Finally we took a distinct elastomeric limit, instead fixing G_C with τ_C infinite (implying an infinite polymer viscosity). Even then we observed a transient spontaneous flow instability (consistent with our 1D work) in which complex LC textures initially form before coarsening slowly in time once polymer stresses become appreciable.

In our study so far, the interaction between polymer and active nematic is indirect, mediated only via the background velocity $\mathbf{v}$. For the remainder of this chapter

we briefly consider the limit in which these sectors become antagonistically coupled at the level of the free energy. This produces an array of novel states which we now explore.

5.6 Explicit coupling

As we have demonstrated in the preceding sections, even when polymer and active nematic are only coupled kinematically (i.e., through the velocity field) the effects are dramatic. In particular, polymer can have a calming effect, suppressing defect creation and promoting coherent flow states with a net throughput (Sec. 5.4.2).

Returning to the situation where τ_C remains finite and comparable to τ_Q, we conclude this chapter by considering a more direct coupling between $\mathbf{Q}$ and $\mathbf{C}$ as prescribed by the free energy,

$$f_{QC} = \kappa \mathrm{Tr}[\mathbf{Q}^2]\,(\mathrm{Tr}[\mathbf{C}-\mathbf{I}]) + 2\chi \mathrm{Tr}[\mathbf{CQ}].$$

Here the first term controls how the polymer pressure shifts the isotropic-nematic transition; for simplicity we suppress this effect by setting $\kappa = 0$. The second term depends on the relative orientations of $\mathbf{Q}$ and $\mathbf{C}$. For $\chi < 0$ it is energetically favourable for $\mathbf{Q}$ and $\mathbf{C}$ to align. For example, experiments (in the passive limit) suggest that single semi-flexible polymers can couple to the nematic director field in this fashion [184]. However this configuration generally arises even for $\chi = 0$ due to the reversible coupling with the velocity field, and the effect of $\chi < 0$ on the dynamics is minor.

Therefore in this section we only consider the more antagonistic coupling $\chi > 0$, where $\mathbf{Q}$ and $\mathbf{C}$ now prefer to be anti-parallel. Given the dimensionality of parameter space even without explicit coupling, we do not perform an exhaustive parameter sweep and instead present a selection of some of the more intriguing and novel states observed. We find that for large values of χ our simulations fail to obtain a finite, steady-state solution for $\mathbf{Q}$ and $\mathbf{C}$, even in 0D. Therefore in our numerics we restrict χ to values $|\chi| < \min(G_Q, G_C)$ for which finite solutions can be found.

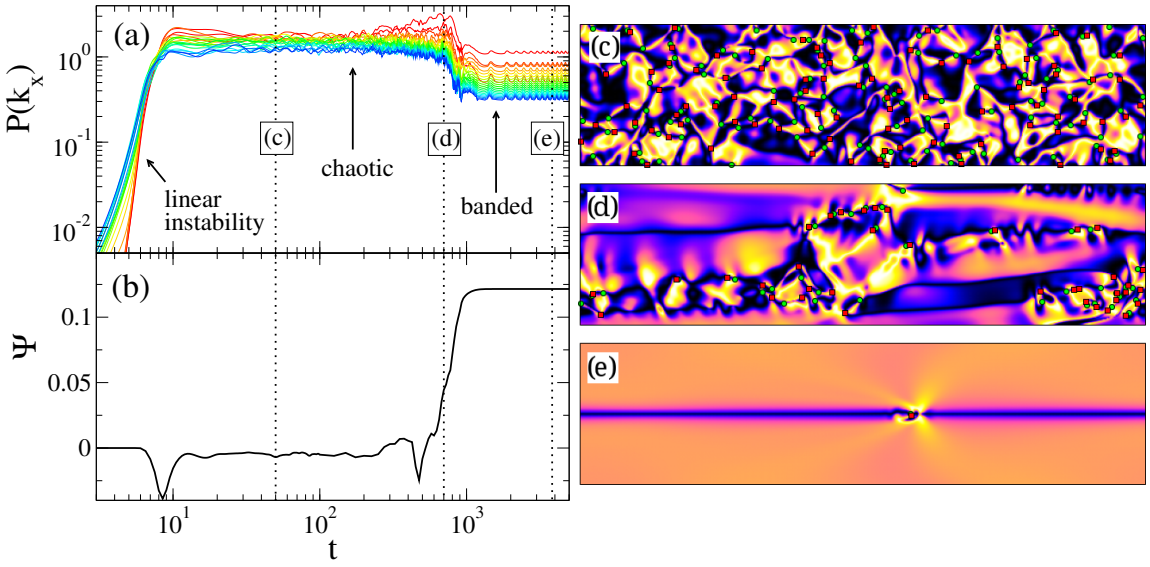

Figure 5.12: Example where an initially chaotic state organises into a coherent shear-banded state with defects (advect with the flow) embedded in the interface. **Left:** Time evolution of the power spectrum $P(k_x, t)$, averaged over y (for $k_x = 1$, red $\rightarrow$ $k_x = 20$, blue). The initial chaotic state has considerable Fourier amplitudes, but these are attenuated once the polymer coupling becomes significant. **Right:** Snapshots of $(n_x n_y)^2$ for the states marked left at times (c) $t = 50$, (d) $t = 700$ and (e) $t = 3800$. **Parameters:** $\zeta = 3.2$, $\Delta = 4 \times 10^{-5}$, $\tau_C = 10$, $\chi = 0.002$.

5.6.1 Example states

5.6.1.1 Shear Bands with interfacial defects

The first example demonstrates an intriguing, polymer-driven disorder-order transition. Choosing parameters characteristic of the chaotic state (when $\chi = 0$), we initially find the defect-rich disordered state observed without polymer (Fig. 5.12c). However as the simulation progresses, ordered regions of nearly uniform director $\hat{\mathbf{n}}$ spread in from the walls towards the centre of the channel, forming an increasingly shear-banded like state (Fig. 5.12d). Eventually, the only remaining evidence of the earlier chaotic state are pairs of defects embedded in the interface (Fig. 5.12e).

This transition can be seen quantitatively by examining the power spectrum $P(k_x, t)$ in Fig. 5.12a. During the initial chaotic phase, the first 20 wavevectors (plotted) contribute significantly to $P(k_x, t)$, indicating appreciable spatial structure in the x-direction, with dynamics aperiodic in time. At long times, once the banded state forms, all amplitudes $P(k_x, t)$ are attenuated, particularly at large

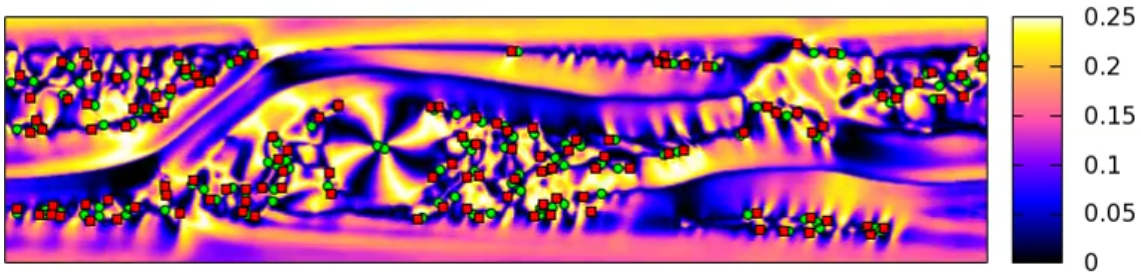

Figure 5.13: Example of an transient spiral structure (spiral region with two green $+\frac{1}{2}$ defects at the centre, cf. Ref. [11]), which is advected along the channel by the surrounding chaotic flow. In this instance, the spiral lasts for a time $\sim 300\tau_Q$. Colourmap shows $(n_x n_y)^2$. **Parameters:** $\zeta = 3.2$, $\Delta = 4 \times 10^{-5}$, $\tau_C = 10$, $\chi = 0.002$.

k_x. This (admittedly extreme) example is consistent with our drag reduction argument, whereby polymer calms short-scale structure. Snapshots of the evolution of this state in Fig. 5.12c/d/e demonstrate a clear transition from a disordered to an ordered state.

Correlated with this suppression of short scale structure is a dramatic increase in the throughput (Fig. 5.12b). While the chaotic state at early times has zero mean throughput, the latter banded-state develops a strong net flow in a spontaneously chosen direction, in this example towards the right.

Interestingly, during the intermediate phase between chaotic and banded states, we occasionally find transient, rotating spiral structures, which when viewed macroscopically[6], possess an integer topological charge +1 (see Fig. 5.13). Such structures are more commonly observed in polar materials. Experiments probing the dynamics of cytoskeletal extracts that comprise polar filaments observe self-organisation resulting in coherent spiral structures for both actomyosin complexes [133] and kinesin/microtubule mixtures [185]. Attempts to theoretically model such materials using a polar order parameter also predict similar structures [186–188].

These spirals are not typically observed in apolar, nematic, materials which instead form $\pm\frac{1}{2}$ defects [94], consistent with the previous numerical results in this chapter (without explicit coupling). (One exception to this is in highly confined

[6]Microscopically, at the heart of the structure, we find a pair of $+1/2$ defects though these are close enough that the effective director field forms a spiral pattern of topological charge +1.

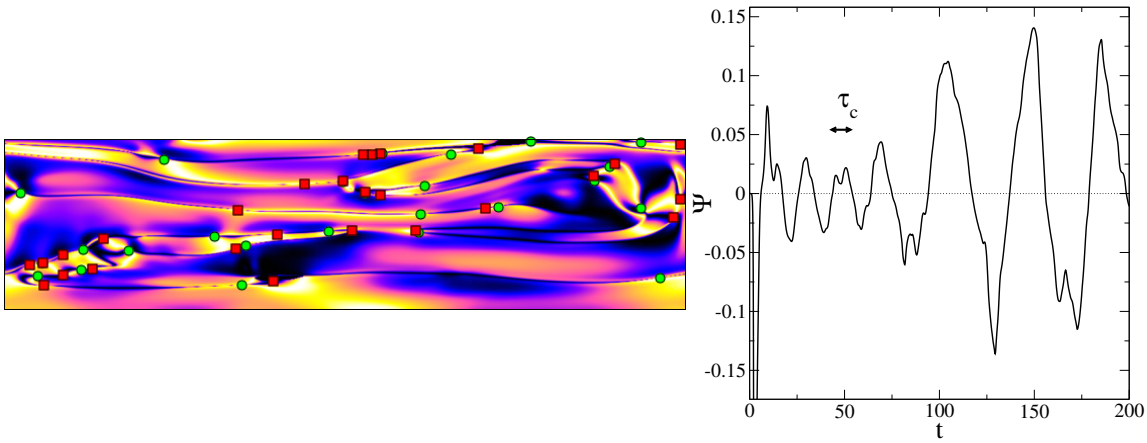

Figure 5.14: Example of an exotic oscillatory state which coherently shuffles left and right on a timescale of order τ_C. **Left:** Snapshot of the state where $(n_x n_y)^2$. **Right:** Throughput time-series showing the oscillatory nature of the state. **Parameters:** $\zeta = 6$, $\Delta = 10^{-4}$, $\tau_C = 10$, $\chi = 0.002$.

cylindrical geometries, as studied in Ref. [11]. There the authors found a single +1 defect at low activities, which then split into a pair of $+1/2$ defects as the activity was increased.) It appears that antagonistic coupling can help promote integer defects, but the detailed mechanism for this remains unclear.

5.6.1.2 Shuffling state

Increasing the activity (with all other parameters fixed) can disrupt the above shear-banded state. The result, Fig. 5.14, is a state that shuffles back and forth as a whole, with defects travelling along regions in which the degree of ordering q (principle eigenvalue of $\mathbf{Q}$) is small. This mechanism is similar to that reported in Ref. [182] (without polymer), where defect motion in 'walls' (regions of high local distortion) was observed. The throughput time-series (Fig. 5.14 bottom) shows that the net flow direction switches direction periodically on a timescale $\sim \mathcal{O}(\tau_C)$, again confirming the direct influence of polymer on the dynamics.

5.6.1.3 Order-disorder coexistence

With a larger coupling constant ($\chi = 0.004$), even stranger states can develop. Fig. 5.15 shows an example of a state exhibiting coexistence between chaotic/oscillatory regions (where the director is in-plane) and pseudo-quiescent regions (where the director is pointing out of the page). Here the active region travels back and forth,

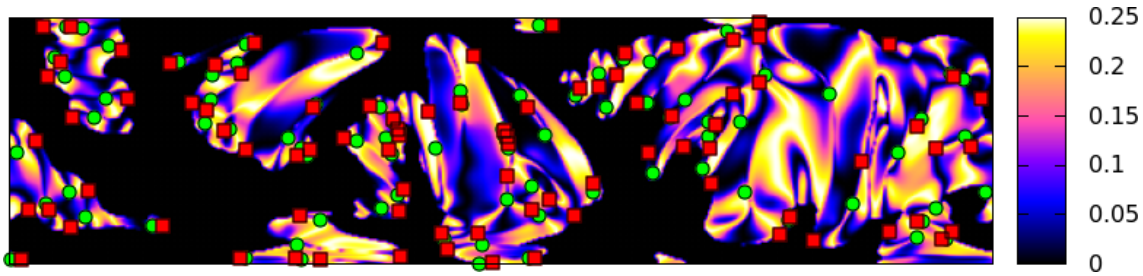

Figure 5.15: Example showing coexistence of 'bubbling' active domains and regions where the director is out of plane (black). **Parameters:** $\zeta = 6$, $\Delta = 10^{-4}$, $\tau_C = 10$, $\chi = 0.004$.

trapped between the plates. These quiescent regions are likely to be a result of our geometry where we embed a 3D order parameter in a 2D space, combined with order parameters whose major axes do not want to be aligned (for $\chi > 0$). It is likely that simulations in 3D space are required to fully resolve the dynamical behaviour of this state, which we expect would show structure and fluctuations also in the z-direction. Repeating the simulations a number of times with different seeds for the 2D perturbation, we find that these pseudo-quiescent regions sometimes grow, and can envelope the whole system.

5.6.1.4 Summary: explicit coupling

Given the complexity of parameter space, we have only devoted a small part of our study to the limit where the order parameters $\mathbf{Q}$ and $\mathbf{C}$ are coupled explicitly at the level of the free energy. In this section we presented a small selection of the states resulting from this more direct coupling.

The first of these exhibits a novel disorder-order transition in which the small-scale structure of an initially chaotic state is smoothed out as the polymeric influence increases until eventually a shear-banded state forms, often with residual defects travelling in the interfacial region. We then described two oscillatory states which (a) shuffle back and forth in the channel on a timescale $\sim \mathcal{O}(\tau_C)$, and (b) exhibit a coexistence of shifting quiescent and active regions. Even this modest selection of states demonstrates the wide range of dynamical behaviour possible in our coupled model. Future work could certainly look at this fascinating explicitly coupled regime, perhaps in a more systematic fashion.

5.7 Conclusions

Chaps. 3 to 5 introduced our novel model for active viscoelastic matter. In a simplified 1D geometry, where all fields may only vary in the y-direction, we established both the linear stability properties (analytically) and the non-linear dynamical behaviour (numerically). These results were used to derive critical activities for the spontaneous flow instability, and demonstrate that flowing states are possible even in the limit $\tau_C \to \infty$. While this 1D assumption greatly simplified the analytical and numerical complexity of our study, it becomes increasingly unphysical as the activity is increased. In this chapter therefore, we took a numerical approach to study the differences and similarities between the 1D and 2D dynamical behaviour.

We began in the limit in which polymer has no influence ($\eta_C \to 0$) where we reported a collaborative study examining how the characteristic lengthscale of the active turbulent state, l^*, scales with activity. Two independent numerical studies in a biperiodic geometry found that $l^* \sim \ell_Q \left(G_Q/\zeta\right)^{1/2}$. This result could in principle allow one to relate experimental control parameters (such as ATP concentration [95]) to the equivalent model parameter (activity). Future studies could extend this to include the effects of polymer. Our results in the channel geometry, that show that defect creation is suppressed as τ_C is increased, suggest that correlation lengths should increase with τ_C.

Remaining briefly in the no-polymer limit, we then adopted the channel geometry of our 1D study. We verified our numerics by comparison with existing work before generalising to include an alternative initial condition. We observed spontaneously flowing states above a critical activity, consistent with our linear stability analysis. Interestingly, we found bistable states at small activities, where the chosen state is strongly dependent on initial condition. Our results highlight the care that must be taken when relating numerically obtained phase diagrams to experiment.

In the turbulent, defect-rich regime typically seen experimentally, the velocity field (without polymer) generally does not produce net material transport. However biological processes such as cytoplasmic streaming (at the subcellular level) or cell migration in confined geometries (at the supracellular level) require net flows. We

introduced an order parameter to quantify the throughput of a given system.

When we include polymer of a relaxation time comparable to the LC, throughputs in the chaotic regime were significantly increased. We described a mechanism, analogous to polymer-controlled drag-reduction in inertial turbulence, where the polymer calms short scale structure and suppresses defect formation, promoting coherent flow states. Based on the above defect scaling results, we might expect that these coherent flows would ultimately be destroyed at very large activities, although our numerics do not extend into this regime.

We then explored the physics of the limit of diverging τ_C, first at fixed viscosity then at fixed modulus G_C. We explored a phenomenon where large polymer deformation would occur in short times. This, we argued, results when the polymeric timescale exceeds the timescale of activity-generated extensional flows, analogous to the (unphysical) behaviour of the Oldroyd-B model in pure extension. In light of these results, future studies might generalise the polymeric constitutive equation to include more physical extensional behaviour, for example by including finite extensibility of the polymer chains. This mechanism then was employed to explain the dynamics of a novel, oscillatory limit cycle where the system switches between quasi-1D banded states and a 2D roll state. Rapid polymeric deformation occurs in the latter (which contains extensional flows), which relaxes during the shear-banded states (which do not).

Setting $\tau_C \to \infty$, we found transient spontaneous flows, consistent with our 1D analytical prediction. The turbulent state that forms initially 'freezes in' as the polymer stress becomes appreciable, after which the LC defects slowly annihilate, and the nematic structure coarsens slowly as a power law in time.

Finally we explored some of the novel states generated when $\mathbf{Q}$ and $\mathbf{C}$ are explicitly coupled. In this limit, for example, states were found where the polymer drives a disorder-order transition. Oscillatory shuffling states were also observed with the timescale of oscillations set by τ_C. We do not perform an exhaustive survey of parameter space, instead sampling a small number of points. The rich array of states observed invites a more systematic exploration of phase space in future works.

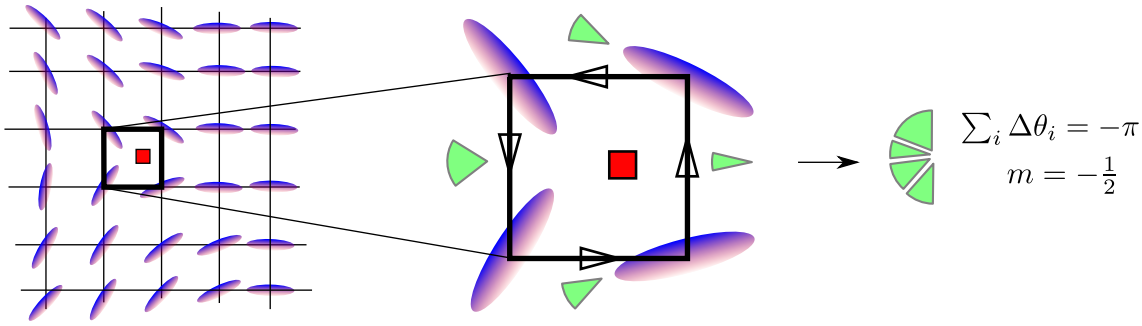

Figure 5.16: Schematic demonstrating how the topological charge and position of a defect is found numerically. The director angle is extracted on the regular grid, and the change in angle integrated round the four nearest grid points. After accounting for the head-tail symmetry of the director $\hat{\mathbf{n}}$, any square where the integrated angle is non-zero contains a defect. Here we demonstrate the process for a $-1/2$ defect (green wedges indicate the angular change from site to site). Red square marks the (approximate) location of the defect core.

5.8 Appendix I: Numerically counting defects

We now describe how we numerically identify and classify topological defects in the director field, following the method first described by Bowick *et al.* [189] (we adopt the algorithm as described in the Appendix of Ref. [190]). As introduced in Sec. 2.3, we solve the PDEs for $\mathbf{Q}$, $\mathbf{C}$ and $\mathbf{v}$ on a regular square grid of spacing Δx. At each spatial point we calculate the director angle θ. We then take the line integral around each square of adjacent grid points, making sure the change in angle between each grid point $\delta\theta_i$ respects the head-tail symmetry of $\hat{\mathbf{n}}$, i.e.,

$$\delta\theta_i = \begin{cases} \theta_{i+1} - \theta_i & \text{if } |\theta_{i+1} - \theta_i| \leq \pi/2 \\ \theta_{i+1} - \theta_i + \pi & \text{if } \theta_{i+1} - \theta_i < -\pi/2 \\ \theta_{i+1} - \theta_i - \pi & \text{if } \theta_{i+1} - \theta_i > +\pi/2. \end{cases} \tag{5.13}$$

The topological charge m is then

$$m = \frac{1}{2\pi} \sum_i \delta\theta_i, \tag{5.14}$$

where non-zero m indicates that a defect lies somewhere between the four points. This procedure is illustrated for a $-1/2$ defect in Fig. 5.16. While we can precisely obtain the charge of the defect, the position is only known to within Δx. However

as we converge our results $\Delta x \to 0$, we can always obtain the defect position with arbitrary precision if required.

5.9 Appendix II: Power spectrum

In the previous chapter we considered the simplified dynamics that arise when we assume invariance in the x and z-directions. In order to examine the stability of these 1D states in 2D, and to allow us to quantify the calming effects of polymer, it is useful to have a quantitative description of the degree of spatial structure in the x-direction.

We take the x Fourier transform of all non-zero order parameters, and combine these in vector form $\phi = (Q_{xx}, Q_{xy}, Q_{yy}, C_{xx}, C_{xy}, C_{yy})$. We then define the power spectrum

$$P(k_x) = \sum_i^6 \int_0^{L_y} dy |\phi_i(k_x, y)|^2, \tag{5.15}$$

where k_x is the wavevector in the x-direction.

6

Viscoelastic flows in porous media

6.1 Introduction

The term "porous media" describes a very broad class of materials that comprise of an interconnected network of cavities of varying size [191]. Given the ubiquity of porous materials, from the artificial (paper, textiles) to the natural (soil, aquifers, biological tissue), it is no surprise that their flow properties have attracted considerable interest from industry, particularly in the oil recovery sector [192–194].

While the behaviour of Newtonian flows in porous media is generally well understood [195], many fluids of industrial importance exhibit non-Newtonian behaviour at high flow rates [38]. Notably, at high flow rates relative to some intrinsic relaxation time of the fluid, a large increase is observed in the pressure drop require to maintain a given flow rate. See, e.g., Ref. [23]. The ability to accurately predict and characterise this increase is of great importance to many industrial processes. Additionally,

at these high flow rates, the flowing state can become unsteady [194,196,197]. Such an instability can pose complications for industrial processing. This phenomenon is also of fundamental interest in the study of elastic instabilities in general [198].

In this chapter we begin by reviewing the large body of literature that considers porous materials, which has enjoyed many successes in modelling flows, at least in simple geometries (Sec. 6.1.1). However our survey demonstrates that conclusive numerical agreement over the nature of both the upturn in the drag, and fluctuations in the flow field, has yet to be reached.

We then outline the idealised geometries within which we can cleanly examine the phenomenology of porous flows in 2D, and define the key dimensionless parameters with which to characterise the flow (Sec. 6.2). A full hydrodynamical treatment of the problem requires care as convergence is notoriously difficult in such geometries [199]. Therefore we have developed three independent numerical techniques during our study, which we describe in Sec. 6.3. Particular focus is given to the immersed boundary method (IBM), as the majority of our results were obtained using this method. These codes are then carefully benchmarked against each other and against known analytical/numerical results.

We present an analysis of the types of flow typically encountered in our model geometries, identifying regions dominated by shear and extension in the Newtonian limit (Sec. 6.4.1). While the velocity field does change as viscoelasticity is introduced, the difference for moderate Weissenberg numbers is sufficiently small that our Newtonian analysis remains pertinent. Therefore given knowledge of a non-Newtonian fluid and its response in simple rheological protocols, this allows us (a) to make qualitative predictions about its response in these complex geometries, and (b) to be able to tailor this response using that information. For example, one could hope ultimately to be able to influence the point at which the upturn in the drag occurs by tuning properties of the viscoelastic fluid.

Numerical results are then presented for several constitutive models in these idealised porous geometries, which capture the large upturn in the drag seen experimentally in a biperiodic flow cell. Without walls we probe how the flow response depends on the cylinder radius R. At small R the Newtonian flow field is charac-

terised by extensional flows in the wake; for large R shearing in the vertical gap between cylinders appears to be the dominant feature. Consistent with this is our observation that the upturn in the drag appears at a constant $We \approx We_{\mathrm{up}}$ *if* one adopts an 'extensional Weissenberg number' at small R and a shear definition at large R.

When walls are included, numerical convergence is particularly difficult. Our initial simulations, which were later discovered to be under-resolved, exhibited the onset of fluctuations above a critical Weissenberg number $We \sim \mathcal{O}(1)$ which grow in magnitude as $(We - We^{\mathrm{osc}})^{1/2}$ consistent with the results of Ref. [25]. However rigorous convergence checks revealed this to be a numerical artefact: we find that resolutions an order of magnitude greater than in Ref. [25] are required for convergence, suggesting their results could be susceptible to a similar numerical issue. We finish the chapter with some concluding remarks about our work and suggest possibilities for future study.

6.1.1 Literature review

Early theoretical attempts at understanding flows in porous media adopted a coarse-grained approach, discarding microscopic details in favour of macroscopic properties. D'arcy [200] wrote a general form relating the pressure drop per unit length $\Delta P/L$ to the mean velocity scale V

$$\frac{\Delta P}{L} = \frac{\eta V}{K}, \tag{6.1}$$

where η is the viscosity and K is the permeability, a constant which should only depend of the properties of the media, but is unknown *a priori*. This permeability was later analytically related to the porosity ϵ (the ratio of free volume to total volume) by the Blake-Kozney-Carman equation [201], which proved successful in describing a range of simple flows. However the validity of this picture remains limited to inertialess, Newtonian flows.

Later studies took a more microscopic view of porous materials, considering idealised geometries constructed from periodic arrays of spheres or cylinders. Sangani and Acrivos [202] studied the drag on square and hexagonal biperiodic arrays of cylinders by deriving analytical expressions in both the dilute and concentrated lim-

its, and by calculating the flow field numerically across the full range of volume fractions. Larson and Higdon reproduced these results using a boundary-integral technique, with more focus on the details of the flow field [203]. Skartsis *et al.* performed finite-element simulations and experiments with carbon fibre beds, finding good agreement with the above studies [195]. They declared the Newtonian problem, at least for the idealised geometries considered in this chapter, solved.

The jump in complexity when making the natural generalisation to include non-Newtonian fluids poses significant further challenges. Experiments based on the biperiodic geometry discussed above, and sketched in Fig. 6.1a, consistently showed a dramatic upturn in the drag on the cylinder (C_D) relative to that observed for a Newtonian fluid of matched viscosity as the degree of viscoelasticity (Weissenberg number We) was increased past a critical value We_c [23, 204, 205]. This increase was typically accompanied by the development of time-dependent flow fields [196]. Additionally at low We a subtle effect was sometimes observed where the drag force initially exhibits a small decrease relative to the Newtonian case [206]. The origin of this is often attributed to shear thinning effects [207, 208].

However early simulations of Oldroyd-B and Upper-Convected Maxwell (UCM) fluids, which do not shear-thin, also observed this decrease [24, 209, 210]. While these studies consistently captured this low We behaviour, the dramatic upturn observed experimentally at high We was not seen, mainly due to insufficient numerical resolution at high We.

A later numerical study of a FENE-CR fluid past a single cylinder between walls [211] obtained steady solutions for a large range of We if symmetry is imposed along the horizontal centreline. With that assumption relaxed, time dependent states develop above a critical We originating from the downstream face of the cylinder. The measured drag for the unsteady states is larger than those with imposed symmetry.

For a linear array of cylinders between walls, Smith *et al.* [212] reproduced some of the experimentally observed characteristics (specifically the wavevector and critical We) of the instability at high We using a numerically calculated linear stability analysis, but the transition to a 3D steady state is contrary to the time-dependent

states found experimentally [196]. Sahin and Wilson extended this work [213], finding that wavelength of the instability scales with the cylinder spacing for closely spaced cylinders, and with the width of the wake for larger cylinder spacings.

More recently, Gillissen used a Lattice-Boltzmann code to study a FENE-P fluid flowing past biperiodic hexagonal array of cylinders without walls [208], finding both the initial downturn and significant upturn. However no time-dependent solutions were reported. Vázquez-Quesada and Ellero performed 2D smooth particle hydrodynamics (SPH) simulations of cylinders between solid walls [25, 214], which also captured both the initial downturn and a appreciable later upturn. However at high We the results depart from earlier numerical work [196] as the authors report a time-dependent state.

Clearly quantitative agreement between independent codes has yet to be reached, particularly with regard to the nature of the upturn in the drag. We are unaware of any single study that considers the variety of constitutive models used here (carefully chosen in order to probe the shear and extensional responses) in such a wide range of geometries (i.e., examining dependence on cylinder radius for two orientations of a biperiodic array, and the dependence on horizontal spacing for arrays of cylinders confined between walls).

The objectives of this numerical study are therefore to capture, characterise and understand:

(a) the mild downturn in drag at low We,

(b) the dramatic increase in drag at higher We,

(c) any time-dependent states (if they exist), which are seen experimentally at high We.

We aim to achieve this by performing continuum simulations in four different idealised periodic cylinder geometries that present the flow with alternating regions of expansion and contraction as well as regions of strong shear. By exploiting the properties of simple polymer constitutive models in shear and extension, we aim to also to understand how these effects stem from the fluid's underlying rheological response, as measured in simpler geometries.

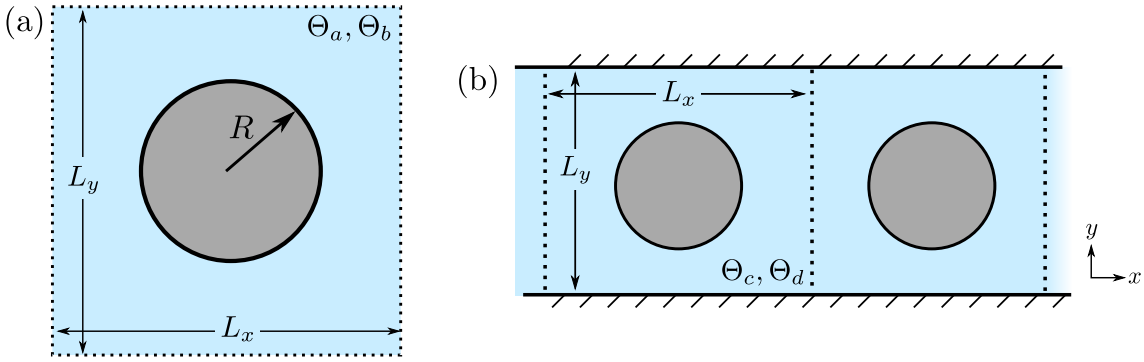

Figure 6.1: Our model of a porous material, with a typical simulation cell indicated by the dashed lines. (a) A square biperiodic array of cylinders, where the imposed flow is orientated at 0° (Θ_a) or 45° (Θ_b). (b) Array of cylinders contained between solid walls, with cylinders spaced by $L_x = 0.625$ (Θ_c) or 1.5 (Θ_d).

6.2 Model

6.2.1 Geometry

Real porous materials exhibit a wide distribution of pore sizes, with morphologies ranging from smooth rounded surfaces to abrupt, angular structures [215]. However as a starting point to understanding flows in generic porous media, we begin here with a simplified model porous geometry. We adopt one of the most common choices, both experimentally and theoretically, and model pores as the spaces between an array of cylindrical posts. We assume spatial invariance of all quantities in the z-direction (parallel to the cylinders) so our simulations are purely two dimensional. We return at the end of the chapter to comment further on this assumption.

In particular, we define several variants of this geometry. The first considers an infinite (biperiodic) array of cylinders of variable radius R (Fig. 6.1a) spaced by $L_x = L_y = L$, with the flow at an angle θ to the array. We consider two cases $\theta = 0°, 45°$ which we label Θ_a and Θ_b. Note that any colour maps presented for the latter orientation are rotated so that the flow is always from left to right. We show in Sec. 6.4.1 that for small R, these geometries are both mainly characterised by extensional flows in the wake of the cylinder. At larger R the behaviour is more distinct: Θ_a becomes more shear dominated in the region around the top/bottom edges of the cylinder and develops small recirculating regions, whereas Θ_b retains a

balance of shear and extensional flows.

In the second model system we include solid walls at $y = 0, L_y$ and place cylinders L_x apart, now periodic only in the x-direction (Fig. 6.1b). This arguably more artificial geometry is more widely considered in the literature. In particular, the single-cylinder limit ($L_x \to \infty$) has become a notable benchmark problem for both Newtonian and non-Newtonian flows (see Sec. 6.3.2.1). Following early studies [24, 25], we fix $R/L_y = 0.25$, and focus on two cylinder spacings, $L_x = 1.5$ (widely spaced) and $L_x = 0.625$ (closely spaced), which we label Θ_c and Θ_d respectively.

We then impose either a flux $Q \equiv VL_y$ (where $V = {}^1/_{L_y} \int_0^{L_y} v_x dy$ is the mean velocity in the flow direction passing a vertical line) or pressure drop ΔP, and measure the remaining quantity. Without walls present, force balance directly relates this pressure drop to the integrated force on the cylinder ($\Delta P = \frac{1}{L_x L_y} \int \mathbf{f} d\mathbf{x}$). With walls there is an extra contribution to ΔP from the drag against the walls. While some earlier studies only report the drag on the cylinder, we choose here to report ΔP (thereby including the drag on the walls) as this is the quantity that is experimentally measurable. Though our results are qualitatively unchanged by this difference, we feel this provides a closer link to experiment. Therefore, unless otherwise specified (e.g., when comparing to older work), all results presented here report the total pressure drop.

In these geometries we consider the dynamics of a simple polymeric fluid with relaxation time τ and elastic modulus G in an incompressible Newtonian background solvent of viscosity η. Experimentally the Reynolds number is generally estimated to be $Re \ll 1$ [24, 216], therefore we work in the limit of Stokes flow ($Re \to 0$). In removing inertial terms from the Navier-Stokes equation, any flow instabilities can be wholly attributed to non-linear effects of the polymeric fluid, specifically elasticity.

6.2.2 Dimensionless parameters

In what follows we work in units of length $[L] = L_y = 1$, time $[T] = L_y^2/Q = L_y/V = 1$ and modulus $[G] = \eta V/L_y = 1$, by considering the following dimensionless quantities.

First we define the post radius $\tilde{R} \equiv {}^{R}/_{L_y}$, and horizontal cylinder spacing $\tilde{L}_x = {}^{L_x}/_{L_y}$; from herein we drop the tildes for clarity. (Additionally one could define the area fraction $\phi = \frac{P\pi R^2}{L_x L_y}$, where P is the number of cylinders. In practice we use a single cylinder for the majority of this study so R is sufficient.)

The ratio of the pressure drop ΔP to flux Q defines the drag coefficient

$$C_D = \frac{L\Delta P}{\eta Q} = \frac{\Delta P}{\eta V}, \tag{6.2}$$

where the solvent viscosity η renders the quantity adimensional. For Stokes flow of a Newtonian fluid, C_D is only dependent on R (i.e., it is independent of what value of Q or ΔP we impose, or indeed the angle of imposed flow).

The degree of viscoelasticity can be parametrised by considering the product of the relaxation time of the polymer and a typical shear-rate in the porous geometry, defining a Weissenberg number *We*. This is typically chosen in the literature as in Eq. 6.3a. However the region of strongest shear is over the tops of the cylinders as the fluid passes through a vertical constriction of size $\frac{L_y - 2R}{\alpha}$ (where $\alpha = 1$ without walls, and $\alpha = 2$ with walls), leading to a typical shear-rate of $\frac{\alpha V}{L_y - 2R}$. We use this to define a more representative Weissenberg number

$$We = \begin{cases} \dfrac{\tau V}{R} & \text{typical literature definition} \quad (6.3a) \\ \alpha \dfrac{\tau V}{L_y - 2R} & \text{our new definition,} \quad (6.3b) \end{cases}$$

which now reflects that *We* should increase as the constriction becomes narrower. (The previous definition decreases as the constriction becomes narrower.) While shortcomings in the use of Eq. 6.3a have been noted before [23, 24], many studies fix $R = 0.25$ for which Eqs. 6.3a and 6.3b (with $\alpha = 2$) are equivalent. Note that Eq. 6.3b effectively defines a shear Weissenberg number. We will later show that recasting our results using an alternative 'extensional Weissenberg number' can be more appropriate for the extension dominated flows seen at small R (Sec. 6.5.2.1).

Defining the viscosity ratio $\beta = \frac{\eta}{\eta + G\tau}$ fixes the polymer modulus, and we retain the common literature value of $\beta = 0.59$ (see e.g., Ref. [217]) to allow comparison with earlier work. Finally we define the normalised drag $\chi = \frac{C_D(We)}{C_D(We=0)}$, which relates the drag coefficient of a non-Newtonian fluid to its behaviour in the Newtonian limit.

imposed parameter	definition	description
$\tilde{R}$	$= R/L_y$	cylinder radius
$\tilde{L}_x$	$= L_x/L_y$	cylinder spacing (in x-direction)
We	$= \alpha V\tau/\left(L_y - 2R\right)$	Weissenberg number ($\alpha = 1$ without walls, $\alpha = 2$ with walls)
β	$= \eta/\left(\eta + G\tau\right)$	viscosity ratio (fixed at 0.59)
measured quantity	**definition**	**description**
C_D	$= \Delta P/\left(V\eta\right)$	drag coefficient (constant for a Newtonian fluid at fixed R, L_x)
χ	$= C_D(We)/C_D(We = 0)$	drag (normalised by Newtonian value)

Table 6.1: Summary of dimensionless parameters. Note that for our choice of units the tildes are redundant, and we now drop them for clarity.

Thus $\chi > 1$ means that a larger pressure drop is required to maintain a given Q relative to the Newtonian case, as is the case at large We.

These dimensionless parameters are collated in Table 6.1. In summary, having fixed $\beta = 0.59$, we vary We along with R (for geometries $\Theta_{a,b}$) or L_x (for $\Theta_{c,d}$) and observe how the normalised drag χ depends on these quantities.

6.2.3 Choice of protocol

Both experimentally and numerically, a choice must be made for which quantity from ΔP and Q to impose and which to measure. In experiments, typically the latter is imposed [197,204,218]; numerically we have the capability to impose either quantity.

Interestingly, the choice of imposed quantity may affect the nature of any fluctuations (if present). If ΔP is imposed then both C_D and We (which both depend on Q) will vary in time for an unsteady flow state. However imposing Q can only lead to fluctuations in C_D, not in We. Therefore a plot of χ against We, where the standard deviation of the time-series of a given quantity is marked with error bars, will differ for the two protocols if fluctuations are observed.

For the biperiodic case (no walls), this distinction is not relevant as we see no difference in our simulation results between imposed Q and imposed ΔP (see

Fig. 6.13a inset). This is consistent with the recent biperiodic simulations of Gillissen [208] (where ΔP is imposed), which also did not display any time-dependence.

However the recent simulations (with walls) of Vázquez-Quesada *et al.* [25] exhibited fluctuations at high values of *We*. Their simulations impose a pressure drop, as appears to be common in earlier studies [24, 208]. Whether the same fluctuations would appear for imposed Q remains an open question. Our own results with walls (also with imposed ΔP) fail to reproduce these fluctuations once the spatial mesh is converged upon and we will argue that the results of Ref. [25] may not be properly converged (see Sec. 6.5.3.2).

6.3 Numerical methods

There are several numerical approaches that one may take to simulate this model geometry, three of which we outline here: (i) an immersed boundary method (IBM), (ii) a phase field method, and (iii) a propagator method. We find excellent agreement between all three in the Newtonian limit. Our results with viscoelasticity included were primarily obtained using (i). Method (ii) has been implemented successfully for moderate *We*, but became unstable at higher *We*. Less progress has been made implementing (iii) for non-Newtonian fluids, and we do not report this here. Therefore unless otherwise stated, all results presented below were obtained using (i), with the other methods used mainly for validation. Descriptions of (ii) and (iii) are given in Apx. 6.7.

6.3.1 Immersed boundary method

The "immersed boundary method" (IBM) was initially developed by Peskin in the context of modelling blood flow past heart valves [219, 220], though the term has since come to describe a general class of related methods [221]. In general terms, the method couples the familiar Eulerian description of the Navier-Stokes equations on a regular grid to a Lagrangian description of a material surface of arbitrary shape (which does not necessarily coincide with a rectangular grid). Information is then transferred between these using smoothed Dirac delta functions. Whilst the

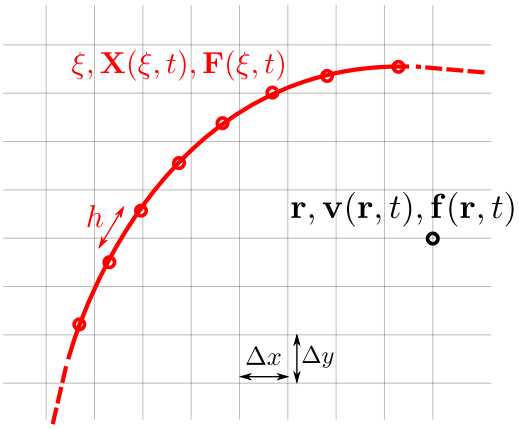

(a) Illustration of a Eulerian grid point (**black** dot sitting on the regular grid) and a series of Lagrangian points (**red** dots, off grid). Numerical discretisations for the Eulerian (Δx, Δy) and Lagrangian (h) fields are also marked.

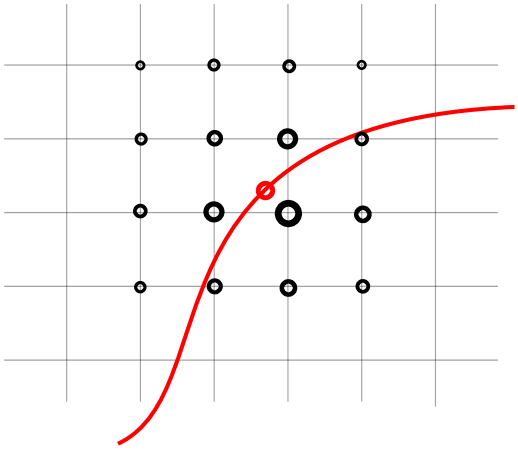

(b) Illustration of, for example, how the Lagrangian force density $\mathbf{F}(\xi,t)$ is distributed to the Eulerian forces $\mathbf{f}(\mathbf{r},t)$. Grid points closer to the Lagrangian point recieve a larger contribution as indicated (roughly) by the size of the black dots.

Figure 6.2: Schematics illustrating the differences between Eulerian and Lagrangian formulations, and how to connect the two.

immersed boundary formulation can in general describe arbitrary translations and deformations, the porous model geometry only requires static posts of fixed shape, which leads to significant simplifications to the algorithm. We begin by presenting the general formulation, then indicate the simplifications that can be made for our model.

Mathematical description. For incompressible Stokes flow in a domain Ω, with a no-slip boundary condition on the cylinder surface Γ, force balance is given by

$$0 = \eta\nabla^2\mathbf{v} + \nabla.\boldsymbol{\Sigma} - \nabla p + \mathbf{f}, \tag{6.4}$$

where $\boldsymbol{\Sigma}$ is a tensor representing the polymeric stress, and $\mathbf{f}$ is an arbitrary body force that we discuss further below. Incompressibility further demands that

$$0 = \nabla.\mathbf{v}. \tag{6.5}$$

In 2D, a fixed position $\mathbf{r} \in \Omega$ in this Eulerian frame is then described by $\mathbf{r} = (x, y)$, with the velocity and force at that point given by $\mathbf{v}(\mathbf{r},t)$ and $\mathbf{f}(\mathbf{r},t)$

respectively. To describe a body of arbitrary shape, we further can define a Lagrangian coordinate $\xi \in \Gamma$ so that the position of the immersed boundary can be written as $\mathbf{X}(\xi, t)$, and the force density in the boundary as $\mathbf{F}(\xi, t)$. The relation between these two formulations is illustrated in Fig. 6.2a.

Given the Lagrangian force density $\mathbf{F}(\xi, t)$, the force on the fluid in the Eulerian frame is given by

$$\mathbf{f}(\mathbf{r}, t) = \int_{\Omega} \mathbf{F}(\xi, t)\delta(\mathbf{r} - \mathbf{X}(\xi, t))d\xi. \tag{6.6}$$

Conversely given the velocity in the Eulerian frame, the velocity of the material boundary $\mathbf{U}$ can be obtained by

$$\mathbf{U}(\xi, t) \equiv \frac{\partial \mathbf{X}(\xi, t)}{\partial t} = \int_{\Omega} \mathbf{v}(\mathbf{r}, t)\delta(\mathbf{r} - \mathbf{X}(\xi, t))d\mathbf{x}. \tag{6.7}$$

Infinitely localised Dirac delta functions are of course unfeasible to to implement numerically as they would introduce unwanted discontinuities. This is avoided by defining a smoothed delta function $\delta_P(\mathbf{r}) = \delta_P^x(x)\delta_P^y(y)$ which distributes the function to neighbouring points (see Fig. 6.2b for schematic). As with the mathematically defined Dirac delta δ, this must integrate to unity and should approach δ as grid spacing $\Delta x, \Delta y \to 0$ [220] (see below for details of the discretisation). While there are multiple candidates for this smoothed function [222, 223], we proceed with the implementation described by Lai & Peskin [224]

$$\delta_P(r) = \begin{cases} \dfrac{1}{8h}\left(3 - 2\dfrac{|r|}{h} + \sqrt{+1 + 4\dfrac{|r|}{h} - 4\left(\dfrac{|r|}{h}\right)^2}\right) & |r| \leq h \\ \dfrac{1}{8h}\left(5 - 2\dfrac{|r|}{h} - \sqrt{-7 + 12\dfrac{|r|}{h} - 4\left(\dfrac{|r|}{h}\right)^2}\right) & h \leq |r| \leq 2h \\ 0 & \text{otherwise,} \end{cases} \tag{6.8}$$

where r is the separation between a given Eulerian and Lagrangian point, and h is the grid spacing in that direction.

Finally we must prescribe an expression for the Lagrangian force density $\mathbf{F}$. For our rigid, non-moving post this is done by specifying an equilibrium configuration for the boundary $\mathbf{X}_0(\xi)$, and imposing a Hookean restoring force when the boundary deviate from this

$$\mathbf{F}(\xi, t) = -\kappa\left(\mathbf{X}(\xi, t) - \mathbf{X}_0(\xi)\right), \tag{6.9}$$

where κ is a large spring constant. Though not required for our purposes, $\mathbf{F}$ can be generalised to include other contributions such as an optimal curvature for deformable objects [225]. Note that in principle $\mathbf{X}_0$ may be made time-dependent to describe moving objects.

While Eqs. 6.4, 6.6, 6.7 and 6.9 provide a general formulation for a deformable, moving boundary, our problem permits some simplifications to be made. Firstly, as our equilibrium configuration $\mathbf{X}_0$ is independent of time, we can differentiate Eq. 6.9 with respect to time, yielding an evolution equation for the force,

$$\frac{\partial \mathbf{F}(\xi,t)}{\partial t} = -\kappa \mathbf{U}(\xi,t). \tag{6.10}$$

Indeed in the limit $\kappa \to \infty$, the post is static so we need not actually evolve the position of the post, i.e., we set $\mathbf{X}(\xi,t) = \mathbf{X}_0(\xi)\ \forall t$. We have carefully checked that this method agrees with the arguably more rigorous method in which we update $\mathbf{X}(\xi, t+\Delta t) = \mathbf{X}(\xi,t) + \Delta t \mathbf{U}(\xi,t)$ at each timestep, allowing the cylinder to deform and move slightly.

Discretisation. Some care is required in numerically discretising the above equations. As before, we discretise the Eulerian equations such that spatial step sizes $h = \Delta x = L_x/N_x = \Delta y = L_y/N_y$. Similarly, a Lagrangian boundary of length L_B is divided into M sections of length $\Delta s = L_B/M$. The optimal ratio of these stepsizes $\alpha = \Delta s/h$, is unclear *a priori*; for too small a value of α we oversample the boundary forces, for too large an α we can suffer from fluid leakage through the spaces between immersed boundary points. In what follows we set $\alpha = 2$, though we have checked that our results are robust to this choice.

The full numerical scheme, at time $t = n\Delta t$, with spatial points denoted $\mathbf{r}_{ij} = (x,y) = (i\Delta x, j\Delta y)$ and Lagrangian point $\xi_k = k\Delta s$ is then

$$\frac{\mathbf{C}^{n+1}(\mathbf{r}_{ij}) - \mathbf{C}^n(\mathbf{r}_{ij})}{\Delta t} = \mathbf{g}\left(\mathbf{C}^{n+1}(\mathbf{r}_{ij}), \mathbf{C}^n(\mathbf{r}_{ij}), \mathbf{v}^n(\mathbf{r}_{ij})\right) \tag{6.11a}$$

$$\frac{\mathbf{F}^{n+1}(\xi_k) - \mathbf{F}^n(\xi_k)}{\Delta t} = -\kappa \int_\Omega \mathbf{v}^n(\mathbf{r}) \delta\left(\mathbf{r} - \mathbf{X}(\xi_k)\right) d\mathbf{r} \tag{6.11b}$$

$$\mathbf{f}^n(\mathbf{r}_{ij}) = \int_\Gamma \mathbf{F}^{n+1}(\xi_k) \delta\left(\mathbf{r}_{ij} - \mathbf{X}(\xi_k)\right) d\xi \tag{6.11c}$$

$$\eta \nabla^2 \mathbf{v}^{n+1} = \nabla p^n - \mathbf{f}^n - \mathbf{\Sigma}(\mathbf{C}^{n+1}) \tag{6.11d}$$

where $\mathbf{g}$ is a general polymer constitutive equation, and where Eq. 6.11d is solved either by streamfunction (when walls are included) or Oseen tensor (without walls) techniques, as described in Sec. 2.1.

In summary, we (a) use an explicit Euler time-stepping scheme to evolve the Lagrangian forces $\mathbf{F}$ so as to effect Hookean restoring springs (Eq. 6.11b) that impose $\mathbf{v} = \mathbf{0}$ at the cylinder surface, (b) transfer these forces to the Eulerian grid $\mathbf{f}$ (Eq. 6.11c), then (c) update the velocity everywhere in the simulation cell using these Eulerian forces (Eq. 6.11d).

The general discretisation outlined above naturally imposes a flux. To instead impose a pressure drop in the biperiodic case, we follow the approach of Teran and Peskin [36] who showed that the flux can be determined by requiring that the integral of the total force (which includes the immersed boundary forces and the external forcing) and its time derivative are zero, i.e., $\int_\Omega \mathbf{f} = \partial_t \int_\Omega \mathbf{f} = \mathbf{0}$. When imposing a pressure drop with walls, the flux naturally results from solving Eq. 6.11 with no-slip and no-permeation boundary conditions at the walls.

6.3.2 Convergence and benchmarking

We have ensured that in what follows, all our results are fully converged on both spatial stepsize and timestep. In the high Weissenberg number regime with walls, we found convergence particularly difficult to achieve. Data from our initial (unconverged) simulation runs in this regime showed fluctuations consistent with a recent study [25], however thorough convergence tests later revealed this to be a numerical artefact (see Sec. 6.5.3).

We begin by verifying our code in the Newtonian limit, for which several analytical results exist. While there is less agreement in the literature for viscoelastic flows (i.e., $We > 0$), we do demonstrate reasonable agreement with earlier studies, at least at small We (see Sec. 6.5.3.1). Of the two geometries, that with cylinders confined between walls has received more attention, at least in recent studies. As there are fewer existing results for the biperiodic system, we mainly verify our results using the three independent codes outlined above (i.e., IBM, phase-field, and propagator methods).

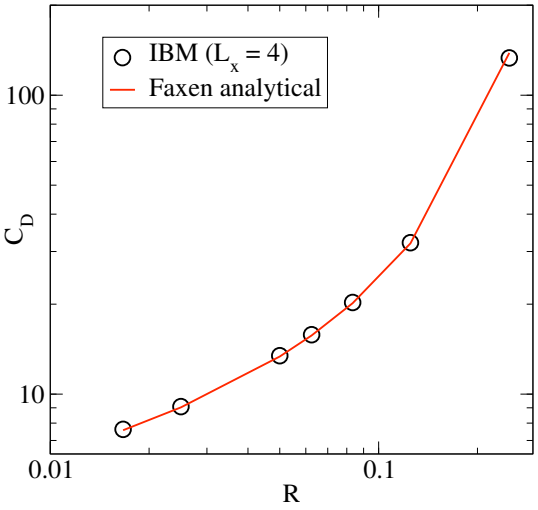

Figure 6.3: Comparison of our IBM simulations with Faxen's analytical result for a single cylinder in a channel [226], for a range of R. We find that a cylinder spacing of $L_x = 4$ is sufficient to reproduce the single cylinder result. The drag force for the largest R is slightly lower than the analytical result, though this is consistent with other numerical studies [24, 227].

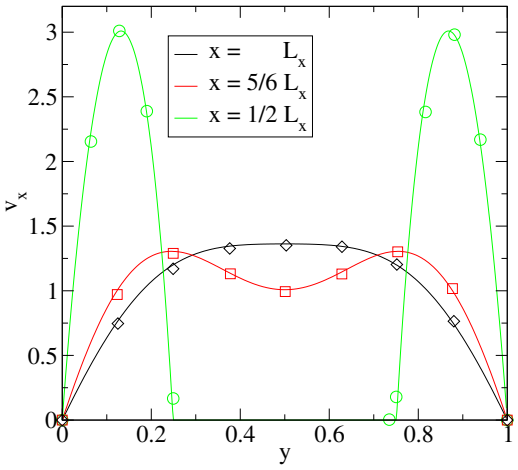

Figure 6.4: Vertical slices of v_x in the channel geometry at various x for $L_x = 1.5$, showing good agreement between our IBM results (solid lines) with the SPH results of Ellero [227] (symbols). The SPH data was extracted using an online tool [228].

6.3.2.1 Validation with walls

Faxen used the method of images to find an analytical solution for a single cylinder between walls [226]. In theory, our simulations require $L_x \to \infty$ to effect a single cylinder; in practice $L_x > 4$ is large enough to satisfactorily reproduce his result, see Fig. 6.3.

Numerical studies of a periodic array of cylinders between walls also provide ample data for comparison, e.g., the recent smoothed particle hydrodynamics (SPH) simulations of Ellero *et al.* [227]. Individual 1D slices of the velocity profile (Fig. 6.4) show excellent quantitative agreement, and full 2D velocity maps of v_x (velocity component in the flow direction) agree for both wide (not shown) and close (Fig. 6.5) spacings of cylinders in the flow direction.

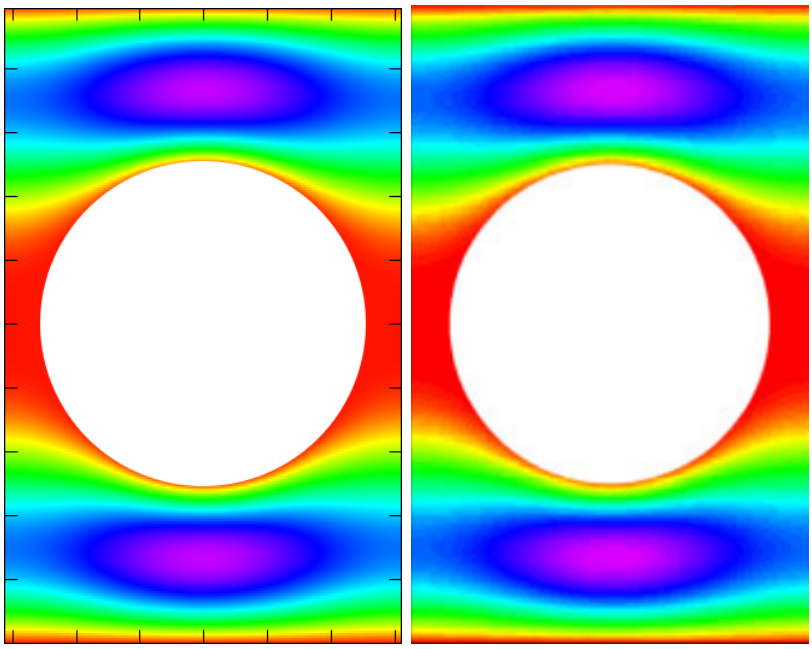

Figure 6.5: Colourmap of v_x in the channel geometry showing good agreement between our simulations (left) and those of Ellero *et al.* [227] (right), for $L_x = 0.625$.

6.3.2.2 Validation without walls

As there is less focus on the biperiodic case in the literature, we first validate the three methods (IBM, phase-field, propagator) against each other. All show excellent agreement when comparing slices of the velocity field (Fig. 6.6), with the caveat that the phase-field method leads to a marginally different flow field, due to a slightly different "effective radius" resulting from the finite interfacial width ℓ. Morris *et al.* benchmark their SPH code for a range of Re [229] and we find good agreement with their results in the $\mathrm{Re} \to 0$ limit (Fig. 6.7).

We must also check that our simulations give sensible results for a wide range of radii, R. Sangani and Acrivos derived analytical expressions for the drag coefficient C_D for a biperiodic array in both the dilute ($R \to 0$) and concentrated ($R \to L/2$) limits, and calculated exact solutions numerically using a series expansion at intermediate R. We find that all three of our simulation methods are in excellent agreement with their work, across the full range of radii (see Fig. 6.8).

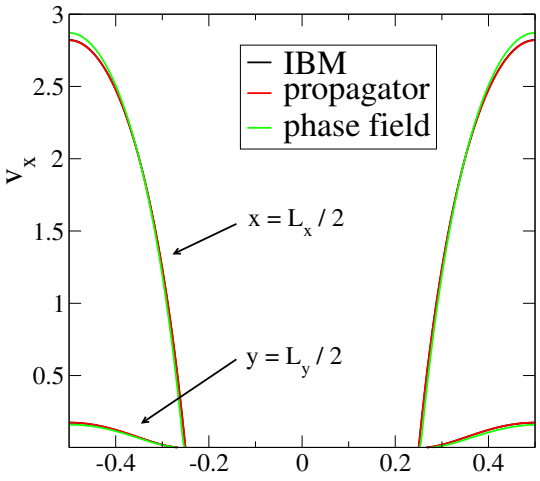

Figure 6.6: Comparison of our three numerical techniques, showing slices of v_x along the horizontal ($y = L_y/2$) and vertical ($x = L_x/2$) centerlines for $R = 0.25$. Velocity at cell edge slightly bigger for phase-field because the diffuse interface between fluid and post leads to an effective radius slightly larger than R. IBM and propagator results are indistinguishable.

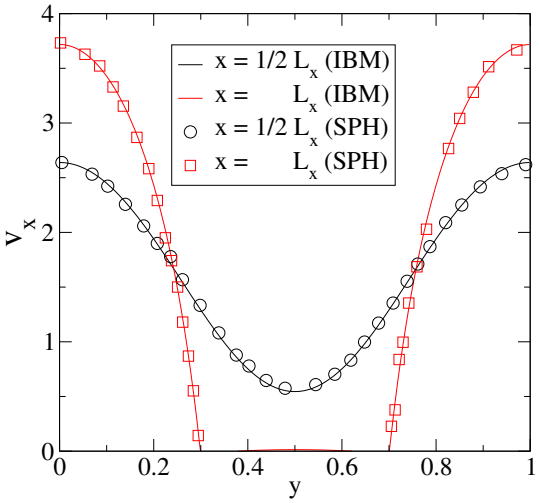

Figure 6.7: Comparison of our IBM results (solid lines) and the SPH results (symbols, with $Re = 0.03$) of Morris *et al.* [229]. Slices of v_x at $x = {}^1\!/_2 L_x, L_x$ for $R = 0.3$ demonstrate excellent agreement between the two codes. Note: a slightly larger flux ($Q = 1.32$) has been imposed to match their parameters. The SPH data was extracted using an online tool [228].

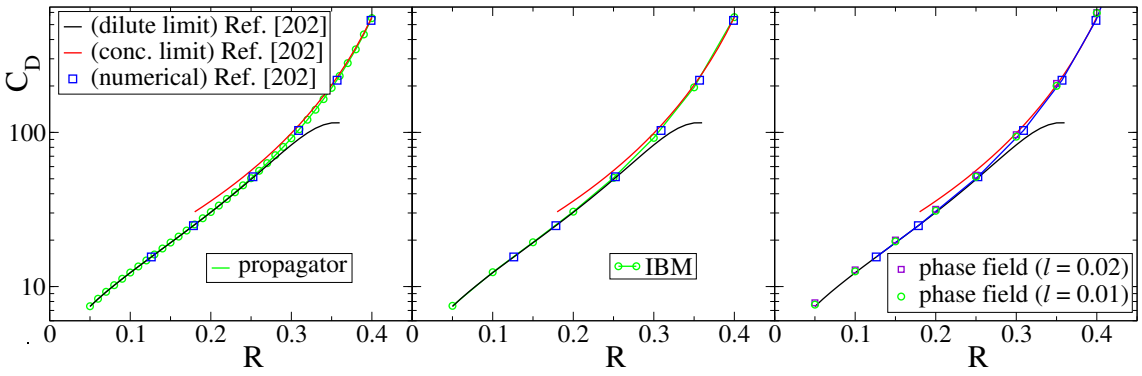

Figure 6.8: Simulations using the propagator (left), immersed boundary (mid) and phase-field (right) methods, all showing excellent agreement with the drag coefficient obtained by Sangani and Acrivos [202], across a wide range of R.

6.4 Newtonian Flows

While this work ultimately aims to understand the flow of complex fluids in porous media, much insight can be gained even by studying the Newtonian behaviour. We have shown that given the maturity of analytical, numerical and experimental studies, there exist many Newtonian benchmarks which our numerical codes can be checked against in quantitative detail.

Analysis of velocity maps can yield crucial information about the character of the flow as it passes the cylinders, elucidating in which regions extensional or shear rheology dominate. These maps remain instructive in the non-Newtonian limit. At small values of We the velocity field is largely unchanged [24, 230], but even for large We the general qualitative description will remain useful. Once we have decomposed the key features of the flow in the Newtonian limit into shear and extension, we can then examine the relevant constitutive curve for a given model to gauge the response. While this cannot provide quantitative information (such as the exact point of upturn) without simulation, this will allow us to make qualitative predictions about the response of different constitutive models.

6.4.1 Flow field characterisation

We have at our disposal a wide range of constitutive models with which we may model polymeric fluids. The behaviour of these models is typically known analytically in simple rheological flows such as planar extension or simple shear. Flows in porous media typically consist of a non-trivial combination of these flow types - for example the region of fluid flow past the top of the cylinder is shear dominated, whereas the region where the flow divides to pass the cylinder is extension dominated. To decode these we must develop a robust description of the *flow character*.

The necessary information is encoded in the velocity gradient tensor, which can

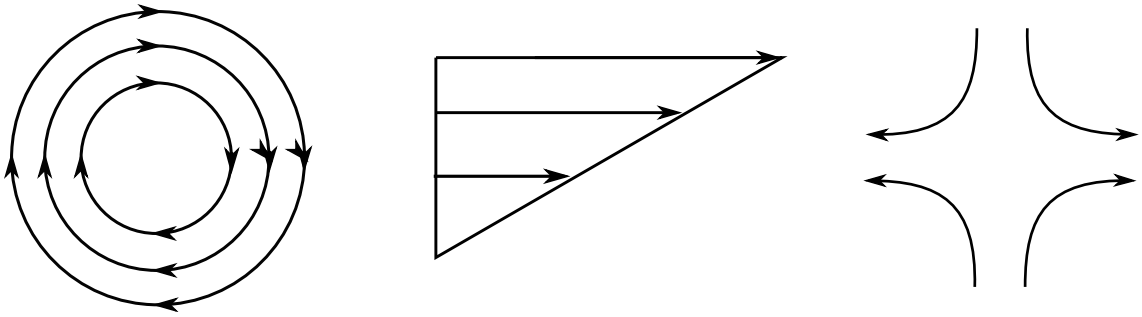

$q = -1$ $q = 0$ $q = +1$

Figure 6.9: A schematic representation of the three main flow types: rotation (left), shear (mid), and extension (right).

be decomposed in symmetric and anti-symmetric contributions,

$$\mathbf{K} = \begin{pmatrix} \partial_x v_x & \partial_x v_y \\ \partial_y v_x & \partial_y v_y \end{pmatrix} \tag{6.12}$$

$$= \underbrace{\dot{\varepsilon} \begin{pmatrix} +1 & 0 \\ 0 & -1 \end{pmatrix} + \frac{\dot{\gamma}}{2} \begin{pmatrix} 0 & +1 \\ +1 & 0 \end{pmatrix}}_{\mathbf{D}\text{, symmetric}} + \underbrace{\frac{\omega}{2} \begin{pmatrix} 0 & +1 \\ -1 & 0 \end{pmatrix}}_{\mathbf{\Omega}\text{, antisymmetric}}. \tag{6.13}$$

The eigenvalues of the symmetric and anti-symmetric parts are respectively

$$\lambda_{\mathbf{D}} = \pm\sqrt{\dot{\varepsilon}^2 + \frac{1}{4}\dot{\gamma}^2} \tag{6.14}$$

$$\lambda_{\mathbf{\Omega}} = \pm\sqrt{-\frac{1}{4}\omega^2}. \tag{6.15}$$

These can be combined (see, e.g., Refs. [205, 208]) to give a frame invariant description of the flow character,

$$q = \frac{\lambda_{\mathbf{D}}^2 - \lambda_{\mathbf{\Omega}}^2}{\lambda_{\mathbf{D}}^2 + \lambda_{\mathbf{\Omega}}^2}. \tag{6.16}$$

There then exist three distinct rheological regimes which can be captured by this analysis. The limit $q = +1$ describes extensional (equivalently pure shear) flows; for $q = -1$, the contribution is solely from $\lambda_{\mathbf{\Omega}}$ instead implying rotational flow. Finally when $q = 0$, the rate of rotation matches the rate of straining. Superimposing rotation ($q = -1$) and pure shear ($q = +1$) then gives us simple shear. The three cases are illustrated in Fig. 6.9.

6.4.2 Results for Newtonian fluids

Armed with a quantitative measure for flow character, we can characterise the flow fields in our porous geometry, for a range of radii and flow configurations. We present colour maps for q in Figs. 6.10/6.11, and interpret their meaning below. One caveat with this analysis is that the *magnitude* of the flow gradient is not represented, e.g., a very large pure extensional flow $\dot{\varepsilon}$ is indistinguishable from a very weak (yet pure) one. However we have checked separately that the key flow regions identified below generally coincide with regions of strong flow gradients.

Geometry Θ_a. For small R (Fig. 6.10 top left), we observe large regions of extension ($q = +1$, white) along the horizontal centreline as the flow diverges to pass around the cylinder and again as it converges downstream. Looking at the vertical gap between cylinders we find a mixture of rotational ($q = -1$ black) and shear ($q = 0$ pink) flows. However the dominant flow type for small R is extension, and this is reflected in our later viscoelastic results (see Fig. 6.17a top row).

However as R increases (Fig. 6.10 top right) the vertical and horizontal gaps between the cylinder and its periodic images become smaller. The flow character shifts, with the flow field now dominated by a large region of strong shearing around the tops of the cylinders. The large extensional region in the cylinder wake is mitigated, and is replaced (for $R > 0.3$ [205]) by recirculating regions. These regions promote a channel-like structure in the flow field [231], resulting in strong shear effects. This analysis is also consistent with our later viscoelastic results which show largest deformation of the polymer around the tops of the cylinders (see Fig. 6.17a bottom row).

Geometry Θ_b. For small R (Fig. 6.10 bottom left), we again see that the flow character is dominated by strong extensional effects along the horizontal centreline. The effect is even more prominent than for Θ_a as the gap between cylinders in which the wake forms is $\left(\sqrt{2}-1\right) L$ longer. Regions of extension also now extend quite far out vertically from the horizontal centreline.

The gaps between the cylinders are smallest in the diagonal directions and, par-

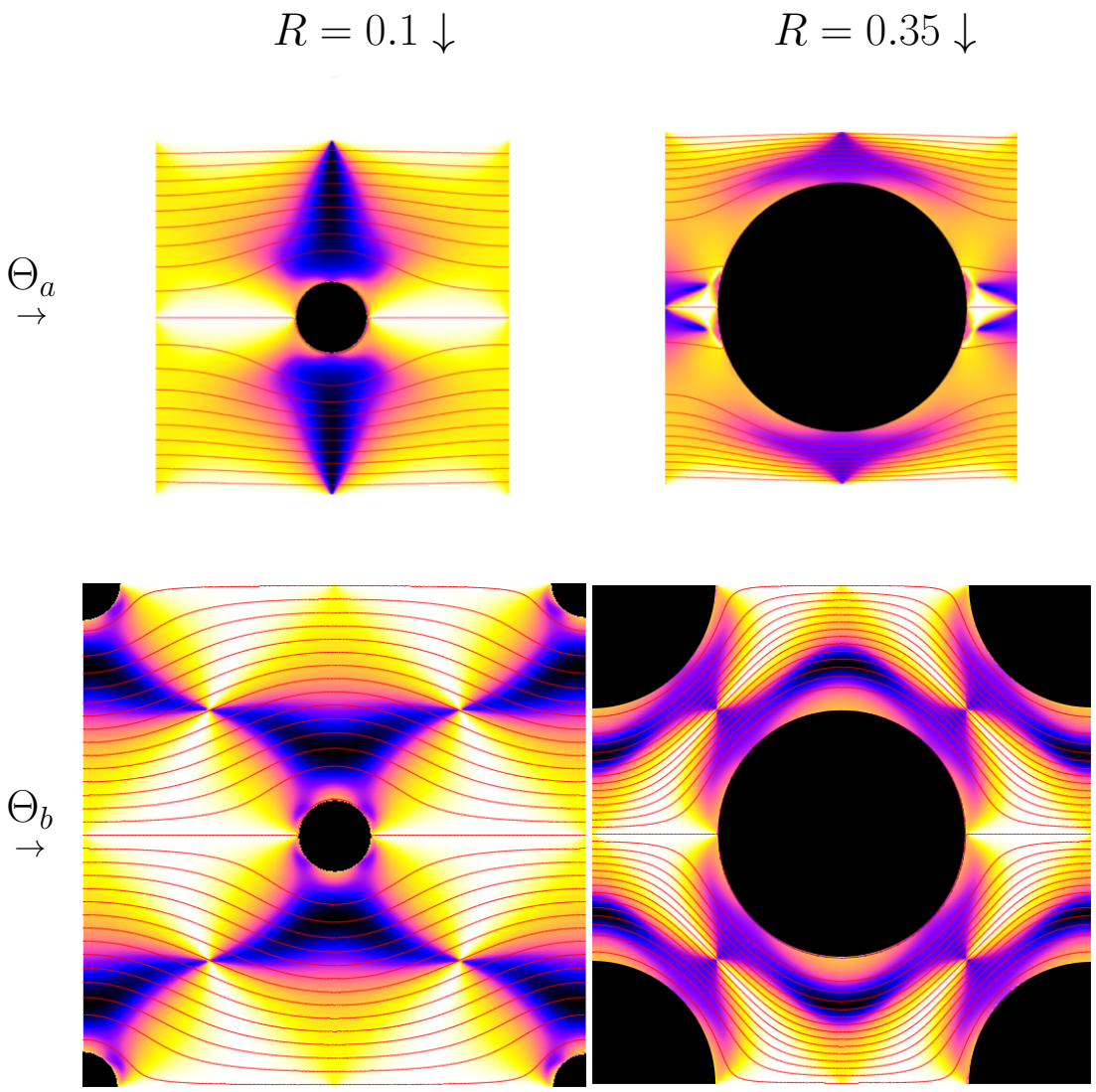

Figure 6.10: Flow character q for $R = 0.1$ (left column), $R = 0.35$ (right column), and for two flow orientations Θ_a (top row), Θ_b (bottom row). Colourmap shows **black** ($q = -1$, rotation) $\rightarrow$ **pink** ($q = 0$, shear) $\rightarrow$ **white** ($q = +1$, extension). Streamlines are marked with red lines. Maps have been orientated so that flow is always from left to right. Lower images also include part of neighbouring unit cell and so appear larger.

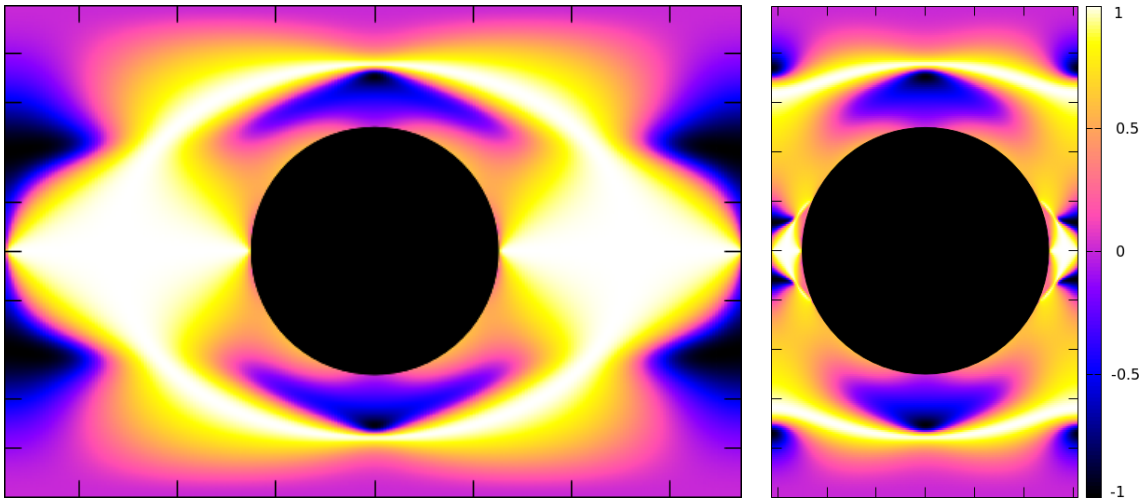

Figure 6.11: Flow character q (Eq. 6.16) for the two channel geometries. *Left:* Geometry Θ_c, where $L_x = 1.5$. *Right:* Geometry Θ_d, where $L_x = 0.625$.

ticularly for large R, strong shear flows can be observed in this region (Fig. 6.10 bottom left). However, contrary to Θ_a, appreciable extensional flows also remain in the wake of the cylinder. This can be understood by thinking of the limit of closely packed cylinders: for Θ_a the wake region disappears as $R \to L/2$, whereas for Θ_b the gap remains open (there is a space of length $(\sqrt{2}-1)R$ for touching cylinders). Our viscoelastic results (see Fig. 6.17) reflect this strong extensional component in the wake, and display appreciable deformation downstream of the cylinder for both small and large R. The flow character of Θ_b appears largely independent of R as the same features remain, only compressed to fit the smaller available area.

Geometries Θ_c/Θ_d. In geometries Θ_c, Θ_d we include solid, planar walls at $y = 0, L_y$. Colourmaps showing the flow character q are given in Fig. 6.11. The main difference with the biperiodic geometries is the region of strong shear ($q = 0$) near the walls, which appears for both cylinder spacings. However, only the closely spaced cylinders exhibit a recirculating regions (as seen for Θ_a at large R). In contrast, flow past the widely spaced (Θ_c) is unbroken. These colour maps also show that extensional flows in the wake are much more significant for Θ_c than for Θ_d, as there is a larger space for the wake to develop.

6.4.2.1 Limitations of analysis

The analysis so far has assumed that the polymer-fluid interaction is completely local. However the effect of advective terms in the polymer constitutive equation, $(\mathbf{v}.\nabla)\mathbf{C}$, cannot be ignored. Deformation in one region, for example due to extension, could then be advected to another region, where for example we might expect shear effects to dominate. By the same argument, diffusive terms (if included) of the form $\nabla^2\mathbf{C}$ could cause deformation to be spread to neighbouring regions, though we expect advective terms to have the most significant effect. Note that $\mathbf{v}(\mathbf{r})$ itself will change once an appreciable polymer stress develops, though for moderate We the effect is small enough for our analysis to remain useful.

6.4.2.2 Implications for non-Newtonian fluids

While the preceding analysis was performed for a Newtonian fluid, the insight gained remains a useful roadmap for a viscoelastic fluid. Based on the colourmaps of q, we might expect qualitatively different responses for a non-Newtonian fluid as we vary R. Specifically increasing R should have more effect for Θ_a, as the flow character exhibits more significant changes (from extension to shear dominated) than for Θ_b (which retains both shear and extensional regions across the range of R). This indeed is the case as we later show in Sec. 6.5.2.1 (compare Figs. 6.17a/b).

In order to understand the upturn in the drag, we can combine our understanding gained from colourmaps of q with knowledge of the rheological response of constitutive models in extension and simple shear. This should also allow us to influence the drag response of a fluid. For example, if for a given geometry the colour map of q shows large regions of extensional behaviour ($q = +1$), we might expect that the FENE-CR model exhibits a lower drag relative to Oldroyd-B, due to differences in their extensional rheology (see Sec. 6.5.1). However, if regions of shear ($q = 0$) are more prominent, then we might expect similar behaviour as both models share the same shear rheology. We now apply the insight gained for simple Newtonian flows to several complex, non-Newtonian fluids, doing so for a variety of geometries.

6.5 Viscoelastic Flows

With confidence in carefully benchmarked numerics, and with a firm understanding of the key flow regimes that arise in our ideal porous geometries for Newtonian flows, we are well placed to investigate the non-Newtonian behaviour. We consider two main classes of geometry: the unbounded biperiodic array of cylinders, and the line of uniformly spaced cylinders confined between walls.

In particular, we are interested in how the normalised drag χ varies as we increase We. Both experimentally [23] and numerically, plotting χ against We consistently shows two key features: an initial mild downturn in χ, followed by a significant increase above $We \approx \mathcal{O}(1)$ beyond which a transition to a time-dependent flowing state is often observed. In this study we aim to capture all these pieces of physics, and make some headway into understanding their origin by exploiting the properties of basic constitutive models in simple rheological protocols.

We are not aware of any 2D numerical study in the biperiodic geometry that captures fluctuations at high We, and while our results using IBM simulations are no exception, we do see the large increase in drag. Backed by our Newtonian analysis in the preceding section, we develop a robust prediction for the value of We at which the upturn occurs.

Interestingly, for pressure-driven flow past closely spaced cylinders with walls, recent SPH simulations have for the first time reported fluctuations which, above a threshold value We_c, scale in magnitude as $\sim (We - We_c)^{1/2}$ [25]. Inspired by this result, we attempt to reproduce these fluctuations using our immersed boundary code. While we do observe fluctuations (and the same scaling) at low resolutions, these disappear at sufficiently fine grid spacing, suggesting the results of Ref. [25] may be a numerical artefact.

6.5.1 Recap of constitutive models

We begin by briefly recapping the rheological properties of the models used in this study (see also Sec. 2.2.3). Despite concerns regarding unphysical behaviour, particularly in strong extensional flows [64], the Oldroyd-B model has remained a bench-

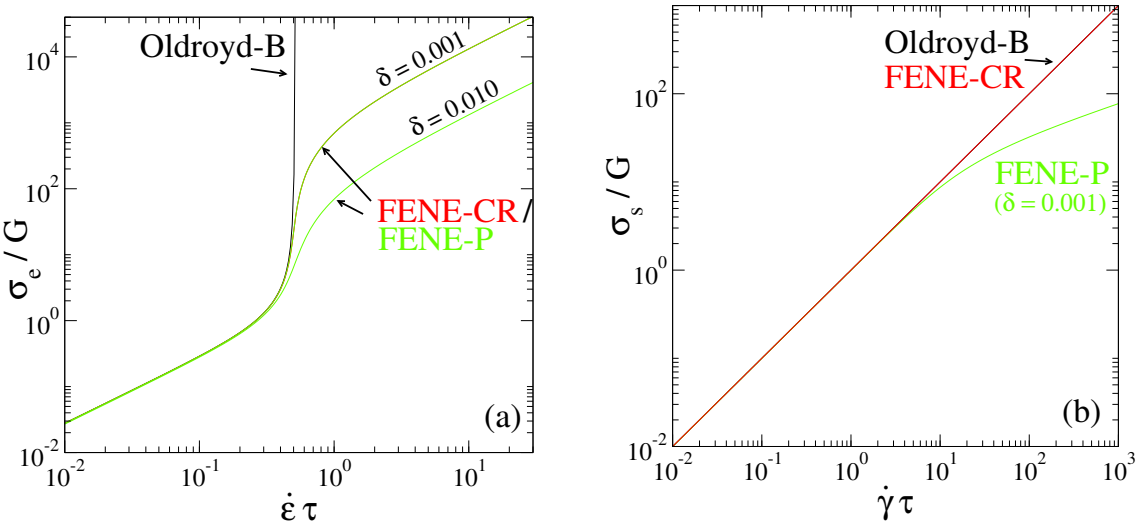

Figure 6.12: Steady state (a) extensional and (b) shear constitutive curves demonstrating the key rheological properties of Oldroyd-B, FENE-CR, and FENE-P models. **Parameters**: $\eta = 0$

mark fluid in studies of flows past cylinders as it provides one of the simplest descriptions of both viscous and elastic behaviour. The model is microscopically motivated by the description of polymer chains as pairs of beads connected by Hookean springs. While this simple description holds at small dimensionless extension rates ($\dot{\varepsilon}\tau \ll 1$), for a steady imposed flow with $\dot{\varepsilon}\tau > 1/2$, molecules tend towards a state of infinite stretch and no steady-state extensional stress is reached, see Fig. 6.12a.

More sophisticated models, such as FENE-CR and FENE-P which we additionally consider here, remedy this by imposing finite extensibility on the chains using a non-linear spring function of the form

$$k(\mathbf{C}) = \frac{1}{1 - \delta \mathrm{Tr}[\mathbf{C}]}, \tag{6.17}$$

where the limit $\delta \to 0$ reduces to Oldroyd-B. The effect on the extensional rheology is shown in Fig. 6.12a where we see that steady-state extensional stresses may be obtained above $\dot{\varepsilon}\tau > 1/2$ for both FENE-CR and FENE-P. Note that the FENE models are indistinguishable in pure extensional flows. Plotting the steady-state shear constitutive curve (Fig. 6.12b) shows that while both Oldroyd-B and FENE-CR have a constant shear viscosity, FENE-P starts to shear thin above $\dot{\gamma}\tau \approx 1$ [232].

Inclusion of diffusive terms. We have included an important modification to the original equations by introducing a diffusive term, $\ell^2/\tau \nabla^2 \mathbf{C}$, where ℓ is a small

lengthscale below which gradients in $\mathbf{C}$ are suppressed. We fix $\ell = 0.01$ in all that follows. Similar modifications to the JS model (which reduces to Oldroyd-B when slip parameter $a = 1$) have been made in the context of shear banding [110]. Specifically in the context of porous media, Gillissen included diffusive terms in his study of a FENE fluid past a biperiodic array of cylinders [208]. Thomases *et al.* also recently showed that a small diffusive contribution can support a finite polymer stress in a qualitatively similar fashion to FENE models [233, 234].

Strictly, gradient terms in $\mathbf{C}$ require a boundary condition (BC) at the walls and at the cylinder surface. For simplicity we choose zero gradient at the walls $\partial_y \mathbf{C} = 0$ (when present). Because our simulations include polymer everywhere, including inside the posts, we do not specify a BC on the cylinder edge. Because no shear banding effects occur for the constitutive models under consideration we anticipate that this is unimportant. Since the results presented here were obtained, we have developed the ability to impose $\partial_\perp \mathbf{C} = 0$ at the cylinder edge (see Sec. 7.8 for details of a related implementation), and future work will include this.

6.5.1.1 Characterisation of polymer

Analogous to the decomposition in Eq. 6.15, we can extract the principle eigenvalue of $\mathbf{C}$

$$\lambda_{\mathbf{C}} = \frac{T + \sqrt{T^2 - 4\Delta}}{2} \tag{6.18}$$

where $T = C_{xx} + C_{yy}$ is the trace, and $\Delta = C_{xx}C_{yy} - C_{xy}C_{xy}$ the determinant of $\mathbf{C}$. This defines a single quantity that, at any point in space, describes the degree of deformation of the polymer molecules in that vicinity allowing us to at least qualitatively compare with experiments which probe the polymeric microstructure, such as flow birefringence [52, 235] or NMR spectroscopy [48].

6.5.2 Biperiodic geometries

We now report our main viscoelastic results, beginning with the simpler class of geometry, i.e., the biperiodic array of cylinders without walls. For a Stokes flow of a Newtonian fluid, there is no difference between the two flow orientations (Θ_a, Θ_b)

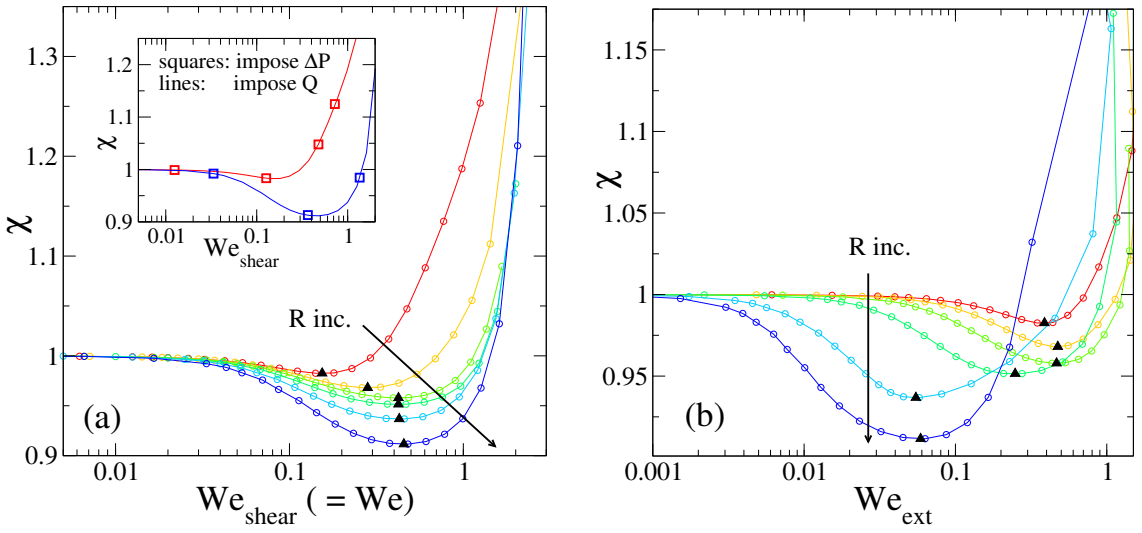

Figure 6.13: Normalised drag χ plotted against (a) shear Eq. 6.19 and (b) extensional Eq. 6.20 Weissenberg numbers for Θ_a. This shows that the upturns (solid black triangles) for large R are given by a constant We_{shear}, and by a constant We_{ext} for small R. Both plots show data from the same set of simulations, for a range of radii $R = 0.10$ (red) $\rightarrow 0.35$ (blue) with an Oldroyd-B fluid. *Inset* (a) demonstrates that we obtain the same drag if we instead impose ΔP and measure Q (and therefore We).

when measuring the force exerted on the cylinder. This results from the linearity of Stokesian force balance and the symmetry of the square array. However given that the flow character q is noticeably different for each configuration, we expect non-Newtonian fluids to exhibit marked differences between the two orientations as we vary R. All of our biperiodic results were obtained by imposing a flux and measuring the pressure drop. However we have explicitly checked that these are unchanged if instead we impose a pressure drop (see Fig. 6.13a inset).

6.5.2.1 Biperiodic geometry: flow orientation Θ_a

Our analysis of configuration Θ_a (where the imposed flow is at 0° to the array) in the Newtonian limit revealed that while the flow field in general comprises a mixture of extensional and shear flows, the clear trend is that extensional flows dominate at small R, and shear flows dominate at large R.

With this in mind, we begin by plotting the normalised drag χ against our definition of the Weissenberg number (which captures the effects of shear between

cylinders),

$$We_{\text{shear}} \equiv We = \alpha \frac{V\tau}{L_y - 2R} \quad \text{where } \alpha = 1 \text{ (no walls)}, \tag{6.19}$$

for a range of post radii R (Fig. 6.13a). At vanishingly small We, we recover the Newtonian limit $\chi = 1$ (as expected by definition). As we increase We, the normalised drag exhibits a slight decrease. While this is consistently observed in other studies [25, 208, 236], the result is counter-intuitive as the fluid under consideration (Oldroyd-B) exhibits neither shear- nor extension-thinning (see Fig. 6.12). However there is not yet a clear explanation for this phenomenon. The depth of the downturn becomes most pronounced at large R, for which shearing flows dominate. Then beyond the upturn, defined as the point at which $\frac{\partial \chi}{\partial We} = 0$, we see the large increase in the drag observed experimentally.

Interestingly, the Weissenberg number at which the upturn occurs, We^{up}, exhibits a dependence on R. We now ask, in light of the understanding gained from the Newtonian flow physics, if we can understand this dependence and therefore try to predict the point of upturn for any cylinder radius.

For large R, the flow field consists mainly of shearing regions (see Fig. 6.10, top right). In Fig. 6.14, we plot the Weissenberg number at which the upturn occurs, defined as $We^{\text{up}} \equiv We\left(\frac{\partial \chi}{\partial We} = 0\right)$, as a function of R. This reveals that for large R our definition of the Weissenberg number, which was motivated by the shear-rate in the gap between cylinders, predicts a single number for the point of the upturn $We^{\text{up}}_{\text{shear}} \approx 0.43$. This demonstrates that the key physics at large R is captured by a shear Weissenberg number.

However at small R, the flow field is dominated by extensional effects in the cylinder wake (see Fig. 6.10, top left), and our shear-based Weissenberg number fails to predict a single point of upturn. We can instead define an extensional Weissenberg number

$$We_{\text{ext}} = \dot{\varepsilon}_{max}\tau, \tag{6.20}$$

where $\dot{\varepsilon}_{max}$ is the maximum extension rate along the horizontal centreline. Replotting the same data using We_{ext} (see Fig. 6.13b), we find that this extensional Weissenberg number yields a single value for the upturn in the small R limit, $We^{\text{up}}_{\text{ext}} \approx 0.45$. Above $R \approx 0.2$, we find that the definition no longer predicts a

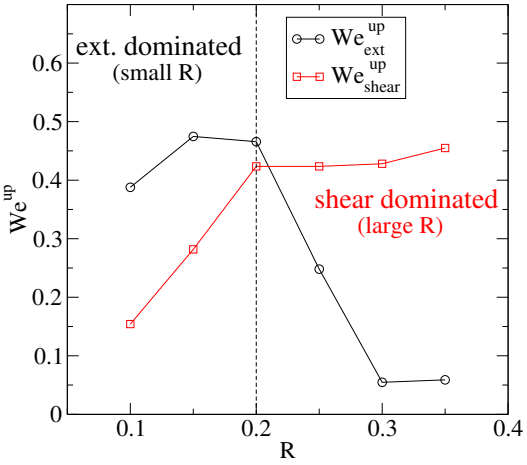

Figure 6.14: Dependence of We^{up} (i.e., the value of We at which the upturn occurs) on R. For large R (where shear dominates), We_{shear} captures a single value for the upturn, whereas for small R (where extension dominates), We_{ext} describes the behaviour better.

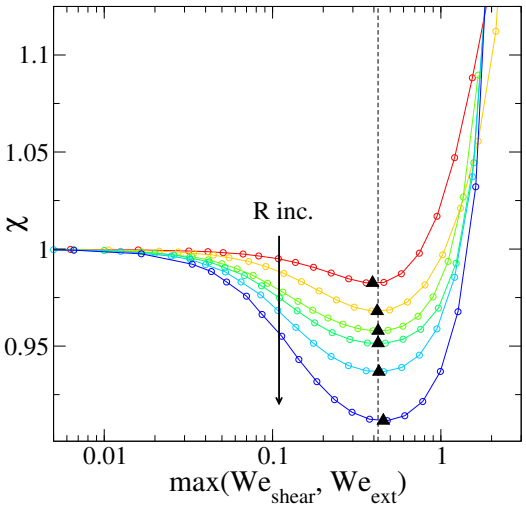

Figure 6.15: Replotting the data in Fig. 6.13 using $\max(We_{\mathrm{shear}}, We_{\mathrm{ext}})$ for any run, we find that the upturn is well described by a single value $We^{\mathrm{up}} \approx 0.42$ (dashed line). Upturns in χ are marked with solid black triangles.

single value, as we transition to the shearing regime. This crossover between shear and extension dominated regimes is most clearly illustrated in Fig. 6.14, where we plot We^{up} against R for our two definitions. This shows a transition between the two regimes at $R \approx 0.2$.

We have shown that no single Weissenberg number can accurately predict the upturn across the full range of R, due the combination of extensional and shear effects. However applying shear- and extensional specific Weissenberg numbers to the large and small R regimes respectively, demonstrates that a single value for the upturn can be obtained, with the crossover occurring at $R \approx 0.2$. This suggests that to predict the Weissenberg number of the upturn We^{up}, at any radius considered here, we could define a composite Weissenberg number, e.g., $We_{\mathrm{comp}} \equiv \max\left(We_{\mathrm{shear}}, We_{\mathrm{ext}}\right)$, which encompasses both shear and extensional regimes. Replotting our data using this definition (Fig. 6.15) demonstrates that we can predict the point of upturn with reasonable accuracy across the full range of radii considered.

Having explored the response of an Oldroyd-B fluid, we now ask how these results are modified by more sophisticated constitutive models (FENE-P and FENE-CR),

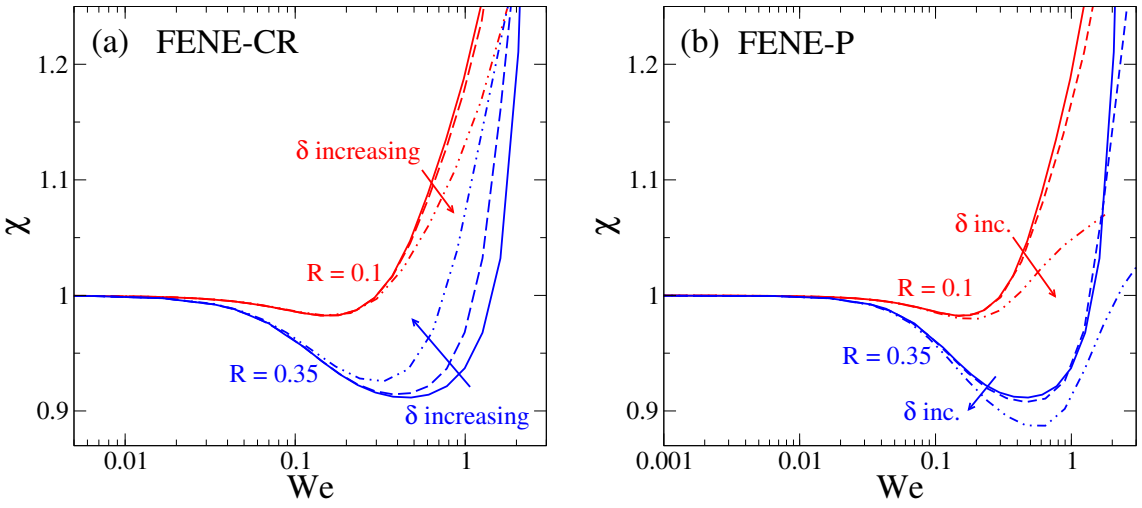

Figure 6.16: Differences in the $\chi - We$ curves between Oldroyd-B and (a) FENE-CR, (b) FENE-P models, for $R = 0.1$ (red curves) and 0.35 (blue curves). **Parameters:** $\delta = 0$ (Oldroyd-B), $0.001, 0.01$, geometry Θ_a.

by focusing on one small $R = 0.1$ (extension dominated) and one large $R = 0.35$ (shear dominated). Additionally we consider colour maps of $\lambda^{\mathbf{C}}$ (the largest eigenvalue of the conformation tensor, Eq. 6.18) to examine where significant deformation occurs.

FENE-CR. In Fig. 6.16a we explore how the $\chi - We$ curves change as the extensibility δ is increased from zero (where $\delta = 0$ corresponds to Oldroyd-B). While the steady-state shear behaviour of FENE-CR is identical to that of Oldroyd-B, in extensional flow the FENE-CR model mitigates the divergence of the steady-state extensional viscosity seen with the Oldroyd-B model (see Fig. 6.12a). Therefore if shear flows are dominant then we should expect little change between the two models. In contrast if extensional flows are strong then there should be a marked difference in the polymer response between FENE-CR and Oldroyd-B.

For small $R = 0.1$ (Fig. 6.16a red curves), we observe that the non-linearity of the spring force only becomes effective once past the upturn, suggesting that extensional deformation is a key component of the drag increase. The colour maps of $\lambda^{\mathbf{C}}$ are also informative. At small R (Fig. 6.17a top row), the flow character q (left panel) tells us that the extensional flows in the wake dominate. As expected, this is reflected in $\lambda^{\mathbf{C}}$ which shows more dramatic deformation for Oldroyd-B (middle

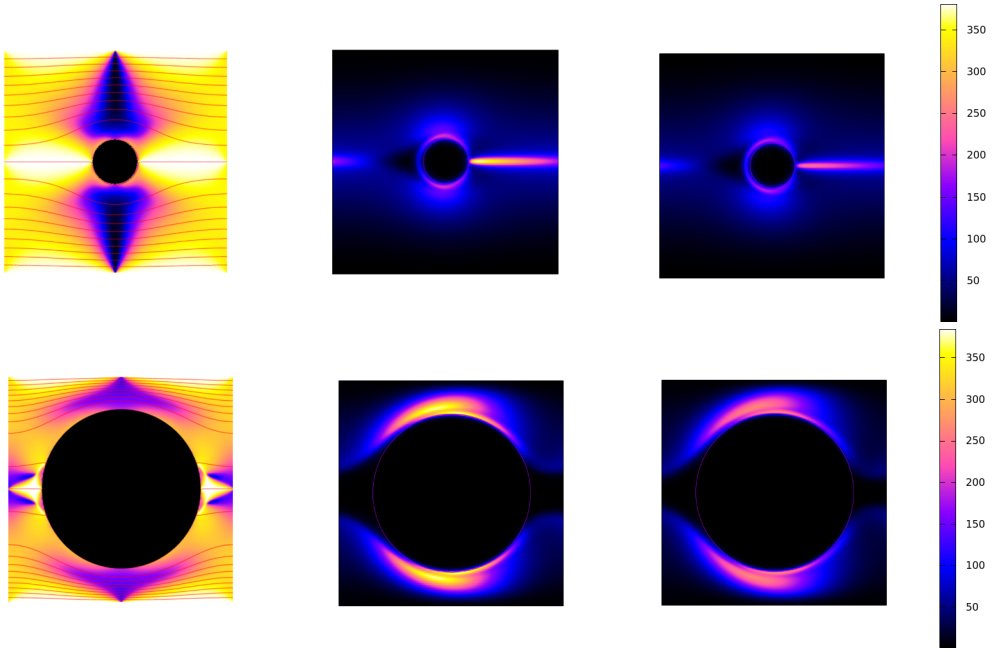

(a) Orientation Θ_a. *Top row*: $R = 0.1$, $We = 0$ (left), $We = 1.25$ (mid and right). *Bottom row*: $R = 0.35$, $We = 0$ (left), $We = 1$ (mid and right).

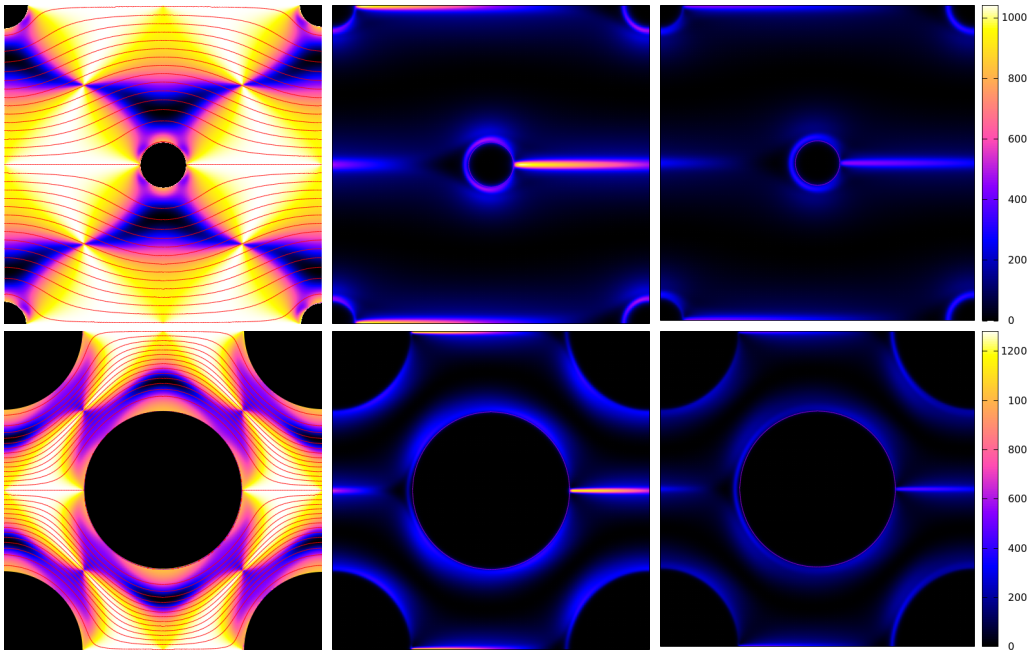

(b) Orientation Θ_b. *Top row*: $R = 0.1$, $We = 0$ (left), $We = 1.25$ (mid and right). *Bottom row*: $R = 0.35$, $We = 0$ (left), $We = 1$ (mid and right).

Figure 6.17: Flow character and response of Oldroyd-B and FENE-CR fluids in Θ_a and Θ_b orientations. Flow is always from the left. *Left col:* flow character q for $We = 0$, where white denotes extension and purple denotes shear, also shown are streamlines (red lines). Principle eigenvalue of strain tensor $\lambda^{\mathbf{C}}$ for Oldroyd-B (*mid col*) and FENE-CR (*right col*, with $\delta = 0.001$). Radii are $R = 0.1$ (*top rows*), $R = 0.35$ (*bottom rows*).

panel) than for FENE-CR (right panel).

Interestingly, at large $R = 0.35$ (Fig. 6.16a blue curves) where shear is the dominant flow character, we observe that the drag increases with δ at a given We, despite both models having the same shear-response. This is qualitatively similar to the results of Liu [196] (differences in values for β and δ make direct comparison difficult). A possible explanation is that polymer molecules undergo elongation upstream, allowing them to align as they pass in the vertical gap between cylinders: as δ increases this elongation is suppressed be the FENE spring force, and the effect is lessened, resulting in an increase in the drag χ.

To add further weight to this argument, we examine the relevant colourmap (Fig. 6.17a bottom row). Indeed we find noticeably less deformation for FENE-CR, even though its shear rheology is indistinguishable from Oldroyd-B. This intriguing result implies that the deformation in the sheared region near the cylinder tops must partly arise from the advected result of earlier extensional deformation, for which the two models differ in response. Our results highlight that while the local analysis of Sec. 6.4 is instructive, convective effects clearly cannot be ignored.

FENE-P. The response of FENE-P, which shear-thins relative to the other models (see Fig. 6.12b), is shown in Fig. 6.16b. For $R = 0.35$, where shear flows are particularly prevalent, the drag decreases relative to Oldroyd-B. This is because the polymer viscosity reduces as the flow rate, and therefore the characteristic shear-rate, increases. Interestingly, this shear-thinning effect appears to overcome the *increase* in drag (relative to Oldroyd-B) observed for the FENE-CR model (see above).

For the smaller radius $R = 0.1$, the shear-thinning effect can still be seen, though we find large values of δ are required before the effect is appreciable (i.e., before the FENE-P data differs significantly from FENE-CR). This is consistent with our assertion that extension dominates at small R, where we expect the key physics to be relatively insensitive to the shear rheology of the fluid.

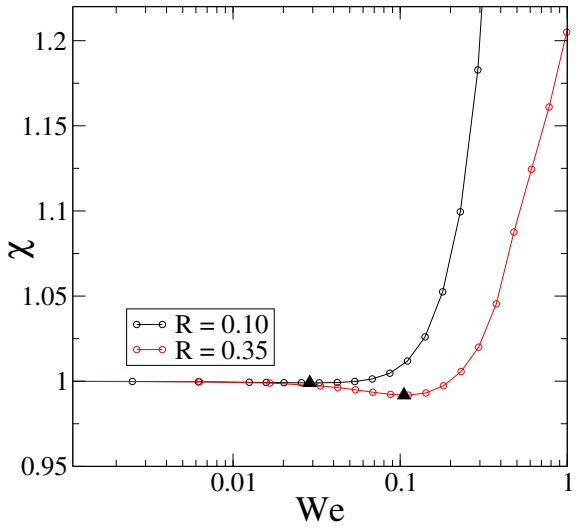

Figure 6.18: Normalised drag χ against We for $R = 0.1, 0.35$, for an Oldroyd-B fluid in geometry Θ_b. Triangles mark the point of upturn in the drag.

6.5.2.2 Biperiodic geometry: orientation Θ_b

For orientation Θ_b (where the imposed flow is at 45°), we still observe a downturn but surprisingly it is significantly less pronounced, see Fig. 6.18. Our results in configuration Θ_a suggest that upstream extensional deformation, which remains a strong feature here, should produce an effective shear thinning effect (despite the fact that in simple shear, Oldroyd-B doesn't shear thin). This however is not reflected in the downturn.

A possible reason could be that shearing in the immediate vicinity of the cylinder top/bottom is less prominent (compare left column of Fig. 6.17a and 6.17b). Particularly at small R we also see that the upturn sets in at a much earlier We, likely due to the greater prominence of regions of extensional flow.

An examination of the colour maps of $\lambda^{\mathbf{C}}$ in Fig. 6.17b reveals that both small and large R are dominated by extensional effects in the cylinder wake. This is consistent with the observation made earlier for Newtonian flows in Sec. 6.4.1 that changing radius has little effect in geometry Θ_b. The large deformation seen in the wake is again mitigated by the extensional regularisation of FENE-CR (compare middle and right columns in Fig. 6.17b).

6.5.2.3 Finite size effects.

Note that we did not find evidence of fluctuations across the full range of parameters explored, for either biperiodic geometry. It is natural to ask whether this absence is due to finite size effects, i.e., are we missing fluctuations with wavelengths greater than L_x?

To address this we repeated simulations for a range of We in both geometries with $L'_x = 2L_x$ (two posts) and $L'_x = 4L_x$ (four posts). In both cases the results were exactly as for the single cylinder, with no fluctuations of any kind observed. While it is possible that fluctuations only appear at wavelengths longer than the maximum of 4 cylinders considered here, this seems unlikely given that we observe no indication of the instability in these smaller simulation boxes.

6.5.3 Walled geometries

We now turn our attention to the walled geometry, which has been more widely considered in the literature [25,211–213,237]. We follow the convention of fixing the cylinder radius at $R = 0.25$ [24, 25] and now take the horizontal distance between cylinder centres, L_x, as the quantity to be varied in our numerics. Note that $L_x = 2R$ corresponds to touching cylinders, and $L_x \to \infty$ is the single cylinder limit.

We consider here two cases, widely spaced (Θ_c, $L_x = 1.5$) and closely spaced (Θ_d, $L_x = 0.625$) cylinders. The former forms a reasonable approximation to the single cylinder limit, and we observe only steady flow solutions for the range of We explored. Our results are in reasonable agreement with previous studies, though we do not reproduce the fluctuating state seen at high We in Ref. [25]. This may by due to convergence issues, as we discuss below.

The more severe diverging-converging nature of the closely-spaced geometry (Θ_d) leads to more intriguing results. Ref. [25] reports time-dependent steady-states that we discuss in detail in Sec. 6.5.3.2 below. While we can reproduce these fluctuations at low numerical resolution, our fully converged results produce only time-independent states, suggesting that the physics reported in that study may be a numerical artefact of poor grid resolution.

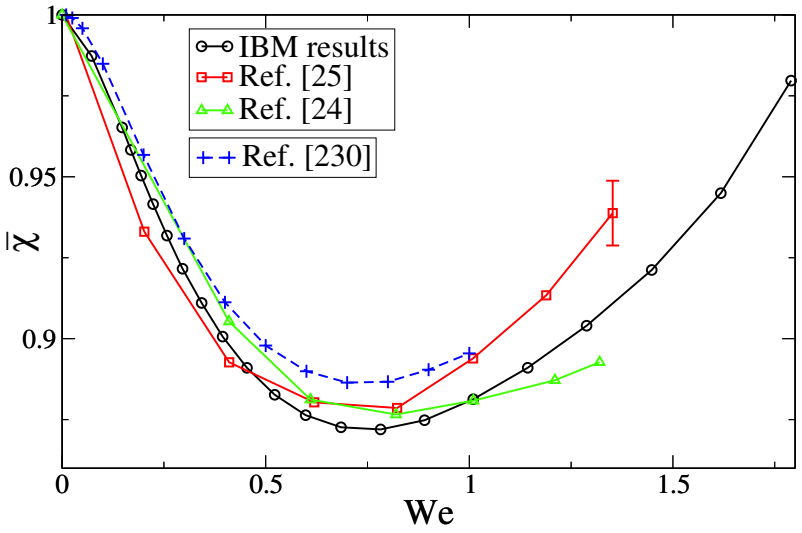

Figure 6.19: Normalised drag against We for widely spaced cylinders Θ_c. Also shown are data for the same parameters from Refs. [24, 25], (and single cylinder data from Ref. [230], blue dashed line). **Note**: to allow comparison with these studies, we temporarily adopt the drag definition which only includes contributions from the cylinder (not the walls), which we label $\bar{\chi}$.

6.5.3.1 Walled geometry: widely spaced Θ_c

In the biperiodic geometries considered thus far, the pressure drop can be directly obtained from the force on the cylinder (see also the discussion in Sec. 6.2.1). In the channel geometry the pressure drop also includes a contribution from the forces on the walls and is no longer equivalent to the cylinder forces alone. For both geometries we report the normalised drag χ which includes wall effects (when present). However in order to compare with earlier works that only report the force on the cylinder (i.e., not the total pressure drop), we also temporarily adopt the normalised cylinder drag $\bar{\chi}$ which ignores the wall contribution (this quantity is only plotted in Fig. 6.19, the remainder of our work uses χ). Note that $\bar{\chi} = \chi$ for biperiodic geometries.

Plotting $\bar{\chi}$ against We in Fig. 6.19 shows qualitatively similar behaviour to the Θ_a biperiodic geometry: initially a downturn is seen in the normalised drag, followed by an upturn at $We \approx 0.8$. We also plot the results of [24, 25] with which we find reasonable qualitative agreement, and quantitative agreement on the point of upturn. Unlike the work of Vázquez-Quesada *et al.* however, we fail to capture fluctuations across the range of We studied. It is possible that such fluctuations might also appear at higher values of We, though we find numerical convergence

impractical once beyond $We \approx 1.75$.

Interestingly, plotting the results of Alves *et al.* for a single cylinder [230] reveals that even $L_x = 1.5$ is a reasonable approximation to this limit, at least in terms of the drag. This is consistent with the observations of Liu *et al.* [24] that for $L_x = 1.5$, the flow at the midpoint between cylinders is "95% that of fully developed channel flow".

Comparing with the closely spaced geometry (Fig. 6.20), we find that the widely spaced cylinders exhibit a significantly larger downturn. Given that the wake region (the gap between cylinders) is 8 times larger for Θ_c, significant extensional flows can develop. Consistent with the mechanism described for Θ_a (where elongated chains upstream can be advected past the shear region at lower stress) it is our observation that the downturn is more pronounced for Θ_c than Θ_d.

6.5.3.2 Walled geometry: closely spaced Θ_d

For the closely spaced cylinders, we now return to our original definition of the normalised drag χ based on the total pressure drop. We initially see a less pronounced downturn in χ at small We relative to Θ_c (Fig. 6.19), but flows similarly remain time-independent Fig. 6.20 (inset). Beyond a critical We, our numerical results *seemingly* exhibit two dramatic yet distinct regions where the drag increases, and time-dependent flows develop, consistent with earlier studies [25]. However we later discovered during rigorous convergence tests that such oscillations are purely a numerical artefact.

We first present the non-converged results and speculate on their relation to existing work in the literature, then present some preliminary (converged) results and discuss how more rapid convergence could be achieved in future studies.

Non-converged results. At a critical Weissenberg number $We^{\text{osc}} \approx 1.85$, our non-converged data exhibits a region where the normalised drag dramatically increases above $\chi = 1$, see Fig. 6.20a. Examining an example time series $We(t)$ in this region (Fig. 6.20b, series B) reveals that the flow becomes oscillatory, with a well defined period $\sim 4\tau$. In this oscillatory regime at least, the magnitude of the

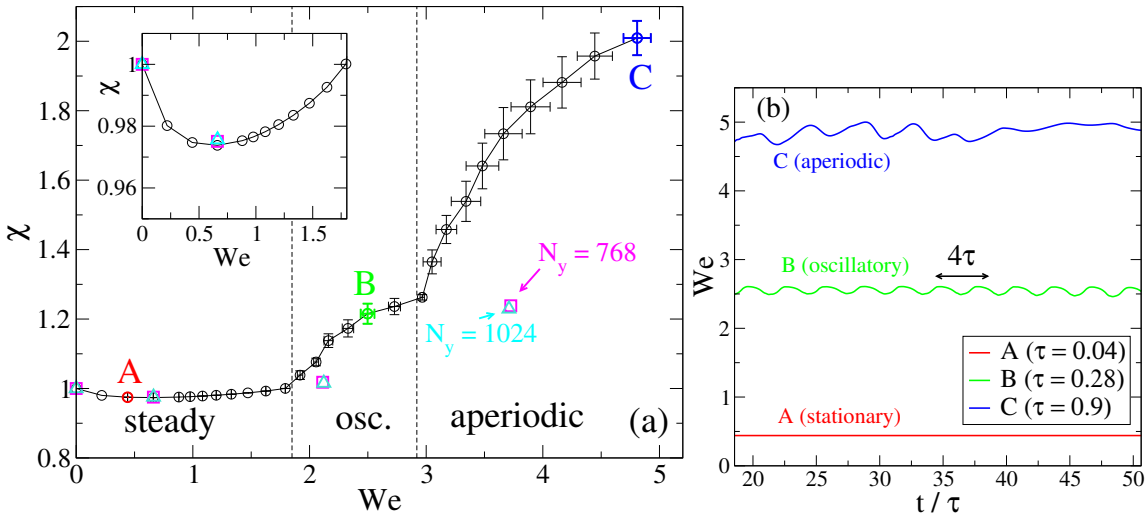

Figure 6.20: (a) Normalised drag against We for the closely spaced geometry Θ_d. For $N_y = 512$ (black circles, **under-resolved**) we observe three regimes: steady (low We), oscillatory (intermediate We), and aperiodic (large We). Inset shows the initial mild downturn. Data from higher resolution runs (red squares $N_y = 768$, green triangles $N_y = 1024$) are also marked. (b) Time series, rescaled by τ, for the marked points in (a) with $N_y = 512$.

fluctuations (taken here as the standard deviation of the time series in Fig. 6.21b) appears to scale as $\sim (We - We^{\text{osc}})^{1/2}$ (see Fig. 6.21b). This is the same scaling as identified by Vázquez-Quesada *et al.* (Fig. 6.21a and Ref. [25]), and is suggestive of a supercritical Hopf bifurcation [128].

At higher We still, a second transition to a distinct time-dependent state can be seen, now characterised by an increasingly aperiodic time series $We(t)$, albeit one where the dominant period is still $\sim 4\tau$ (see Fig. 6.20b, series C). This is also accompanied by a large increase in the drag. The scaling behaviour of the fluctuations in this regime is harder to ascertain without longer statistical averaging, however a least-squares fit suggests that these also grow as $\sim (We - We^{\text{aper}})^{1/2}$, where $We^{\text{aper}} \approx 2.95$. (See Fig. 6.21b.)

Converged results. The time required to run the above simulations (with $N_y = 512$) is of the order of weeks. This is mainly because the Hookean restoring force for the immersed boundary involves a large spring constant (see Eq. 6.10), which in turn demands particularly small timesteps.

In order to run simulations at higher resolutions within a practical timeframe, we

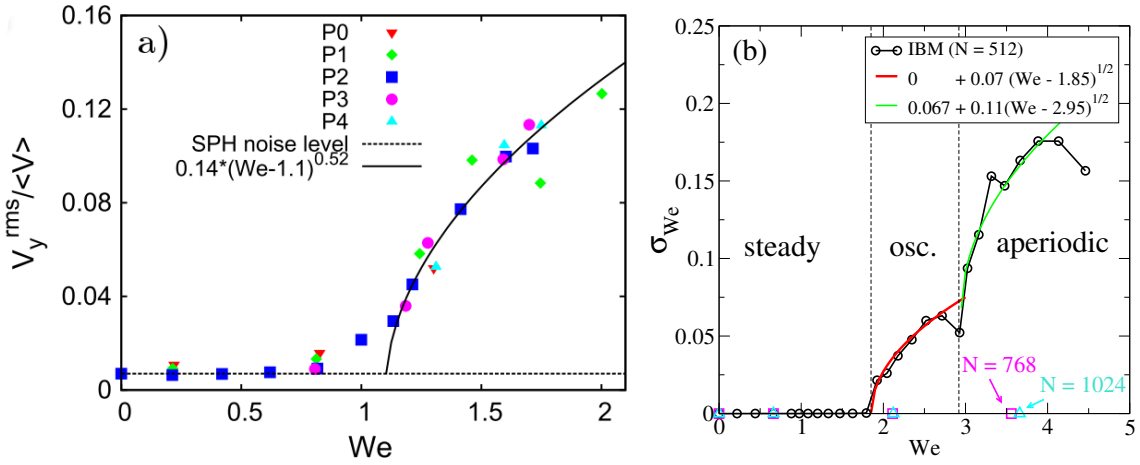

Figure 6.21: (a) Data from Ref. [25] showing a increase in fluctuations above $We^{osc} \sim 1.1$. (b) Plot of the standard deviation σ_{We} against mean μ_{We}, extracted from the time series $We(t)$. Data from higher resolution runs (magenta squares $N_y = 768$, cyan triangles $N_y = 1024$) are also marked.

found it necessary to develop a parallel version of the code. However the increased computational cost means we have only checked a small number of points, which we overlay on Figs. 6.20, 6.21 (magenta squares $N_y = 768$, cyan triangles $N_y = 1024$).

At small We, this shows that our results are converged for $N_y = 512$. However as We increases, we see that $N_y = 512$ is no longer sufficient to resolve the dynamics and that $N_y = 768$ or even $N_y = 1024$ is required. Importantly, at these higher resolutions the fluctuations seen for $N_y = 512$ disappear, suggesting that Hopf-like instability described in Fig. 6.21b is simply an artefact of under-resolution.

The maximum resolution used in the SPH simulations of Ref. [25] is 120×192 particles. While SPH resolutions can not directly be compared with the number of points in a finite-difference scheme, we suspect that the fluctuations reported in that study are a numerical artefact of similar origin. Our results show that, in order to fully converge, resolutions *an order of magnitude finer* than used in Ref. [25] are required. Another possible explanation for the difference is that the SPH method used in Ref. [25] intrinsically requires a non-zero Reynolds number, although this is small enough ($\mathrm{Re} \sim \mathcal{O}(10^{-2})$) that inertial instabilities are unlikely to be responsible. Another consequence of the method is that the fluid is not completely incompressible (in contrast we set $\nabla.\mathbf{v} = 0$), meaning that there is finite speed of sound.

We have checked that the results presented earlier in this chapter do not suffer

from under-resolution. In those cases, the contractive-expansive nature of the flow is considerably less severe than for θ_d, and the convergence requirements are less severe.

Strategies for faster convergence. Clearly the severe convergence requirements of the confined cylinder geometry are problematic. We finish by proposing some strategies for increasing the efficiency of our numerics in future works.

The main timestep constraint arises for the immersed boundary force evolution equation (see Eq. 6.10). In contrast the timestep required for the polymeric dynamics is comparatively large. Therefore one strategy might then be: at each 'polymeric timestep' (which is relatively large), iteratively solve immersed boundary forces at a much smaller timestep (with $\mathbf{C}$ fixed). Another option might be to adopt the method proposed by Hulsen *et al.* [199], which casts the polymer constitutive equation in a form where the logarithm of the conformation tensor $\mathbf{C}$ is evolved, leading to increased numerical stability.

6.6 Conclusions

The problem of viscoelastic flow past an array of cylinders, acting as a minimal model of a real porous material, has attracted the attention of the fluid dynamics community for a some time. Part of the reason the field remains so active is that numerical convergence is notoriously difficult, and some 20 years after the initial viscoelastic simulations were performed consensus is yet to be reached. Specifically, the benchmark problem of 2D pressure-driven flow of an Oldroyd-B fluid past an array of confined cylinders, and whether unsteady solutions exist at high We, remains open.

Our results using immersed boundary simulations demonstrated that poorly converged results can still produce plausible physics at high We. For example at large We, using resolutions comparable with Ref. [25] (who report fluctuations), we observed the development of oscillatory steady-states where the timescale of fluctuations is set by the polymer relaxation time τ. These grew in magnitude as $\sim (We - We_{osc})^{1/2}$, as reported in Ref. [25]. We found that resolutions an order of

magnitude greater than Ref. [25] were required for full convergence, at which the above fluctuations no longer appear. Importantly, seemingly convincing physics can arise in non-converged simulations, where oscillations appear on a timescale set by the polymer relaxation time.

Convergence in the lesser studied biperiodic geometry was easier to obtain. We began in this geometry by considering Newtonian flow, which we analysed to identify the regions dominated by shear or extension. When the imposed flow is head on Θ_a, the flow field at small R is dominated by extensional flows in the wake of the cylinder. In contrast at large R, shearing past the cylinder tops dominates. Our viscoelastic results suggest that care should be taken when defining the Weissenberg number, as many numerical studies fix the cylinder size and therefore do not fully explore the dependency of We on R. Indeed by adopting separate definitions of shear and extensional Weissenberg numbers at large and small R respectively, we can accurately predict the point of upturn in the drag for all R considered. While our extensional Weissenberg number is unknown *a priori*, our results do illustrate that the physics of flow in porous media is not well represented by a single dimensionless number. The dominant flow type varies greatly with pore size, and this should be accounted for in any definition of the Weissenberg number.

The above flow character analysis is local and neglects the effects of advection. To address this, we studied how the polymer deformation varies between constitutive models whose rheological behaviour is identical in simple shear, but different in extension (i.e., comparing Oldroyd-B and FENE-CR models). Interestingly, at large R, we observed less deformation in the shearing regions for FENE-CR, despite both models sharing a common shear rheology. This suggests that upstream extensional deformation may also contribute as the polymer is advected through the vertical gap between cylinders.

While the upturn in the drag can be reliably captured using a minimal 2D model of viscoelastic flow in porous media, it appears that the time-dependent states seen experimentally at larger We remain elusive. Whether these states would eventually develop at large enough We, or in fully 3D simulations, would form a natural extension for future work (see Sec. 8.2 for details).

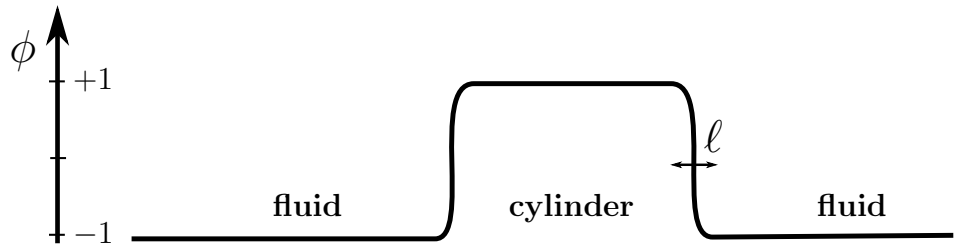

Figure 6.22: Schematic demonstrating how the phase field method works, plotting the profile of ϕ in a slice through a cylinder. Solid regions ($\phi = +1$) are separated from fluid regions ($\phi = -1$) by a diffuse interface of width ℓ.

6.7 Appendix I: Alternative numerical methods

The main numerical method used in this chapter is the immersed boundary method (described in Sec. 6.3). However during the project we also developed two other numerical methods: as these proved impractical at high *We*, these were mainly used to verify the immersed boundary code (at low to intermediate *We*).

6.7.1 Phase field

The phase field method, inspired by the work of Tanaka [238], models everywhere in the simulation cell as containing polymer, including inside the cylinders. Note that this technique is related to the phase field model used in Chap. 7. As both phase field and propagator methods only form a minor part of the study, we only briefly sketch their derivations here.

We introduce a phase field ϕ which prescribes which regions of the simulation are fluid ($\phi = -1$) and which are solid ($\phi = +1$). The relaxation time and elastic modulus of the polymer are then made functions of ϕ

$$\tau = \tau(\phi) = \tau_{\text{fluid}} + \left(\frac{\phi + 1}{2}\right) \tau_{\text{solid}} \tag{6.21}$$

$$G = G(\phi) = G_{\text{fluid}} + \left(\frac{\phi + 1}{2}\right) G_{\text{solid}}, \tag{6.22}$$

where $\tau_{\text{fluid}} G_{\text{fluid}} = \frac{\eta(1-\beta)}{\beta}$, and $\tau_{\text{solid}} G_{\text{solid}}$ is converged $\to \infty$. These functions are chosen to yield values describing a typical polymer (or Newtonian fluid with $\tau_{\text{fluid}} \to 0$) in the fluid region, and very large in the cylinder region so as to effect a solid cylinder.

The two phases are separated by a tanh profile of width ℓ to avoid discontinuities in the simulation. An visual overview of the method is given in Fig. 6.22. For the dynamics of ϕ we then take

$$\partial_t \phi + \mathbf{v}.\nabla\phi = 0. \tag{6.23}$$

Finally we tether the solid post in place by introducing a Hookean restoring force

$$\mathbf{f}(\mathbf{r}, t) = -\kappa\phi(\mathbf{r}, t)\left(\mathbf{x}_{CM}(t) - \mathbf{x}_0\right), \tag{6.24}$$

where $\mathbf{x}_{CM}(t)$ is the centre of mass position of the cylinder, $\mathbf{x}_0$ is the desired location, and κ is a large spring constant which we converge $\kappa \to \infty$. This in practice renders $\mathbf{v} = \mathbf{0}$ in Eq. 6.23, resulting in a static post.

6.7.2 Propagator method

Whereas the latter methods impose tether forces allowing us to converge on a no-slip boundary condition at the cylinder surface (by taking $\kappa \to \infty$), our third method rigorously imposes it. Credit is due to Prof. Suzanne Fielding who developed the method (in the context of squirming microswimmers [239], though it is also descends from the Stokesian Dynamics formulation of Brady and Bossis [240]).

We sketch here the derivation. First we add a source term to the Stokes force balance equation for the p^{th} cylinder of the form

$$\mathbf{f}_p(r, \theta) = \delta(r - R)\mathbf{f}(\theta), \tag{6.25}$$

where δ is the Dirac delta function, and (r, θ) are radial coordinates relative to the cylinder centre. Radial and tangential components of this $\mathbf{f}$ are then decomposed into Fourier modes in θ.

In order to satisfy force balance, we construct the matrix which describes the linear relationship between velocities and forces. We invert this to find the Fourier components $e^{im\theta}$ of $\mathbf{f}$ needed to ensure that the velocity boundary conditions (no-slip and no-permeation) are satisfied at the cylinder surface. These Fourier components then allow us to reconstruct the velocities anywhere in the cell. We converge our numerics on the number of surface modes.

The generalisation to include polymer is rather involved. Briefly, gradients in the polymer stress contribute a second source term to force balance $\mathbf{S} = \nabla.\boldsymbol{\Sigma}$ which is known, and when Fourier transformed can be included in the linear algebra problem outlined above. Velocities are reconstructed with the inclusion of this extra source term, and in turn are fed back into the polymer evolution equation. While we successfully managed to implement this viscoelastic generalisation, the increased CPU time required to calculate the flow everywhere in the simulation cell at each timestep proved prohibitively large for practical use, particularly at large *We*.

7

Contact line dynamics

7.1 Introduction

Understanding the way in which a contact line (the line along which an interface separating two immiscible fluids intersects a solid boundary wall) moves under an imposed flow is a problem of fundamental importance in wetting dynamics. It underpins a wide range of phenomena in nature, for example in the functional adaptation of many biological systems [2,241,242], as well as in technological applications: from oil recovery [243] to inkjet printing and microfluidics [244]. From these examples, it has become clear that experimental progress needs to be accompanied by the development of physical models and computational methods that can accurately capture wetting dynamics, even in complex geometries.

We begin by introducing some basic concepts in wetting and relate these to the contact line singularity, before reviewing previous theoretical and numerical

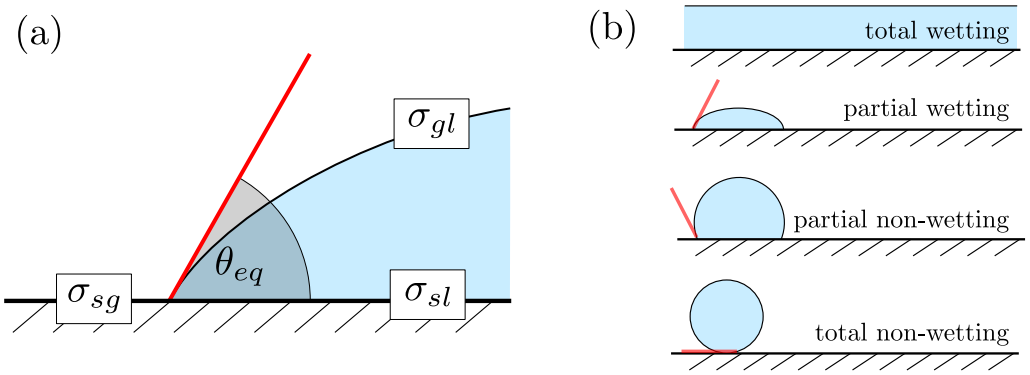

Figure 7.1: (a) Schematic of a liquid droplet on a solid substrate at equilibrium, and the equilibrium contact angle it defines, θ_{eq}. Marked are the surface tensions for the solid, liquid and gas phases. (b) Examples of four possible states corresponding to $\theta_{eq} = 0$ (complete wetting), $0 < \theta_{eq} < 180°$ (partial wetting/non-wetting), and $\theta_{eq} = 180°$ (completely dry). Also marked (where possible) are the tangents that the droplet makes to the surface (red lines).

attempts to remedy it.

Wetting. The fluid mechanics of wetting has attracted a long history of study [245]. Over two centuries ago, Young related the contact angle of a fluid droplet at equilibrium on a smooth solid substrate to the surface tensions between solid, liquid and gas (σ_{gl}, σ_{sg}, σ_{sl}) via the formula [26]

$$\cos\theta_w = \frac{\sigma_{sg} - \sigma_{sl}}{\sigma_{gl}}, \tag{7.1}$$

which we illustrate schematically in Fig. 7.1a. This represents the minimum free-energy configuration of the droplet. There are then several possible states that the droplet can adopt, depending on the properties of the fluid and the substrate.

If $\sigma_{gl} = \sigma_{sg} - \sigma_{sl}$, then the contact angle is zero and the resulting state is one of perfect or *complete wetting*, i.e., the equilibrium state consists of a macroscopic liquid layer covering the whole substrate. States where $0 < \theta_{eq} < 90°$ are then referred to as *partially wetting*. For $\theta_{eq} > 90°$ the droplet is described as *partially non-wetting*, characterised by the intrusion of gas 'wedges' from the sides on the droplet forming a bead. The other extremum is then $\theta_{eq} = \pi$, i.e., the *total non-wetting state*. The latter is particularly rare save, for example, mercury on a solid surface. Examples of these are all given in Fig. 7.1b. Transitions between these states can be driven by changing the surface tension. For example, Lee *et al.* showed that a non-wetting

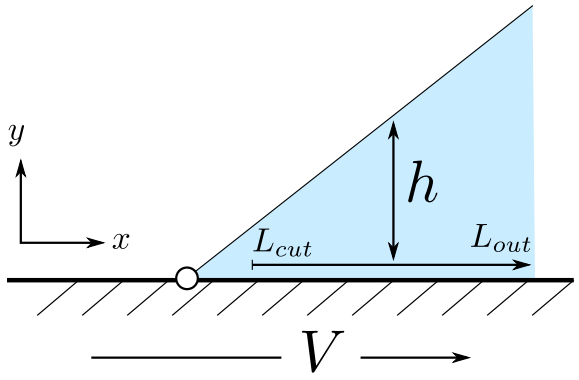

Figure 7.2: Schematic of the wedge flow in the vicinity of a contact line, from the frame of reference in which the contact line is static. The contact line points in the direction perpendicular to the page (at the white circle).

material can be made to wet (partially or totally) by lowering the surface tension on the fluid interface using surfactants [246].

Note that Eq. 7.1 also applies if we replace the gas phase with a second liquid, immiscible with the original liquid phase, as considered throughout this chapter. Our model describes two immiscible fluids with neutral wetting conditions, i.e., with an equilibrium contact angle $\theta_{eq} = 90°$. However other wetting conditions can easily be included by introducing a more general boundary condition [28, 30].

While the static behaviour of a droplet can be treated purely from free energy considerations, for most practical applications the fluids are not at rest and the dynamics of the fluid-fluid interface become important.

Contact line singularity. Any purely macroscopic treatment, where the two fluids are considered to be separated by a strictly sharp interface, and subject to a strictly no-slip condition on the fluid-velocity at the solid wall, has long been recognised to predict a non-integrable stress singularity for any non-zero velocity of the contact line [247, 248]. To understand the origin of this singularity, it is instructive to consider fluid motion in the reference frame of the contact line (see Fig. 7.2).

We recap here the simplified argument of de Gennes [248]. The typical velocity gradient as we approach the contact line from the right is $d_y u_x \sim V/h$. The viscous dissipation across the film width is $\int_0^h dy \eta \left(d_y u_x\right)^2 = \eta h \left(\frac{V}{h}\right)^2$ [249]. Integrating this

from a reference L_{out} in towards a cutoff distance L_{cut} from the contact line gives a viscous dissipation per time per length of

$$D_{visc} \approx \int_{L_{cut}}^{L_{out}} \eta h \left(\frac{V}{h}\right)^2 dx \approx \eta \frac{V^2}{\theta} \int_{L_{cut}}^{L_{out}} \frac{dx}{x} = \frac{\eta V^2}{\theta} \ln(L_{out}/L_{cut}), \tag{7.2}$$

where we have used the fact that $h(x) \approx \theta x$ for small contact angles. This diverges logarithmically in the limit of slip, i.e., $L_{cut} \to 0$. This is clearly at odds with the commonplace experience that the contact line does, in fact, move!

To regularise this singularity, the macroscopic picture must be supplemented by additional physics that intervenes on shorter, microscopic lengthscales. One approach is to relax the no-slip boundary condition on the fluid velocity, by inserting a slip boundary condition in a region of microscopic size ξ in the vicinity of the contact line. This can be done by hand [250, 251], for example by imposing a slip velocity $v_s = U \exp(-|x|/\xi)$, where x is the distance along the wall away from the contact line, or by choosing $v_s = \xi\sigma/\eta$, where σ and η are the wall stress and fluid viscosity respectively. In any computational study, slip can also arise indirectly as a numerical artefact [252].

Diffuse interface modelling. Another approach is to keep the no-slip boundary condition and instead to recognise that any interface between two fluids can never be perfectly sharp, but in practice must have some non-zero microscopic diffuse width ℓ. Accordingly, the use of diffusive interface models [28, 253] has gained increasing popularity in recent years. A diffuse interface model of liquid-gas coexistence then accommodates contact line motion by a condensation-evaporation mechanism which, in some small region within close proximity of the contact line, slowly transfers matter from one side of the interface to the other [27, 254–256]. Similarly, a diffuse interface model of coexisting immiscible binary fluids accommodates contact line motion via a slow intermolecular diffusion of the two fluids across the interface between them, again acting in a small region in the vicinity of the contact line [28, 29, 255].

Diffuse interface models [28,253] are also convenient to implement numerically. A phase field (which we describe using a scalar order parameter $\phi(\mathbf{x}, t)$) is introduced to distinguish one fluid from another, with the length scale that characterises the

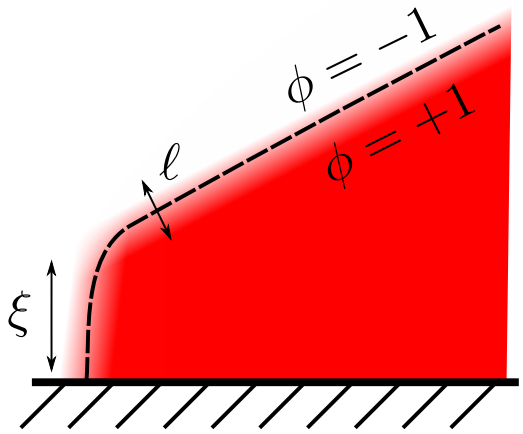

Figure 7.3: Schematic illustration of a diffuse interface model in the vicinity of the slip region, where bulk fluid phases (where the order parameter $\phi_\pm = \pm 1$) are separated by a interface of finite width ℓ. The characteristic slip length ξ is also marked.

variation of this field across the interface between the fluids prescribing the interfacial width, ℓ. (See Fig. 7.3.) An advection-diffusion (Cahn-Hilliard) equation then determines the evolution of this order parameter, and hence of the interface position. This is solved in tandem with the Navier-Stokes equation for the fluid velocity field. A key advantage of this approach is that all computational grid points are treated on an equal footing, without any need to explicitly track the position of the interface. In this way, even complex flow geometries can be simulated conveniently.

It is important to emphasize, as first elucidated by Cox [257], that although the physical origins of contact line motion may differ according to the detailed microscopic physics invoked (wall slip, intermolecular diffusion across the interface, etc.), the macroscopic hydrodynamics far from the contact line nonetheless converges to a universal solution that is informed by the microscopics only in the sense of being rescaled by a single parameter, the "slip length" ξ, that emerges from this underlying microscopic physics. An important problem within any model of the microscopics is therefore to determine this emergent slip length ξ: not only because it is a key variable that determines the macroscopic wetting and fluid dynamics, but also because it sets a scale to which other length scales (surface heterogeneities, droplet size, etc.) must be compared.

Aims of chapter. With that motivation in mind, the primary aim of this chapter is to determine the scaling of the slip length within a diffuse interface model of immiscible binary fluids. We assume the fluids to have matched viscosity η, and denote by M the mobility parameter characterising the rate of intermolecular diffusion in the Cahn-Hilliard equation. In the existing literature, (at least) three apparently contradictory scalings have been proposed. Several authors (e.g., Refs. [28,30]) suggest that $\xi \sim l_D$ where $l_D = (M\eta)^{1/2}$ is the characteristic lengthscale below which intermolecular diffusion dominates advection and above which the opposite is true. For convenience we call this the diffusion length in what follows, and we emphasise that it is determined only by the macroscopic quantities M and η. In contrast, Briant and Yeomans [29] suggest a different scaling, $\xi \sim \sqrt{l_D \ell}$, which is the geometric mean of the macroscopic diffusion length and the microscopic interface width. And while these two proposed scalings do not have any dependence on the imposed flow velocity, Ref. [258] in contrast suggested that the slip length *does* depend on the velocity as $\propto V_0^{-1/2}$.

In view of these apparently contradictory predictions, an important contribution of this work is to provide a coherent picture that fully reconciles two of these existing predictions, by showing each to apply in a different regime of parameter space. (Qualitative similarities with the third are found at large velocities, though we do not obtain their precise scaling.) This is achieved by extensive numerical studies performed across unprecedently wide ranges of the two relevant control parameters. Specifically, we explore four decades of the dimensionless ratio $M\eta/\ell^2 = l_D^2/\ell^2$ of the (squared) macroscopic diffusion length to the (squared) microscopic interface width; and three decades of the Capillary number $\mathrm{Ca} \equiv \eta V_0/\sigma$, which adimensionalises the imposed flow velocity V_0 in terms of an intrinsic interfacial velocity scale (here σ is the interfacial surface tension, see Eq. 7.6). Moreover, we use three different, independently designed (and coded) numerical methods, and show their results to be in excellent quantitative agreement across all decades.

For small values of the Capillary number Ca, corresponding to low imposed flow velocities, we demonstrate that the slip length converges to a well-defined value that is independent of the velocity V_0. Any dependence on the velocity is only

observed for Ca > 0.01, and while we do observe a decrease in the slip length in this fast flowing regime, our data do not appear to recover the power law $\xi \propto V_0^{-1/2}$ proposed analytically in Ref. [258].

The chapter generally focuses on the slow flow regime, Ca < 0.01, in which the slip length ξ is independent of the flow rate V_0. We show that, in the limit of large l_D/ℓ, the slip length scales as $\xi \propto l_D$, informed only by the macroscopic lengthscale l_D. This agrees with the original prediction of Refs. [28, 30] and corresponds to the sharp interface limit of the diffuse interface model, in which the microscopic length ℓ essentially drops out of the problem, apart from the role it plays in regularising the contact line singularity. In contrast, for small l_D/ℓ we find that the slip length scales as $\xi \propto (l_D\ell)^{1/2}$, as proposed by Ref. [29]. This corresponds to the diffuse interface limit in which the emergent slip length does depend on the underlying microscopic length ℓ. In this way we reconcile the two previously apparently contradictory scalings, showing each to apply in a different limiting regime of l_D/ℓ. The crossover between these two is furthermore consistent with the sharp interface limit discussed by [30].

The fact that the slip length ξ is in general different from the interface width l, and indeed greatly exceeds it for large l_D/ℓ, has a clear practical consequence for any simulation: the resolution of the full wetting dynamics appears only on a lengthscale corresponding to the larger of the interface width and the slip length. This, in turn, limits the region of parameter space that can be considered reliable in any numerical study.

We provide additional evidence for the distinction between the diffuse interface limit $l_D/\ell \ll 1$, in which the microscopic physics informs ξ, and the sharp interface limit $l_D/\ell \gg 1$, in which it does not, by performing further simulations in which the we modify the interfacial (microscopic) contribution to the underlying free energy functional of the binary fluid (Sec. 7.4.2). We show that the slip length depends on this modification only in the diffuse interface regime. In the sharp interface regime of large l_D/ℓ, the slip length continues to depend only on the macroscopic dynamical variables, η and M, free of this modification to the microscopic interfacial term.

Finally, we test the validity of Cox's formula [257] for the dynamic contact angle

as function of the Capillary number in the different slip length regimes (Sec. 7.4.3). Our numerical results are in good agreement with Cox's analytical result if we allow the slip length to be rescaled by a dimensionless parameter. Moreover this parameter appears, suggestively, to converge to unity in the sharp interface limit, but is significantly smaller in the diffuse interface limit.

We now describe the models, methods and setups we employ to compute the slip lengths and dynamic contact angles, then present our results in Sec. 7.4. Finally, we summarise our key findings and discuss avenues for further work in Sec. 7.5.

7.2 Model

In this section we specify the model that we shall use throughout this chapter, starting with the thermodynamics in Sec. 7.2.1 then the dynamical equations of motion in Sec. 7.2.3. We then specify the flow geometry and boundary conditions in Sec. 7.2.4.

7.2.1 Thermodynamics

We consider a binary mixture of two mutually phobic fluids, A and B, and denote the volume fraction of fluid A by the continuum phase field $\phi(\mathbf{r}, t)$. The volume fraction of fluid B is then simply 1-ϕ by mass conservation and need not be considered separately. We consider a Landau free energy [169]

$$F = \int_V f_\phi \, dV = \int_V \left[\frac{G}{4}(\phi^2 - 1)^2 + \frac{G\ell^2}{2}(\nabla\phi)^2 \right] dV, \tag{7.3}$$

which allows a coexistence of two bulk phases: an A-rich phase with $\phi_A = 1$ and a B-rich phase with $\phi_B = -1$. The bulk constant G has dimensions of energy per unit volume (or equivalently of force per unit area, and so modulus). If the two fluids have different affinities to the solid surface, a surface (wetting) contribution to the free energy must be added [30, 259, 260] to the right hand side of Eq. 7.3.

The chemical potential μ follows as a functional derivative of free energy density ψ_b with respect to ϕ, giving

$$\mu = -G\phi + G\phi^3 - G\ell^2 \nabla^2\phi. \tag{7.4}$$

In equilibrium the chemical potential $\mu = 0$. Assuming a flat interface of infinite extent in the $y - z$ plane, with the interfacial normal in the x direction and the interface located at $x = 0$, we then obtain an interfacial solution of the form

$$\phi = \tanh\left(\frac{x}{\sqrt{2}\ell}\right), \tag{7.5}$$

with a homogeneous B-rich phase for $x \ll -\ell$ and homogeneous A-rich phase for $x \gg \ell$. The interfacial constant ℓ specifies the characteristic length scale over which ϕ varies in between these two phases, and so corresponds to the interfacial width. The surface tension associated with this interface is given by [29]

$$\sigma = \frac{2\sqrt{2}G\ell}{3}. \tag{7.6}$$

7.2.2 Generalisation of Landau ϕ^4 theory

So far, we have specified the Landau free energy in the form most commonly used in the literature. It will also be instructive in what follows to consider the extent to which our results for the slip length do or don't depend on the microscopic details of the model used. Accordingly, we now generalise the free energy slightly to give

$$F' = \int_V f'_\phi \, dV = \int_V \left[\frac{G}{4}(\phi^2 - 1)^2 + \frac{Gl^2}{2}(\nabla\phi)^2 + \alpha\frac{Gl^4}{4}(\nabla^2\phi)^2\right] dV. \tag{7.7}$$

Compared to the original free energy defined above, this has an additional interfacial curvature term of amplitude set by α. The associated chemical potential is

$$\mu = G\left(-\phi + \phi^3 - \ell^2\,\nabla^2\phi - \alpha\ell^4\,\nabla^4\phi\right). \tag{7.8}$$

It is important to note that the bulk terms are unaltered, with the modification affecting only interfacial gradient terms involving powers of $l\,\nabla$. A careful comparison of the original model, for which $\alpha = 0$, with this generalised model, for which $\alpha > 0$, will allow us to demonstrate below that the contact line's slip length is independent of the microscopic details, as specified by α, in the sharp interface regime $l_D/l \gg 1$. In contrast, in the diffuse interface regime $l_D/l \ll 1$ we do find that the slip length depends on the microscopics, via α.

7.2.3 Equations of motion

The dynamics of the order parameter field is specified by the Cahn-Hilliard equation (see e.g., [169]) generalised to include an advective term:

$$(\partial_t + \mathbf{v}.\nabla)\,\phi = M\nabla^2\mu. \tag{7.9}$$

Here M is the molecular mobility, which we assume constant. The fluid velocity and pressure fields, $\mathbf{v}(\mathbf{r},t)$ and $p(\mathbf{r},t)$, obey the continuity and Navier-Stokes equations

$$\partial_t\rho + \nabla.(\rho\mathbf{v}) = 0, \tag{7.10a}$$

$$\rho\,(\partial_t + \mathbf{v}.\nabla)\,\mathbf{v} = \eta\nabla^2\mathbf{v} - \nabla p - \phi\nabla\mu. \tag{7.10b}$$

We denote by ρ and η the fluid density and viscosity respectively, assuming throughout that the two fluids are perfectly matched in both density and viscosity. In the Navier-Stokes equation, gradients in the chemical potential contribute an additional forcing term to the fluid motion, $\phi\nabla\mu$, which can also be written as $-\mu\nabla\phi$ [261].

We assume throughout incompressible flow and also take the inertialess limit of zero Reynolds number (Stokes flow). These limits can be implemented exactly for two of our numerical methods (MI and MII described in Sec. 7.3 below) by setting to zero the terms on the left-hand-sides of Eq. 7.10a (incompressibility) and Eq. 7.10b (zero inertia). The Lattice-Boltzmann method (MIII) intrinsically requires a small but non-zero inertia and compressibility, though our numerical results confirm the effects of this difference to be negligible for the problem considered here.

7.2.4 Geometry, initialisation and boundary conditions

We consider flow between infinite flat parallel plates a distance L_y apart, with plate normals in the y direction. The phase field is initialised in an equilibrium state with a bridge of A-rich phase, in which $\phi = +1$, separated by two vertical diffuse interfaces of width ℓ at $x = L_x/4$ and $3L_x/4$ from B-rich phases on either side, where $\phi = -1$. The equilibrium contact angle is taken to be $\theta_{eq} = 90°$ (see Fig. 7.4), corresponding to neutral wetting conditions. Throughout we define the position of the interface itself by the locus $\phi = 0$.

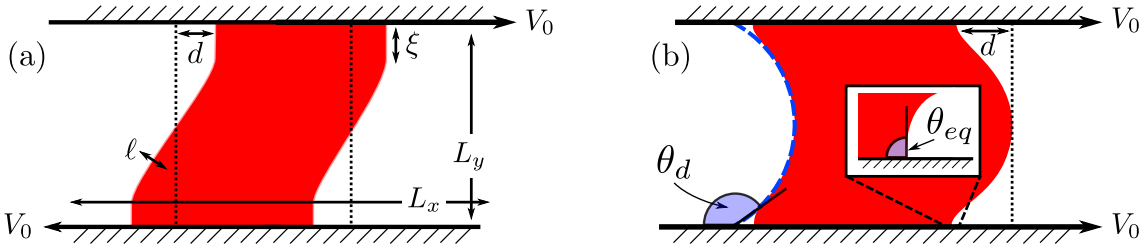

Figure 7.4: Schematics illustrating typical steady-states in our channel geometry, in the reference frame in which the contact line is static. Marked are the key lengthscales: slip-length ξ, interface displacement d, channel dimensions L_x, L_y, and diffuse interface width ℓ. In panel (a) a shear flow is imposed by moving the plates with equal and opposite velocities $\pm V_0$. In panel (b) a Poiseuille flow is imposed by applying a pressure drop along the length of the channel. The definitions for the dynamic (θ_d, macroscopic) and equilibrium (θ_{eq}, microscopic) contact angles are also shown.

The fluid is taken to be initially at rest with $\mathbf{v} = 0$ everywhere. Starting from this initial condition, we then implement one of two common flow protocols: boundary-driven planar Couette flow and pressure-drive planar Poiseuille flow.

In the first of these, a constant shear-rate $\dot{\gamma}$ is applied by moving the top and bottom plates at velocities $V_0 = \pm\frac{1}{2}\dot{\gamma}L_y$. This deforms the phase field and for small $\mathrm{Ca} \equiv \eta V_0/\sigma \lesssim 0.1$ a steady state is reached in which the interface has displaced a distance $d \propto \pm\mathrm{Ca}$ at the top and bottom walls, as shown in Fig. 7.4a. The deformed bridge is then stationary, with the contact lines moving at a velocity $\mp V_0$ relative to the top and bottom walls.

In the Poiseuille protocol the flow is driven by an imposed pressure drop ΔP along the length of the channel. A steady state then develops in which the bridge migrates along the channel at a constant speed, with the contact lines moving along each wall with a measured velocity V_0. In the reference frame of the contact line, therefore, both walls move with a velocity $-V_0$. By fitting the interface in the central region of the channel (between $y = \frac{1}{4} \to \frac{3}{4}$) to a circle, see Fig. 7.4b, we define the dynamic contact angle θ_d as the angle of intersection this circle makes with the wall. The dynamic contact angle is in general different from the equilibrium contact angle.

In the flow direction x the cell is taken to have length $L_x = 2L_y$, with periodic boundary conditions on both ϕ and $\mathbf{v}$. All quantities are assumed invariant in the z direction. At the plates we assume boundary conditions of no-slip and no-permeation for the fluid velocity. As there are subtle differences in the ϕ boundary

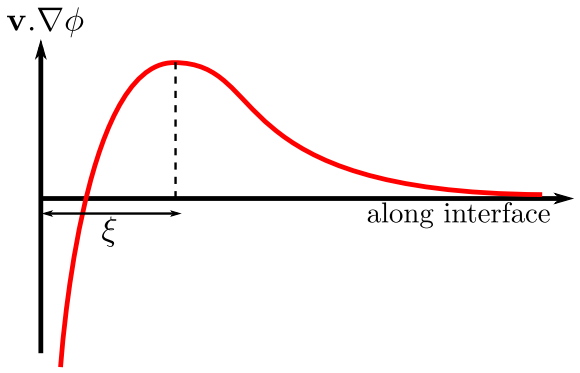

Figure 7.5: Illustration of our definition of the slip length ξ, defined as the position of the first local maximum of $\mathbf{v}.\nabla\phi$ as measured along the interface (defined as the locus $\phi = 0$).

condition between the three numerical methods (which have no appreciable effect on our results), we defer discussion of these to the relevant numerical sections.

7.2.5 Definition of the slip length

In steady state, the Cahn-Hilliard equation of motion for the order parameter reads

$$\mathbf{v}.\nabla\phi = M\nabla^2\mu. \tag{7.11}$$

In Fig. 7.5, we plot the way in which $\mathbf{v}.\nabla\phi$ typically varies along the fluid-fluid interface (taken as the locus $\phi = 0$). Ref. [29] defines the slip length as the point at which $M\nabla^2\mu$ reaches -10% of the value at the wall after passing the first maximum, as measured along the interface. We adopt a related definition and take the slip length ξ to be given by the distance from the wall of this local maximum.

7.2.6 Dimensionless groups

In what follows we work in units of length $[L] = L_y = 1$, time $[T] = \tau \equiv \ell^2/(MG) = 1$ and modulus $[G] = G$. After taking the zero Reynolds limit $\rho \to 0$ and fixing the aspect ratio $\frac{L_x}{L_y} = 2$, there remain four dimensionless parameters which we can vary. The main parameter for our study is the ratio of diffusive and interfacial lengthscales $M\eta/\ell^2$ which we vary in the range $0.0025 \to 10$, and where the lower and upper limits correspond to the diffuse and sharp limits.

We will later demonstrate that the slip length converges as the Capillary number, $\mathrm{Ca} = \eta V_0/\sigma \to 0$ (see Fig. 7.9a). However we also later explore the effect of non-zero

parameter	value	description
$M\eta/\ell^2$	$10^{-3} \to 10^{1}$	ratio of diffusive and interfacial lengthscales
$\mathrm{Ca} = \eta V_0/\sigma$	$10^{-4} \to 10^{-1}$	Capillary number
ℓ/L_y	$0.01 \to 0.025$	ratio of interface width to system size
α	$0, 0.1, 1$	strength of curvature term

Table 7.1: Summarised list of dimensionless parameters for our contact line study.

Ca on the dynamic contact angle in Sec. 7.4.3. We chose $\Delta x < \ell \ll L_y$, taking care to avoid finite size effects (see Sec. 7.3.1.1). We find that our results are unchanged for $\ell/L_y \lesssim 0.02$, consistent with other studies [30]. These key dimensionless parameters are summarised in Table 7.1.

7.3 Numerical methods

We have described in detail our model for a two-phase fluid (where phases are separated by a diffuse interface of width ℓ) and explained how externally driven flows can be imposed using either Planar-Couette and Poiseuille protocols. Now we detail how this model can be solved numerically. In Ref. [262], we report a numerical study where three independent codes were used, demonstrating excellent agreement between all three. Here we focus on the method contributed by this author (*Method I*); a brief overview of the other techniques used (*Method II / Method III*) is given in Apx. 7.8. Unless otherwise specified, any data shown was obtained using *Method I*.

7.3.1 Method I

Within this method, at each numerical timestep we separately (a) solve the hydrodynamic sector of the dynamics to update the fluid velocity field $\mathbf{v}$ at fixed phase field ϕ, then (b) update the phase field at fixed fluid velocity field. In part (a) we use a streamfunction formulation to ensure that the incompressibility condition is automatically satisfied (see Sec. 2.1.1).

For the phase field dynamics in (b) we use a third order upwind scheme to update the convective term on the left hand side of Eq. 7.9. The gradient terms on the right hand side are solved using a Fourier spectral method using both sine and cosine modes in the periodic x direction and only cosine modes in the y direction for consistency with the imposed boundary conditions

$$\partial_y \phi = \partial_y^3 \phi = \partial_y^5 = 0 \tag{7.12}$$

at the walls $y = 0, L_y$. The last equality need only be imposed in the case $\alpha \neq 0$. Note that while this condition automatically ensures zero gradient of the chemical potential (as used for Methods II and III), it is actually a stronger condition than that in demanding all the relevant odd derivatives of ϕ to vanish separately. We do, however, find no difference in our numerical results between these boundary conditions.

For the time-stepping we adopt a method originally proposed by Eyre [263] (and later studied in depth in Ref. [264]) which splits the free energy term into an expansive part, $-\nabla^2\phi$, and a contractive part, $\nabla^2(\phi^3)$, $-\nabla^4\phi$. These are then distributed between the n^{th} and $(n+1)^{th}$ timesteps as

$$\frac{\phi^{n+1} - \phi^n}{\Delta t} = MG\left[\left(-\ell^2\nabla^4\phi + 2\nabla^2\phi\right)^{n+1} + \left(\nabla^2\phi^3 - 3\nabla^2\phi\right)^n\right], \tag{7.13}$$

where Δt is the timestep. This method permits significantly larger timesteps than, for example, a Crank-Nicolson algorithm in which all terms are split equally between the n^{th} and $(n+1)^{th}$ timesteps. When present, i.e., for $\alpha > 0$, the sixth order gradient term is treated fully implicitly.

In our study we vary $M\eta/\ell^2$ (ratio of diffusive and interfacial lengthscales) over four decades. The details of numerical convergence then depend on whether $M\eta/\ell^2$ is much greater or less than 1. For $M\eta/\ell^2 \ll 1$, slip lengths are of the order of the interfacial thickness ℓ and require a fine grid to be accurately resolved. However in this limit the system reaches a steady-state relatively quickly. For $M\eta/\ell^2 \gg 1$ the converse is true: the larger slip lengths involved permit usage of a coarser grid but simulations take much longer to equilibrate. While these effects do cancel to a degree, our simulations generally take longer at large values of $M\eta/\ell^2$. We have explicitly verified that all our results are converged by checking that the slip length

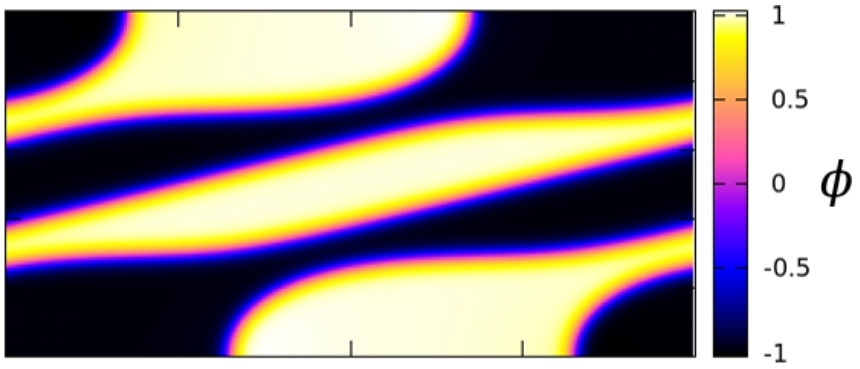

Figure 7.6: Example of a simulation where finite-size effects are pathological. Colourmap shows ϕ where interfacial displacement d is so large that the phases wrap round the simulation cell (which is periodic in the x-direction), and interact with the central region. We avoid this by converging $\mathrm{Ca} \to 0$ (and therefore $d \to 0$).

is not significantly changed after halving both space- and time-step, see Apx. 7.6 for full convergence details.

7.3.1.1 Finite-size effects

In Apx. 7.7 we show that the steady-state displacement of the interface d increases linearly with the Capillary number $\mathrm{Ca} = \eta V_0/\sigma = \eta V_0/\sqrt{8/9}G\ell$; increasing $M\eta/\ell^2$ at fixed wall speed also then increases the displacement. When $d \sim \mathcal{O}(L_x/2)$, the interface wraps around due to the periodic boundary conditions in the x-direction and can interact with the remaining interfacial region in the vicinity of $x, y = (L_x/2, L_y/2)$ where $\mathbf{v} \approx \mathbf{0}$. A pathological example of this phenomenon is given in Fig. 7.6. As d is proportional to the Ca, if any parameter selection suffers from such finite-size effects, we can simply use a smaller value of Ca to reduce the displacement. (See Fig. 7.13 for details.)

In principle, in the limit of very large $M\eta/\ell^2$ the slip length ξ can also approach the channel width size L_y. However this can be avoided by reducing ℓ/L_y (effectively making the channel wider). We have explicitly checked that all results presented in this chapter do not suffer from either of these finite-size effects.

7.4 Results

Having introduced our model, and the three independent numerical techniques used to solve it, we now present our main results. We start in Sec. 7.4.1 by considering the standard ϕ^4 Landau free energy ($\alpha = 0$), before in Sec. 7.4.2 appraising the robustness of our findings to the inclusion of the additional interfacial gradient (curvature) term in the free energy ($\alpha > 0$). In Sec. 7.4.3, we compare our numerical results for the dynamic contact angles to the analytical predictions of Cox [257].

7.4.1 Standard ϕ^4 theory

As discussed previously, two apparently contradictory scaling laws have been proposed for the contact line's slip length ξ in the existing literature. Several authors have proposed [28,30] that the slip length is proportional to the diffusive lengthscale l_D, which describes the length below which intermolecular diffusion dominates advection and above which the opposite is true, giving $\xi \propto l_D = (M\eta)^{1/2}$. In contrast, the lattice Boltzmann simulations and scaling arguments of Ref. [29] suggest that the slip length depends not only on this macroscopic diffusive lengthscale l_D, but also on the microscopic interfacial width ℓ, such that $\xi \propto (l_D\ell)^{1/2}$.

To resolve this apparent discrepancy we have performed extensive numerical simulations of the moving contact line problem across four decades of the relevant dimensionless control parameter $M\eta/\ell^2 = l_D^2/\ell^2$. Moreover, to ensure our results are free of algorithmic artefacts we have used (across the entire range) the three different, independently designed and coded numerical techniques just described. We focus the discussion in this section on the case of planar Couette flow, returning to consider planar Poiseuille flow subsequently.

The slip length, as determined by our three numerical techniques, is plotted against $M\eta/\ell^2$ in Fig. 7.7. As can be seen, all three give virtually indistinguishable results across all four decades of $M\eta/\ell^2$. Over this range we can distinguish two distinct regimes: a (i) diffuse interface regime when $M\eta/\ell^2 \ll 1$, in which $\xi \propto (l_D\ell)^{1/2}$, and (ii) a sharp interface regime when $M\eta/\ell^2 \gg 1$, in which $\xi \propto l_D$. In between these two distinct regimes is a broad crossover window that itself spans

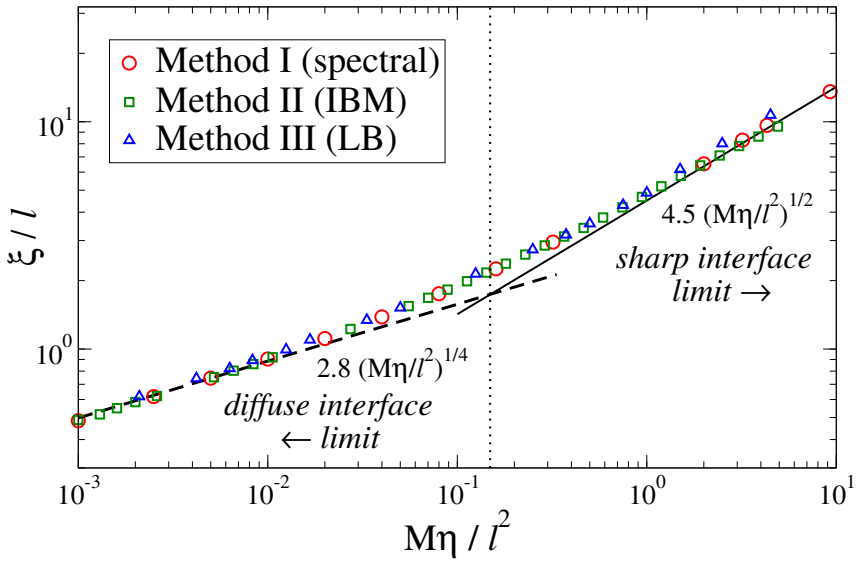

Figure 7.7: Data from all three numerical methods for Couette flow clearly demonstrating both the diffuse- and sharp-interface limits for small and large $M\eta/\ell^2$ respectively.

around the decade either side of $M\eta/\ell^2 \approx 0.15$. In this way, importantly, our results encompass and unify both of the two previously apparently contradictory scalings put forward in the literature, by showing each to apply in a different regime of the relevant dimensionless control parameter, $M\eta/\ell^2$.

In addition to the two basic lengthscales l_D and ℓ present in the model equations, out of which the slip lengthscale ξ emerges in the manner just described, there are two other lengthscales set by the system size L_y and the discretisation scale Δx. We have ensured that the results presented in Fig. 7.7 are independent of possible finite size effects due to L_y and Δx. The former is a particular hazard in the limit of large $M\eta/\ell^2$, where the slip length ξ becomes large (see Sec. 7.3.1.1). On the other hand, the simulation results are susceptible to the latter in the limit of small $M\eta/l^2$, where the slip length becomes small. Therefore we carefully converge $\Delta x \to 0$ in all our results (see Apx. 7.6 for convergence details).

Scaling arguments. Having shown that our numerical results capture both the sharp interface limit of $\xi \propto l_D$ (for large $M\eta/\ell^2$), and the diffusive interface limit of $\xi \propto (l_D\ell)^{1/2}$ (for small $M\eta/\ell^2$), we are now in a position to reprise carefully the scaling arguments put forward in the earlier literature for each of these two scaling forms separately, and to discuss the validity of the assumptions made in arriving at

these functional forms.

Yue *et al.* [30] provided a scaling argument in the sharp interface limit by integrating the Stokes and steady-state Cahn-Hilliard equations over a slip region of spatial extent set by the slip length ξ. Integrating the Stokes equation gives

$$\int_{-\xi}^{\xi} \left[\eta\nabla^2\mathbf{v} - \nabla p + \mu\nabla\phi\right] dx = 0. \tag{7.14}$$

Because the pressure attains the same, constant value on either side of the interface, far from the contact line, the contribution from the second term in the integral is zero. If $V_{\max}$ and $\mu_{\max}$ represent the magnitudes of the velocity and the chemical potential for a given flow setup, the first term scales as $\eta V_{\max}/\xi$, while the third term is proportional to $\mu_{\max}$. Thus, we have

$$\mu_{\max} \sim \eta V_{\max}/\xi. \tag{7.15}$$

Carrying out a similar analysis for the Cahn-Hilliard equation,

$$\int_{-\xi}^{\xi} \left[\mathbf{v}.\nabla\phi - M\nabla^2\mu\right] dx = 0, \tag{7.16}$$

gives

$$V_{\max} \sim M\mu_{\max}/\xi. \tag{7.17}$$

Combining Eqs. 7.15 and 7.17, then gives the scaling law prediction

$$\xi \sim (M\eta)^{1/2}, \tag{7.18}$$

which our numerical results indeed confirmed in the sharp interface limit $M\eta/\ell^2 \gg 1$.

To understand the way in which this sharp interface prediction then breaks down in the diffuse interface regime $M\eta/\ell^2 \ll 1$ requires a careful consideration of the spatial window of integration in Eqs. 7.14 and 7.16. In particular, in this diffuse interface limit the slip length ξ is *less* than the interfacial width ℓ: recall the bottom leftmost data points in Fig. 7.7. But to capture the key physics, one must make sure still to integrate over the entire width ℓ of the interface and not just over a spatial window of a size equal to the (smaller) slip length ξ, otherwise the variation in ϕ across the interface will not be fully accounted for. Integrating the Stokes and

Cahn-Hilliard equations in this way then gives

$$\int_{-\ell}^{+\ell} [\eta \nabla^2 \mathbf{v} - \nabla p + \mu \nabla \phi] \, dx = 0, \tag{7.19}$$

$$\int_{-\ell}^{+\ell} [\mathbf{v}.\nabla \phi - M \nabla^2 \mu] \, dx = 0, \tag{7.20}$$

and the following scalings

$$\mu_{\max} \sim \eta V_{\max} \ell / \xi^2, \tag{7.21}$$

$$V_{\max} \sim M \mu_{\max} \ell / \xi^2, \tag{7.22}$$

$$\xi^4 \sim M \eta \ell^2. \tag{7.23}$$

This was indeed the analysis performed in Ref. [29]. The scaling law and numerical results obtained by these authors are therefore not incorrect. They are merely probing a different region of phase space compared to the other authors.

In between the sharp and diffuse interface regimes is a smooth crossover where the behaviour varies smoothly from one scaling law to another. We define the crossover point by fitting the power laws in the sharp and diffuse interface regimes separately, and finding where these two fits intersect each other. This occurs at $l_D/\ell = 0.38$, in broad agreement with the sharp interface criterion $l_D/\ell > 0.25$ proposed by Yue *et al.* [30].

We finally note that the values of the slip length presented in Fig. 7.7 are independent of the wall velocity, and correspondingly of the Capillary number $\mathrm{Ca} = \eta V_{\mathrm{wall}}/\sigma$, provided that $\mathrm{Ca} \lesssim 0.01$. We later demonstrate this independence explicitly for the case of planar Poiseuille flow (see Fig. 7.9).

7.4.2 Influence of a curvature term

In this section we test the extent to which our results for the slip length do or do not depend on the microscopic details of the diffuse interface model. In particular, we might intuitively expect the slip length to be independent of microscopics in the sharp interface regime, but dependent on microscopics in the diffuse interface regime. Our results below indeed confirm this intuition.

There are many possible ways to modify the basic Landau ϕ^4 theory for which we presented results in the previous subsection. We focus here on the simple but

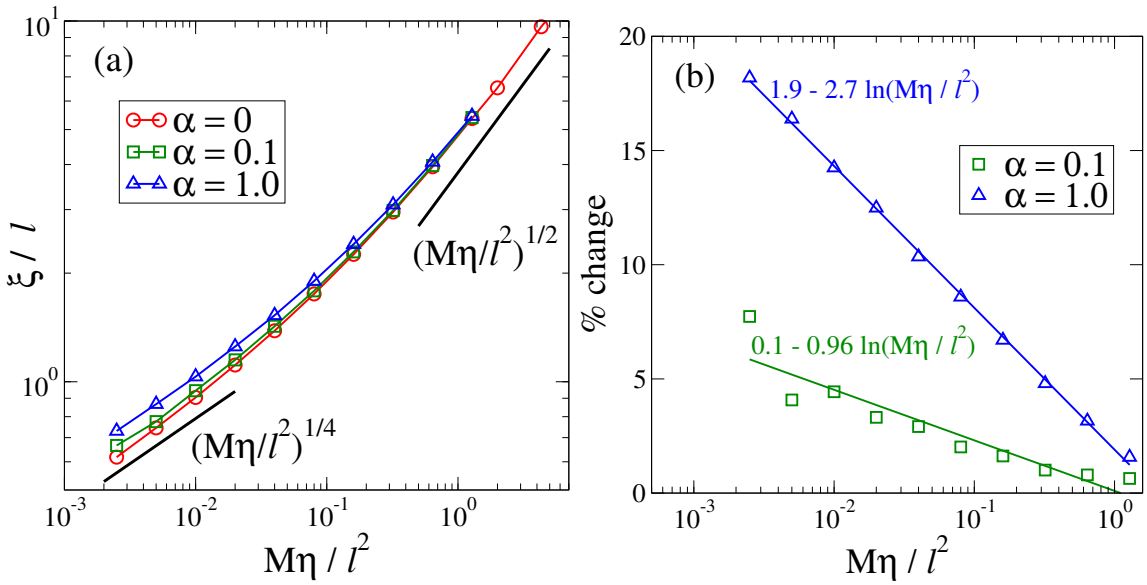

Figure 7.8: Numerical data demonstrating how slip lengths in the diffuse-interface limit are affected by the inclusion of a curvature free energy term in planar Couette flow. (a) Slip length ξ normalised by ℓ against $M\eta/\ell^2$ for $\alpha = 0$ (red circles), 0.1 (green squares), and 1 (blue triangles). (b) Plot of percentage change (relative to $\alpha = 0$) as a function of $M\eta/\ell^2$, which becomes negligible above $M\eta/\ell^2 \sim \mathcal{O}(1)$.

non-trivial extension made by introducing the additional interfacial curvature term with a strength set by α in Eq. 7.7.

Fig. 7.8 shows our numerical results for $\alpha = 0.1$ and 1.0. Shown in the same plot for comparison are our original results, already presented in the previous subsection, for the ϕ^4 theory ($\alpha = 0$). As can be seen, the introduction of the curvature term quantitatively affects the slip length in the diffuse interface regime. This is to be expected: in this regime the physics of the problem is determined not only by macroscopic quantities, but by the microscopic gradient contributions to the free energy.

As the control parameter $M\eta/l^2$ increases into the sharp interface regime the dependence of the slip length on this microscopic parameter α dramatically decreases so as to become negligible in the sharp interface limit $M\eta/\ell^2 \to \infty$. This is expected intuitively. The role of the curvature term is to modify the flow and interfacial profile within a length scale comparable to ℓ.

In the sharp interface limit, the dominant length scale which determines the diffusive transport across the fluid-fluid interface, ξ, is larger than l. Thus, the

scaling argument presented in the previous sub-section is still valid. In the diffuse interface limit, on the other hand, the variation of the order parameter is intrinsically coupled to the flow around the contact line. We find that, for small α, the net effect of the curvature term is to broaden the diffuse interface. This is consistent with the results in Fig. 7.8, where the effective slip length ξ increases with α.

7.4.3 Relation to Cox's result

The results presented so far have demonstrated that, in the sharp interface limit, the emergent slip length is independent of the microscopic details of the models employed. In particular, it is independent of the form of the diffusive gradient terms that prescribe the structure of the interface between the phases. Instead, it depends only on the macroscopic physical constants of the model.

While this is clearly an important finding in terms of our physical understanding of the moving contact line problem, in numerical practice this sharp interface limit $M\eta/l^2 \to \infty$ can be difficult to attain. The time taken to attain a steady state increases dramatically with increasing $M\eta/l^2$. Accordingly, inordinately long run times were required to obtain the rightmost data points in Fig. 7.7.

With this in mind, we now turn to address a question of practical numerical importance: do simulations carried out in the diffuse interface regime still reproduce the expected macroscopic dynamics far from the contact line? We study this question in the context of the Poiseuille flow protocol. (See Fig. 7.4b for a schematic.)

We first check that the slip length obtained for Poiseuille flow is equivalent to that for planar Couette flow. In Fig. 7.9a, we show that the slip length converges to a constant value $\xi \to \xi_0$ as $\mathrm{Ca} \to 0$, as for the Couette protocol[1]. The slip length starts to decrease as Ca is increased above $\mathrm{Ca} \approx 0.01$, although we do not appear to reproduce the scaling $V_0^{-1/2}$ of Ref. [258]. The slip lengths for the Poiseuille flow are plotted in the inset of Fig. 7.9a, and they are compared to the best fit power laws extracted for planar Couette flow in both the diffuse and sharp interface regimes. This shows excellent agreement, demonstrating that the slip length is a

[1]The variation in ξ for $\mathrm{Ca} < 0.01$ is less than 0.5%.

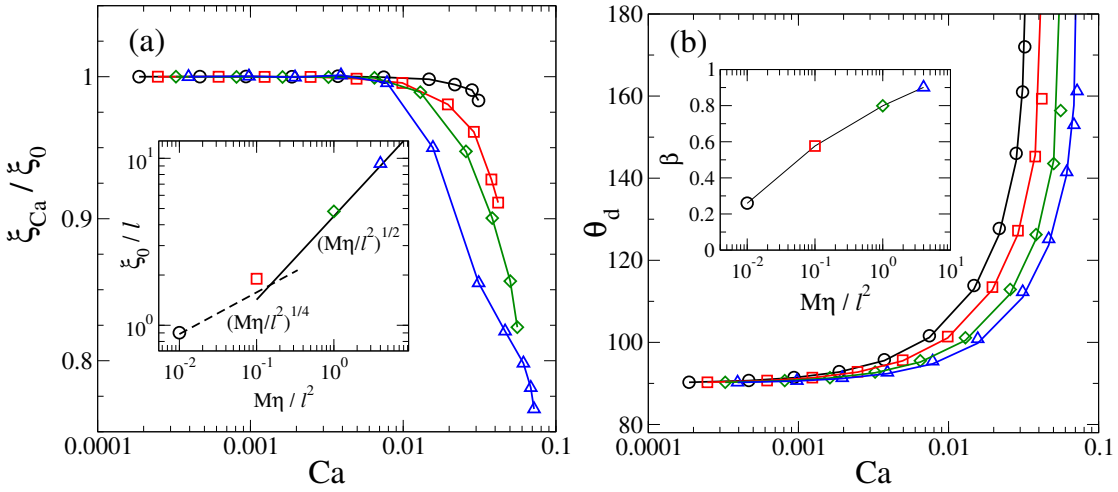

Figure 7.9: Numerical data for the Poiseuille flow protocol for increasing Ca, where $M\eta/l^2 = 0.01$ (black circles ◯), 0.1 (red squares □), 1 (green diamonds ◇), 4 (blue triangles △). (a) Demonstration that the slip length converges to a constant value ξ_0 as $\mathrm{Ca} \to 0$. The inset shows that the measured value of ξ_0 (using the Poiseuille flow protocol) is in good agreement with the best fit power laws obtained for shear flow in Fig. 7.7. (b) Symbols mark the dynamic contact angle θ_d as measured from simulation. The solid lines show the analytical predictions of [257] where $\delta = \beta\xi_{\mathrm{Ca}}/L_y$. The inset shows the best fit values of β which appear to converge $\beta \to 1$ in the sharp interface limit, $M\eta/l^2 \to \infty$.

general property of the fluid mixture, and not dependent on a specific flow protocol.

Next we study how the dynamic contact angle, defined in Fig. 7.4b, depends on the Capillary number Ca. The simulation results are to be compared to the analytical predictions of Cox [257], who derived the following relation

$$g(\theta_d) = g(\theta_{eq}) + \mathrm{Ca}\ln(\delta^{-1}), \tag{7.24}$$

where θ_d is the dynamic contact angle, θ_{eq} is the contact angle at equilibrium (here 90°), and δ is the ratio of the microscopic slip length to some characteristic macroscopic lengthscale of the system, which we choose here to be the channel width L_y. For fluids of matched viscosity, the function g is defined as follows

$$g(\theta) = \int_0^{\theta} \frac{\pi\phi(\pi-\phi) + (2\pi\phi - \pi^2)\sin\phi\cos\phi - \pi\sin^2\phi}{2\pi^2\sin\phi}\, d\phi. \tag{7.25}$$

The simulation results are plotted in Fig. 7.9b for four values of $M\eta/\ell^2$, including parameters belonging in the diffuse and sharp interface limits, as well as the crossover regime. Choosing $\delta = \beta\xi_{\mathrm{Ca}}/L_y$, where β is a fitting parameter, we find that across

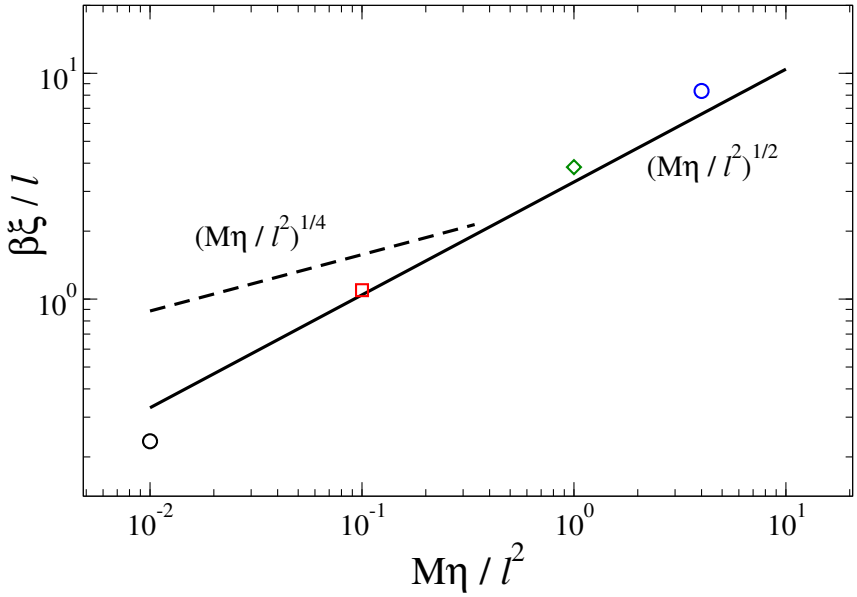

Figure 7.10: Plot of slip lengths from Fig. 7.9a (inset) after correction by the factor β (as obtained in Fig. 7.9b). The power laws expected from the sharp and diffuse interface limits are also shown for reference. Fitting the data to $\left(M\eta/\ell^2\right)^n$ finds $n \approx 0.59$.

the full range of both Ca and $M\eta/\ell^2$, the dynamic contact angle θ_d depends on Ca in a functional form which is in excellent agreement with Cox's formula. Interestingly, as shown in the inset of Fig. 7.9b, the fitting parameter β appears to converge to unity in the sharp interface limit, $M\eta/\ell^2 \to \infty$.

Our results therefore suggest that simulations in the diffuse interface limit can still reliably capture the correct macroscopic physics (such as the dynamic contact angle θ_d), so long as the slip length is suitably corrected. Increasingly minor corrections are needed as one approaches the sharp interface limit, and we expect that Cox's result would be directly obtained for $M\eta/\ell^2 \to \infty$. A final demonstration of this process is given in Fig. 7.10. If we rescale the slip lengths shown in Fig. 7.9a inset by the corresponding value of β, we find that our data approximately recovers the sharp interface scaling of $\xi/\ell \propto (M\eta/\ell^2)^{1/2}$, even in the diffuse interface limit. This demonstrates that one can convincingly reproduce the physics of the sharp interface limit using diffuse interface simulations, which crucially are more accessible numerically.

7.5 Conclusions

The problem of the moving contact line, and the paradoxical implications that arise in a continuum fluid dynamical treatment, still attracts attention several decades after its conception. Apparent discrepancies in the scaling behaviour of the slip length (the lengthscale near the wall at which the fluid interface deviates from its macroscopic behaviour) have the potential to threaten the legitimacy of previous numerical studies. A key result of our work, obtained using careful numerics spanning several orders of magnitude in the relevant control parameter, is to show that in fact both scalings are correct and simply describe different limiting behaviours.

In the diffuse interface limit, corresponding to when the ratio of the macroscopic diffusion length l_D and interface width ℓ is small, we find that the slip length scales as the geometric mean of the two lengths as in Ref. [29], i.e., $\xi \sim \sqrt{l_D \ell}$. Conversely for large l_D/ℓ, i.e., in the sharp interface limit, the slip length simply scales as $\xi \sim l_D$ as obtained in Refs. [28,30]. The crossover occurs at $l_D/l \approx 0.38$, in broad agreement with the sharp interface criterion of Ref. [30]. Our results also show that the slip lengths obtained in planar Couette and Poiseuille flow protocols agree, indicating that the above scalings are generic. As long as care is taken to use the larger of l_D and ℓ when considering the physics of the slip region, the appropriate scaling laws can also be recovered analytically.

We then demonstrated that modifying the microscopic interfacial terms in the free energy functional of our model affects the value of the slip length only in the diffuse interface regime. In the sharp interface limit, the slip length depends only on macroscopic dynamical variables and not on the specifics of the interface model.

Finally we showed that the dynamic contact angle dependence on the Capillary number Ca is in excellent agreement with theoretical prediction by Cox [257], if we allow the slip length to be rescaled by a dimensionless prefactor. This prefactor appears to converge to unity in the sharp interface limit, but is significantly smaller in the diffuse interface limit. Therefore as long as one corrects appropriately, our results show that simulations in the diffuse interface limit (for which numerical convergence is easier to obtain) can still produce the correct macroscopic physics.

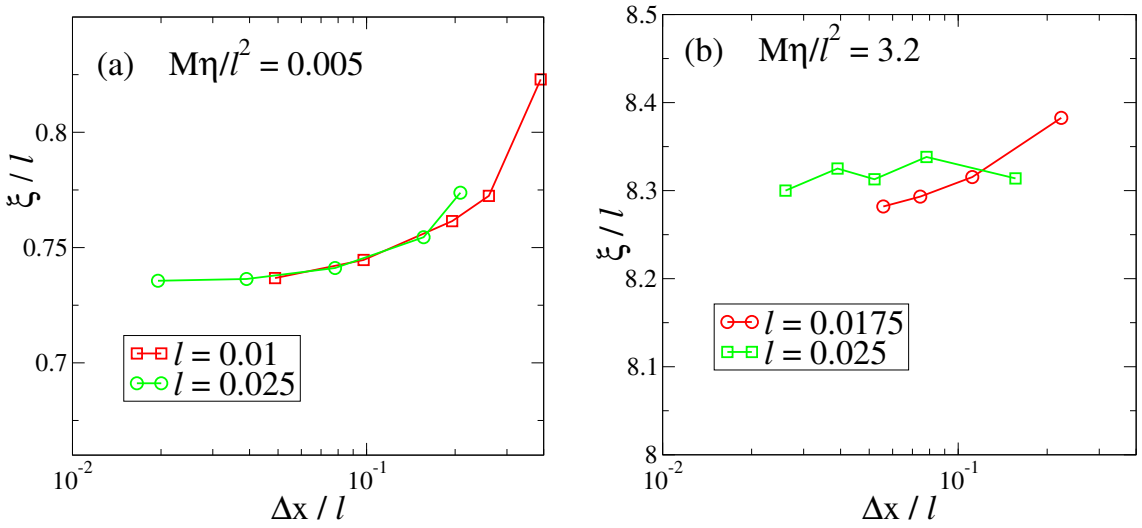

Figure 7.11: Data from convergence tests that were performed for our spectral method for example points in (a) the diffuse interface limit ($M\eta/\ell^2 = 0.005$) and (b) the sharp-interface limit ($M\eta/\ell^2 = 3.2$).

7.6 Appendix I: Numerical convergence

Grid convergence. We present convergence tests in Fig. 7.11 for two different values of $M\eta/\ell^2$, within the diffuse and sharp interface limits respectively. Interestingly, in the former limit we observe a curve collapse when we rescale the spatial stepsize Δx by ℓ, suggesting that as long as the interface is sufficiently resolved (here sufficiently resolved means $\sim 12 \rightarrow 20$ grid points), the width itself does not appear to matter.

In the sharp interface limit, we observe a slight oscillation for the larger of the interfacial widths tested. This could be due to an aliasing effect where the measured value of the slip length is weakly dependent on the proximity of the nearest numerical grid point. Note that while there is some variation ξ even for the smallest grid sizes, the size of the symbol used to display this data point in Fig. 7.7 is $\sim \mathcal{O}(1)$, i.e., twice the y-range considered in Fig. 7.11b. Therefore we can be confident that our data is sufficiently converged for the purposes of our study.

Phase conservation. The Cahn-Hilliard equation is phase conservative [169]. Therefore as a final numerical check, we verify that variations in the total phase

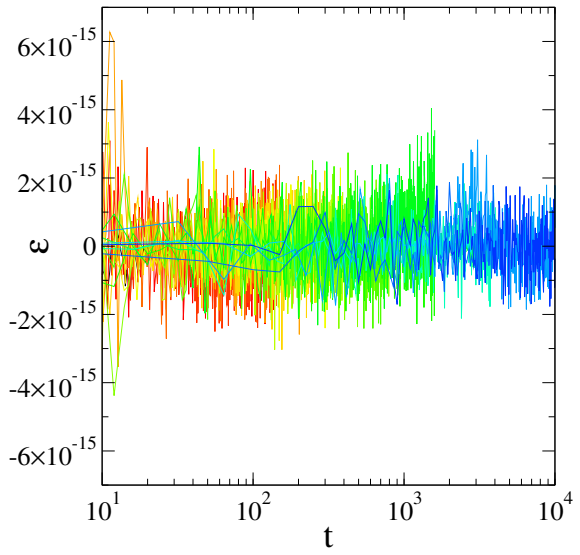

Figure 7.12: Plot of the numerical error ε, defined as the difference between the integrals of ϕ at time 0 and t, i.e., $\varepsilon(t) = \int [\phi(t) - \phi(0)]\, dA$. As the Cahn-Hilliard equation is conservative, this should be zero. We indeed find all our simulations remain comfortably within machine precision for all parameters. Shown is data for $M\eta/\ell^2 = 0.0025$ (red lines) $\rightarrow 2$ (blue lines), with $\alpha = 1$.

remain negligible, i.e., the quantity

$$\varepsilon(t) = \int [\phi(t) - \phi(0)]\, dA \tag{7.26}$$

remains of the order of machine precision throughout the simulation. In Fig. 7.12 we plot $\varepsilon(t)$ demonstrating that changes to the total phase indeed remain within machine precision, even when curvature is included, i.e., $\alpha \neq 0$.

7.7 Appendix II: Interfacial displacement

While not crucial to our understanding of the slip length, it is still useful to ascertain how the displacement of the interface d, as defined in Fig. 7.4, scales with our key dimensionless quantities. For example, this allows us to circumvent finite-size effects where the interface interacts with itself after wrapping around on our periodic simulation box (see Sec. 7.3.1.1).

We show in Fig. 7.13 that d scales linearly with the Capillary number Ca. Therefore finite-size effects can always be avoided by reducing the wall velocity (as Ca $\propto V_0$). The inset in Fig. 7.13 shows minor deviations from this linear scaling

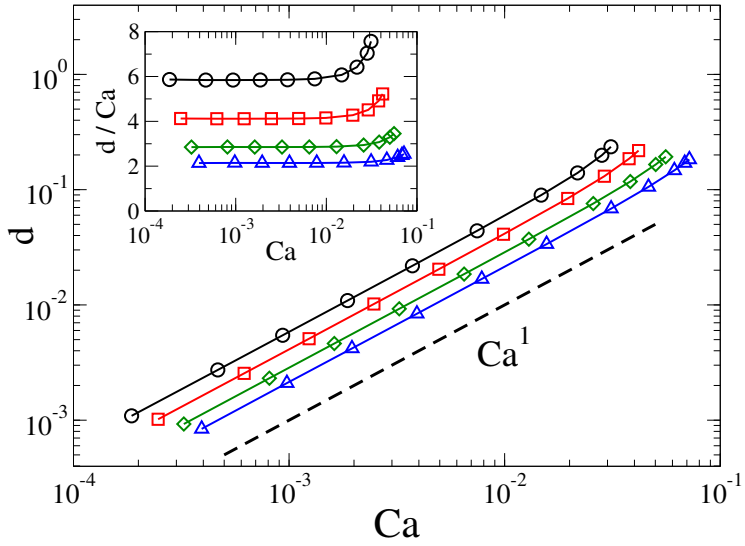

Figure 7.13: Demonstration of how the interfacial displacement d, as defined in Fig. 7.4, scales with Ca for Poiseuille flow (with $\ell = 0.01$). *Inset:* Plot of d/Ca showing minor deviations from the linear fit at large Ca. **Parameters:** $M\eta/l^2 = 0.01$ (black circles ◯), 0.1 (red squares □), 1 (green diamonds ◇), 4 (blue triangles △).

at large Ca. Because most of our results are presented in the Ca $\to$ 0 limit this is inconsequential.

7.8 Appendix III: Alternative numerical methods

In this appendix we provide a brief overview of the other two numerical methods used in Ref. [262], as we compare data from *Method I* against these.

Method II: Immersed boundary

In method II we use a biperiodic box that conveniently enables us to solve both the hydrodynamic sector of the dynamics (again in the incompressible streamfunction formulation at zero Reynolds number) and the diffusive part of the concentration dynamics using fast Fourier transforms in both spatial dimensions.

To incorporate the walls of the flow cell at $y = 0, L_y$, a set of immersed boundary forces are included using smoothed Peskin delta functions as source terms in the Stokes equation along the desired location of each wall (as discussed in Sec. 6.3.1 in the context of porous media, see also Refs. [220, 224]). The force required to ensure

zero velocity at the location of each delta function is then evolved as

$$\partial_t \mathbf{F} = -\kappa \left(\mathbf{V} - \mathbf{V}_0 \right), \tag{7.27}$$

where $\mathbf{V}_0$ is the prescribed wall velocity, and where κ is a spring constant which we converge $\kappa \to \infty$ in successive runs.

For the phase field, we assume the boundary conditions $\partial_y \mu = 0$ at the plates $y = 0, L_y$. This is implemented in an analogous way to the no-slip boundary condition, by means of adding an extra source term contribution

$$\partial_t \phi = -K \hat{\mathbf{n}}.\nabla \mu \tag{7.28}$$

to the equation of motion for the concentration at the location of the Peskin delta functions, where $\hat{\mathbf{n}}$ is a unit vector normal to the wall.

Method III: Lattice Boltzmann

Method III employs a standard free energy lattice Boltzmann method to solve the binary fluid equations of motion [260]. The algorithm derives from the Boltzmann equation: by representing a typical volume element of fluid at each grid point with a particle velocity distribution function, the continuum continuity equations (Eq. 7.10) can be solved. An analogous distribution function describes the phase field. Full details of the scheme may be found in Ref. [262].

A bounce-back rule for the distribution functions is used to ensure no-slip and no-penetration boundary conditions at the two walls [265] (i.e., boundary conditions $\partial_y \mu = 0$ are satisfied at the plates $y = 0, L_y$).

8

Conclusions

In this thesis we have considered a variety of topics within soft matter physics with strong biological and industrial themes, for which zero Reynolds number fluid dynamics plays an integral role. Some of the problems considered are long-standing, where our contribution has been to carefully resolve the differences between contradictory results within the literature. Other topics are more nascent, and naturally lead to more exploratory studies. The latter describes our active matter study, whose results we now summarise.

8.1 Viscoelastic active matter

Summary of main results. As is customary in hydrodynamic stability, we considered the stability and dynamics of our model of viscoelastic active matter in a space of increasing dimensions:

- in 0D we obtained the homogeneous base state (both with and without the effect of external shear)
- in 1D we treated the linear stability of this base state to perturbations in the direction normal to the walls, and numerically studied the resulting nonlinear dynamics as τ_C is increased
- in 2D we used nonlinear simulations to study how the dynamics of our coupled model depend on the polymer relaxation time

The stability of active matter within a Newtonian fluid background has received much attention. One of the seminal results of active matter theory is the generic spontaneous flow instability, in which orientationally ordered phases were shown to be intrinsically unstable [77, 78].

One of our key results was the generalisation of this to include coupling with a polymeric medium, where we showed that the bulk active nematic flow instability persists even in the presence of polymer. Perhaps surprisingly, this result holds even for divergent polymer relaxation times (which we denote as the elastomeric limit), as might describe a crosslinked polymer gel within the cell cytoskeleton. Simulations in 1D confirmed that such states exist, where the nonlinear dynamical behaviour consists of oscillatory states with travelling shear-bands.

As one might expect given the large number of degrees of freedom in our coupled model, the rheological response of viscoelastic matter is highly complex. We systematically explored the flow instabilities in passive liquid-crystal and polymer sectors, and the spontaneous flow instability in active matter. While previous studies have shown that isotropic states can spontaneously flow close to the isotropic-nematic transition [15], our results show that this instability is general and extends deep into the isotropic phase, given a sufficiently large activity. The mechanism for the isotropic instability can be made apparent by considering the shear-stress in the limit $\bar{\dot{\gamma}} \to 0$. We demonstrated that the negative active stress must exceed the positive LC and solvent stresses before spontaneous flows may occur: the activity at which this occurs matches our stability analysis exactly.

We then took a numerical approach to study the 2D dynamics. Starting in the limit in which the relaxation time of the polymer is so rapid that the dynamics do not contribute, we examined how the characteristic lengthscale of the 'activity-driven turbulence' phase, l^*, scales with activity. As experimental studies become increasingly sophisticated [94, 95, 159], the need for a clear connection between experiment and theory becomes increasingly apparent. Contradictory scalings within the literature [173, 177] prompted a collaborative study using two different formulations of active nematics, with independently developed numerical methods [32]. We unambiguously demonstrated that $l^* \sim \sqrt{G_Q/\zeta}$, provided the system is free of finite-size effects. In principle our results could be used to connect experimental control parameters (such as the concentration of ATP or persistence length of the filaments) to the relevant model parameters (activity ζ, Frank length ℓ_Q).

Then, by adding polymer of increasingly long relaxation times τ_C, we examined the effect of viscoelasticity on the phase behaviour, with particular focus on the active turbulent phase. In this phase, without polymer present, confined active matter doesn't produce appreciable net material transport [87]. However, subcellular examples such as actomyosin or kinesin-microtubule complexes are thought to play a role in cytoplasmic streaming [1,266,267], a process in which nutrients and organelles are transported within the cell. Motivated by these results, we showed that as one increases τ_C, defect creation in the turbulent phase is suppressed resulting in a more coherent flow field, creating states with a clear net throughput. For very large τ_C, the flow is arrested and throughputs drop back towards zero. We hope that these results might prompt further experimental studies into the role of viscoelasticity in confined active matter.

We then demonstrated that these spontaneously flowing states still can occur in the elastomeric limit $\tau_C \to \infty$, consistent with our linear stability analysis. The turbulent state that initially forms contains regions of strong extensional flow; this rapidly deforms the polymer and the chaotic nematic texture freezes in, before gradually coarsening. Finally we examined the effect of including an antagonistic free energy coupling between the polymer and nematic sectors. Depending on the strength of the coupling, we find an extreme example of the above drag reduction effect,

regions where the director is rotated out of plane, and oscillatory states that shuffle within the channel on a timescale $\mathcal{O}(\tau_C)$.

Outlook for future work. We have studied the role of confinement in promoting coherent flow states (see e.g., Sec. 5.4.2). *In vitro*, cells must navigate through complex geometries such as the extracellular matrix [10]. The channel geometry employed in Chaps. 3 to 5 is much simpler in comparison. An interesting extension could be to model active matter in a porous geometry (e.g., as considered in Chap. 6). This is related to, but distinct from, the work of Ref. [162] where a passive droplet was embedded in an active fluid within a channel.

One of the more ambitious extensions of our active matter study might be to develop a minimal model of the cell. For example, one could introduce a phase field to allow the degree of polymer viscoelasticity, as parametrised by modulus G_C and relaxation time τ_C, to vary as a function of space and time (see Sec. 6.7.1 for details in the context of porous media). This could be used to effect a deformable nucleus, which could be subject to rotation by the surrounding active fluid. While previous studies have adopted similar approaches [163], we are not aware of any which consider viscoelasticity throughout the model cell, or where the rigidity of the nucleus can be controlled with ease.

Finally we could adopt a more physical model for the polymeric sector. While its simplicity makes it ideal for this study (for which the rheology of the cytoskeleton is modelled at a coarse-grained level), the Oldroyd-B model exhibits notable deficiencies in pure extensional flows [64]. The chaotic activity-driven states reported in Sec. 5.5.1 contain strong extensional flows, and while we still expect the general physics to hold, where rapid activity-driven deformation of the polymer was observed, the effect of FENE regularisation (as described in Sec. 2.2.3.2) would no doubt be insightful.

8.2 Viscoelastic flows in porous media

Summary of main results. Leaving the biological theme behind, the remaining topics in the thesis concerned externally driven flows, particularly those of industrial

interest. In this first study, we developed 2D model porous geometries consisting of periodic arrays of cylinders within which to study the dynamics and response of a viscoelastic fluid. Experimentally, a large upturn in χ (the pressure drop required to maintain a given flux) is consistently observed at high Weissenberg numbers (We) which is typically accompanied by time-dependent states. Using several popular models of polymer viscoelasticity in our simplified model geometries, we attempted to capture this upturn and any associated effects (if present) numerically.

A surprising level of insight can be gained from analysing of the Newtonian flow field. By comparing the rheological response of a given fluid in simple viscometric flows (such as simple shear or extension) with the dominant type of flow deformation in (Newtonian) porous flows, we made qualitative predictions regarding the response of our different constitutive models. For example, we found that flow past a small cylinder produces strong extensional flows in the wake; models which produce smaller extensional stresses in pure extensional flow (e.g., compare FENE-CR and Oldroyd-B) exhibited less dramatic upturn in the drag.

However a purely local analysis, in which advective effects are ignored, fails to capture the physics in full. Flows past large cylinders appeared to be dominated by shearing in the vertical gap between cylinders. However models with identical shear but differing extensional rheologies produced different drag responses, leading us to conclude that upstream extension deformation must also play a role.

Finally we attempted to reproduce the results of an intriguing recent study [25] which, contrary to previous work, reported time-dependent states when the cylinders were confined between walls. While our initial simulations displayed fluctuations in the flux (at fixed pressure drop) which grow in magnitude as $\sim (We - We_c)^{1/2}$ (as in that study), these disappeared at very fine grid resolutions, an order of magnitude larger than used in Ref. [25]. While our results suggest that 2D flows of an Oldroyd-B fluid remain time-dependent, at least within the range of numerically accessible We, the equivalent study in 3D remains open as we now discuss.

Outlook for future work. One of the most natural generalisations to our 2D porous media study is to consider three-dimensional flow. Experimental studies re-

port crossing streaklines in the time-dependent flow regime [194, 196], suggesting that the instability is 3D in nature. The severe convergence requirements demonstrated in Sec. 6.5.3.2 make this a daunting task, though this could be improved with parallel simulation code and algorithmic refinements. The transition to 3D could also be made by only including a small number of Fourier modes in the z-direction initially.

Another option might be to explore related geometries where contractive/expansive flows are still present, but where numerical convergence is more feasible. Wavy-walled channels reproduce some of the key flow features of porous media [268, 269], but avoid the stagnation point in the cylinder wake which can be numerically difficult to resolve. Future studies could examine the effect of varying the amplitude and phase of the channel wall structure, and could be readily implemented using our immersed boundary numerical methods. Finally we could also consider the effect of selecting a more microscopically motivated model, such as the Rolie-Poly model which describes entangled polymeric materials [270, 271].

8.3 Contact line dynamics

Summary of main results. The final topic considered in this thesis addressed a long-standing problem in fluid dynamics concerning the physics of the moving contact line. Using a diffuse interface model in which two fluid phases are separated by an interface of width ℓ, we studied numerically the response under an externally applied shear or pressure drop. In particular we focused on the 'slip length' ξ, the emergent lengthscale at which the shape of the fluid-fluid interface deviates from its macroscopic behaviour as one approaches the contact line. The question of how the slip length scales with (a) the diffusive lengthscale l_D at which diffusive and advective effects are comparable and (b) the interface width ℓ, remains unclear in the existing literature.

By varying l_D/ℓ over several decades, our numerical results reconciled two contradictory scaling behaviours which have been reported in the literature: if l_D is smaller than the interface width ℓ (i.e., the diffuse interface limit of Ref. [29]), then

$\xi \sim \sqrt{l_d \ell}$, whereas if l_D/ℓ is large then $\xi \sim l_D$ (i.e., the sharp interface limit of Refs. [28, 30]). One might then expect that the exact details of the microscopic model do not matter in the latter limit where the slip length no longer depends on ℓ. By modifying the free energy functional to include a curvature term we showed that this is indeed the case. Reassuringly, we also found that the slip length does not depend on the flow protocol used suggesting that the physics of the contact line captured in this study should apply generally in more complex geometries.

The above results focus on the limit in which the Capillary number $\mathrm{Ca} \to 0$; we concluded our study by comparing our numerical data for increasing Ca against the established analytical result of Cox [257] who predicted that the dynamic contact angle θ_d, i.e., the angle at which the macroscopic interface shape would intersect the wall, increases and eventually diverges as Ca is increased. We found excellent agreement between the two, *if* one allows ξ to be rescaled by a constant prefactor. Encouragingly, this prefactor appears to converge to unity in the sharp interface limit in which Cox's original calculation was performed. Perhaps more remarkable is the fact that our results deep into the diffuse interface regime still reproduce the correct macroscopic physics, if slip lengths are corrected appropriately.

Ideally one would like the slip length to be independent of the interface width ℓ as this is essentially a numerical parameter, if one considers that real fluid interfaces are typically many orders of magnitude thinner than any macroscopic length. Indeed our simulations which approach the sharp interface limit appear to reproduce key analytical results without need for correction. Simulations in the diffuse interface regime overestimate the slip length relative to an 'ideal' sharp interface limit; an important contribution of our work is to show that if this is carefully corrected for then one can effect sharp interface hydrodynamics at reduced numerical cost.

Interestingly, experimental systems consisting of colloid-polymer mixtures are known to phase separate into colloid-rich and colloid-poor domains, with an interface width that is of order 1 micron [272, 273], much larger than the typical value for molecular fluids. It would be interesting to see if such a system can be exploited to realise the different contact line slip regimes discussed here experimentally.

Outlook for future work. We demonstrated that even for simple planar Couette or Poiseuille flows, numerical solution of the contact line dynamics requires care. However identification of the two clear limiting cases (diffuse and sharp interface limits), and the convergence criteria within each of these paves the way for future computational work.

Our study made the assumption that both fluid phases were of matched viscosity. A natural generalisation would be to include fluids of differing viscosities $\eta_{\pm}$. We can speculate that the leading order effect of such a change is that the viscosity in our dimensionless control parameter, $M\eta/\ell^2$, maps to some combination of the new viscosities, e.g., $M\eta/\ell^2 \to M\sqrt{\eta_+\eta_-}/\ell^2$.

Another logical extension might be to introduce a more complex geometries. The immersed boundary method, which was successfully employed in the contact line study (see Sec. 7.8), naturally describes non-trivial geometries. Pressure driven flow past a biperiodic array of cylinders (as used in the porous media study in Chap. 6) might provide an ideal starting point. Such a study should be of particular interest to oil recovery, where insight into multiphase flows within a porous medium is desired [243]. For example, our simulations could be generalised to describe an oil droplet squeezing out of a constriction when subjected to a pressure drop.

We could also apply our understanding of physics in the slip region to the problem of the rolling droplet. While detailed analytical results exist [274], a careful comprehensive numerical treatment of the problem has not yet been attempted.

Finally, we hope that the results presented in this thesis will help unify the understanding of several long-standing problems in fluid mechanics (i.e., contact line dynamics & flows in porous media), and encourage further study of viscoelastic active matter, both experimentally and theoretically.

Bibliography

[1] R. E. Goldstein and J.-W. van de Meent. A physical perspective on cytoplasmic streaming. *Interface Focus*, **5**, 20150030–20150030, 2015.

[2] Y. Zheng, X. Gao, and L. Jiang. Directional adhesion of superhydrophobic butterfly wings. *Soft Matter*, **3**, 178, 2007.

[3] A. R. Vasavada and A. P. Showman. Jovian atmospheric dynamics: an update after Galileo and Cassini. *Reports Prog. Phys.*, **68**, 1935–1996, 2005.

[4] C. Dombrowski, L. Cisneros, S. Chatkaew, R. E. Goldstein, and J. O. Kessler. Self-Concentration and Large-Scale Coherence in Bacterial Dynamics. *Phys. Rev. Lett.*, **93**, 098103, 2004.

[5] J. Dunkel, S. Heidenreich, K. Drescher, H. H. Wensink, M. Bär, and R. E. Goldstein. Fluid Dynamics of Bacterial Turbulence. *Phys. Rev. Lett.*, **110**, 228102, 2013.

[6] L. Giomi, M. J. Bowick, P. Mishra, R. Sknepnek, and M. C. Marchetti. Defect dynamics in active nematics. *Philos. Trans. A. Math. Phys. Eng. Sci.*, **372**, 16, 2014.

[7] E. Lauga. Propulsion in a viscoelastic fluid. *Phys. Fluids*, **19**, 083104, 2007.

[8] X. N. Shen and P. E. Arratia. Undulatory Swimming in Viscoelastic Fluids. *Phys. Rev. Lett.*, **106**, 208101, 2011.

[9] S. K. Lai, Y. Y. Wang, D. Wirtz, and J. Hanes. Micro- and macrorheology of mucus. *Adv. Drug Deliv. Rev.*, **61**, 86–100, 2009.

[10] S. Even-Ram and K. M. Yamada. Cell migration in 3D matrix. *Curr. Opin. Cell Biol.*, **17**, 524–532, 2005.

[11] F. G. Woodhouse and R. E. Goldstein. Spontaneous circulation of confined active suspensions. *Phys. Rev. Lett.*, **109**, 168105, 2012.

[12] L. R. Serbus, B.-J. Cha, W. E. Theurkauf, and W. M. Saxton. Dynein and the actin cytoskeleton control kinesin-driven cytoplasmic streaming in Drosophila oocytes. *Development*, **132**, 3743–3752, 2005.

[13] S. Rafaï, L. Jibuti, and P. Peyla. Effective viscosity of microswimmer suspensions. *Phys. Rev. Lett.*, **104**, 1–4, 2010.

[14] A. Sokolov and I. S. Aranson. Reduction of viscosity in suspension of swimming bacteria. *Phys. Rev. Lett.*, **103**, 2–5, 2009.

[15] M. E. Cates, S. M. Fielding, D. Marenduzzo, E. Orlandini, and J. M. Yeomans. Shearing Active Gels Close to the Isotropic-Nematic Transition. *Phys. Rev. Lett.*, **101**, 068102, 2008.

[16] M. C. Marchetti, J.-F. Joanny, S. Ramaswamy, T. B. Liverpool, J. Prost, M. Rao, and R. A. Simha. Hydrodynamics of soft active matter. *Rev. Mod. Phys.*, **85**, 1143–1189, 2013.

[17] K. Kruse, J. F. Joanny, F. Jülicher, and J. Prost. Contractility and retrograde flow in lamellipodium motion. *Phys. Biol.*, **3**, 130–137, 2006.

[18] L. Petitjean, M. Reffay, E. Grasland-Mongrain, M. Poujade, B. Ladoux, A. Buguin, and P. Silberzan. Velocity fields in a collectively migrating epithelium. *Biophys. J.*, **98**, 1790–1800, 2010.

[19] G. Salbreux, J. Prost, and J.-F. Joanny. Hydrodynamics of Cellular Cortical Flows and the Formation of Contractile Rings. *Phys. Rev. Lett.*, **103**, 058102, 2009.

[20] L. Giomi and A. DeSimone. Spontaneous division and motility in active nematic droplets. *Phys. Rev. Lett.*, **112**, 147802, 2014.

[21] A. Y. Chen, Z. Deng, A. N. Billings, U. O. S. Seker, M. Y. Lu, R. J. Citorik, B. Zakeri, and T. K. Lu. Synthesis and patterning of tunable multiscale materials with engineered cells. *Nat. Mater.*, pages 1–9, 2014.

[22] D. A. Gagnon, N. C. Keim, X. Shen, and P. E. Arratia. Fluid-induced propulsion of rigid particles in wormlike micellar solutions. *Phys. Fluids*, **26**, 103101, 2014.

[23] B. Khomami and L. D. Moreno. Stability of viscoelastic flow around periodic arrays of cylinders. *Rheol. Acta*, **36**, 367–383, 1997.

[24] A. W. Liu, D. E. Bornside, R. C. Armstrong, and R. A. Brown. Viscoelastic flow of polymer solutions around a periodic, linear array of cylinders: comparisons of predictions for microstructure and flow fields. *J. Non-Newtonian Fluid Mech.*, **77**, 153–190, 1998.

[25] A. Vázquez-Quesada and M. Ellero. SPH simulations of a viscoelastic flow around a periodic array of cylinders confined in a channel. *J. Non-Newtonian Fluid Mech.*, **167-168**, 1–8, 2012.

[26] T. Young. An Essay on the Cohesion of Fluids. *Philos. Trans. R. Soc. London*, **95**, 65–87, 1805.

[27] P. Seppecher. Moving contact lines in the Cahn-Hilliard theory. *Int. J. Eng. Sci.*, **34**, 977–992, 1996.

[28] D. Jacqmin. Contact-line dynamics of a diffuse fluid interface. *J. Fluid Mech.*, **402**, 57–88, 2000.

[29] A. J. Briant and J. M. Yeomans. Lattice Boltzmann simulations of contact line motion. II. Binary fluids. *Phys. Rev. E*, **69**, 031603, 2004.

[30] P. Yue, C. Zhou, and J. J. Feng. Sharp-interface limit of the Cahn-Hilliard model for moving contact lines. *J. Fluid Mech.*, **645**, 279, 2010.

[31] H. Kusumaatmaja and J. M. Yeomans. Modeling contact angle hysteresis on chemically patterned and superhydrophobic surfaces. *Langmuir*, **23**, 6019–6032, 2007.

[32] P. M. Mishra, E. J. Hemingway, S. M. Fielding, and M. C. Marchetti. Correlation lengths in active nematics (in preparation), 2015.

[33] D. J. Acheson. *Elementary Fluid Dynamics*. Oxford Applied Mathematics and Computing Science Series. Clarendon Press, 1990.

[34] S. M. Fielding. Vorticity structuring and velocity rolls triggered by gradient shear bands. *Phys. Rev. E*, **76**, 016311, 2007.

[35] D. Saintillan and M. J. Shelley. Instabilities, pattern formation, and mixing in active suspensions. *Phys. Fluids*, **20**, 123304, 2008.

[36] J. M. Teran and C. S. Peskin. Tether Force Constraints in Stokes Flow by the

Immersed Boundary Method on a Periodic Domain. *SIAM J. Sci. Comput.*, **31**, 3404–3416, 2009.

[37] J. R. Blake. A note on the image system for a stokeslet in a no-slip boundary. *Math. Proc. Cambridge Philos. Soc.*, **70**, 303, 1971.

[38] R. G. Larson. *The Structure and Rheology of Complex Fluids*. Oxford University Press, 1999.

[39] S. M. Fielding. Viscoelastic Taylor-Couette Instability of Shear Banded Flow. *Phys. Rev. Lett.*, **104**, 198303, 2010.

[40] P. D. Olmsted, O. Radulescu, and C.-Y. D. Lu. Johnson-Segalman model with a diffusion term in cylindrical Couette flow. *J. Rheol.*, **44**, 257, 2000.

[41] S. M. Fielding and P. D. Olmsted. Nonlinear Dynamics of an Interface between Shear Bands. *Phys. Rev. Lett.*, **96**, 104502, 2006.

[42] P. Coussot. Yield stress fluid flows: A review of experimental data. *J. Non-Newtonian Fluid Mech.*, **211**, 31–49, 2014.

[43] R. G. Larson. *Constitutive Equations for Polymer Melts and Solutions*. Butterworths, 1988.

[44] P. D. Olmsted. Perspectives on shear banding in complex fluids. *Rheol. Acta*, **47**, 283–300, 2008.

[45] N. A. Spenley, M. E. Cates, and T. C. B. McLeish. Nonlinear rheology of wormlike micelles. *Phys. Rev. Lett.*, **71**, 939–942, 1993.

[46] C. Pujolle-Robic and L. Noirez. Observation of shear-induced nematic-isotropic transition in side-chain liquid crystal polymers. *Nature*, **409**, 167–171, 2001.

[47] P. E. Boukany and S.-Q. Wang. A correlation between velocity profile and molecular weight distribution in sheared entangled polymer solutions. *J. Rheol.*, **51**, 217, 2007.

[48] R. W. Mair and P. Callaghan. Observation of shear banding in worm-like micelles by NMR velocity imaging. *Europhys. Lett.*, **36**, 719–724, 1996.

[49] L. Bécu, S. Manneville, and A. Colin. Spatiotemporal dynamics of wormlike micelles under shear. *Phys. Rev. Lett.*, **93**, 018301, 2004.

[50] P. Tapadia and S. Q. Wang. Direct Visualization of Continuous Simple Shear

in Non-Newtonian Polymeric Fluids. *Phys. Rev. Lett.*, **96**, 016001, 2006.

[51] I. Kunita, K. Sato, Y. Tanaka, Y. Takikawa, H. Orihara, and T. Nakagaki. Shear Banding in an F-Actin Solution. *Phys. Rev. Lett.*, **109**, 248303, 2012.

[52] J. P. Decruppe, R. Cressely, R. Makhloufi, and E. Cappelaere. Flow birefringence experiments showing a shear-banding structure in a CTAB solution. *Colloid Polym. Sci.*, **273**, 346–351, 1995.

[53] M. M. Britton and P. Callaghan. Nuclear magnetic resonance visualization of anomalous flow in cone-and-plate rheometry. *J. Rheol.*, **41**, 1365, 1997.

[54] M. M. Britton and P. Callaghan. Shear banding instability in wormlike micellar solutions. *Eur. Phys. J. B*, **7**, 237–249, 1999.

[55] L. Chen, C. Zukoski, B. Ackerson, H. Hanley, G. Straty, J. Barker, and C. Glinka. Structural changes and orientaional order in a sheared colloidal suspension. *Phys. Rev. Lett.*, **69**, 688–691, 1992.

[56] D. Bonn, J. Meunier, O. Greffier, A. Al-Kahwaji, and H. Kellay. Bistability in non-Newtonian flow: Rheology of lyotropic liquid crystals. *Phys. Rev. E*, **58**, 2115–2118, 1998.

[57] O. Radulescu and P. Olmsted. Matched asymptotic solutions for the steady banded flow of the diffusive Johnson-Segalman model in various geometries. *J. Non-Newtonian Fluid Mech.*, **91**, 143–164, 2000.

[58] F. A. Morrison. *Understanding Rheology*. Topics chemical engineering : A series of textbooks and monographs. Oxford University Press, 2001.

[59] M. Johnson and D. Segalman. A model for viscoelastic fluid behavior which allows non-affine deformation. *J. Non-Newtonian Fluid Mech.*, **2**, 255–270, 1977.

[60] C.-Y. D. Lu, P. D. Olmsted, and R. C. Ball. Effects of Nonlocal Stress on the Determination of Shear Banding Flow. *Phys. Rev. Lett.*, **84**, 642–645, 2000.

[61] J.-F. Berret, D. C. Roux, and G. Porte. Isotropic-to-nematic transition in wormlike micelles under shear. *J. Phys. II*, **4**, 1261–1279, 1994.

[62] C. Grand, J. Arrault, and M. E. Cates. Slow Transients and Metastability in Wormlike Micelle Rheology. *J. Phys. II*, **7**, 1071–1086, 1997.

[63] F. Greco and R. C. Ball. Shear-band formation in a non-Newtonian fluid model

with a constitutive instability. *J. Non-Newtonian Fluid Mech.*, **69**, 195–206, 1997.

[64] J. M. Rallison and E. Hinch. Do we understand the physics in the constitutive equation? *J. Non-Newtonian Fluid Mech.*, **29**, 37–55, 1988.

[65] R. B. Bird, C. F. Curtiss, R. C. Armstrong, and O. Hassager. *Dynamics of Polymeric Liquids, Vol. 2, Kinetic Theory.* Wiley, New York, 2nd edition, 1987.

[66] M. Chilcott and J. M. Rallison. Creeping flow of dilute polymer solutions past cylinders and spheres. *J. Non-Newtonian Fluid Mech.*, **29**, 381–432, 1988.

[67] S. M. Fielding. Linear Instability of Planar Shear Banded Flow. *Phys. Rev. Lett.*, **95**, 134501, 2005.

[68] S. M. Allen and J. W. Cahn. A microscopic theory for antiphase boundary motion and its application to antiphase domain coarsening. *Acta Metall.*, **27**, 1085–1095, 1979.

[69] P. W. Bates and A. Chmaj. An integrodifferential model for phase transitions: stationary solutions in higher space dimensions. *J. Stat. Phys.*, **95**, 1119–1139, 1999.

[70] W. H. Press, S. A. Teukolsky, W. T. Vetterling, and B. P. Flannery. *Numerical Recipes in C: The Art of Scientific Computing.* Cambridge University Press, New York, NY, USA, 2nd edition, 1992.

[71] J. Boyd. *Chebyshev and Fourier spectral methods.* Dover Publications, 2001.

[72] E. O. Brigham and R. E. Morrow. The Fast Fourier Transform. *IEEE Spectr.*, **4**, 63–70, 1967.

[73] Y. Hatwalne, S. Ramaswamy, M. Rao, and R. A. Simha. Rheology of Active-Particle Suspensions. *Phys. Rev. Lett.*, **92**, 118101–, 2004.

[74] P. G. de Gennes and J. Prost. *The Physics of Liquid Crystals.* International Series of Monographs on Physics. Clarendon Press, 1995.

[75] J. R. Blake. A spherical envelope approach to ciliary propulsion. *J. Fluid Mech.*, **46**, 199, 1971.

[76] S. Ramaswamy. The Mechanics and Statistics of Active Matter. *Annu. Rev. Condens. Matter Phys.*, **1**, 323–345, 2010.

[77] R. Aditi Simha and S. Ramaswamy. Hydrodynamic Fluctuations and Instabilities in Ordered Suspensions of Self-Propelled Particles. *Phys. Rev. Lett.*, **89**, 058101, 2002.

[78] D. Saintillan and M. J. Shelley. Instabilities and Pattern Formation in Active Particle Suspensions: Kinetic Theory and Continuum Simulations. *Phys. Rev. Lett.*, **100**, 178103, 2008.

[79] S. Ramaswamy and M. Rao. Active-filament hydrodynamics: instabilities, boundary conditions and rheology. *New J. Phys.*, **9**, 423–423, 2007.

[80] S. A. Edwards and J. M. Yeomans. Spontaneous flow states in active nematics: A unified picture. *Europhys. Lett.*, **85**, 18008, 2009.

[81] R. Voituriez, J.-F. Joanny, and J. Prost. Spontaneous flow transition in active polar gels. *Europhys. Lett.*, **70**, 404–410, 2005.

[82] F. Jülicher, K. Kruse, J. Prost, and J.-F. Joanny. Active behavior of the Cytoskeleton. *Phys. Rep.*, **449**, 3–28, 2007.

[83] A. N. Beris and B. J. Edwards. *Thermodynamics of flowing systems: with internal microstructure*, volume 36. Oxford University Press, USA, 1994.

[84] A. Sokolov, I. S. Aranson, J. O. Kessler, and R. E. Goldstein. Concentration dependence of the collective dynamics of swimming bacteria. *Phys. Rev. Lett.*, **98**, 1–4, 2007.

[85] H. Gruler, U. Dewald, and M. Eberhardt. Nematic liquid crystals formed by living amoeboid cells. *Eur. Phys. J. B*, **11**, 187–192, 2012.

[86] L. Giomi, L. Mahadevan, B. Chakraborty, and M. Hagan. Excitable Patterns in Active Nematics. *Phys. Rev. Lett.*, **106**, 218101, 2011.

[87] S. M. Fielding, D. Marenduzzo, and M. E. Cates. Nonlinear dynamics and rheology of active fluids: Simulations in two dimensions. *Phys. Rev. E*, **83**, 041910, 2011.

[88] T. Thoresen, M. Lenz, and M. L. Gardel. Reconstitution of contractile actomyosin arrays. *Biophys. J.*, **100**, 2698–2705, 2011.

[89] G. H. Koenderink, Z. Dogic, F. Nakamura, P. M. Bendix, F. C. MacKintosh, J. H. Hartwig, T. P. Stossel, and D. a. Weitz. An active biopolymer network controlled by molecular motors. *Proc. Natl. Acad. Sci. U. S. A.*, **106**, 15192–7,

2009.

[90] P. Dalhaimer, D. E. Discher, and T. C. Lubensky. Crosslinked actin networks show liquid crystal elastomer behaviour, including soft-mode elasticity. *Nat. Phys.*, **3**, 354–360, 2007.

[91] D. Humphrey, C. Duggan, D. Saha, D. Smith, and J. Käs. Active fluidization of polymer networks through molecular motors. *Nature*, **416**, 413–416, 2002.

[92] B. Alberts, A. Johnson, J. Lewis, M. Raff, K. Roberts, and P. Walter. *Molecular Biology of the Cell*. Garland Science, 5 edition, 2008.

[93] K. Kruse, J.-F. Joanny, F. Jülicher, J. Prost, and K. Sekimoto. Generic theory of active polar gels: a paradigm for cytoskeletal dynamics. *Eur. Phys. J. E. Soft Matter*, **16**, 5–16, 2005.

[94] T. Sanchez, D. T. N. Chen, S. J. DeCamp, M. Heymann, and Z. Dogic. Spontaneous motion in hierarchically assembled active matter. *Nature*, **491**, 431–4, 2012.

[95] G. Henkin, S. J. DeCamp, D. T. N. Chen, T. Sanchez, and Z. Dogic. Tunable dynamics of microtubule-based active isotropic gels. *Philos. Trans. R. Soc. A Math. Phys. Eng. Sci.*, **372**, 20140142, 2014.

[96] A. W. Decho. Microbial exopolymer secretions in ocean environments: their roles in food webs and marine processes. *Ocean. Mar. Biol. Annu. Rev*, **28**, 73–153, 1990.

[97] J. M. Teran, L. Fauci, and M. J. Shelley. Viscoelastic Fluid Response Can Increase the Speed and Efficiency of a Free Swimmer. *Phys. Rev. Lett.*, **104**, 038101, 2010.

[98] S. E. Spagnolie, B. Liu, and T. R. Powers. Locomotion of Helical Bodies in Viscoelastic Fluids: Enhanced Swimming at Large Helical Amplitudes. *Phys. Rev. Lett.*, **111**, 068101, 2013.

[99] T. D. Montenegro-Johnson, D. J. Smith, and D. Loghin. Physics of rheologically enhanced propulsion: Different strokes in generalized Stokes. *Phys. Fluids*, **25**, 081903, 2013.

[100] Y. Bozorgi and P. T. Underhill. Effect of viscoelasticity on the collective behavior of swimming microorganisms. *Phys. Rev. E*, **84**, 061901, 2011.

[101] Y. Bozorgi and P. T. Underhill. Role of linear viscoelasticity and rotational diffusivity on the collective behavior of active particles. *J. Rheol.*, **57**, 511, 2013.

[102] D. Marenduzzo, E. Orlandini, and J. M. Yeomans. Hydrodynamics and rheology of active liquid crystals: a numerical investigation. *Phys. Rev. Lett.*, **98**, 118102, 2007.

[103] E. J. Hemingway, A. Maitra, S. Banerjee, M. C. Marchetti, S. Ramaswamy, S. M. Fielding, and M. E. Cates. Active Viscoelastic Matter: From Bacterial Drag Reduction to Turbulent Solids. *Phys. Rev. Lett.*, **114**, 098302, 2015.

[104] S. Ramaswamy, R. A. Simha, and J. Toner. Active nematics on a substrate: giant number fluctuations and long-time tails. *Europhys. Lett.*, **62**, 196, 2002.

[105] S. T. Milner. Dynamical theory of concentration fluctuations in polymer solutions under shear. *Phys. Rev. E*, **48**, 3674–3691, 1993.

[106] P. Olmsted. Private communication, 2013, 2015.

[107] N. Kuzuu and M. Doi. Constitutive equation for nematic liquid crystals under weak velocity gradient derived from a molecular kinetic equation. *J. Phys. Soc. Japan*, **52**, 3486–3494, 1983.

[108] D. Marenduzzo, E. Orlandini, M. E. Cates, and J. M. Yeomans. Steady-state hydrodynamic instabilities of active liquid crystals: Hybrid lattice Boltzmann simulations. *Phys. Rev. E*, **76**, 031921, 2007.

[109] G. Jayaraman, S. Ramachandran, S. Ghose, A. Laskar, M. S. Bhamla, P. B. S. Kumar, and R. Adhikari. Autonomous Motility of Active Filaments due to Spontaneous Flow-Symmetry Breaking. *Phys. Rev. Lett.*, **109**, 158302, 2012.

[110] O. Radulescu, P. D. Olmsted, and C.-Y. D. Lu. Shear banding in reaction-diffusion models. *Rheol. Acta*, **38**, 606–613, 1999.

[111] E. Bertin, H. Chaté, F. Ginelli, S. Mishra, A. Peshkov, and S. Ramaswamy. Mesoscopic theory for fluctuating active nematics. *New J. Phys.*, **15**, 085032, 2013.

[112] B. J. Edwards, A. N. Beris, and M. Grmela. Generalized constitutive equation for polymeric liquid crystals Part 1. Model formulation using the Hamiltonian (poisson bracket) formulation. *J. Non-Newtonian Fluid Mech.*, **35**, 51–72,

1990.

[113] H. J. Wilson and S. M. Fielding. Linear instability of planar shear banded flow of both diffusive and non-diffusive Johnson-Segalman fluids. *J. Non-Newtonian Fluid Mech.*, **138**, 181–196, 2006.

[114] P. Martin, O. Parodi, and P. Pershan. Unified Hydrodynamic Theory for Crystals, Liquid Crystals, and Normal Fluids. *Phys. Rev. A*, **6**, 2401–2420, 1972.

[115] A. Kumar, A. Maitra, M. Sumit, S. Ramaswamy, and G. V. Shivashankar. Actomyosin contractility rotates the cell nucleus. *Sci. Rep.*, **4**, 3781, 2014.

[116] D. Marenduzzo, E. Orlandini, M. E. Cates, and J. M. Yeomans. Lattice Boltzmann simulations of spontaneous flow in active liquid crystals: The role of boundary conditions. *J. Non-Newtonian Fluid Mech.*, **149**, 56–62, 2008.

[117] S. Zhou, A. Sokolov, O. D. Lavrentovich, and I. S. Aranson. Living liquid crystals. *Proc. Natl. Acad. Sci. U. S. A.*, **111**, 1265–70, 2014.

[118] H. See, M. Doi, and R. G. Larson. The effect of steady flow fields on the isotropic-nematic phase transition of rigid rod-like polymers. *J. Chem. Phys.*, **92**, 792, 1990.

[119] P. D. Olmsted and S. T. Milner. Strain-Induced Nematic Phase Separation in Polymer Melts and Gels. *Macromolecules*, **27**, 6648–6660, 1994.

[120] D. A. Head, A. J. Levine, and F. C. MacKintosh. Deformation of cross-linked semiflexible polymer networks. *Phys. Rev. Lett.*, **91**, 108102, 2003.

[121] C. Storm, J. J. Pastore, F. C. MacKintosh, T. C. Lubensky, and P. A. Janmey. Nonlinear elasticity in biological gels. *Nature*, **435**, 191–4, 2005.

[122] P. Pullarkat, P. Fernandez, and A. Ott. Rheological properties of the Eukaryotic cell cytoskeleton. *Phys. Rep.*, **449**, 29–53, 2007.

[123] M. R. Mofrad. Rheology of the Cytoskeleton. *Annu. Rev. Fluid Mech.*, **41**, 433–453, 2009.

[124] M. Warner and E. M. Terentjev. *Liquid Crystal Elastomers*. International Series of Monographs on Physics. OUP Oxford, 2003.

[125] T. C. Lubensky, R. Mukhopadhyay, L. Radzihovsky, and X. Xing. Symmetries and elasticity of nematic gels. *Phys. Rev. E*, **66**, 011702, 2002.

[126] L. Cisneros, J. O. Kessler, S. Ganguly, and R. E. Goldstein. Dynamics of swimming bacteria: Transition to directional order at high concentration. *Phys. Rev. E*, **83**, 061907, 2011.

[127] Wolfram Research, Inc., Mathematica, Version 10.0, Champaign, IL, 2014.

[128] S. H. Strogatz. *Nonlinear Dynamics and Chaos: With Applications to Physics, Biology, Chemistry, and Engineering*. Studies in Nonlinearity. Westview Press, 2008.

[129] T. B. Liverpool and M. C. Marchetti. Instabilities of Isotropic Solutions of Active Polar Filaments. *Phys. Rev. Lett.*, **90**, 138102, 2003.

[130] A. Ahmadi, M. C. Marchetti, and T. B. Liverpool. Hydrodynamics of isotropic and liquid crystalline active polymer solutions. *Phys. Rev. E - Stat. Nonlinear, Soft Matter Phys.*, **74**, 1–23, 2006.

[131] L. Giomi, L. Mahadevan, B. Chakraborty, and M. Hagan. Banding, excitability and chaos in active nematic suspensions. *Nonlinearity*, **25**, 2245–2269, 2012.

[132] G. Salbreux, J.-F. Joanny, J. Prost, and P. Pullarkat. Shape oscillations of non-adhering fibroblast cells. *Phys. Biol.*, **4**, 268–284, 2007.

[133] V. Schaller, C. Weber, C. Semmrich, E. Frey, and A. R. Bausch. Polar patterns of driven filaments. *Nature*, **467**, 73–7, 2010.

[134] A. Aradian and M. E. Cates. Instability and spatiotemporal rheochaos in a shear-thickening fluid model. *Europhys. Lett.*, **70**, 397–403, 2004.

[135] X. Serra-Picamal, V. Conte, R. Vincent, E. Anon, D. T. Tambe, E. Bazellieres, J. P. Butler, J. J. Fredberg, and X. Trepat. Mechanical waves during tissue expansion. *Nat. Phys.*, **8**, 628–634, 2012.

[136] S. Banerjee, K. J. C. Utuje, and M. C. Marchetti. Propagating Stress Waves During Epithelial Expansion. *Phys. Rev. Lett.*, **114**, 1–5, 2015.

[137] G. Fenteany, P. A. Janmey, and T. P. Stossel. Signaling pathways and cell mechanics involved in wound closure by epithelial cell sheets. *Curr. Biol.*, **10**, 831–838, 2000.

[138] M. E. Cates and S. M. Fielding. Rheology of giant micelles. *Adv. Phys.*, **55**, 799–879, 2006.

[139] T. A. Waigh. Microrheology of complex fluids. *Reports Prog. Phys.*, **68**, 685–742, 2005.

[140] D. Mizuno, C. Tardin, C. F. Schmidt, and F. C. MacKintosh. Nonequilibrium mechanics of active cytoskeletal networks. *Science*, **315**, 370–3, 2007.

[141] G. Foffano, J. S. Lintuvuori, A. N. Morozov, K. Stratford, M. E. Cates, and D. Marenduzzo. Bulk rheology and microrheology of active fluids. *Eur. Phys. J. E. Soft Matter*, **35**, 9775, 2012.

[142] G. Foffano, J. S. Lintuvuori, K. Stratford, M. E. Cates, and D. Marenduzzo. Colloids in Active Fluids: Anomalous Microrheology and Negative Drag. *Phys. Rev. Lett.*, **109**, 028103, 2012.

[143] P. Nghe, E. Terriac, M. Schneider, Z. Z. Li, M. Cloitre, B. Abecassis, and P. Tabeling. Microfluidics and complex fluids. *Lab Chip*, **11**, 788–794, 2011.

[144] E. Jones, T. Oliphant, P. Peterson, et al. SciPy: Open source scientific tools for Python. `http://www.scipy.org`, 2001.

[145] T. E. Oliphant. Python for Scientific Computing. *Comput. Sci. Eng.*, **9**, 10–20, 2007.

[146] P. D. Olmsted and C.-Y. D. Lu. Phase separation of rigid-rod suspensions in shear flow. *Phys. Rev. E*, **60**, 4397–4415, 1999.

[147] Y. Renardy. Spurt and instability in a two-layer Johnson-Segalman liquid. *Theor. Comput. Fluid Dyn.*, **7**, 463–475, 1995.

[148] L. Giomi, T. B. Liverpool, and M. C. Marchetti. Sheared active fluids: Thickening, thinning, and vanishing viscosity. *Phys. Rev. E*, **81**, 051908, 2010.

[149] T. B. Liverpool and M. C. Marchetti. Rheology of active filament solutions. *Phys. Rev. Lett.*, **97**, 1–4, 2006.

[150] E. Eiser, F. Molino, G. Porte, and O. Diat. Nonhomogeneous textures and banded flow in a soft cubic phase under shear. *Phys. Rev. E*, **61**, 6759–6764, 2000.

[151] P. Glendinning. *Stability, Instability and Chaos: An Introduction to the Theory of Nonlinear Differential Equations*. Cambridge Texts in Applied Mathematics. Cambridge University Press, 1994.

[152] A. Aradian and M. E. Cates. Minimal model for chaotic shear banding in

shear thickening fluids. *Phys. Rev. E*, **73**, 041508, 2006.

[153] S. M. Fielding and P. D. Olmsted. Spatiotemporal Oscillations and Rheochaos in a Simple Model of Shear Banding. *Phys. Rev. Lett.*, **92**, 084502, 2004.

[154] B. Chakrabarti, M. Das, C. Dasgupta, S. Ramaswamy, and a. K. Sood. Spatiotemporal Rheochaos in Nematic Hydrodynamics. *Phys. Rev. Lett.*, **92**, 055501–, 2004.

[155] S. M. Fielding and P. D. Olmsted. Kinetics of the shear banding instability in startup flows. *Phys. Rev. E*, **68**, 036313, 2003.

[156] N. Kamiya. The protoplasmic flow in the myxomycete plasmodium as revealed by a volumetric analysis. *Protoplasma*, **39**, 344–357, 1950.

[157] P. G. Drazin and W. H. Reid. *Hydrodynamic Stability*. Cambridge University Press, second edition, 2004.

[158] X. L. Wu and A. Libchaber. Particle diffusion in a quasi-two-dimensional bacterial bath. *Phys. Rev. Lett.*, **84**, 3017–3020, 2000.

[159] F. C. Keber, E. Loiseau, T. Sanchez, S. J. DeCamp, L. Giomi, M. J. Bowick, M. C. Marchetti, Z. Dogic, and A. R. Bausch. Topology and dynamics of active nematic vesicles. *Science*, **345**, 1135–1139, 2014.

[160] H. Wioland, F. G. Woodhouse, J. Dunkel, J. O. Kessler, and R. E. Goldstein. Confinement stabilizes a bacterial suspension into a spiral vortex. *Phys. Rev. Lett.*, **110**, 5, 2013.

[161] E. Tjhung, D. Marenduzzo, and M. E. Cates. Spontaneous symmetry breaking in active droplets provides a generic route to motility. *Proc. Natl. Acad. Sci. U. S. A.*, **109**, 12381–6, 2012.

[162] G. D. Magistris, A. Tiribocchi, C. A. Whitfield, R. J. Hawkins, M. E. Cates, and D. Marenduzzo. Spontaneous motility of passive emulsion droplets in polar active gels. *Soft Matter*, **10**, 7826–7837, 2014.

[163] E. Tjhung, A. Tiribocchi, D. Marenduzzo, and M. E. Cates. A minimal physical model captures the shapes of crawling cells. *Nat. Commun.*, **6**, 5420, 2015.

[164] T. Lämmermann, B. L. Bader, S. J. Monkley, T. Worbs, R. Wedlich-Söldner, K. Hirsch, M. Keller, R. Förster, D. R. Critchley, R. Fässler, and M. Sixt.

Rapid leukocyte migration by integrin-independent flowing and squeezing. *Nature*, **453**, 51–55, 2008.

[165] S. R. K. Vedula, M. C. Leong, T. L. Lai, P. Hersen, A. J. Kabla, C. T. Lim, and B. Ladoux. Emerging modes of collective cell migration induced by geometrical constraints. *Proc. Natl. Acad. Sci. U. S. A.*, **109**, 12974–9, 2012.

[166] J. P. Hernandez-Ortiz, P. T. Underhill, and M. D. Graham. Dynamics of confined suspensions of swimming particles. *J. Phys. Condens. Matter*, **21**, 204107, 2009.

[167] N. Mermin. The topological theory of defects in ordered media. *Rev. Mod. Phys.*, **51**, 591–648, 1979.

[168] P. M. Chaikin and T. C. Lubensky. *Principles of Condensed Matter Physics*. Cambridge University Press, 2000.

[169] A. Bray. Theory of phase-ordering kinetics. *Adv. Phys.*, **43**, 357–459, 1994.

[170] G. Tóth, C. Denniston, and J. M. Yeomans. Hydrodynamics of topological defects in nematic liquid crystals. *Phys. Rev. Lett.*, **88**, 105504, 2002.

[171] L. Giomi, M. J. Bowick, X. Ma, and M. C. Marchetti. Defect Annihilation and Proliferation in Active Nematics. *Phys. Rev. Lett.*, **110**, 228101, 2013.

[172] J.-F. Joanny and J. Prost. Active gels as a description of the actin-myosin cytoskeleton. *HFSP J.*, **3**, 94–104, 2009.

[173] L. Giomi. The geometry and topology of turbulence in active nematics. *arXiv:1409.1555*, (preprint 2014).

[174] H. H. Wensink, J. Dunkel, S. Heidenreich, K. Drescher, R. E. Goldstein, H. Löwen, and J. M. Yeomans. Meso-scale turbulence in living fluids. *Proc. Natl. Acad. Sci. U. S. A.*, **109**, 14308–13, 2012.

[175] C. M. White and M. G. Mungal. Mechanics and Prediction of Turbulent Drag Reduction with Polymer Additives. *Annu. Rev. Fluid Mech.*, **40**, 235–256, 2008.

[176] S. P. Thampi, R. Golestanian, and J. M. Yeomans. Velocity Correlations in an Active Nematic. *Phys. Rev. Lett.*, **111**, 118101, 2013.

[177] S. P. Thampi, R. Golestanian, and J. M. Yeomans. Vorticity, defects and correlations in active turbulence. *Philos. Trans. A. Math. Phys. Eng. Sci.*,

372, 14, 2014.

[178] T. Vachaspati and A. Vilenkin. Formation and evolution of cosmic strings. *Phys. Rev. D*, **30**, 2036–2045, 1984.

[179] O. Reynolds. An Experimental Investigation of the Circumstances Which Determine Whether the Motion of Water Shall Be Direct or Sinuous, and of the Law of Resistance in Parallel Channels. *Philos. Trans. R. Soc. London*, **174**, 935–982, 1883.

[180] L. He, X. Wang, H. L. Tang, and D. J. Montell. Tissue elongation requires oscillating contractions of a basal actomyosin network. *Nat. Cell Biol.*, **12**, 1133–1142, 2010.

[181] K. Dierkes, A. Sumi, J. Solon, and G. Salbreux. Spontaneous Oscillations of Elastic Contractile Materials with Turnover. *Phys. Rev. Lett.*, **113**, 148102, 2014.

[182] S. P. Thampi, R. Golestanian, and J. M. Yeomans. Instabilities and topological defects in active nematics. *Europhys. Lett.*, **105**, 18001, 2014.

[183] S. M. Fielding, R. Larson, and M. E. Cates. Simple Model for the Deformation-Induced Relaxation of Glassy Polymers. *Phys. Rev. Lett.*, **108**, 048301, 2012.

[184] Z. Dogic, J. Zhang, A. Lau, H. Aranda-Espinoza, P. Dalhaimer, D. E. Discher, P. Janmey, R. Kamien, T. C. Lubensky, and A. Yodh. Elongation and Fluctuations of Semiflexible Polymers in a Nematic Solvent. *Phys. Rev. Lett.*, **92**, 125503, 2004.

[185] F. Nédélec, T. Surrey, A. C. Maggs, and S. Leibler. Self-organization of microtubules and motors. *Nature*, **389**, 305–8, 1997.

[186] K. Kruse, J.-F. Joanny, F. Jülicher, J. Prost, and K. Sekimoto. Asters, Vortices, and Rotating Spirals in Active Gels of Polar Filaments. *Phys. Rev. Lett.*, **92**, 078101, 2004.

[187] J. Elgeti, M. E. Cates, and D. Marenduzzo. Defect hydrodynamics in 2D polar active fluids. *Soft Matter*, **7**, 3177, 2011.

[188] X. Yang, D. Marenduzzo, and M. C. Marchetti. Spiral and never-settling patterns in active systems. *Phys. Rev. E - Stat. Nonlinear, Soft Matter Phys.*, **89**, 012711, 2014.

[189] M. J. Bowick, L. Chandar, E. A. Schiff, and A. M. Srivastava. The Cosmological Kibble Mechanism in the Laboratory: String Formation in Liquid Crystals. *Science*, **263**, 943–945, 1994.

[190] D. Huterer and T. Vachaspati. Distribution of singularities in the cosmic microwave background polarization. *Phys. Rev. D*, **72**, 043004, 2005.

[191] J. R. Philip. Flow in Porous Media. *Annu. Rev. Fluid Mech.*, **2**, 177–204, 1970.

[192] A. C. Payatakes. Dynamics of Oil Ganglia During Immiscible Displacement in Water-Wet Porous Media. *Annu. Rev. Fluid Mech.*, **14**, 365–393, 1982.

[193] T. Sochi. Flow of non-newtonian fluids in porous media. *J. Polym. Sci. Part B Polym. Phys.*, **48**, 2437–2767, 2010.

[194] A. Clarke, A. M. Howe, J. Mitchell, J. Staniland, L. Hawkes, and K. Leeper. Mechanism of anomalously increased oil displacement with aqueous viscoelastic polymer solutions. *Soft Matter*, **11**, 3536–3541, 2015.

[195] L. Skartsis, B. Khomami, and J. L. Kardos. Resin flow through fiber beds during composite manufacturing processes. Part II: Numerical and experimental studies of newtonian flow through ideal and actual fiber beds. *Polym. Eng. Sci.*, **32**, 231–239, 1992.

[196] A. W. Liu. *Viscoelastic flow of polymer solutions around arrays of cylinders: comparison of experiment and theory.* PhD thesis, Massachusetts Institute of Technology, 1997.

[197] F. J. Galindo-Rosales, L. Campo-Deaño, F. T. Pinho, E. Bokhorst, P. J. Hamersma, M. S. Oliveira, and M. A. Alves. Microfluidic systems for the analysis of viscoelastic fluid flow phenomena in porous media. *Microfluid. Nanofluidics*, **12**, 485–498, 2011.

[198] E. S. G. Shaqfeh. Purely Elastic Instabilities in Viscometric Flows. *Annu. Rev. Fluid Mech.*, **28**, 129–185, 1996.

[199] M. A. Hulsen, R. Fattal, and R. Kupferman. Flow of viscoelastic fluids past a cylinder at high Weissenberg number: Stabilized simulations using matrix logarithms. *J. Non-Newtonian Fluid Mech.*, **127**, 27–39, 2005.

[200] H. D'arcy. *Les fontaines publiques de la ville de Dijon.* Dalmont, Paris, 1856.

[201] P. C. Carman. Fluid flow through granular beds. *Chem. Eng. Res. Des.*, **15**, 32–48, 1937.

[202] A. Sangani and A. Acrivos. Slow flow past periodic arrays of cylinders with application to heat transfer. *Int. J. Multiph. Flow*, **8**, 193–206, 1982.

[203] R. E. Larson and J. J. L. Higdon. Microscopic flow near the surface of two-dimensional porous media. Part 2. Transverse flow. *J. Fluid Mech.*, **178**, 119, 1987.

[204] C. Chmielewski. The effect of polymer extensibility on crossflow of polymer solutions through cylinder arrays. *J. Rheol.*, **36**, 1105, 1992.

[205] L. Skartsis. Polymeric flow through fibrous media. *J. Rheol.*, **36**, 589, 1992.

[206] R. Chhabra, P. Uhlherr, and D. Boger. The influence of fluid elasticity on the drag coefficient for creeping flow around a sphere. *J. Non-Newtonian Fluid Mech.*, **6**, 187–199, 1980.

[207] G. R. Moss and J. P. Rothstein. Flow of wormlike micelle solutions through a periodic array of cylinders. *J. Non-Newtonian Fluid Mech.*, **165**, 1–13, 2010.

[208] J. J. J. Gillissen. Viscoelastic flow simulations through an array of cylinders. *Phys. Rev. E*, **87**, 023003, 2013.

[209] K. K. Talwar and B. Khomami. Flow of viscoelastic fluids past periodic square arrays of cylinders: inertial and shear thinning viscosity and elasticity effects. *J. Non-Newtonian Fluid Mech.*, **57**, 177–202, 1995.

[210] A. Souvaliotis and A. N. Beris. Spectral collocation/domain decomposition method for viscoelastic flow simulations in model porous geometries. *Comput. Methods Appl. Mech. Eng.*, **129**, 9–28, 1996.

[211] P. J. Oliveira and A. I. Miranda. A numerical study of steady and unsteady viscoelastic flow past bounded cylinders. *J. Non-Newtonian Fluid Mech.*, **127**, 51–66, 2005.

[212] M. Smith, Y. Joo, R. C. Armstrong, and R. A. Brown. Linear stability analysis of flow of an Oldroyd-B fluid through a linear array of cylinders. *J. Non-Newtonian Fluid Mech.*, **109**, 13–50, 2003.

[213] M. Sahin and H. J. Wilson. A parallel adaptive unstructured finite volume method for linear stability (normal mode) analysis of viscoelastic fluid flows.

J. Non-Newtonian Fluid Mech., **155**, 1–14, 2008.

[214] M. Grilli, A. Vázquez-Quesada, and M. Ellero. Transition to Turbulence and Mixing in a Viscoelastic Fluid Flowing Inside a Channel with a Periodic Array of Cylindrical Obstacles. *Phys. Rev. Lett.*, **110**, 174501, 2013.

[215] P. E. Øren and S. Bakke. Reconstruction of Berea sandstone and pore-scale modelling of wettability effects. *J. Pet. Sci. Eng.*, **39**, 177–199, 2003.

[216] A. C. (Schlumberger). Private communication, 2014.

[217] G. H. McKinley, R. C. Armstrong, and R. A. Brown. The Wake Instability in Viscoelastic Flow past Confined Circular Cylinders. *Philos. Trans. R. Soc. A Math. Phys. Eng. Sci.*, **344**, 265–304, 1993.

[218] J. L. Duda, S. A. Hong, and E. E. Klaus. Flow of polymer solutions in porous media: inadequacy of the capillary model. *Ind. Eng. Chem. Fundam.*, **22**, 299–305, 1983.

[219] C. S. Peskin. *Flow Patterns Around Heart Valves: A Digital Computer Method for Solving the Equations of Motion*. PhD thesis, Yeshiva University, 1972.

[220] C. S. Peskin. The immersed boundary method. *Acta Numer.*, **11**, 479–517, 2002.

[221] R. Mittal and G. Iaccarino. Immersed Boundary Methods. *Annu. Rev. Fluid Mech.*, **37**, 239–261, 2005.

[222] R. P. Beyer and R. J. LeVeque. Analysis of a One-Dimensional Model for the Immersed Boundary Method. *SIAM J. Numer. Anal.*, **29**, 332–364, 1992.

[223] E. Saiki and S. Biringen. Numerical Simulation of a Cylinder in Uniform Flow: Application of a Virtual Boundary Method. *J. Comput. Phys.*, **123**, 450–465, 1996.

[224] M.-C. Lai and C. S. Peskin. An Immersed Boundary Method with Formal Second-Order Accuracy and Reduced Numerical Viscosity. *J. Comput. Phys.*, **160**, 705–719, 2000.

[225] A. L. Fogelson and C. S. Peskin. A fast numerical method for solving the three-dimensional stokes' equations in the presence of suspended particles. *J. Comput. Phys.*, **79**, 50–69, 1988.

[226] O. Faxen. Forces exerted on a rigid cylinder in a viscous fluid between two

parallel fixed planes. *Proc. R. Swed. Acad. Eng. Sci.*, **187**, 1–13, 1946.

[227] M. Ellero and N. A. Adams. SPH simulations of flow around a periodic array of cylinders confined in a channel. *Int. J. Numer. Methods Eng.*, **86**, 1027–1040, 2011.

[228] Webplotdigitizer: software for extracting data from graphs. `http://arohatgi.info/WebPlotDigitizer/`. Accessed: 2014-10-15.

[229] J. P. Morris, P. J. Fox, and Y. Zhu. Modeling Low Reynolds Number Incompressible Flows Using SPH. *J. Comput. Phys.*, **136**, 214–226, 1997.

[230] M. A. Alves, F. Pinho, and P. J. Oliveira. The flow of viscoelastic fluids past a cylinder: finite-volume high-resolution methods. *J. Non-Newtonian Fluid Mech.*, **97**, 207–232, 2001.

[231] P. D. M. Spelt, T. Selerland, C. J. Lawrence, and P. D. Lee. Flows of inelastic non-Newtonian fluids through arrays of aligned cylinders. Part 1. Creeping flows. *J. Eng. Math.*, **51**, 57–80, 2005.

[232] A. G. Lee, E. S. G. Shaqfeh, and B. Khomami. A study of viscoelastic free surface flows by the finite element method: HeleShaw and slot coating flows. *J. Non-Newtonian Fluid Mech.*, **108**, 327–362, 2002.

[233] B. Thomases and M. J. Shelley. Emergence of singular structures in Oldroyd-B fluids. *Phys. Fluids*, **19**, 103103, 2007.

[234] B. Thomases, M. J. Shelley, and J.-L. Thiffeault. A Stokesian viscoelastic flow: Transition to oscillations and mixing. *Phys. D Nonlinear Phenom.*, **240**, 1602–1614, 2011.

[235] G. R. Moss and J. P. Rothstein. Flow of wormlike micelle solutions past a confined circular cylinder. *J. Non-Newtonian Fluid Mech.*, **165**, 1505–1515, 2010.

[236] S. Claus and T. Phillips. Viscoelastic flow around a confined cylinder using spectral/hp element methods. *J. Non-Newtonian Fluid Mech.*, **200**, 131–146, 2013.

[237] M. Sahin. Parallel large-scale numerical simulations of purely-elastic instabilities behind a confined circular cylinder in a rectangular channel. *J. Non-Newtonian Fluid Mech.*, **195**, 46–56, 2013.

[238] H. Tanaka and T. Araki. Simulation Method of Colloidal Suspensions with Hydrodynamic Interactions: Fluid Particle Dynamics. *Phys. Rev. Lett.*, **85**, 1338–1341, 2000.

[239] R. Matas-Navarro, R. Golestanian, T. B. Liverpool, and S. M. Fielding. Hydrodynamic suppression of phase separation in active suspensions. *Phys. Rev. E*, **90**, 032304, 2014.

[240] J. F. Brady and G. Bossis. Stokesian Dynamics. *Annu. Rev. Fluid Mech.*, **20**, 111–157, 1988.

[241] A. R. Parker and C. R. Lawrence. Water capture by a desert beetle. *Nature*, **414**, 33–34, 2001.

[242] D. L. Hu, B. Chan, and J. W. M. Bush. The hydrodynamics of water strider locomotion. *Nature*, **424**, 663–666, 2003.

[243] N. Morrow. Wettability and Its Effect on Oil Recovery. *J. Pet. Technol.*, **42**, 1476–1484, 1990.

[244] P. Tabeling and S. Chen. *Introduction to Microfluidics*. OUP Oxford, 2010.

[245] D. Bonn, J. Eggers, J. Indekeu, and J. Meunier. Wetting and spreading. *Rev. Mod. Phys.*, **81**, 739–805, 2009.

[246] K. S. Lee, N. Ivanova, V. M. Starov, N. Hilal, and V. Dutschk. Kinetics of wetting and spreading by aqueous surfactant solutions. *Adv. Colloid Interface Sci.*, **144**, 54–65, 2008.

[247] C. Huh and L. E. Scriven. Hydrodynamic model of steady movement of a solid/liquid/fluid contact line. *J. Colloid Interface Sci.*, **35**, 85–101, 1971.

[248] P. G. De Gennes. Wetting: Statics and dynamics. *Rev. Mod. Phys.*, **57**, 827–863, 1985.

[249] L. D. Landau and E. M. Lifshitz. *Fluid Mechanics*. Course of Theoretical Physics, Vol. 6. Butterworth-Heinemann, 2 edition, 1987.

[250] M.-Y. Zhou and P. Sheng. Dynamics of immiscible-fluid displacement in a capillary tube. *Phys. Rev. Lett.*, **64**, 882–885, 1990.

[251] P. D. M. Spelt. A level-set approach for simulations of flows with multiple moving contact lines with hysteresis. *J. Comput. Phys.*, **207**, 389–404, 2005.

[252] M. Renardy, Y. Renardy, and J. Li. Numerical simulation of moving contact

line problems using a volume-of-fluid method. *J. Comput. Phys.*, **171**, 243–263, 2001.

[253] D. M. Anderson, G. B. McFadden, and A. A. Wheeler. Diffuse-interface methods in fluid mechanics. *Annu. Rev. Fluid Mech.*, **30**, 139–165, 1998.

[254] A. J. Briant, A. J. Wagner, and J. M. Yeomans. Lattice Boltzmann simulations of contact line motion. I. Liquid-gas systems. *Phys. Rev. E - Stat. Nonlinear, Soft Matter Phys.*, **69**, 031602, 2004.

[255] C. M. Pooley, H. Kusumaatmaja, and J. M. Yeomans. Modelling capillary filling dynamics using lattice Boltzmann simulations. *Eur. Phys. J. Spec. Top.*, **171**, 63–71, 2009.

[256] F. Diotallevi, L. Biferale, S. Chibbaro, G. Pontrelli, F. Toschi, and S. Succi. Lattice Boltzmann simulations of capillary filling: Finite vapour density effects. *Eur. Phys. J. Spec. Top.*, **171**, 237–243, 2009.

[257] R. G. Cox. The dynamics of the spreading of liquids on a solid surface. Part 1. Viscous flow. *J. Fluid Mech.*, **168**, 169, 1986.

[258] H.-Y. Chen, D. Jasnow, and J. Viñals. Interface and Contact Line Motion in a Two Phase Fluid under Shear Flow. *Phys. Rev. Lett.*, **85**, 1686–1689, 2000.

[259] J. W. Cahn. Critical point wetting. *J. Chem. Phys.*, **66**, 3667, 1977.

[260] C. M. Pooley, H. Kusumaatmaja, and J. M. Yeomans. Contact line dynamics in binary lattice Boltzmann simulations. *Phys. Rev. E - Stat. Nonlinear, Soft Matter Phys.*, **78**, 1–9, 2008.

[261] D. Jacqmin. Calculation of Two-Phase Navier-Stokes Flows Using Phase-Field Modeling. *J. Comput. Phys.*, **155**, 96–127, 1999.

[262] H. Kusumaatmaja, E. J. Hemingway, and S. M. Fielding. Moving contact line dynamics: from diffuse to sharp interfaces. pages 1–24, 2015.

[263] D. Eyre. An unconditionally stable one-step scheme for gradient systems. *Unpubl. Artic.*, pages 1–15, 1998.

[264] F. Guillén-González and G. Tierra. On linear schemes for a Cahn-Hilliard diffuse interface model. *J. Comput. Phys.*, **234**, 140–171, 2013.

[265] A. J. C. Ladd and R. Verberg. Lattice-Boltzmann Simulations of Particle-Fluid Suspensions. *J. Stat. Phys.*, **104**, 1191–1251, 2001.

[266] K. Van Gestel, R. H. Köhler, and J.-P. Verbelen. Plant mitochondria move on F-actin, but their positioning in the cortical cytoplasm depends on both F-actin and microtubules. *J. Exp. Bot.*, **53**, 659–667, 2002.

[267] S. Ganguly, L. S. Williams, I. M. Palacios, and R. E. Goldstein. Cytoplasmic streaming in Drosophila oocytes varies with kinesin activity and correlates with the microtubule cytoskeleton architecture. *Proc. Natl. Acad. Sci.*, **109**, 15109–15114, 2012.

[268] H. Yatou. Flow pattern transition accompanied with sudden growth of flow resistance in two-dimensional curvilinear viscoelastic flows. *Phys. Rev. E - Stat. Nonlinear, Soft Matter Phys.*, **82**, 036310, 2010.

[269] J. Zilz, R. J. Poole, M. A. Alves, D. Bartolo, B. Levaché, and A. Lindner. Geometric scaling of a purely elastic flow instability in serpentine channels. *J. Fluid Mech.*, **712**, 203–218, 2012.

[270] A. E. Likhtman and R. S. Graham. Simple constitutive equation for linear polymer melts derived from molecular theory: Rolie-Poly equation. *J. Non-Newtonian Fluid Mech.*, **114**, 1–12, 2003.

[271] T. Reis and H. J. Wilson. Rolie-Poly fluid flowing through constrictions: Two distinct instabilities. *J. Non-Newtonian Fluid Mech.*, **195**, 77–87, 2013.

[272] D. G. A. L. Aarts, R. P. A. Dullens, H. N. W. Lekkerkerker, D. Bonn, and R. van Roij. Interfacial tension and wetting in colloidpolymer mixtures. *J. Chem. Phys.*, **120**, 1973, 2004.

[273] S. A. Setu, R. P. Dullens, A. Hernández-Machado, I. Pagonabarraga, D. G. Aarts, and R. Ledesma-Aguilar. Superconfinement tailors fluid flow at microscales. *Nat. Commun.*, **6**, 7297, 2015.

[274] S. R. Hodges, O. E. Jensen, and J. M. Rallison. Sliding, slipping and rolling: the sedimentation of a viscous drop down a gently inclined plane. *J. Fluid Mech.*, **512**, 95–131, 2004.